



Pedro Miguel Pinto Gonçalves Gouveia Pedrosa

Mestre em Genética Molecular e Biomedicina

Gold Nanoparticles to Tackle Drug Resistance in Cancer

Dissertação para obtenção do Grau de Doutor em
Biociências Moleculares

Orientador: Prof. Doutora Maria Alexandra Núncio de Carvalho Ramos
Fernandes, Professora Auxiliar, Faculdade de Ciências e Tecnologia da
Universidade Nova de Lisboa.

Co-orientador: Prof. Doutor Pedro Miguel Ribeiro Viana Baptista,
Professor Catedrático, Faculdade de Ciências e Tecnologia da
Universidade Nova de Lisboa

Júri:

Presidente: Doutor Paulo Manuel Assis Loureiro Limão Vieira

Arguentes: Prof. Doutor Nuno Fernando Duarte Cordeiro Correia dos Santos
Prof. Doutor Lino da Silva Ferreira

Vogais: Prof. Doutor Armando José Latourrette de Oliveira Pombeiro

Prof. Doutor João Carlos dos Santos Silva e Pereira de Lima

Prof. Doutora Maria Alexandra Núncio de Carvalho Ramos Fernandes



Julho de 2019

Pedro Miguel Pinto Gonçalves Gouveia Pedrosa

Mestre em Genética Molecular e Biomedicina

Gold Nanoparticles to Tackle Drug Resistance in Cancer

Dissertação para obtenção do Grau de Doutor em
Biociências Moleculares

Orientador: Prof. Doutora Maria Alexandra Núncio de Carvalho Ramos Fernandes, Professora Auxiliar, Faculdade de Ciências e Tecnologia da Universidade Nova de Lisboa.

Co-orientador: Prof. Doutor Pedro Miguel Ribeiro Viana Baptista, Professor Catedrático, Faculdade de Ciências e Tecnologia da Universidade Nova de Lisboa

Júri:

Presidente: Doutor Paulo Manuel Assis Loureiro Limão Vieira

Arguentes: Prof. Doutor Nuno Fernando Duarte Cordeiro Correia dos Santos
Prof. Doutor Lino da Silva Ferreira

Vogais: Prof. Doutor Armando José Latourrette de Oliveira Pombeiro
Prof. Doutor João Carlos dos Santos Silva e Pereira de Lima
Prof. Doutora Maria Alexandra Núncio de Carvalho Ramos Fernandes

Julho de 2019

COPYRIGHT

Autorizo os direitos de copyright da minha tese de doutoramento, com o título:

“Gold Nanoparticles to Tackle Drug Resistance in Cancer”.

A Faculdade de Ciências e Tecnologia e a Universidade Nova de Lisboa têm o direito, perpétuo e sem limites geográficos, de arquivar e publicar esta dissertação através de exemplares impressos reproduzidos em papel ou de forma digital, ou por qualquer outro meio conhecido ou que venha a ser inventado, e de a divulgar através de repositórios científicos e de admitir a sua cópia e distribuição com objetivos educacionais ou de investigação, não comerciais, desde que seja dado crédito ao autor e editor.

ACKNOWLEDGEMENTS

Começo por agradecer à Fundação para a Ciência e Tecnologia pelo financiamento a esta tese PD/BD/105734/2014, às instituições que me acolheram no programa doutoral em Biociências Moleculares e providenciaram todos os meios necessários ao desenvolvimento desta tese. Ao departamento de Ciências da Vida, à Faculdade de Ciências e Tecnologia, às unidades de investigação UCIBIO e ao ITQB da Universidade NOVA de Lisboa.

A execução deste projeto só foi possível com a participação de várias pessoas. Pelo seu contributo intelectual, de trabalho, e motivação. Por tudo o que não está visível ao longo dos capítulos, mas sem o qual eles não fariam sentido. Porque o mais importante é invisível aos olhos.

Deixo um agradecimento aos meus orientadores Alexandra e Pedro, por me proporcionarem todas as condições para a realização desta tese. Por todas as discussões científicas e não científicas; por tudo o que aprendi convosco e por serem uma peça importante do meu desenvolvimento académico e pessoal. Pelas oportunidades, pela amizade e pela confiança. À Alexandra por me ter acolhido como orientando, debaixo da sua asa, por ouvir, motivar e cuidar. Ao Pedro pela energia de todos os dias; pelas ideias frutíferas e loucas e que resultaram nesta tese; obrigado aos dois pelo caminho que fizemos juntos e do qual me orgulho. Ao Prof. João Carlos Lima pela capacidade ímpar de ensinar; pelas discussões científicas, pela paciência, pelo prazer que é aprender consigo.

Obrigado aos meus companheiros de jornada, Fábio, Bruno, Raquel, Sara, Rita Cabral, Milton, Rita Mendes, Ana Sofia, Ana Cordeiro, Letícia, Larginho, Catarina, Luís, pelo sentido que deram ao dia a dia. A todos os alunos de licenciatura, mestrado e intercâmbios, que passaram pelos laboratórios 315 e 319, com os quais tive oportunidade de aprender. Aos meus colegas do programa doutoral de biociências moleculares. Obrigado me terem proporcionado momentos memoráveis de diversão. Um beijinho especial à Raquel pelas gargalhadas que se ouvem desde os corredores, e um abraço especial ao Bruno e ao Fábio pela amizade. Pelas horas e horas de conversas, partilhas e silêncios. Pelas saudades que ficarão sempre daqueles tempos. E, acima de tudo, por estarem sempre lá.

Alguns talvez não saibam o papel fundamental que tiveram neste percurso. Para eles guardo este espaço, para lhes dar o devido reconhecimento. Aos meus pais, irmão e avós, por terem feito de mim aquilo que sou. Por me mimarem, cuidarem e me ensinarem aquilo que não vem nos livros, no google, nem no youtube. À Márcia, pelo carinho, amor e paciência incansáveis, de aturar um pinguim que as vezes tem mau feitio.

“Cada um que passa na nossa vida, passa sozinho, mas não vai só, nem nos deixa só; deixa um pouco de si, leva um pouco de nós”

Antoine de Saint-Exupéry

RESUMO

A quimioterapia é a forma mais comum de tratamento de cancro, contudo falha frequentemente devido à aquisição de resistência celular. É urgente o avanço na compreensão dos mecanismos celulares de resistência celular, bem como de novas estratégias ao seu combate. A nanomedicina, têm desenvolvido novas ferramentas para o diagnóstico e tratamento do cancro. Nesta tese explorámos cinco estratégias para ultrapassar a resistência adquirida a fármacos: i) novos compostos anticancerígenos, ii) nanovetorização e direcionamento de compostos, iii) hipertermia com nanopartículas de ouro (AuNP) e sua combinação com quimioterapia, iv) bloqueio da angiogénese, através de quimioterapia, AuNP e radiação laser, v) silenciamento genético de bombas de efluxo mediado por AuNP.

Começámos por caracterizar o mecanismo de ação de um novo composto anti tumoral (ZnD), que mostrou elevada toxicidade em células derivadas de cancro do colon (HCT116 DR) resistente a doxorubicina, um fármaco de primeira linha. Vetorizámos o ZnD utilizando AuNP, resultando num aumento de toxicidade em xenógrafos de HCT116 DR em ratinho. Tirando vantagem das propriedades foto térmicas das AuNP, combinámos quimioterapia com foto-hipertermia de radiação visível, revelando-se eficaz contra HCT116 DR. Sendo a angiogénese um dos marcos do desenvolvimento cancerígeno, procurámos comprometê-la utilizando um péptido anti-angiogénico, vetorizado em AuNP conjuntamente com irradiação laser. Conseguimos com esta estratégia uma redução de 91% de vascularização *in vivo*. Tentámos também silenciar o ARN mensageiro da bomba de efluxo ABCB1, causa principal de resistência à doxorubicina, através de AuNP funcionalizadas com oligonucleótidos complementares. Concluímos que apesar do silenciamento ser efetivo, as células não voltavam ao fenótipo sensível, necessitando de mais estudos.

No geral, esta tese mostra o potencial da nanotecnologia no tratamento do cancro, tanto através da quimioterapia, como de técnicas de cirurgia, onde os lasers verdes já são utilizados. Este trabalho, pode ser aplicado a tumores resistentes a fármacos, aumentando a eficácia do tratamento.

Termos-chave: Cancro; Nanopartículas de Ouro; Nanomedicina; Fototerapia; Hipertermia; Resistência Fármacos.

ABSTRACT

The most common type of cancer treatment, chemotherapy, often fails due to the acquisition of resistance. It is therefore of the utmost importance to better understand the cellular mechanisms of resistance, while developing new strategies to tackle drug resistance. Nanomedicine promises to develop new tools for diagnosing and treating of diseases, improving human health. This thesis explored five main strategies to overcome drug resistance in cancer cells: i) new anti-cancer compounds, ii) nanovectorisation and targeting of compounds, iii) gold nanoparticles (AuNP) for hyperthermia and combination with chemotherapy iv) AuNP assisted angiogenesis arrest with laser ablation and chemotherapy v) AuNP mediated gene silencing of efflux pumps.

We started by characterizing the mechanism of action of a new anti-tumour compound (ZnD), that was able to reduce the viability of a colon cancer cell line (HCT116 DR) resistant to doxorubicin (DOX), a first-line chemotherapeutic. We vectorized our compound with AuNP, resulting in increased toxicity to HCT116 DR mouse xenografts. Taking advantage of the photothermal properties of AuNP, we combined chemotherapy with photo hyperthermia by irradiating AuNP with a green laser. Hyperthermia was especially effective against HCT116 DR.

Since angiogenesis is a milestone in cancer development, we aimed to prevent it, using an anti-angiogenic peptide vectorized with AuNP and laser irradiation, resulting in a vascularization reduction of 91% *in vivo*. We have observed that ABCB1 efflux pump was the major cause of resistance of DOX resist cell line, therefore we silenced its mRNA with an anti-sense oligonucleotide AuNP. Our results showed that although the silencing was effective, cells did not return to a sensitive phenotype, requiring further experiments.

Altogether this thesis shows the potential of nanotechnology for cancer treatment, both in chemotherapy and in surgery, where green lasers are already used. This work can be applied to drug resistant tumours, increasing the efficacy of treatment.

Keywords: Cancer; gold nanoparticles; Nanomedicine; Phototherapy; Hyperthermia; Drug Resistance.

LIST OF PUBLICATIONS

Included in this thesis:

- **Pedrosa P**, Vinhas R, Fernandes A, Baptista PV. Gold Nanotheranostics: Proof-of-Concept or Clinical Tool?. *Nanomaterials*. 2015, 5(4):1853-1879 DOI: 10.3390/nano5041853
- **Pedrosa P**, Heuer-Jungemann A, Kanaras AG, Baptista PV. Potentiating angiogenesis arrest *in vivo* via laser irradiation of peptide functionalised gold nanoparticles. *Journal of Nanobiotechnology*. 2017, 15:85 DOI: 10.1186/s12951-017-0321-2
- Mendes R, **Pedrosa P**, Lima JC, Fernandes AR, Baptista PV. Photothermal enhancement of chemotherapy in breast cancer by visible irradiation of Gold Nanoparticles. *Scientific Reports*. 2017, 7(7):10872 DOI: 10.1038/s41598-017-11491-8
- **Pedrosa P**, Mendes R, Cabral R, Martins L, Baptista PV, Fernandes AR. Combination of chemotherapy and Au-nanoparticle phototherapy in the visible light to tackle doxorubicin resistance in cancer cells. *Scientific Reports*. 2018, 8:11429 DOI: 10.1038/s41598-018-29870-0
- **Pedrosa P**, Carvalho A, Baptista PV, Fernandes AR. Inorganic Coordination Chemistry: where we stand in cancer treatment? In *Basic Concepts Viewed from Frontier in Inorganic Coordination Chemistry*. Edited by Dr. Takashiro Akitsu. IntechOpen. 2018 DOI: 10.5772/intechopen.80233
- **Pedrosa P**, Corvo ML, Ferreira-Silva M, Martins P, Cola MC, Costa P, Martins C, Martins LMDR, Baptista PV, Fernandes AR. Targeting cancer resistance via multifunctional gold-nanoparticles: Cetuximab for improving delivery. *International Journal of Molecular Sciences*. 2019, 20(21): 5510 DOI: 10.3390/ijms20215510
- Rodrigues C, Raposo L, Pombo I, **Pedrosa P**, Fernandes AR, Baptista PV. Nanotheranostics targeting the tumour microenvironment. *Frontiers in Bioengineering and Biotechnology*. 2019, 7:197 DOI: 10.3389/fbioe.2019.00197
- **Pedrosa P**, Lima JC, Fernandes AR, Baptista PV. Temperature and salt mediated semi-reversible aggregation of PEG coated gold nanoparticles. 2020 (in preparation)

LIST OF ABBREVIATIONS

- 2D – two-dimensional
- 3D – Three Dimensional
- AGR2 – Anterior Gradient 2
- ASO – Antisense Oligonucleotides
- AuNP – Gold nanoparticles
- BSA – Bovine Serum Albumin
- CAM – Chorioallantoic Membrane
- CoD – $[\text{CoCl}(\text{H}_2\text{O})(1,10\text{-phenanthroline-5,6-dione})_2][\text{BF}_4]$
- CT – Computed Tomography
- CTCF – Corrected Total Cell Fluorescence
- DLS – Dynamic Light Scattering
- DMEM – Dulbecco's Modified Eagle Medium
- DMSO – Dimethyl sulfoxide
- DOX – Doxorubicin
- DTT – Dithiothreitol
- EDC – N-(3-Dimethylaminopropyl)-N'-ethylcarbodiimide hydrochloride
- EDTA – Ethylenediaminetetraacetic Acid
- EGFR – Epidermal Growth Factor Receptor
- EMA – European Medicines Agency
- EPR – Enhanced Permeability Retention
- FBS – Fetal Bovine Serum
- FDA – Food Drug Administration
- FITC – Fluorescein Isothiocyanate
- FLT-1 – Fms Related Tyrosine Kinase 1
- HER2 – Human Epidermal Growth Factor Receptor 2
- HIF – Hypoxia-Induced Factor
- HIV – Human Immunodeficiency Virus
- HSPs – heat shock proteins
- ICP-MS – Inductively Coupled Plasma Mass Spectrometry
- IL – Interleukins
- JC-1 – 5,5,6,6-tetrachloro-1,1,3,3 tetraethylbenzimidazolylcarbocyanine iodide
- MDR – Multidrug Resistance
- MDR1 – Multidrug Resistance Protein 1
- MES – 2-Morpholinoethanesulfonic acid monohydrate,
- MMP – Matrix Metalloproteinases

MRI – Magnetic Resonance Imaging
MRP1 – Multidrug Resistance-Associated Protein 1
MTS – 3-(4,5-dimethylthiazol-2-yl)-5-(3-carboxymethoxyphenyl)-2-(4-sulfophenyl)-2H-tetrazolium
NADH – Nicotinamide adenine dinucleotide
NanoZnD – AuNP@PEG@BSA@ZnD@CETUXIMAB
NHS – N-Hydroxysuccinimide
NIR – Near-Infrared
NRP-1 – Neuropilin-1 Receptor
NSCLC – Non-Small Cell Lung Cancer
PBS – Phosphate Buffer Saline
PEG – Poly-Ethylene Glycol
PET – Positron Emission Tomography
PhenDION – 1,10-phenanthroline-5,6-dione
PI – Propidium Iodide
PMSF – Phenylmethylsulfonyl Fluoride
PNB – Plasmonic Nanobubbles
PTT – Photothermal Therapy
R&D – Research & Development
rhTNF – Recombinant Human Tumour Necrosis Factor Alpha
ROS – Reactive oxygen species
RPMI – Roswell Park Memorial Institute 1640 medium
SCLC – Small Cell Lung Cancer
SDS – Sodium Dodecyl Sulphate
SPECT – Photon Emission Computed Tomography
TAE – Tris Acetate EDTA
TAMRA – Tetramethylrhodamine
TEM – Transmission Electron Microscopy
TGF - Transforming Growth Factor
US – Ultrasound
UV-Vis – Ultraviolet Visible
VEGF – Vascular Endothelial Growth Factor
VEGFR – Vascular Endothelial Growth Factor Receptor
ZnD – [Zn(1,10-phenanthroline-5,6-dione)₂]Cl₂

TABLE OF CONTENTS

ACKNOWLEDGEMENTS	V
RESUMO.....	VII
ABSTRACT	IX
LIST OF PUBLICATIONS	XI
LIST OF ABBREVIATIONS	XIII
TABLE OF CONTENTS	XV
LIST OF FIGURES	XIX
LIST OF TABLES	XXIII
LIST OF EQUATIONS.....	XXV
CHAPTER 1 – INTRODUCTION.....	1
1.1 CANCER	2
1.2 CANCER PROGRESSION.....	3
1.2.1 Sustaining proliferative signalling	4
1.2.2 Evading growth suppressors	5
1.2.3 Evading programmed cell death	5
1.2.4 Enabling replicative immortality.....	5
1.2.5 Tumour microenvironment and energy metabolism.....	6
1.2.6 Inducing angiogenesis.....	7
1.2.7 Evading the immune system	8
1.2.8 Activating Invasion and Metastasis.....	9
1.3 DIFFERENT TYPES OF COLORECTAL, LUNG AND BREAST CANCER	10
1.4 CANCER THERAPY	12
1.4.1 Surgery.....	12
1.4.2 Radiotherapy.....	12
1.4.3 Chemotherapy.....	13
1.4.4 Immunotherapy.....	16
1.4.5 Gene therapy.....	17
1.4.6 Thermal therapy.....	19
1.5 CANCER RESISTANCE TO TREATMENT	20
1.6 NANOMEDICINE.....	22
1.6.1 Gold Nanoparticles	24
1.6.2 Targeting and Delivery	26
1.6.3 Therapeutic Agents.....	28
1.6.4 Phototherapy.....	30

1.6.5 Tackling angiogenesis	31
1.6.6 Multimodal Imaging	32
1.6.7 Theragnostic in cancer	34
1.6.8 From Research Lab to the Clinic	35
1.6.9 Commercial Impact	36
1.7 SCOPE OF THESIS	40
CHAPTER 2 – MATERIALS AND METHODS	41
2.1 MATERIALS	42
2.1.1 Reagents	42
2.1.2 Equipment	45
2.2 METHODS	46
2.2.1 Cell culture	46
2.2.2 Cell viability	46
2.2.2.1 MTS assay	46
2.2.2.2 Trypan blue assay	47
2.2.3 3D cell culture	47
2.2.3.1 Cells imbedded alginate beads	47
2.2.3.2 Histological preparation	47
2.2.4 RNA expression analysis	47
2.2.5 Western Blot	48
2.2.6 Synthesis and characterization of gold nanoparticles	49
2.2.6.1 Synthesis of gold nanoparticles	49
2.2.6.2 AuNP characterization	49
2.2.6.3 Functionalization of AuNP with PEG (AuNP@PEG)	49
2.2.7 Actinometry	50
2.2.8 Statistical analysis	50
CHAPTER 3 – NOVEL INORGANIC MOLECULES FOR CHEMOTHERAPY	51
3.1 INTRODUCTION	52
3.2 METHODS	53
3.2.1 Cell death mechanism	53
3.2.1.1 Hoechst 33258 labelling	53
3.2.1.2 Quantification of cell death by flow cytometry	53
3.2.1.3 Caspase-3/-7 Activity	54
3.2.1.4 Mitochondrial membrane potential	54
3.2.1.5 Cell cycle analysis	54
3.2.2 Chromosomal DNA alterations	55
3.2.2.1 Chromosomal Aberrations	55
3.2.2.2 Genotoxicity assessment	55
3.2.3 Proteomics	56
3.2.3.1 Preparation of protein extracts and two-dimensional electrophoresis	56

3.2.3.2 Analysis of differentially expressed proteins	57
3.2.3.3 Protein spot identification	57
3.2.4 ABCB1 inhibition assays	57
3.3 RESULTS AND DISCUSSION.....	57
3.3.1 ZnD as a cytotoxic and cytostatic molecule	57
3.3.2 ZnD and DOX-resistant cancer cells	63
3.3.3 Assessment of cell viability in 3D models.....	68
3.4 CONCLUSIONS	71
CHAPTER 4 – NANOVECTORIZING MOLECULES FOR CHEMOTHERAPY	73
4.1 INTRODUCTION	74
4.2 METHODS	75
4.2.1 Interaction studies of ZnD with albumin	75
4.2.2 Western blot	75
4.2.3 Assembly of Au-nanoconjugates and characterization.....	76
4.2.4 AuNP Internalization Studies	76
4.2.4.1 Confocal Fluorescence microscopy.....	76
4.2.4.2 Flow cytometry	77
4.2.5 Co-cultures – Selectivity Assay	77
4.2.6 Animal model assays	77
4.2.7 Histological analysis	78
4.3 RESULTS AND DISCUSSION.....	78
4.3.1 Expression of EGFR in tumour and normal cells lines	78
4.3.2 Nanof ormulation synthesis and characterization.....	80
4.3.3 AuNP internalization studies.....	83
4.3.4 Cytotoxicity of nanoconjugates in EGFR overexpressing cell lines.....	85
4.3.5 In Vivo Assays	91
4.3.6 Conclusions	96
CHAPTER 5 – AUNP FOR COMBINED CHEMOTHERAPY AND PHOTOTHERAPY	97
5.1 INTRODUCTION	98
5.2 MATERIALS AND METHODS	100
5.2.1 AuNP@PEG synthesis and characterization	100
5.2.2 Irradiation of cells.....	100
5.2.3 Statistics	100
5.3 RESULTS AND DISCUSSION.....	100
5.3.1 Laser Characterization	100
5.3.2 AuNP@PEG irradiated by laser	102
5.3.3 Photothermal Therapy induced by visible irradiation on AuNP in cells.....	107
5.3.4 Combined photo-chemotherapy Therapy	113

5.4 CONCLUSIONS	119
CHAPTER 6 – AUNP PHOTOTHERAPY TO PREVENT NEO-ANGIOGENESIS.....	121
6.1 INTRODUCTION	122
6.2 MATERIALS AND METHODS	123
6.2.1 Synthesis and functionalization of AuNP.....	123
6.2.2 RNA expression analysis	123
6.2.3 Ex ovo CAM assay.....	123
6.2.4 Blood vessel modulation experiments	124
6.2.5 Statistical analysis.....	124
6.3 RESULTS AND DISCUSSION	124
6.3.1 Nanoconjugate characterisation	124
6.3.2 Laser effect on albumen and blood	125
6.3.3 Irradiating CAM with AuNP@antiP	128
6.3.4 Gene Expression Analysis	130
6.4 CONCLUSIONS	132
CHAPTER 7 – AUNP GENE SILENCING TO OVERCOME DRUG RESISTANCE.....	133
7.1 INTRODUCTION	134
7.2 MATERIALS AND METHODS	135
7.2.1 Functionalization of AuNP with ASO.....	135
7.3 RESULTS AND DISCUSSION.....	135
7.3.1 AuNP@ASO synthesis and characterization.....	135
7.3.2 Gene Silencing.....	137
7.4 CONCLUSIONS	139
CHAPTER 8 – CONCLUSIONS AND FUTURE PERSPECTIVES.....	141
8.1 CONCLUSIONS	142
8.2 FINAL CONSIDERATIONS AND FUTURE PERSPECTIVES	143
REFERENCES	147
A PPENDICES.....	189

LIST OF FIGURES

Fig. 1.1 Incidence and mortality rates of different types of cancer in Europe and Portugal.....	2
Fig. 1.2 Schematics of the Hallmarks of Cancer Progression.....	4
Fig. 1.3 Schematics of different mechanisms of acquired drug resistance.	21
Fig. 1.4 Different types of nanoparticles and their applications in theragnostic.....	25
Fig. 1.5 Schematics of a multifunctional approach.....	29
Fig. 3.1 Molecular formula of ZnD ($[\text{Zn}(1,10\text{-phenanthroline-5,6-dione})_2]\text{Cl}_2$).	53
Fig. 3.2 Hoechst staining of HCT116 cells exposed to ZnD.	58
Fig. 3.3 Evaluation of apoptosis level.....	59
Fig. 3.4 Mitochondrial membrane potential	60
Fig. 3.5 Cell cycle evaluation	61
Fig. 3.6 Chromosomal Aberrations.....	61
Fig. 3.7 Comet assay.....	62
Fig. 3.8 Methodology for the growth of DOX resistant HCT116.....	63
Fig. 3.9 Microscopy Images of HCT116 DR.....	64
Fig. 3.10 MTS assay of HCT116 DR.	64
Fig. 3.11 2-DE proteome map of HCT116 DR untreated cells.....	65
Fig. 3.12 2-DE proteome map of HCT116 DR treated with ZnD	66
Fig. 3.13 Alginate beads	69
Fig. 3.14 Optical microscopy images of histological cut of HCT116	70
Fig. 3.15 MTS assay of HCT116 cells inside alginate beads	71
Fig. 4.1 Schematic representation of the NanoZnD strategy.	75
Fig. 4.2 Expression of EGFR in A549, H1975, HCT116 DR and HCT116 cells.....	79
Fig. 4.3 Fluorescence spectra of BSA excited at 275 nm, with different concentrations of ZnD....	80
Fig. 4.4 TEM image of spherical citrate AuNP	81
Fig. 4.5 Characterization of PEG functionalization at AuNP surface.....	82
Fig. 4.6 AuNP construct with several functionalization layers.....	83
Fig. 4.7 Confocal fluorescence microscopy of HCT116 cells	84
Fig. 4.8 Flow Cytometry of AuNP@PEG@CETUX.	85
Fig. 4.9 Cell viability assessment of the control nanoconjugates	86
Fig. 4.10 Cell viability assessment of the nanoconjugates in various cell lines	87
Fig. 4.11 Cell viability assessment of Free ZnD and nanoconjugates	89
Fig. 4.12. Immunofluorescent images of HCT116 and Fibroblasts primary cell co-culture	90
Fig. 4.13 Co-culture fluorescence analysis.	91
Fig. 4.14 Comparison of tumour area measured after excision	92
Fig. 4.15 Tumour growth rate in mice model.	93

Fig. 4.16 A. Images of mice tumour xenografts	94
Fig. 4.17 Organ to body weight of liver and spleen of tested mice.	95
Fig. 5.1 Schematics of combined chemo-hyperthermia to tackle Resistant DOX HCT116.....	99
Fig. 5.2 Strategy for assessing efficacy of AuNP based PTT in the visible.	101
Fig. 5.3 Laser calibration measurements.	102
Fig. 5.4 TEM image of spherical citrate AuNP	102
Fig. 5.5 Characterization of PEG functionalization at AuNP surface.....	103
Fig. 5.6 Heat capacity of AuNP.....	104
Fig. 5.7 Characterisation of Photothermal Effect of Gold Nanoparticles.	105
Fig. 5.8 AuNP@PEG UV-Vis variation with temperature increase.....	105
Fig. 5.9 AuNP side scattering in PBS 1× and increased temperature.....	106
Fig. 5.10 AuNP@PEG aggregation profile at different temperatures and ionic strength.....	106
Fig. 5.11 Photograph of laser irradiation setup.....	108
Fig. 5.12 Trypan blue assay of HCT116 cells irradiated with green laser.....	111
Fig. 5.13 Cell viability of HCT116 exposed to AuNP@PEG and Laser.....	112
Fig. 5.14 Reduction in cell viability by MTS of HCT116 DR and HCT116.....	112
Fig. 5.15 Irradiation of HCT116 DR in a 3D model of alginate.....	113
Fig. 5.16 Combined chemo and PTT induced by visible light and AuNP.....	114
Fig. 5.17 Cell viability via the MTS assay in MCF-7 cells	115
Fig. 5.18 AuNP construct with several functionalization layers.....	116
Fig. 5.19 Cell death induced by the combined AuNP@PEG based phototherapy and CoD.....	118
Fig. 5.20 Cell death induced by AuNP@PEG and CoD.....	119
Fig. 6.1 TEM images of AuNP@antiP (A) and AuNP@scramble (B).....	125
Fig. 6.2 Green laser irradiation of albumen	126
Fig. 6.3 Green laser irradiation of albumen	126
Fig. 6.4 Temperature variation of albumen after green laser irradiation.	127
Fig. 6.5 Green Laser Irradiation of blood	127
Fig. 6.6 Photographs of CAM.....	128
Fig. 6.7 CAM images 24 h after application of the nanoformulation and irradiation.....	129
Fig. 6.8 Percentage of newly formed vessels.....	129
Fig. 6.9 Gene expression heatmap for data retrieved from qPCR.	131
Fig. 6.10 Gene expression analysis of CAM for <i>FLT-1</i> , <i>MMP-9</i> , <i>IL-8</i> , <i>VEGFA</i> genes.....	132
Fig. 7.1 Schematics of the hypothesis of <i>ABCBI</i> silencing.....	135
Fig. 7.2 In silico hybridization analysis.....	136
Fig. 7.3 DLS AuNP characterization of AuNP@ASO.	136
Fig. 7.4 Expression analysis of <i>ABCBI</i> mRNA, normalized to 18s, and AuNP@PEG.	137
Fig. 7.5 Cell Viability of AuNP@ASO, DOX and Tariquidar.	138

Fig. 7.6 Western blot of ABCB1 and β -Actin (control) in HCT116 and HCT116 DR.	138
Fig. 7.7 Cell viability of HCT116 DR exposed to different concentrations of Tariquidar	139
Fig. A.1 Top view of the blueprint of manual well plate mover.....	189
Fig. A.2 Perspective view of the blueprint of manual well plate mover.....	190

LIST OF TABLES

Table 1.1 Clinically approved metal compounds for anti-cancer therapeutic application.....	16
Table 1.2 Currently approved nanomedicines in the clinic.	23
Table 1.3 Compilation of gold strategies.....	38
Table 2.1 List of reagents	42
Table 2.2 List of equipment.....	45
Table 2.3 List of primers, size of amplicon and melting temperature	48
Table 3.1 Relative IC ₅₀ (μM) of ZnD in HCT116, HCT116 DR, A549 and H1975.....	58
Table 3.2 Fold variance of proteins	66
Table 3.3 IC ₅₀ (μM) at 48 h of Dox and ZnD in monolayer and alginate hydrogel beads	71
Table 4.1 Nanoconjugates' functionalization moieties and hydrodynamic size.....	82
Table 4.2 Cell viability obtained for HCT116, HCT11 DR, A549 and H1975 cell lines.....	88
Table 5.1. Optimization of AuNP-induced PTT.....	109
Table 5.2 Values for the relative IC ₅₀ of HCT116 and HCT116 DR.....	116
Table 5.3 Characterization of AuNP by Dynamic Light Scattering and Zeta Potential	117
Table 5.4 Characterization of NanoCoD.	117
Table 6.1 Peptide Amino Acid Sequences.....	125

LIST OF EQUATIONS

Equation 2.1	47
Equation 5.1	103
Equation 5.2	104

CHAPTER 1 – INTRODUCTION

The literature review presented in this chapter provides for a general contextualization of the thesis, which shall be more focused within each individual chapter. Also, some of the information herein presented has been published, whole or in part, elsewhere. The author of this thesis reviewed and critically discussed the references cited in the text.

- **Pedrosa P**, Vinhas R, Fernandes A, Baptista PV. Gold Nanotheranostics: Proof-of-Concept or Clinical Tool? *Nanomaterials*. 2015, 5(4):1853-1879 DOI: 10.3390/nano5041853
- **Pedrosa P**, Carvalho A, Baptista PV, Fernandes AR. Inorganic Coordination Chemistry: where we stand in cancer treatment? In *Basic Concepts Viewed from Frontier in Inorganic Coordination Chemistry*. Edited by Dr. Takashiro Akitsu. IntechOpen. 2018 DOI: 10.5772/intechopen.80233
- Rodrigues C, Raposo L, Pombo I, **Pedrosa P**, Fernandes AR, Baptista PV. Nanotheranostics targeting the tumour microenvironment. *Frontiers in Bioengineering and Biotechnology*. 2019, 7:197 DOI: 10.3389/fbioe.2019.00197

1.1 Cancer

Cancer is the second leading cause of death worldwide [1]. Among the most frequent human cancers, prostate cancer in men and breast cancer in women are the most frequent, while for children, blood cancers are the most common. Colorectal cancer is the second most common in Europe representing 13% of the incidence in 2018, and the most common in Portugal representing 18% of the incidence in the same period. In the same year, lung and colorectal cancer together were responsible for more than 30% of cancer deaths. The expenditure on cancer in Europe in 2014 was estimated to be €83.2 billion representing €164 per capita in Europe and €61 per capita in Portugal. These data depict the social and economic impact of this disease (Fig. 1.1) [2, 3].

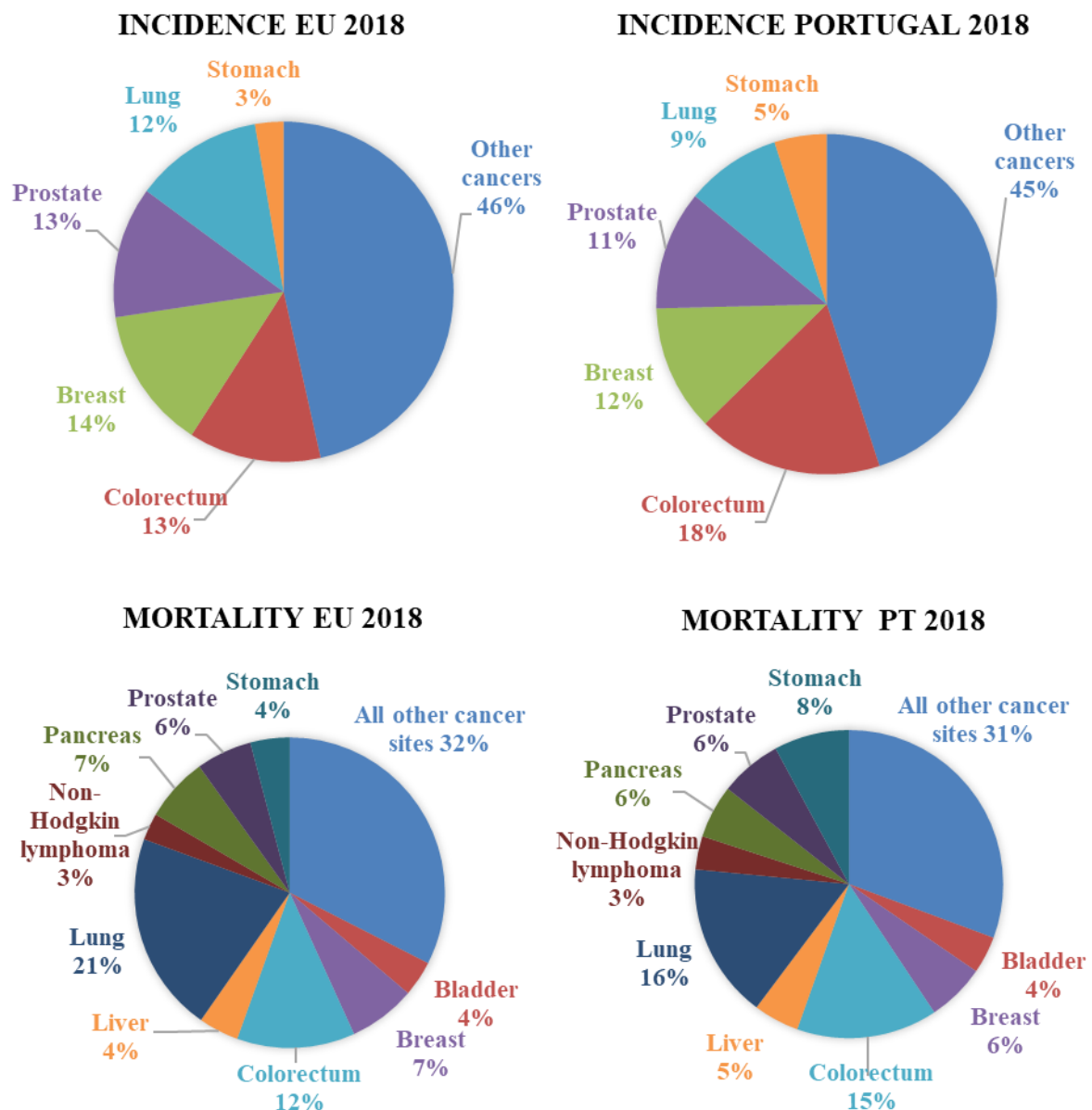


Fig. 1.1 Incidence and mortality rates of different types of cancer in Europe and Portugal.

Cancer must be understood as a complex combination of a variety of diseases that impact multiple aspects of cells and molecular regulation within tissues [4]. Due to its complexity and to distinct modes of presentation, coupled to the individual heterogeneity, these alterations usually take time to present clear symptoms, whose late diagnosis severely hampers effective treatment. Early diagnosis significantly increases the success of treatment, raising the importance of routine check-ups to detect pre-malignant lesions and alterations, as well as initial (usually) less aggressive forms of the disease [5]. About 90 to 95% of cancers develop due to environment aspects and lifestyle. Currently, it is proposed that between 30% and 50% of cancer derived fatalities are preventable by modifying lifestyle and avoiding exposure to major risk factors, such as: tobacco, alcohol consumption, obesity, sedentarism, and chronic infections [6–8].

Cancer cells are the result of several mutations in crucial genes that compromise their normal function, disturbing the cell cycle, and leading to uncontrolled proliferation. Proto-oncogenes are responsible for adequate control of cell division and growth, becoming oncogenes after genetic mutation. In addition, tumour suppressor genes can work as a defence mechanism but when mutated can allow uncontrolled cell division. Most of these molecular alterations are induced by direct mutations to the DNA, epigenetic changes of chromatin or the result of altered expression patterns of regulatory pathways, both at the RNA and protein level. Still, cells have highly effective DNA repair mechanisms that attempt to correct any physico-chemical damage to DNA, such as base excision repair, nucleotide excision repair or mismatch repair. While mostly preventing the onset of genome mutations, these mechanisms sometimes fail to correct the damage and, as a result, mutations prevail and accumulate [9–11].

Risk factors increase the chances of cancer by increasing the probability of mutations in the genome. Chemical compounds, especially those interacting with DNA, have a role in the formation of gene mutations. Carcinogenic substances influence the cytoplasm and nucleus of cells directly or indirectly, and lead to genetic disorders and mutations. Other sources of gene mutation rely on radiation or infections such as. Human Papilloma Virus in cervical and oropharyngeal cancers, and *Helicobacter pylori* in stomach cancer [6–8].

1.2 Cancer progression

For mutated cells to progress into cancer they must be able to: have self-sufficient cell division, be insensitive to cell division stop signals, resist to cell death, have infinite division potential, form new blood vessels (neo-angiogenesis), invade other tissues, survive in hypoxia and evade the immune system. With the continuous division of cancer cells, and acquisition of mutations, they become genetically unstable. It is common to observe heterogeneous tumour masses, that may respond differently to therapy. After disease establishment, early and precise diagnosis is the key for adequate therapy and increased survival [5, 11]. In the following subsection we will elaborate on each cancer hallmark, to understand cancer progression (Fig. 1.2).

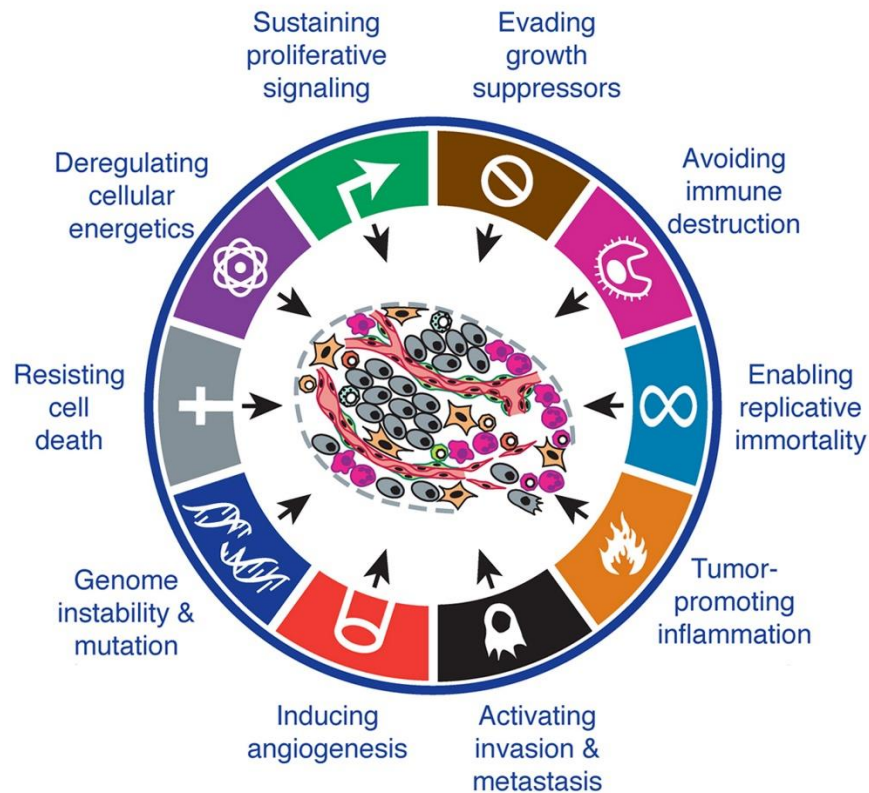


Fig. 1.2 Schematics of the Hallmarks of Cancer Progression. Reprinted from Cell, 144-5(29), Douglas Hanahan, Robert A., Hallmarks of Cancer: The Next Generation, Copyright 2019, with permission from Elsevier.

1.2.1 Sustaining proliferative signalling

Sustaining proliferative signalling is the basic step for cancer development. Healthy tissues have a tight control of their division cycle and production of growth factors. Cells become tumorigenic by deregulating its mitosis and maintaining a continuous signal to divide. This deregulation can happen in different ways: cancer cells can produce growth factors which they ultimately respond to, in an autocrine proliferative stimulation; they can stimulate healthy tissue to produce growth factors; they can increase the number of growth factor receptors, becoming hyperresponsive to normal growth factor levels; or they can structurally alter their growth factor receptor, to be always active independently of ligand interaction [10, 11]. An example of the latter are deregulations in epidermal growth factor receptor (EGFR). EGFR is part of the ErbB receptor family of receptor tyrosine kinases. It exerts critical functions in epithelial cell physiology and is frequently overexpressed and/or mutated in several human cancers [12]. Receptor transphosphorylation, which is dependent of ligand binding, activates an intracellular signalling cascade of multiple pathways that deliver the information to the nucleus for the activation of genes responsible for cell proliferation, survival, differentiation and angiogenesis [12, 13]. These mutations lead to the continuous signalling for cell proliferation.

1.2.2 Evading growth suppressors

For cancer progression, a second step must be accomplished after sustained proliferation. Cells must be able to evade growth suppressors. Tumour suppressors are generally proto-oncogenes that limit cell growth, regulating proliferation [14]. Retinoblastoma and TP53 associated proteins are the two classical tumour suppressors that regulate complementary cellular regulatory circuits that decide if cells should divide, halt division, or undergo apoptosis [15, 16]. Retinoblastoma proteins work as a gatekeeper, analysing mainly extracellular signals and deciding if cells should proceed with the cell cycle. On the other hand, TP53 proteins generally decide upon different types of intracellular stress signals. If the nucleotide pool levels are unbalanced, there is a deprivation of glucose, oxygenation or excessive genomic damage, TP53 pathway can stop cell cycle progression until the cell returns to a normal condition. When the conditions are extreme, TP53 can also summon apoptotic signals. When defected, these pathways allow uncontrolled cell division [14–16].

1.2.3 Evading programmed cell death

The next step in cancer development is the capacity of cancer cells to evade programmed cell death, persisting in stress conditions. Apoptosis is one of the cell's natural form of suicide. It is a type of programmed cell death characterized by cell shrinkage, membrane blebbing, chromatin condensation and nuclear fragmentation (apoptotic bodies) [17]. Apoptotic cells are phagocytised before they release toxic products to the intercellular space, thus they do not induce an inflammatory response. Apoptosis can be triggered by an intrinsic or extrinsic pathway. The extrinsic pathway is triggered by binding of external signalling [17], involving for example the Fas ligand/receptor. The intrinsic pathway is more frequently associated as a barrier to cancer development. It can be activated by intracellular stimuli, including DNA damage, growth factor deprivation, and oxidative stress. It depends on the release of cytochrome c and other pro-apoptotic proteins from the intermembrane space of mitochondria. This interaction is followed by the assembly of the death-inducing signalling complex [18, 19]. Cancer cells are, generally, more sensitive to apoptosis, meaning that they are closer to triggering the apoptotic pathway than normal cells. This sensitivity comes from the dual upregulation of proapoptotic and antiapoptotic proteins and environmental stressors that endure low availability of nutrients or hypoxia [20, 21]. Tumour cells can evolve several tactics to circumvent apoptosis. TP53 is commonly affected, abolishing the critical damage sensor from the apoptosis. Cancer cells can also evade apoptosis by increasing the expression of antiapoptotic factors (BCL-2, BCL-XL) or survival signals (IGF11/2), or by downregulating proapoptotic regulators (BAX, BIM, PUMA) [22].

1.2.4 Enabling replicative immortality

For a tumour to persist, after passing the described steps, it must enable replicative immortality. Normal cells have a limited number of division cycles before they enter a senescent state, when cells stop dividing but remain viable until they ultimately die by apoptosis. This mechanism of limiting cell

cycles is regulated by telomeres. Telomeres are multiple tandem hexanucleotide repeats in the extremities of chromosomes that protect end-to-end chromosomal fusions. During the cell cycle these repeats are progressively lost, generating unstable dicentric chromosomes and cell death. An alternative recombination-based telomere maintenance mechanism. Hence, telomere shortening works like an internal clock that determines the number of divisions a cell can undertake. To survive, cancer cells overexpress telomerase, a DNA polymerase that extends the telomeres. By keeping the telomeres' length long enough to avoid triggering apoptosis, these cells keep replicating in an immortal state [23, 24].

1.2.5 Tumour microenvironment and energy metabolism

When cells divide indefinitely a tumour mass is generated, and a cellular environment is created where the centre of the mass and the periphery have different conditions. The tumour microenvironment is created by the interplay between growing tumour cells and surrounding environment. Its composition varies according to the anatomical region of the tumour and the genetic and phenotypic traits of tumour cells [25, 26]. However, common features can be found. The micro-environment of epithelial tumours is generally composed by tumour cells, the extracellular matrix, stromal cells (including fibroblasts, mesenchymal stromal cells), cells from the blood and lymphatic systems and occasionally adipocytes, and cells from the immune system (including macrophages, T and B lymphocytes and natural killer cells). Different microenvironments force cancer cells to adapt in order to survive creating a heterogenic mass of cells. The first constraint observed in tumour cells is oxygen and nutrient supply that cannot be sustained by adjacent blood vessels [11]. In these settings, the oxygen scarcity experienced by growing tumour cells induces the expression of cellular response to hypoxia, principally via hypoxia-induced factors (HIF) [27]. HIF family of transcriptional factors is composed by HIF1, HIF2 and HIF3 proteins that activate genes involved in glucose metabolism, angiogenesis, cell proliferation, migration and immune system modulation [27–29]. The HIF together with high energetic requirements, trigger a metabolic adjustment in tumour cells from oxidative phosphorylation to the aerobic glycolysis, in a process known as Warburg effect [30]. This metabolic switch remains even in the presence of oxygen and results in an increased production of lactate. To compensate the lower efficiency of glycolysis compared with mitochondrial oxidative phosphorylation, cancer cells upregulate glucose transporters increasing the glucose concentration in the cytoplasm [14, 31, 32]. Glycolytic switch also allows the channelling of glycolytic intermediates into various biosynthetic pathways, which include nucleosides and amino acids synthesis. The high level of lactate in the cytoplasm leads to the upregulation of efflux pumps for lactic and carbonic acid secretion, giving tumour cells the conditions to survive and thrive, contributing also for multidrug resistance (MDR) [33, 34]. The accumulation of lactate in the tumour extracellular space leads to its acidification. Interestingly, it has been found in some tumours two subpopulations of cancer cells that cooperate in their energy metabolism. One subpopulation consists

of anaerobic glycolytic cells that secrete lactate, whereas the second subpopulation preferentially imports the lactate and uses it as their main energy source, in the citric acid cycle [35–37].

The glycolytic metabolism and increased proliferation of tumour cells result in increased reactive oxygen species (ROS) production, promoting genomic instability on one side, and inducing antioxidant defences on the other side [30]. To increase the levels of oxygen and nutrients in the tumour and reduce toxic waste concentration, tumour cells promote the formation of new blood vessels.

1.2.6 Inducing angiogenesis

The word cancer appeared due to the resemblance of a tumour and surrounding vessels to a ‘crab’ which is the meaning of the word in Latin. Because of the inhospitable conditions of the tumour microenvironment cells start to secrete factors that promote the formation of new blood vessels – angiogenesis. Angiogenesis is an important hallmark in cancer progression and it has been demonstrated that solid tumours cannot grow bigger than 2-3 mm without creating their own blood supply [38]. The low levels of oxygen induce the expression of vascular endothelial growth factor A (VEGF-A) and its receptor (VEGFR) via HIF-1 α [39]. The VEGF pathway can also be upregulated by sequestering of VEGF ligands in the extracellular matrix. Upon the activation and release of extracellular matrix-degrading proteases VEGF ligands are released. VEGF-A is a potent and specific inducer of mitosis for vascular endothelial cells and signals the production of matrix metalloproteinases (MMPs). The MMPs degrade the extracellular matrix of cells permitting the migration of endothelial cells. In turn, the endothelial cells start to divide and migrate, organizing themselves into hollow tubes that gradually develop into a network of blood vessels, helped by adhesion factors, such as integrin α and β [40–43].

In this process, the negative regulators that inhibit the formation of blood vessels work as an internal counterbalance of angiogenesis by expressing a set of proteins that include, angiostatin, interferon, platelet factor 4, endostatin, prolactin 16 kDa fragment, thrombospondin, and tissue inhibitor of MMP-1, -2, and -3. To initiate angiogenesis, the upregulation of angiogenic factor is as essential as the downregulation of the anti-angiogenics. Angiostatin for example induces apoptosis in endothelial cells and in tumour cells, while inhibiting the migration and the formation of tubules in endothelial cells [44, 45]. The unbalanced concentration levels of angiogenic and anti-angiogenic signals, end up in the formation of vessels with defective or discontinuous basement membranes, resulting in leaking vasculature with chaotic organization unevenly distributed along the tumour, excessive vessel branching, erratic blood flow and micro haemorrhaging [41].

Interestingly, some studies propose a correlation between the levels of angiogenic factors in tissue and the aggressiveness of a tumour, using these values as predictors for high risk patients with a poor prognosis. The association between the expression of VEGF and prognosis has been described in colorectal cancer [46–48], breast cancer [49–52], and lung cancer [53–55], among others [56–58].

The formation of lymphatic vessels, named tumour-associated lymphoangiogenesis, is sustained by the secretion of VEGF-C and VEGF-D by tumour cells, immune cells, and other stromal cells. In this

event, lymphatic endothelial cells form single layer lymph capillaries with minimal basement membrane, that join to collecting lymphatic vessels with a basement membrane and valves that prevent retrograde flow. The formation of lymphatic vessels around a tumour is correlated with poor prognosis, since it favours metastatic propagation in distal organs. On the other side, lymphatic endothelial cells have a prominent role in immune system modulation, contributing for anti-tumour immunity [59, 60].

1.2.7 Evading the immune system

The participation of the immune system in tumour development is not fully understood. It is believed that the immune system monitors and eliminates the formation of nascent tumours. This is majorly supported by the rise of certain cancers in immunocompromised individuals [61] and by the high incidence of malignancies in patients receiving immunosuppressive therapy after organ transplantation or HIV infection [62]. However, the fact that people with fully functional immune systems also develop cancer, indicates that this concept of immunosurveillance is only part of the story. Today the most consensual concept is immunoediting, that constitutes a dynamic process that simultaneously prevents tumours, and shapes the immunogenicity of developing tumours. Immunoediting can be defined in three parts: elimination, equilibrium and escape [63–65]. Although these parts will further be explained separately, it is noteworthy that they continually shift between each other over time, representing an interplay between tumour and immune system, depending on the immune system state and properties of the tumour microenvironment. Elimination represents the common view of immunosurveillance, when a forming tumour is rejected and killed by the immune system. If the tumour is not completely destroyed, it may enter a senescent state (equilibrium) in which the immune system controls tumour growth and which may stay unaltered for many years. This concept is supported by fact that tumours can remain dormant in cured patients for many years, and relapse after long periods [63, 66]. In certain cases, tumour cells may escape from immune restriction and start proliferating in an uncontrolled manner, leading to tumours. This happens due to selective pressure in tumour cells by the immune system, where only cell that are less immunogenic or more resistant to lysis survive [67]. Tumours can also create an immunosuppressive microenvironment by recruiting specific immune cells that favour tumour growth and progression [68, 69]. Importantly, the molecular signals composition of the tumour microenvironment determine the clinical outcome by promoting the tumour escape to immunosurveillance or tumour constrain [70]. Once in the tumour microenvironment, monocytes can differentiate into two different types of macrophages depending on the chemical composition at the tumour location: M1-type macrophages are formed in the presence of interferon gamma, and M2-type macrophages appear when exposed to different interleukins (IL, e.g. IL-4 or IL-10), transforming growth factor beta (TGF- β), granulocyte-macrophage colony stimulating factor, annexin A1 or tumour cell-surface molecules [71, 72]. This macrophage polarization is crucial for tumour prognosis, as M1-type are correlated with a good prognosis, while tumour associated macrophages generally have the M2 phenotype and contribute for tumour growth, angiogenesis, invasion and metastasis [71–74].

Inflammation is usually displayed in the tumour, promoted initially by tumour cells (intrinsic pathway) [75]. A pro-inflammatory environment is usually accompanied by a poor prognosis [70, 75]. Tumour associated macrophages-mediated secretion of IL-1 cytokines contribute for chronic inflammation and strengthen a pro-tumoral micro-environment [76]. The role of the lymphoid lineage cells in tumour progression is also contradictory. While B cells and regulatory T cells create an immunosuppressive microenvironment, innate cytotoxic lymphocytes, natural killer cells and natural killer T cells are immunostimulant [64, 77–79]. In different types of cancers, the increased expression of Granulocyte-macrophage colony stimulating factor and VEGF induce the production of myeloid-derived suppressive cells at the bone marrow that are recruited to the tumour microenvironment where they remain undifferentiated [80]. The presence of myeloid-derived suppressive cells is generally correlated with a poor prognosis, as they are involved in angiogenesis and suppression of natural killer cells and CD8+ cytotoxic T cells [80, 81].

1.2.8 Activating Invasion and Metastasis

In epithelial cancers, growing tumour cells are supported in an extracellular matrix with altered biochemical and biomechanical properties when compared with healthy tissue. The low oxygenation and inflammatory environment induce alterations in extracellular matrix proteins that result in desmoplasia, characterized by the growth of fibrous or increased thickness of tumour surrounding connective tissue. The degree of desmoplasia increases as the tumour progresses and is preponderant in metastatic dissemination and clinical outcome [82, 83].

Stromal cells are also important for tumour development and prognosis. Mesenchymal stromal cells are recruited to the tumour due to the inflammatory environment and, according to its chemical composition, they may promote or inhibit the tumour progression [84, 85]. Moreover, the inflammation and consequent secretion of TGF- β induce the differentiation of fibroblasts into cancer associated fibroblasts. Besides tumour cells, cancer associated fibroblasts are the most abundant cell type in tumours and play an important role in increased desmoplasia [86–88].

The presence of hypoxia increases desmoplasia and the interactions between the several cell players in the tumour microenvironment favours the epithelial-to-mesenchymal transition of tumour cells resulting in the formation of cancer stem cells [73, 89, 90]. The epithelial-to-mesenchymal transition process results in disruption of intracellular adhesion and loss of cell polarity, conferring migratory ability to cancer stem cells. These cells can enter adjacent blood or lymph vessels and travel to another anatomical location where they can experience the reverse process - mesenchymal-to-epithelial transition. The formation of distant tumour nodes is called micro metastases, that grow into micro metastatic lesions and later macroscopic tumours. This step is termed colonization - implantation of a primary tumour into a secondary location [73, 89, 90]. MMPs have an important role in epithelial-to-mesenchymal transition, being responsible for the detachment of tumour cells from the extracellular matrix promoting cancer stem cells formation [91].

In an initial stage, it is the genomic profile of tumour cells that determines tumour maturation. As the cancer progresses, the intercellular communication between tumour and neighbour cells dictates tumour microenvironment and tumour progression, contributing for intra- and inter-tumour heterogeneity [11, 92]. Central in these communications are exosomes, endosomal pathway derived vesicles with 30-100 nm diameter, composed by a lipid bilayer with membrane proteins, entrapping soluble proteins, signalling molecules, including cytokines, chemokines and growth factors, and nucleic acids including mRNA and miRNA [93]. Importantly, the content of the exosomes depends on the cell of origin, often reflecting the physiological condition of the cell [94]. After release to the extracellular milieu, exosomes can be internalized by secondary cells adjacent to the primary cell or travel through the vascular or lymphatic system to other anatomical location where they can be internalized by local cells. Once internalized, exosomes are able to modify the phenotype of the recipient cell that will adjust to the incoming signals [95, 96]. Tumour cell derived exosomes have an important role in tumour progression, including for example in immune system modulation, contributing to tumoral transition of adjacent cells and preparation of the metastatic niche at a new anatomical location [96, 97].

1.3 Different types of colorectal, lung and breast cancer

Depending on the type of cancer they have different origins and different presentations. For example, sarcomas originate in muscle tissue, adenoma in gland cells, carcinoma in mesenchymal tissue, lymphoma in lymphocytes, etc. As colorectal, breast and lung cancers are the most incident and deadly, we used these types of cancer as models for our work. Thus, we will explore their different presentations.

In colorectal cancers, adenocarcinomas are the clear majority. The first stages of the tumours start with polyps that continue to grow and can then turn into malignant tumours. Polyps can grow in two different shapes, flat and pedunculated. Flat polyps are harder to detect in colon cancer screening and are more common than previously thought. Pedunculated polyps have a mushroom-like shape. There are five types of polyps: adenomatous (tubular adenoma), hyperplastic, serrated, villous adenoma and inflammatory. Certain types are more likely to become cancerous than others. Adenomatous represent about 70% of all polyps, which when found, are generally tested for cancer. Only a small percentage become cancerous, but almost all malignant polyps began as adenomatous. Villous adenomas represent approximately 15 % of polyps detected in colon cancer screening. This type of polyp has a high risk of turning cancerous and as they are commonly flat shaped, they are more difficult to remove. The process of polyps developing to colon cancer is in the span of years. With regular screening and accurate diagnostic, they can be found and surgically removed before they grow. Other less common types of colon cancer can also occur, colorectal sarcomas (gastrointestinal stromal tumours), lymphomas and carcinoids. Colon cancer has a high genetic component, up to 15% of colorectal cancer patients have family members with colorectal cancer, excluding colorectal cancer syndromes [98–100].

Lung cancer has two main classifications: small cell lung cancer (SCLC) and non-small cell lung cancer (NSCLC). These two types have different outcomes and are treated differently. NSCLC begins in the epithelial cells and can be: an adenocarcinoma, if cancer starts in mucus gland cells (40 % of all NSCLC cases); a squamous cell carcinoma if it begins in the cells that line the airways (30 % of all NSCLC cases); a large-cell undifferentiated carcinoma if cells can be found anywhere in the lung (10 to 15 % of all cases of NSCLC). NSCLC accounts for almost 90% of lung cancer cases. SCLC can begin in nerve cells or hormone-producing cells. Once the lung tumour grows, cancer cells may be carried away in the blood stream, or lymph. It is common, especially for SCLC to invade chest lymphatic nodes [101, 102].

Breast cancer has two forms, invasive or non-invasive. Invasive breast cancer spreads into surrounding tissues while the non-invasive stays in the milk ducts (ductal carcinoma) or lobules (lobular carcinoma) in the breast. Ductal carcinoma makes up most breast cancers. Lobular carcinoma when circumscribed to one breast is not considered cancer. Both ductal and lobular carcinomas can become invasive. However, the second has an associated risk factor for developing invasive breast cancer in both breasts. Other less common types of breast cancer are medullary, mucinous, tubular, metaplastic, papillary or inflammatory. The latter is a faster-growing type of cancer that accounts for 1% to 5% of all breast cancers. Breast cancers can be hormone receptor-positive if they express oestrogen (ER+) or progesterone receptors (PR+). This type of cancer depends on these hormones to proliferate, and although it may occur at any age, it is more common in women after menopause. About 60% to 75% of breast cancers are hormone receptor positive. About 15% to 20% of breast cancers rely on human epidermal growth factor receptor 2 (HER2) to progress. These cancers have an overexpressed HER2 gene and are called “HER2-positive”. HER2-positive breast cancers grow more quickly and can be either hormone receptor-positive or hormone receptor-negative. Tumours that express none of the receptor are triple-negative, corresponding to approximately 15% of invasive breast cancers. Triple-negative breast cancer is more common among younger women, and women with a mutation in the BRCA1 or BRCA2 genes. Thus, it is recommended that women with triple-negative breast cancer younger than 60 years old be tested for BRCA gene mutations [103, 104].

Most types of cancer can also be categorized into four stages depending on their progression state. Stage I is characterized by a small tumour that has not grown deeply into other tissues. It also has not spread to the lymph nodes or other parts of the body. It is often called early stage cancer and can in general be surgically removed. Stage II indicate larger tumours that have grown more deeply into nearby tissue. However, it has not spread to lymph nodes. Stage III is generally associated with lymph node invasion but not to other parts of the body. Stage IV. means that the cancer has spread to other organs besides the primary organ. It is also called advanced or metastatic cancer.

1.4 Cancer therapy

Cancer therapy relies on the selective killing of aberrant malignant cells while protecting healthy tissue. Surgery is still the most effective treatment for localized primary tumours, curing more patients than any other single therapy, even after the appearance of radiation therapy and chemotherapy in the 1940s [105, 106]. Currently, the standard of care is focusing on the development of a combination of therapeutic strategies to strike cancer cells in a highly specific and direct way, ensuring that all the malignant and aberrant cells are destroyed. The understanding that the immune system plays a relevant role in the development of cancer, has also opened the gate for therapeutic strategies that make use of this powerful innate system to tackle cancerous cells. Bellow, I shall discuss some of these critical aspects in further detail.

1.4.1 Surgery

The increasing success in cancer treatment can be attributed mainly to the major improvements in surgery. The beginning of the 20th century marked a turn in the development of cancer surgery techniques, such as Halstedian principals. In the first fifteen years of the century, several surgery techniques were carried out for the first time for oncological purposes, such as radical suprapubic prostatectomy, abdominoperineal resection, radical hysterectomy and lobectomy [105, 106]. Later, non-invasive procedures appeared, such as laparoscopic colectomy, videothoracoscopy, radiofrequency ablation and radiosurgery, limiting the size of incisions, wound healing time, pain and risk of infection [107–109]. Over the years, surgery has become gradually more sophisticated and less aggressive. Mastectomy – whole breast removal – has been replaced in some cases by quadrantectomy and more recently lumpectomy – only removing the tumour – without loss of survival [110]. Tissue conserving surgical procedures have also been proposed, such as breast-conserving surgery, with sentinel-node ablation to improve aesthetic results and avoid lymphedema; laryngoscopic laser surgery in early laryngeal cancer [111]; and a robotic surgical system (Da Vinci®) designed to facilitate complex surgery using a minimally invasive approach, controlled by a surgeon from a console. The system is commonly used for prostatectomies, but it can also be used for lung and colorectal cancer surgery [112, 113]. The main trend in surgery remains, to reduce the impact on healthy tissues while removing as much tumour cells as possible. This field will see a revolution in the following decades with the evolution of new computerized imaging tools, lasers and robotics, reducing the cost effectiveness of surgeries, and expanding its application to different cancer types.

1.4.2 Radiotherapy

The discovery of X-ray radiation in the end of the 19th century paved the way to radiotherapy. Radiation therapy, based on high-powered energy beams, like X-rays or protons, is used to destroy cancer cells since they are more susceptible to radiation than normal cells. Radiation source can be external, from a machine, or internal, using radioactive isotopes inside the body (brachytherapy). The

X-rays or radioactive particles are painless and invisible and do not contaminate surrounding people after treatment. The first cancer case cured exclusively by radiation occurred in 1898. Today it is applied in approximately 45% of new cancer cases and is responsible for 40% of cancer cures with lower cost than other therapies. It is commonly used in combination with surgery and/or chemotherapy (as adjuvant therapy) [114, 115]. In lung cancer treatment, radiotherapy is used in every stage of both NSCLC and SCLC. In the early stages of disease development, when patients cannot undergo surgery, stereotactic radiotherapy is applied. In contrast, radio chemotherapy or radical radiotherapy are used locally in advanced stages. In stage IV cases radiotherapy can be employed as a palliative treatment [116, 117]. For colorectal cancer, radiotherapy is not standard treatment. It is used in advanced disease cases (stage III/IV) as neoadjuvant. Two preoperative regimens have been established, short-course radiotherapy and long-course chemoradiotherapy, both reducing the risk of local relapse. In fewer cases, intraoperative and particle radiotherapy can be used as treatment options for locally relapse patients [118]. Radiation therapy is also used in the treatment of breast cancer, but not in all cases. It is used in early stages as a preventive measure for women who had breast-conserving surgery to avoid relapse in the breast or nearby lymph nodes or in most advanced stages as adjuvant therapy to reduce metastatic tumour size. Brachytherapy can also be used along with external beam radiation to boost radiation to the tumour site [119].

With the advance in computer science, it is possible to create three-dimensional X-ray therapy, such as intensity-modulated radiation therapy. It takes advantage of computed tomography (CT) scans to map the tumour, providing a three-dimensional reconstruction that can be accurately targeted [120]. One of the latter advances in this field is image-guided radiation therapy. This technology records a video sequence of tumour/patient movement, compensating body movement such as breathing. This reduces toxicity to other tissues, since the beam is focused to tumour volume instead of healthy tissues [121]. The current trends in radiotherapy have been fractionated dose delivery, localized radiation by means of improvement of computer-based tomography and advances in X-ray production.

1.4.3 Chemotherapy

Chemotherapy uses one or more chemical chemotherapeutic agents as part of a standardized regimen, intending to cure, prolong the life, or reduce the symptoms of cancer patients [122]. Chemotherapy can be used as: neoadjuvant, aiming to reduce the size of the primary tumour before local treatment (radiotherapy or surgery); combined therapy, when it is used simultaneously with other types of treatment; adjuvant, given after a local treatment to prevent micro metastasis, and reduce relapse rates; and maintenance, giving low-dose treatment to prolong remission [123]. Chemotherapy works by killing cancer cells usually by blocking cell division and/or promoting cell death via apoptosis. It is generally administered systemically, and its action is not specific to tumour cells. However, as tumour cells divide more rapidly than normal cells, they are more affected. Many side effects of chemotherapy are associated with this lack of selectivity. In the last years, a lot of effort has been put

in the development of novel targeted therapies towards specific molecular or genetic targets, which inhibit growth-signals like receptor tyrosine kinases (referred to as targeted therapy) [12, 124, 125] or growth-promoting signals from classic endocrine hormones (referred as hormonal therapy) [126, 127].

The tyrosine kinase inhibitors are a family of small molecules or peptides that inhibit either cytosolic or receptor tyrosine kinases. These molecules work by directly competing with the ATP binding site of tyrosine kinases (genistein, lavendustin C, imatinib, erlotinib, gefitinib), by allosteric inhibition of the tyrosine kinase (lavendustin A), by inhibiting ligand binding to receptor tyrosine kinases (e.g., cetuximab), inhibiting tyrosine kinase interaction with other proteins (e.g., UCS15A, p60-v-Src inhibitor peptide) or by destabilizing the tyrosine kinase (e.g., herbimycin A and radicicol). Among these only imatinib, cetuximab, erlotinib and gefitinib are common in clinical practice, while the majority are not available for clinical use [12, 124, 125]. The type of therapy is common in several types of cancer including lung and colorectal cancer [128, 129].

Hormone therapy consists in the manipulation of the endocrine system to inhibit the production or activity of specific hormones or by administration of hormones. Hormonal therapy is used for several types of cancers including breast and prostate. It is commonly used as adjuvant or neoadjuvant therapy to reduce the risk of cancer relapse, however in some cases it can be used metastasis and relapses [126, 127]. There are three main types of hormone therapies: inhibitors of hormone synthesis, hormone receptor antagonists and hormone replacement. Aromatase inhibitors are inhibitors of hormone synthesis used for the treatment of breast cancer in postmenopausal women. Oestrogen production in the ovaries ceases when women reach menopause, but other tissues continue producing oestrogen through effect of aromatase on androgens produced by the adrenal glands. Blocking the activity of aromatase drops the oestrogen levels to extremely low levels, arresting growth of hormone-responsive cancer cells [126, 130, 131]. Hormone receptor antagonists compete with the normal receptor of a given hormone preventing receptor activation. Target receptors are located on the cell surface, for as peptide and glycoprotein hormones, or intracellularly, as steroid hormone receptors. Selective oestrogen receptor modulators and anti-androgens are two types of hormone receptor antagonists [132]. In contrast with these therapies that seek to block hormone signalling to cancer cells, hormone replacement therapy works by giving specific hormone agonists that inhibit cell growth or have cytotoxic effect on tumour cells. Although it is not clear the mechanism of action of these therapies, progestogens, androgens, and oestrogens, are used for the treatment of hormone-responsive, advanced breast cancer [133].

Anthracyclines appeared in the early 1960's and are considered a mainstay of cancer chemotherapy for several decades being doxorubicin (DOX) the most used. DOX is one of the most potent antineoplastic drugs in single or combined therapy due to its wide spectrum of action. It is used to treat a large variety of solid tumours and haematological malignancies [134, 135]. DOX acts by intercalating in DNA base pairs and by binding to DNA-associated enzymes. It hampers DNA replication, RNA transcription and promotes DNA breaks. Cell growth is inhibited at phases G1 and G2, and with the failure of the DNA repair system, the apoptosis pathway is triggered. Its side effects can be severe,

affecting different organs including the heart, brain, liver and kidney, thus dosage needs to be carefully considered from case to case [136–138]. Several attempts have been made to decrease DOX side effects including targeted drug delivery [139–145]. DOX-loaded pegylated liposomes are approved for clinical practice. Encapsulation into liposomes greatly reduces the interaction with the plasma allowing longer bloodstream retention after intravenous administration. PEGylation allows the liposomes to go undetected by the immune system and avoid clearance. The liposomes' small size allows them to pass through the leaky blood vessels that supply the tumour. Encapsulated DOX accumulates at the tumour site in contrast to free DOX, with significant impact to the therapeutic window of the drug [144, 146].

A breakthrough in chemotherapy was the appearance of metal complex agents which erupted with the discovery of cisplatin, approved for clinical use by the Food and Drug Administration (FDA) in 1978 (Table 1.1). Accompanied by the success of cisplatin-based drugs, other coordination compounds based on platinum, gold, ruthenium, titanium, copper, etc. were explored for their anticancer potential with some reports of (pre)clinical and clinical candidates [147]. In biological systems, reactions rely on metal ions, such as zinc, iron and copper, for normal functioning. Such transition metals are involved in several biological processes, from electron transfer to protein active sites or as enzyme cofactors. Their intracellular concentration is tightly regulated, otherwise it can lead to the development of various pathological disorders [148]. A common characteristic of these metals is their ability to form ROS at higher concentrations, which explains, to some extent, their role as cancer modulators [149]. Cancer cells are known to have a different redox metabolism from normal cells, with augmented levels of intracellular ROS, mostly due to increased metabolic activity and hypoxia, especially in the core of solid tumours. Anticancer metal complexes, due to their redox properties, have been shown to disturb cancer cellular redox homeostasis resulting in enhanced levels of oxidative stress which are not well tolerated. For most metal compounds DNA is the main intracellular target (e.g., cisplatin, carboplatin, oxaliplatin). The interaction of these molecules with DNA can cause damage, creating adducts in cancer cells that block their division and lead to cell death [150, 151].

Table 1.1 Clinically approved metal compounds for anti-cancer therapeutic application.

Name	Description	Target Cancer	Approved
Platinol	Cisplatin	Metastatic testicular, ovarian and bladder cancers	FDA approval
Paraplatin	Carboplatin	Advanced ovarian Cancer	FDA approval
Eloxatin	Oxaliplatin	Advanced colorectal cancer in combination with 5-FU and leucovorin	FDA approval
Aqupla	Nedaplatin	urological tumours	Approval in Japan
Lobaplatin	1,2-diammino-1-methylcyclobutane-platinum(II)-lactate	Inoperable metastatic breast and small cell lung cancer	Approval in China
Heptaplatin	Cisplatin analogue	Gastric cancer	Approval in Korea

The current trend in chemotherapy development is targeted chemotherapy, by coupling established formulations with new carriers that specifically target cancer cells, thus increasing specificity and reducing side effects.

1.4.4 Immunotherapy

Cancer immunotherapies are the most recently approved, including preventive and therapeutic cancer vaccines, immune checkpoint inhibitors, a bi-specific T- cell engager, chimeric antigen receptor T-cell therapy, and monoclonal antibodies [66, 75, 79]. Among these, chimeric antigen receptor T cells had great interest lately for curing patients in terminal stages. In this type of treatment, a patient's T cells are purified from their own blood and altered in the laboratory to recognise a certain protein receptor on the patient's cancer cells [152]. Because cancer immunotherapy acts in the immune system, it can work independent of tumour type or mutations. Immunotherapy can be combined with chemotherapy, or radiotherapy. The efficacy of chemotherapy combined with immunotherapy may depend on the drug, and the administration regimen.

One of the fields that has seen greater advances is the development of monoclonal antibodies production [153, 154]. Several therapies have emerged targeting specific receptors that are overexpressed in cancer cells. Cetuximab (Erbix) is a monoclonal antibody that acts against the extracellular domain of EGFR. It was FDA approved in 2003, in combination with chemotherapy for colon cancer and in 2006 for head and neck cancers. The EGFR is part of the ErbB receptor family of receptor tyrosine kinases. It exerts critical functions in epithelial cell physiology [12] and is frequently overexpressed and/or mutated in several human cancers. The receptor transphosphorylation, which is

dependent of ligand binding, activates an intracellular signalling cascade of multiple pathways that deliver the information to the nucleus for the activation of genes responsible for cell proliferation, survival, differentiation and angiogenesis [12, 13].

Cetuximab showed clinical benefit for colorectal cancers that overexpress EGFR independent of EGFR mutations, however they have low efficiency in K-RAS mutated tumours [129, 155, 156]. It has been shown that it has synergistic anti-tumour effects in combination with radiotherapy, in squamous cell carcinoma of oropharynx and larynx. Cetuximab improved locoregional control and overall survival when administered in these settings [157, 158]. It was found to be well tolerated in combination with cisplatin, or carboplatin, and fluorouracil and it can sensitize cells to radiation and chemotherapy, possibly by blocking the associated activation of DNA protein kinase enzymes involved in the repair of DNA damage induced by radiation and chemotherapy [159]. Combined radiation and cetuximab therapy nearly doubled the median survival in certain patients with stage I head and neck cancer [160]. Other EGFR targeting molecules won FDA approval: Panitumumab showed activity as single treatment in metastatic colorectal cancer resistant to standard chemotherapy; gefitinib and erlotinib, among others [161].

Bevacizumab (Avastin) is another monoclonal antibody currently used in therapy regimens. It targets VEGF preventing its interaction with VEGF receptors (VEGFR-1 and VEGFR-2). It was first approved in the EU in 2005, for the treatment of metastatic colorectal cancer and later approved for treatment of several primary and metastatic cancers as well as for the treatment of recurrent, platinum-sensitive or platinum-resistant epithelial ovarian, fallopian tube and primary peritoneal cancer [162]. As stated before, VEGF promotes the proliferation and migration of vascular endothelial cells, increasing vascular permeability, and promotes survival of endothelial cells via the inhibition of apoptosis. Solid tumour growth is dependent on the formation of new blood vessels – angiogenesis – to supply oxygen and nutrients to the tumour core. Angiogenesis plays a critical role in tumour growth, invasion and metastasis. Therefore, blocking tumour angiogenesis can be a therapeutic option to treat solid tumours. Anti-angiogenic therapy poses some advantages over conventional chemotherapy since it is not directed at killing cells by affecting mitosis but by blocking their supply of nutrients. As angiogenesis is a rare event in tissues other than growing tumour, it is well tolerated by patients and has few side effects [43, 48, 163–166].

Recognition and management of toxicity associated with cancer immunotherapy will be a key factor for clinical success. The continuous research of tumour associated markers that can be used as antigens will be essential for the development of cancer immunotherapy.

1.4.5 Gene therapy

Gene therapy started to be fully developed in the early 1990s with the first clinical trials. It consists on editing or modulating the genetic information of an individual to treat a disease. Gene therapy can target nuclear DNA, using genome editing tools such as clustered regularly interspaced short

palindromic repeats (CRISPR/Cas9), or RNA, using anti-sense oligonucleotides and RNA interference [167–169]. DNA targeting therapies tend to have a permanent effect in cells, while RNA strategies are transient. Both strategies seek to restore missing functionality, or shutdown a dysfunctional gene. The main challenge in gene therapy is to deliver the genetic material to cells, using transfection vectors. They aim at sustaining stable nucleic acid transport and expression with minimal side effects. These transfection vectors can be liposomes, viral particles, recombinant proteins or inorganic nanoparticles, each bearing individual advantages and disadvantages [167–169]. Viral vectors for gene transfer include adenoviruses, which are the most common gene delivery systems in clinical settings, adeno-associated viruses, herpes simplex-1 viruses, retroviruses and lentiviruses. Viruses can be efficient gene carriers, but they have limited DNA cargo capacity and can cause immunogenicity. Synthetic delivery systems generally avoid immune responses and carry higher amounts of cargo [170]. Single-stranded antisense oligonucleotides (ASO) consist in a synthetic oligonucleotide vectorized in cells, that is complementary to an RNA target. The enzyme RNase H cleaves the RNA strand of DNA-RNA hybrids, decreasing their pool and consequent protein translation. Also, ASOs can block gene expression by sterically blocking the ribosome to anchor to RNA. In RNA interference a small double strand RNA is vectorized inside cells targeting a specific mRNA sequence. Then the RNA-induced silencing complex, loses one of the strands, and the remaining strand (the guide strand) binds to complementary RNA. This process is mediated by the RNA-induced silencing complex which ultimately cleaves the targeted RNA. One of the main challenges in gene silencing methods is that oligonucleotides are unstable inside cells. For that reason, modified nucleic acids, or nanotechnology materials are used to increase their stability [171, 172].

Some gene therapy products are already available in the market for clinical use. The first approved for human use, only in China, was Gendicine for the treatment of head and neck squamous cell cancer in combination with radiotherapy. Other approved gene therapies rely on the use of engineered T cells. Chimeric T cell receptors are extracted from a patient and genetically modified to “attack” a specific protein. Cells are then injected back into the patient targeting cancer cells and working as a living drug. Two therapies are approved for clinical practice, for treatment of B-cell acute lymphoblastic leukaemia (Tisagenlecleucel, Kymriah) and large B-cell lymphoma (Axicabtagene ciloleucel, Yescarta) [173].

1.4.6 Thermal therapy

Thermal therapy, also called hyperthermia, is a type of treatment in which body tissues are exposed to temperatures up to 45°C. Treatment can be local, regional or whole-body. Exposure of tissues to high temperatures increases the fluidity of membranes, promotes protein denaturation, and can cauterize blood vessels [174]. Research has shown that hyperthermia can be used to specifically heat neoplastic tissue, with minimal effect on normal cells, allowing their use in cancer therapy [175–177]. Hyperthermia treatment is generally performed using microwaves, ultrasounds, radiofrequency or lasers. By focusing the radiation to a specific site, it can affect cancer cells with a minimally invasive procedure. Most of these methods rely on the use of a probe inserted through a body cavity to the tumour site. These methods are most often applied to treat tumours that cannot be removed with standard surgery or for patients who cannot go through surgery. Its efficacy is related to the temperature achieved during the treatment, as well as its duration and tissue tolerance. To assure the desired temperature, the tumour and surrounding tissues are monitored with thermometers [174–177]. Imaging techniques, such as computed tomography can be used to guide the probes proper positioning [178, 179]. Hyperthermia can be repeated for relapse tumours. It is almost always used in combination with other therapies like surgery, radiation or chemotherapy. Drug sensitization through hyperthermia can be found in several anti-cancer drugs, specially alkylating agents. The increase in temperature enhances tissue perfusion and facilitates the absorption of the chemotherapeutic through the cell membrane. Even cells that have shown to be resistant to a specific drug, can respond when combined with thermal therapy. Thus, chemotherapy becomes more effective, and less toxic. Results from clinical trials have shown hyperthermia to be beneficial in the treatment of several types of solid tumours, with improved overall survival, compared with patients who only receive radiotherapy or chemotherapy [180–182]. An example is the work developed by Valdagni and Amichetti to treat head and neck tumours. They demonstrated, on a Phase III randomized trial, that combined treatment of hyperthermia and radiation therapy, significantly improved patients' survival and did not increase acute or late toxicity [183]. Also, medical reports on the conjugation of liposomal DOX and hyperthermia show that the combined therapy is effective and well tolerated [184, 185]. Hyperthermia is a promising approach to improve cancer treatment, but it is still largely experimental. With the developments in technology the benefits of hyperthermia will significantly increase. The refinements in heating delivery and monitoring strategies will enable an accurate thermal dose control, arriving to deeper organs without affecting superficial tissue. Integration with emerging imaging technologies, such as non-invasive magnetic resonance-based thermometry, and nanotechnology thermal probes will push hyperthermia to the next level of cancer treatment.

1.5 Cancer resistance to treatment

One of the main causes in cancer treatment failure is the acquisition of resistance to chemotherapy. Many cancer types are initially susceptible to pharmaceutical treatment but, over time they start to develop drug tolerance. Drug resistance is a well-studied phenomenon that results from events that increase cancer cell survival (Fig. 1.3). The major mechanisms of acquired drug resistance are: change in drug metabolism, change in drug target, increased drug efflux, decreased drug uptake, increased DNA damage repair, and increased resistance to apoptosis. Some anticancer drugs require metabolic activation, thus one of the ways cancer cells can develop to resist is through decreasing drug activation [186–188]. An example is platinum resistance that can occur through overexpression of metallothionein and thiol glutathione, that inactivate the drug [151, 189]. Cells can also alter the drug target, to reduce the efficacy of the drug. For example, certain anticancer drugs target topoisomerase II, which prevents DNA super-coiling and under-coiling, stabilizing the DNA-topoisomerase II complex. This leads to inhibition of DNA synthesis, halting the mitotic processes. Resistance to topoisomerase II-inhibiting drugs has been described by mutations in the topoisomerase II gene, avoiding drug recognition [190]. The same is observed in EGFR family and down-stream signalling (RAS, SRC, RAF, and MEK), generally overexpressed in many tumours. Mutations in these genes hinder drug recognition and compromise therapy [161].

DNA damage repair has a key role in anticancer drug resistance. Radiotherapy as well as many chemotherapy drugs directly or indirectly damage DNA. DNA damage response mechanisms can repair the drug-induced damage. In platinum chemotherapy harmful DNA crosslinks, leading to apoptosis. However, resistance to platinum-based drugs can arise by nucleotide excision repair and homologous recombination, reversing platinum damage, meaning that the efficacy of DNA-damaging therapies relies on the failure of the cancer cells DNA damage response. Mutations in apoptosis-related genes can also result in drug tolerance. For instance, apoptosis is triggered by the tumour suppressor TP53, in response to chemotherapy, which is found mutated in 50% of cancers. Alternatively, inactivation of P53 regulators such as caspase-9 and its cofactor, also leads to drug resistance. In several types of cancers, BCL-2 family proteins, as well as other antiapoptotic proteins, are highly expressed, avoiding apoptosis and increasing cell survival [114, 134, 191].

One of the most studied mechanisms of cancer resistance is via drug efflux. Efflux pumps are a member of transporter family proteins that bind to a given substrate in the transmembrane domain and mediated by ATP hydrolysis, push the substrate out of the cell. ABC transporter family is the most studied and is highly expressed in the epithelium of the liver, intestine and blood brain barrier, preventing overaccumulation of toxins within the cell. Being part of physiological processes, ABC transporters are also involved in the mechanism of drug resistance in cancer cells. The most studied are multidrug resistance protein 1 (MDR1), multidrug resistance-associated protein 1 (MRP1), and breast cancer resistance protein. These transporters have unspecific substrates, being able to efflux a variety

of xenobiotics, protecting cancer cells from many first line chemotherapies. They are commonly overexpressed in resistant cancer cells [192–194].

Reducing the uptake of the drugs can also occur. If a drug depends on a transporter to enter the cell cancer cells can acquire resistance by reducing the numbers of transporters. Mutations in these transporters can also inhibit and reduce the absorption of the drugs. The resistance to Methotrexate, for example, is mediated by the human folate carriers. Gene mutation in these carriers reduces the tendency of the drugs to bind the transporter in the patients with acute lymphoblastic leukaemia [188].

Characterising the genetic profile of tumours can have important implications in the treatment of relapses. Primary resistance to EGFR inhibitors therapy has been found in patients with alterations in specific genes. Resistance to gefitinib and erlotinib therapy is described in patients with point mutations in EGFR (T790), BRAF, PIK3CA, or up regulation in MET, HER2 or loss of PTEN [191]. Resistance to ALK inhibitors occurs due to upregulation or mutations in ALK (L1196M), or activation of EGFR or KRAS, that bypass the inhibition induced by crizotinib [195]. Second generation inhibitors afatinib and ceritinib are FDA approved and promise treatment to patients who no longer respond to first generation tyrosine kinase inhibitors for EGFR or ALK.

Cancer progenitor cells are often drug resistant. These cells remain dormant in patients seemingly in remission and can later cause cancer relapse. Due to the plethora of mechanisms of cancer resistance, the current paradigm believes that combination therapy increases the chances of an effective treatment because it reduces the probability of simultaneous resistance via two or more mechanisms. The future steps in anticancer therapy should not only be focused on combined therapy but also in strategies to eliminate cancer progenitor cells. To achieve that continuous efforts, need to be performed to understand the underlying mechanisms of progenitor cancer cells persistence.

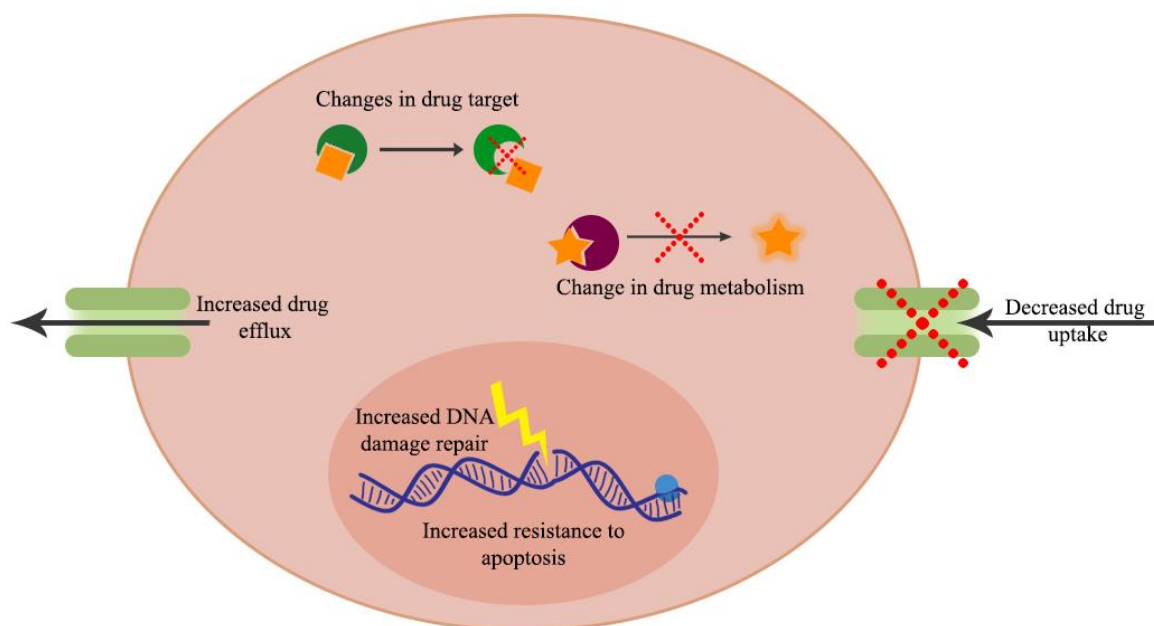


Fig. 1.3 Schematics of different mechanisms of acquired drug resistance.

1.6 Nanomedicine

The most consensual definition states that nanotechnology is the study and use of structures between 1 and 100 nanometres in size. The need for a less general definition led the European Commission to name it as “the study of phenomena and fine-tuning of materials at atomic, molecular and macromolecular scales, where properties differ significantly from those at a larger scale”. The National Technology Initiative defines nanotechnology as “the understanding and control of matter at dimensions between approximately 1 and 100 nanometres, where unique phenomena enable novel applications”. From these definitions we should take three important points about nanotechnology, i) it relies on nanometre scale, ii) the properties of the nanomaterial need to differ significantly from the bulk, iii) needs to be controllable. Nanotechnology has been revolutionizing several sectors like: energy, environment, information technology and medicine [196], and it was described “as an upcoming economic, business and social phenomenon” by Thomas Theis (Director of Physical Sciences at the IBM Watson Research Center) [197].

Growing interest in the medical applications of nanotechnology is leading to the rapid development of nanomedicine [198]. The Medical Standing Committee of the European Science Foundation states that “Nanomedicine is the science and technology of diagnosing, treating, and preventing disease and traumatic injury, of relieving pain, and of preserving and improving human health, using molecular tools and molecular knowledge of the human body”. Several nanomaterials have been described in the last decades, made of noble metals, carbon, heavy metals, etc. and can take many forms: nanoparticles, nanowires, nanotubes and nanofilms. Each nanomaterial can have unique properties at nanoscale. For example, carbon nanotubes are excellent conductors with exceptional strength; iron oxide nanoparticles are superparamagnetic; while gold nanoparticles (AuNP) have unique optical properties. Nanostructures’ primary advantages are that their size is at the same scale of biomolecules, and their augmented surface area-to-volume ratio allows an increased interphase area in a small mass; they have favourable drug release profiles, and can be modified with targeting agents that allow them to reach tumour tissue and release drugs in a stable and controlled manner [199]; they can be used to encapsulate and vectorize small molecules that have poor solubility, facilitating their travel through the bloodstream and renal clearance. Nanoparticles, due to their reduced size, have also the advantage of accumulating naturally in tumours by EPR effect [199]. Currently, a wide variety of nanoformulations are being investigated for cancer treatment, including lipid-based, polymer-based, inorganic, viral, and drug-conjugated nanoparticles. Some of these are already approved for clinical use (Table 1.2).

Table 1.2 Currently approved nanomedicines in the clinic. Adapted from [199].

Name	Type	Active drug	Year approved	Diameter	Type of cancer
Zinostatin stimalamer	Polymer protein conjugate	Styrene maleic anhydride neocarzinostatin (SMANCS)	Japan (1994)	not described	Renal cancer
Doxil/caelyx	Liposome (PEGylated)	Doxorubicin	FDA (1995), EMA (1996)	80-90 nm	HIV-associated Kaposi's sarcoma, ovarian cancer, metastatic breast cancer, multiple myeloma
DaunoXome	Liposome (non-PEGylated)	Daunorubicin	FDA (1996)	45 nm	HIV-associated Kaposi's sarcoma
Lipo-Dox	Liposome	Doxorubicin	Taiwan (1998)	180 nm	Kaposi's sarcoma, breast and ovarian cancer
Myocet	Liposome	Doxorubicin	EMA (2000)	190 nm	Breast cancer
Abraxane	Nanoparticle albumin bound	Paclitaxel	FDA (2005) EMA (2008)	130 nm	Advanced non-small-cell lung cancer, metastatic pancreatic cancer, metastatic breast cancer
Oncaspar	PEG protein conjugate	L-Asparaginase	FDA (2006)	50-200 nm	Leukaemia
Genexol-PM	PEG-PLA polymeric micelle	Paclitaxel	South Korea (2007)	20-50 nm	Breast cancer, Lung cancer, Ovarian cancer
MEPACT	Liposome (non-PEGylated)	Mifamurtide	EMA (2009)	not described	Osteosarcoma
NanoTherm	Iron oxide nanoparticle	-	EMA (2010)	20 nm	Thermal ablation glioblastoma
Marqibo	Liposome (non-PEGylated)	Vincristine	FDA (2012)	100 nm	Philadelphia chromosome negative acute lymphoblastic leukemia
MM-398 (Onivyde)	Liposome (PEGylated)	Irinotecan	FDA (2015)	80-140 nm	Metastatic pancreatic cancer (2nd line)

1.6.1 Gold Nanoparticles

AuNP have been extensively studied mostly due to their unique optical properties, easy synthesis and functionalization, and low toxicity. AuNP exhibit a surface plasmon resonance conferring them a light extinction cross sections, 5 to 6 times higher than common fluorophores. They can enhance fluorescence or quench fluorophores in its vicinity, and enhance the Raman scattering of molecules on a process called surface enhanced Raman scattering. They also have the capacity to convert light to heat with efficiencies that can reach almost 100% depending on their size. AuNP range in diameter from small atom clusters of 2-5 nm up to 100 nm particle, and each size can have different properties. Smaller particles tend to extinct light in blue region of the spectrum, and have almost neglectable scattering, while bigger particles extinct light in the red region mainly by scattering. Also, their shape can vary, from spheres, hollow, rods, diamonds, prisms, cages, either single solid bodies or in a core shell format with other metals [200, 201]. Different combinations of sizes and shapes can serve different purposes, taking advantage of each NP optical properties, photothermal capability in the infrared and near-infrared (NIR), biofunctionalization potential and toxicity [202, 203].

Many synthesis methods of AuNP have been described, in water, organic solvents or even interphases. The most common are water-based and rely on the same principle: chloroauric acid (HAuCl_4) is dissolved in water, then a reducing agent reduces Au^{3+} ions to Au^0 . These atoms start to aggregate in clusters growing in diameter until they get saturated of capping agent that protects them from aggregation, and then they precipitate in the form of sub-nanometre particle. The concentration of gold salt, reducing agent and capping agent is crucial to set the final AuNP size and shape. One of the quickest protocols describes the synthesis in five minutes, by adding sodium citrate to chloroauric acid, assisted by microwave radiation. Gold surface has a high affinity to certain groups, namely thiols, amines and phosphates. The development of several surface functionalization tools enabled AuNP to be decorated with almost any kind of biomolecules, from imaging moieties (e.g., fluorophores, quenchers, reporters) to targeting molecules (e.g., antibodies, peptides, sugars), stabilizers (e.g. PEG), and even therapeutic agents (e.g., chemicals, therapeutic oligonucleotides) (Fig. 1.4).

The number of potential applications in medicine as increased since they have been considered to exhibit low toxicity and high chemical stability [204–206]. Despite the divisive studies about AuNP' toxicological impact *in vivo*, spherical AuNP between 10 and 60 nm in diameter are generally considered as non-toxic. In fact, toxicity may vary with administration route, concentration and surface coverage but also with the nanoparticles' sizes and shapes. The difficulty in standardization of the nanoconjugates, their characterization and of the effect of monitorization, has largely hampered forming a clear-cut definition for nanosafe AuNP [207, 208]. For example, larger particles, 45 nm in size, have been demonstrated to exhibit higher cytotoxicity at a lower concentration ($10 \mu\text{g}\cdot\text{mL}^{-1}$) than those 13 nm in size ($75 \mu\text{g}\cdot\text{mL}^{-1}$) [209]. Oral and intraperitoneal administration routes showed higher toxicity than tail vein injection [210]. Sharp-edged nanoparticles tend to have higher cytotoxicity than rounded

ones, with several studies showing that lower concentrations are needed for stars and flowers to induce toxicity, compared to nanospheres [211, 212]. On the other hand, sharp-edged conformations are more prone to endosomal escape favouring drug delivery [213]. Extensive and standardized studies on nanotoxicity are needed to effectively assess the effect of AuNP in the human body, but that can only be achieved after establishing characterization criteria for the nanomaterial, that assure that the comparable materials are being used across studies.

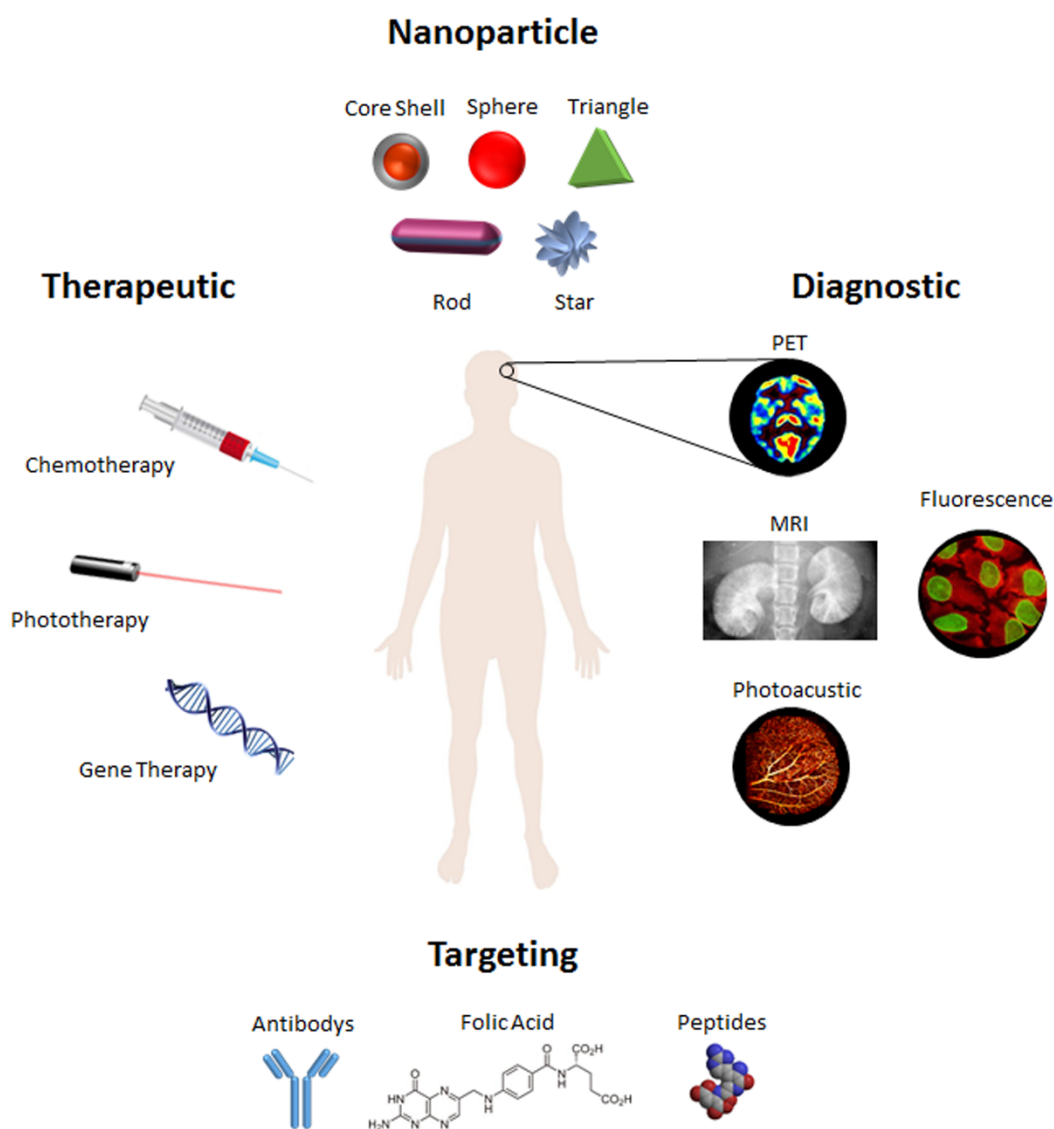


Fig. 1.4 Different types of nanoparticles and their applications in theragnostic. Schematic overview of the possible functionalization and application of AuNP as nanocarriers for theragnostic.

1.6.2 Targeting and Delivery

AuNP can be functionalized with molecules to provide for targeting and to enhance stability and biocompatibility *in vivo*. There is a wide range of stabilizers available that may also act as therapeutic agents (e.g., miRNA, siRNA, DNA, peptides and antibodies) or to reduce NPs' immunogenicity (e.g., PEG). In fact, polyethylene glycol (PEG) of different molecular weights is one of the most frequently used biomolecules to increase NPs' circulation half-life and improve cellular uptake [214, 215]. When referring to PEG grafting to AuNP' surfaces, bi-functional PEGs (with a thiol group in one extremity and another group at the other end – amine, carboxylic, biotin, azide) have been widely used for direct coupling to another molecule of interest via straightforward chemistry with high yield [204, 216]. AuNP can be further engineered to trick the immune system, avoid removal from circulation (by becoming trapped in the liver, kidneys, spleen) or to cross biological barriers (e.g., blood-brain barrier), in order to increase therapeutic efficacy and allow systemic tracking [217].

Passive targeting takes advantage of the fact that vessels surrounding the tumours are leaky, due to incomplete endothelial linings, allowing nanomedicines to reach the tumour through the enhanced permeability retention (EPR) effect alone. Generally, particles between 10 nm and 60 nm in diameter tend to passively accumulate in tumour tissues enabling, for instance, higher drug payload at the tumour site and circulating half-lives about 100 times longer than that of free anticancer drugs, with reduced systemic toxicity [218, 219]. However, this strategy depends greatly on the degree of tumour vascularization and angiogenesis and on heterogeneous blood flow, which limit drug uptake and homogenous distribution within the tumour. Several approaches may overcome these limitations, for instance, using vasoconstrictive drugs. These agents cause normal vessels to constrict and blood pressure to increase, while tumour vessels do not respond to this effect because of insufficient muscular structure, thus leading to a relative increase in the input function of tumour tissues [220]. These leaky effects may also have an important role in the treatment of other pathologies. Spivak and co-workers developed and tested a gold nanoformulation for drug delivery and treatment of heart failure by demonstrating that levosimendan functionalized AuNP (Simdax®) were able to accumulate in the endothelial cells of infarcted arterioles and capillaries. The nanoformulation showed significant cardioprotective effects in DOX-induced heart failure rats, higher than that of Simdax® alone. When comparing the route of administration (intravenous injection, sonoporation – cell permeation by ultrasounds and local, and intrapleural (local delivery) injection, the best results were obtained using intrapleural injection, showing the importance of the administration route for effective treatment [221].

Another strategy relies on attaching targeting moieties to the nanoparticle surface. Typically, nanoparticles reach target cells through ligand-receptor interactions that induce receptor-mediated endocytosis and drug release inside the cell [219]. Peptide conjugation to AuNP is one method by which active and specific targeting may be used for enhanced tumour accumulation/delivery [222]. Successful targeting has also been achieved via functionalizing AuNP with antibodies that target specific receptors

overexpressed by cancer cells. EGFR and folate receptors are two well-known overexpressed proteins in cancer cells used for designing antibody-gold nanoconjugates for active targeting [223, 224]. EGFR exists on the cell surface and it is mostly activated by binding of EGF and TGF- α . Genetic mutations led to EGFR permanent activation and uncontrolled cell division independently of the EGF or TGF α presence. About 30% of epithelial cancers show misregulation in EGFR or other family members [225]. The use of Cetuximab (Erbix[®], Merck, Germany), an FDA approved monoclonal antibody that specifically binds EGFR and turns off its downstream signalling pathways, has been shown to be a useful targeting and therapeutic moiety in mice, vectorizing the nanoparticles to the tumour site [224, 226, 227]. Most of the accumulated particles stayed in the tumour for 72 h post tail-vein injection [223]. Others have also described the use of EGFR targeted ligands for active targeting [228], such as C225 antibody [229, 230]. It was shown that using this antibody, increases the uptake of nanoparticles by mice xenographs in EGFR-positive compared to EGFR-negative cells [230]. Folate receptor is responsible for the internalization of folic acid and several studies confirmed that about 80%-90% of ovarian tumours overexpress this receptor [231]. Drug-folate conjugates have therefore been at the forefront for selective tumour targeting in preclinical studies [139, 232–236]. It was demonstrated that folate functionalized nanoparticles were 4.7 times more directed to tumour cells and internalized by endocytosis into lysosomes when compared to non-functionalized NPs [237].

Targeting has been crucial for the development of vectorization systems capable of site-specific accumulation/retention enabling nanoparticles to deliver their cargo on site for improved therapeutic effect [218]. Some authors have been focusing their attention on developing nanovectorization systems that mediate cargo delivery upon a particular stimulus, such as pH, increased heat, ultrasound, light and magnetic field. Tumour cells usually become hypoxic and exhibit high glycolytic activity, thus producing carbonic and lactic acids [238]. Coating nanoparticles with pH Low Insertion Peptides increase efficiency of targeting acidic diseased tissues. Being membrane peptides, they have affinity to cellular membranes and targets extracellular acidity. In contrast to other pH-sensitive systems, it tracks acidity at the surface of cancer cells [239]. Photothermal conversion of light into heat can increase target cells' temperature, enough to directly kill cells [240], but also to release therapeutic moieties at the tumour site [241]. In fact, a study shows the photothermal induced release of DOX from DOX-loaded gold nanocages. By the degradation of a thermal sensitive polymer covering the NPs when the medium reaches 45 °C, DOX is released in a time dependent manner. Authors were able to significantly decrease cell viability of breast cancer cells *in vitro*, by precisely controlling DOX release [242]. In a similar manner, ultrasounds and magnetic fields can locally increase temperature and precisely deliver cargo. Despite the broad range of targeting approaches, there is still much more to explore in this field with many groups still looking for new effective targeting moieties that allow tumour specific accumulation and retention for improving drug release and therapeutic efficacy [218, 238].

1.6.3 Therapeutic Agents

Drug discovery coupled with preclinical studies strongly focus on overcoming general issues that hamper the efficacy of drugs, such as limited solubility, high toxicity, high dosage, nonspecific delivery and short circulating half-lives. Due to the advances in nanotechnology-based drug delivery, the current idea has been to repackage classic drugs using targeted delivery systems to increase patient compliance, extend the product life cycle and reduce healthcare costs. These agents might be a small drug, a peptide/antibody, a ribozyme, a siRNA or an ASO [243]. Probably the most studied and used concept has been the previously mentioned Doxil[®] (Janssen Products, LP, Horsham, PA), where DOX has shown improved efficacy when encapsulated into PEGylated liposomes. In fact, traditional chemotherapy drugs have followed suit and been encapsulated and delivered in similar engineered vesicles.

AuNP and DOX nanoformulations attempted to mimic their liposome counterpart and showed promising advantages, such as increased targeting and functionalization as well as the possibility to couple with phototherapy and to act as imaging/contrast agents [142, 146]. Various AuNP shapes have been functionalized with DOX – stars [244], clusters [245], shells [246], hollow spheres [247], *etc.* – showing the versatility of the nanoconstructs and their ease of functionalization. All previous examples were tested *in vivo* and have shown increased efficiency when compared with DOX alone, as well as lower levels of cytotoxicity.

AuNP have been also applied in approaches with other anti-tumour drugs (e.g., platinum (IV) prodrugs [248], 5-Fluorouracil [249], Irinotecan [237], Camptothecin [250]). Dhar and collaborators showed a significant increase in cytotoxic effects for the Pt(IV)-AuNP complex when compared with the free Pt(IV) prodrug, as well as the free cisplatin. The Pt(IV) prodrug was activated into its cytotoxic form, cisplatin, only after crossing the cell membrane and undergoing intracellular reduction [248]. Camptothecin is a cytotoxic quinoline alkaloid which inhibits DNA topoisomerase I [251]. Camptothecin showed remarkable anticancer activity in preliminary clinical trials for a broad spectrum of tumours but also low solubility and adverse effects. Shi and collaborators described the use of gold hollow, nanocage shells layered with mesoporous silica and a thermosensitive polymer loaded with Camptothecin. The drug is tightly packed inside the nanoconstruct with a “leakage” of only 6.8% to the medium after 14 h in *in vitro* conditions. NIR triggered release of the drug leading to increased tumour cell death, compared with the only NIR and nanocarrier experiment [250]. For rheumatoid arthritis treatment, iron-AuNP have been functionalized with methotrexate allowing for simultaneous chemophototherapy and imaging with lower dose (0.05%) without compromising efficacy and/or increasing toxicity [252].

Gene therapy has been receiving increasing attention in tumour suppression due to the possibility to downregulate specific oncogene expression or to sensitize cells in an intra-cellular targeting process. In particular, small interfering RNA has shown potential to downregulate specific gene expression in

cancer cells [204]. Since naked siRNAs show extremely short half-lives due to cellular RNases activity and poor chemical stability, the development of efficient delivery vehicles for *in vivo* applications remains a major obstacle in translating siRNA into effective therapeutics. AuNP have been widely used as nanovectorization for gene silencing strategies [253–258]. Almost all the different shapes and sizes of AuNP reported above have been used to vectorize gene silencing elements into cancer cells [258–260]. Feng Yin reported the use of a light-triggered therapy using gold nanorods as nanocarriers for dual-delivery of DOX and *KRAS* gene siRNA. The synergistic effect of the chemo- and gene-therapy allowed the reduction of the tumour volume rate by 90% *in vivo* [261]. Gold spheres were described for siRNA targeting and delivery [262, 263] using models of increasing complexity (cells, hydra and mice), achieving effective silencing of *c-MYC* gene (~65% reduction in expression). It was also shown that covalently bounded siRNAs were more effective silencers than siRNAs adsorbed on the surface of the NPs [263]. Different molecular concepts for gene silencing rather than siRNA have also been used to block a particular gene.

Our group was pioneer in the use of hairpin ssDNA structures vectorized via AuNP to particularly silence any possible RNA mediated pathway inside the cell [258, 264, 265]. In fact, the molecular actuator thus developed – gold nanobeacon – can be visualized *in situ* while silencing (See Figure 2), since the hairpin may be further functionalized with a fluorophore, whose fluorescence is triggered once the silencing event occurs. The potential of this system has been further characterized *in vitro* and *in vivo* with low toxicity [206, 263, 266]. Furthermore, this system was shown to be effective *in vivo* in a promising approach to combat multi-drug resistant tumours, combining in the same particle an antitumor agent (5-fluorouracil) with silencing of MRP1, a gene associated with acquired resistance in several tumours. *In vivo* results showed a remarkable tumour size reduction, from the synergic effect of the two agents [249].

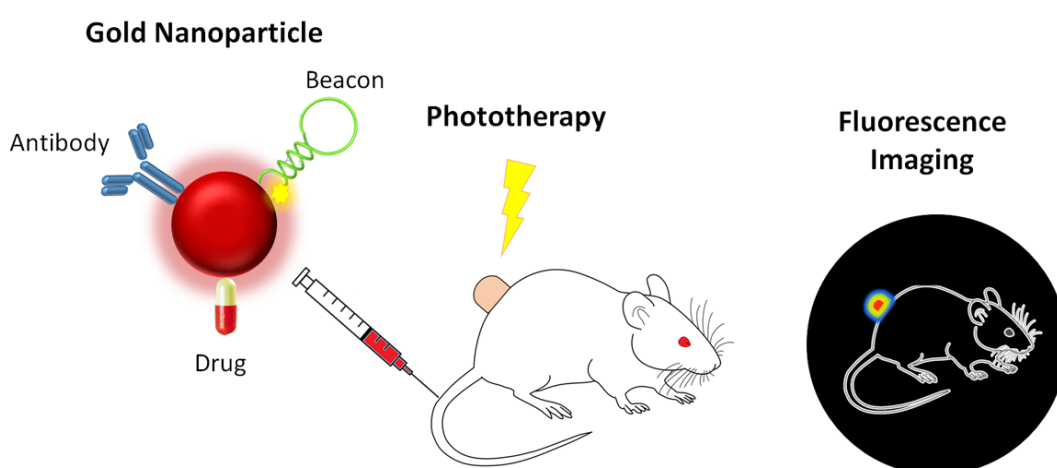


Fig. 1.5 Schematics of a multifunctional approach, coupling targeting, chemotherapy, gene therapy, phototherapy and diagnostics by fluorescent imaging.

1.6.4 Phototherapy

Photothermal therapy (PTT) is based on the selective sensitization of cells to thermal damage, or hyperthermia, near 45 °C. What is more, traditional PTT may be coupled to AuNP and profit two ways: (i) the possibility to vectorize additional cargo and use the nanoparticle as scaffold for selective targeting; and (ii) enhance PTT by the AuNP' ability to convert absorbed photons into thermal energy. By modulating the AuNP' shape and/or shell thickness, it is possible to shift the localized surface plasmon resonance (LSPR) peak of AuNP toward the NIR, allowing deeper light penetration into tissues. Moreover, the laser energy required to achieve this transformation is far below that stipulated in medical safety standards. AuNP-mediated PTT is predominantly associated with nanorods, nanoshells and nanocages [202, 267]. One of the reported strategies was to use functionalized gold nanorods with chemotoxic cisplatin, biocompatible polypeptide poly-l-glutamic acid and tumour targeting folic acid. When administered systemically on tumour-bearing mice, and in combination with localized NIR laser, the resulting hybrid nanoparticles were able to significantly inhibit tumour growth and dissemination of cancer cells from the primary site to the lung by eliminating the peripheral tumour blood vessels (a similar approach is depicted in Fig. 1.5).

Another interesting strategy that can be coupled to nanosized structures is photodynamic therapy, which involves the administration of a nontoxic agent that acts as a photosensitizer and a laser source. Photoexcitation of the photosensitizer leads to the generation of free radicals, which destroy tumour tissue. The chosen wavelength of irradiating light should ideally be one that is absorbed to a greater degree by the tumour tissue relative to the surrounding healthy tissue [228, 268]. Combining photodynamic therapy with AuNP has proven to be a good strategy to overcome two of its major limitations: the dark toxicity of the photosensitizer and the poor selectivity of the cellular uptake of between the target cells and normal tissues. In fact, a study describes the targeted delivery of AuNP functionalized with EGF peptide and the photodynamic agent Pc 4. *In vitro* experiments show that the nanoconjugate is two-fold more efficient at killing tumour cells than free Pc 4, due to enhanced localization in early endosomes [228]. In another research work, AuNP were functionalized with methylene blue, a known photosensitizer; polystyrene-alt-maleic acid, a polymer that prevents methylene blue leakage; and transferrin, for specific receptor-mediated endocytosis. Au@polymer/methylene blue-transferrin were excited by a dark red-light source at 660 nm and showed a two-fold enhancement of photodynamic therapy efficiency toward *in vitro* cervical cancer cells over the use of free methylene blue at four times dosage. Besides being an effective and easy way to induce cell apoptosis, this system proved to be safe since no significant dark toxicity was found [269].

1.6.5 Tackling angiogenesis

The development of new blood vessels from pre-existing vessels is essential to modulate tumour microenvironment, increasing the levels of oxygen, nutrients and decreasing toxic metabolites [40]. A major advantage of AuNP in cancer treatment is their capacity to disrupt signal transduction from tumour mesenchymal cells to epithelial cells as well as inhibiting angiogenic phenotypes *in vitro* [270]. Among VEGF subtypes, the isoform VEGF165, a heparin binding protein, is the most potent cytokine in angiogenic process. By binding with tyrosine kinase receptor VEGFR-2, a cascade signal is initiated ultimately leading to the proliferation and migration of endothelial cells and angiogenesis [271, 272]. Therapeutic antibodies targeting VEGF165 have been developed and are currently applied in the clinics to inhibit VEGF165. Naked AuNP have been reported as inhibitors of pro-angiogenic such as VEGF165, basic fibroblast growth factors and placental growth factor [165]. The naked surface of AuNP inhibits heparin-binding growth factors, by changing its conformation. However, they do not affect the activity of non-heparin binding growth factors, like VEGF121 and EGF. These results have been corroborated *in vivo*, where VEGF/vascular permeability factor induced permeability was inhibited by AuNP [271, 272]. Zhang et al., 2019 state that AuNP also influence angiogenesis, diminishing the tube formation and migration of endothelial cells, by blocking the VEGF-VEGFR2 signalling from tumour microenvironment cells to endothelial cells [270]. Another study stated that AuNP promote tumour vasculature normalization while increasing blood perfusion and reducing hypoxia [273].

Not only naked AuNP but also AuNP-conjugates have been described as modulators of angiogenesis. Recombinant human endostatin is an anti-angiogenic agent used for tumour treatment. Pan et al., 2017 developed a recombinant human endostatin–AuNP that reduced cell migration and tube formation *in vitro* (human umbilical vein endothelial cells cells), induced by anterior gradient 2 (AGR2). AGR2 is one of the latent tumour angiogenesis factors, and have been mostly related to tumour cell proliferation, transformation, migration and drug resistance. Results of *in vivo* experiments, using metastatic colorectal cancer xenografts, indicated that recombinant human endostatin–AuNP increase pericyte expression while inhibiting VEGFR2 and anterior gradient 2. These indicate that this nano-conjugation might be used to normalize tumour vessels using AGR2 as an anti-angiogenic tumour target [274]. Kanaras group as reported a peptide, designed to selectively interact with VEGFR1 for inhibition of angiogenesis. By grafting the peptide on AuNP, authors show that the nano-construct can influence the extent and morphology of vascular structures, without causing toxicity [275, 276]. By exposing a chicken chorioallantoic membrane (CAM) to the AuNP-peptide, our group showed that the nano-formulation is more effective at inhibiting angiogenesis than the free peptide [277]. These studies show that AuNP can be used to alter the expression of anti-angiogenic factors, under biological conditions. The use of nanoparticles to control angiogenesis opens a new door in targeted drug delivery and therapy for angiogenesis.

1.6.6 Multimodal Imaging

The implementation of imaging techniques for diagnostic purposes enables the non-invasive assessment of anatomical, functional and molecular information, with image-guided drug delivery gaining much attention nowadays [278]. The imaging modalities most often used in the clinics are CT, ultrasound, magnetic resonance imaging (MRI), positron emission tomography (PET), single-photon emission computed tomography (SPECT), photoacoustic tomography and fluorescence imaging [279]. When choosing an imaging technique, one should take into consideration several parameters: target tissue, resolution, sensitivity, contrast and implementation. CT is a commonly used diagnostic imaging tool offering broad availability at a relatively modest cost. This modality usually provides image contrast to visualize tissue density differences and may be tuned to distinguish between normal and cancerous tissue. However, the iodinated molecules that are typically used as CT contrast enhancers tend to undergo a rapid renal clearance and nonspecific vascular permeation causing a decrease in the technique sensitivity. MRI displays high spatial resolution and soft tissue contrast but is expensive and time-consuming. Ultrasound imaging offers high resolution at much lower cost than MRI or PET/SPECT but has low depth penetration. PET/SPECT are particularly suited for targeted *in vivo* molecular imaging and their advantages include high sensitivity, absence of tissue penetration limit, and the ability to make quantitative measurements, however, these techniques expose the patient to ionizing radiation. Photoacoustic tomography allows the reconstruction of images with improved spatial resolution and excellent image contrast when compared to conventional optical imaging [279–283].

Imaging techniques can take advantage of the photoacoustic phenomenon that is generated upon formation of nanobubbles. Shao *et al.* describe the use of this technique for gold nanoparticle tracking in mice, observing individual gold clusters, however, it works best on soft tissues and has depth-of-field limitations [284]. AuNP are also optimal contrast agents for CT, due to the relatively high X-ray attenuation of gold and the stability of gold colloids. Since gold has higher absorption than iodine, AuNP can achieve better contrast with lower X-ray dose [285]. On the contrary, AuNP do not possess intrinsic properties that enable their visualization through MRI; hence, they are usually combined with super-paramagnetic iron oxide, gadolinium or manganese, demonstrating significant contrast enhancement in tumour models [252]. Furthermore, *in vivo* studies with gold nanorods labelled with radioactive iodine enabled photothermal therapy towards ovarian cancer and monitoring of nanoparticles' distribution via SPECT/CT imaging. Tumour sites were clearly visualized from the SPECT images even at 24 h post-injection [286].

Fluorescence imaging is highly suitable for high-throughput screening with high sensitivity, providing detailed molecular profiling with subcellular resolution, enabling multicolour imaging and being relatively inexpensive, but has low tissue penetration and spatial resolution, thus limiting its applications in clinical settings. Using the NIR part of the spectrum for fluorescence-based imaging, spatial resolution is improved and autofluorescence is highly reduced making the technique much more

attractive for clinical applications [287]. Indeed, a study combined chemo-, photo-, and thermotherapies with fluorescence imaging capability for diagnosis under NIR light illumination. For that purpose, it was developed a nanoplatform consisting of: a core biodegradable matrix loaded with Dox; a gold nanoshell, required for thermal therapy and drug encapsulation/release; and an outer layer consisting of plasma protein human serum albumin, for stealthiness, to which the fluorescent dye indocyanine green was conjugated, thus providing the nanostructure the capability to emit fluorescence in the NIR range, but also to produce singlet oxygen species (essential for the photodynamic therapy); finally, folic acid was also covalently linked to the protein surface for targeting. The effectiveness of the contrast agent was clearly enhanced by positioning the dye near the metal surface while tuning the plasmon resonance of the nanoshell to the emission wavelength of the fluorophore. *In vivo* fluorescence imaging using tumour-bearing mice demonstrated that the nanoconjugates are localized and retained in the tumour region for at least 48 h. Moreover, a larger fluorescence emission was perceived when using these nanostructures in comparison with the images obtained with similar NPs synthesized without the gold nanoshell component [234].

Owing to their underlying physical principles and distinct benefits/drawbacks, one can take advantage of combining two or more techniques in a single nanocarrier, avoiding a repeated challenge to the patient's immune system and providing more accurate and dependable data on the patient's condition than using a single imaging moiety [288, 289]. Combining CT, surface-enhanced Raman scattering (SERS, of molecules adsorbing on a noble metal surface) and thermal imaging, it was possible to accurately detect gold stars located in the tumour and further confirm photothermal effectiveness with a thermal camera [290]. Other successful examples of combined imaging modalities using AuNP include: a multicomponent nanocapsule used for real-time ultrasound and high resolution MRI for image guided photothermal tumour ablation [291].

Since the challenges of efficient tumour treatment include accurately identifying the location and size of tumours and monitoring the effectiveness of therapy after treatment, integration of contrast-enhanced diagnostic imaging capability with photothermal therapy is a winning bet in the fight against cancer. Overall AuNP can be compared with toolbox that allows diagnosis, imaging therapy in the same platform. This concept is called theragnostic, a new field of medicine which combines specific diagnostic and local targeted therapy and treatment response monitoring. Theragnostic allows a transition from conventional medicine to a more personalised and precise.

1.6.7 Theragnostic in cancer

Significant efforts have been made in the past years towards understanding the genetic and pathophysiological processes contributing to malignant transformation and tumorigenesis. The overwhelming amount of information thus retrieved is now being translated into the field of biomarker discovery and foster cancer therapy by selective interference with cancer hallmarks. Despite these efforts, conventional cancer therapy, including surgery, chemotherapy and radiation, lack target cell specificity and are often disconnected from individual diagnosis. Also, the efficacy of conventional therapeutic strategies is often limited by the acquisition of MDR by tumour cells and by poor drug penetration into the tumour [292]. This is why several molecular targeted therapeutics have been designed to selectively target tumour cells, the benefits being improved efficacy and decreased toxicity [293]. These novel targeted therapeutics may be engineered to simultaneously provide information about delivery, biodistribution and diagnostics, e.g., as imaging agents allowing disease detection at its early and asymptomatic stages [216]. Theragnostic, has promised to significantly increase the precision and effectiveness of treatment, shifting the current clinical standard from generalized procedures to a personalized or precise approach [294–297]. Consequently, theragnostic shows particular impact in heterogeneous diseases that require individualized and tailored methods of treatment and monitoring, such as cancer [285, 298, 299], rheumatoid arthritis [300], infection and cardiology [301, 302].

With proven results *in vivo*, and single cell precision, plasmonic nanobubbles (PNB) are an example of an innovative, valuable tool in theragnostic [303]. PNBs are generated due to the interaction of short, high-energy optical pulses and plasmonic nanoparticles. Depending on the laser intensity, the precision of the shockwaves can disrupt lysosomes – promoting lysosomal escape – or cellular membranes leading to cell death. PNB have therefore a mechanical effect by nature and not a thermal one. The PNB have also interesting optical properties, greatly enhancing light scattering around the nanoparticle, and have increased photoacoustic signal, making them good imaging probes for diagnostics [229, 230, 304]. In mouse models, PNB were able to detect between 3 and 30 residual cancer cells which were undetectable with current methods. Then PNB-guided surgery destroyed those cells preventing local recurrence. Nanotechnology has proven its capability to engineer solutions to enhance theragnostic monitoring therapeutic efficacy noninvasively and in real-time. This tailored approach enables physicians to customize treatment based on each patient's responses and needs, thereby preventing unwanted deleterious side-effects or sub-optimal dosage that might lead to drug resistance, incomplete remission and relapse [298, 305, 306].

1.6.8 From Research Lab to the Clinic

The use of gold in medicine dates to 2500 BC when Chinese and Arabic physicians used gold preparations in their practice. Medieval physicians used mixtures of colloidal gold for various ulcerative skin conditions. In the 20th century, several formulations of gold salts were used to treat tuberculosis, *lupus vulgaris*, syphilis and rheumatism. In 1997, Guy Abraham and Peter Himmel reported the use of 20 nm AuNP for rheumatism treatment in 10 patients with doses of 30 mg [307]. Their results showed a “rapid and dramatic” positive effect on the tenderness and swelling of joints with no evidence of toxicity in any of the patients. Since then, there have been no follow up studies on AuNP for rheumatism in clinical settings.

Recombinant human tumour necrosis factor alpha (rhTNF) was applied in the 80s with remarkable antitumor effects in mice, inducing apoptosis, cytolysis or cytostasis of tumour cells. However, multiple phase II studies with more than 156 patients, resulted in only one complete and one partial response at the maximum tolerated dose, which may correlate to low therapeutic dose at disease site. CYT-6091 from Cytimmune was the first product on clinical trial using AuNP for patients with advanced solid tumours (NCT00356980, NCT00436410). The nanoformulation is composed of PEGylated 27 nm AuNP functionalized with rhTNF. It was administered systemically to 30 patients at doses of rhTNF that were previously shown to be toxic, without detectable side effects [308]. In addition, gold was found in breast tumour tissue but not in healthy breast tissue showing the potential of this approach. Phase II clinical trials are ongoing, aiming at understanding if this nanotechnology approach induces greater vascular leak by dynamic contrast-enhanced MRI and to evaluate the safety and efficacy of CYT-6091.

AuroLase[®] is an FDA-approved pilot study that uses silica-gold nanoshells with a NIR laser for photothermal therapy (NCT00848042, NCT01679470). Nanoparticles called AuroShells are injected intravenously in the patient’s blood stream and accumulate passively in the tumour. This clinical trial was designed to evaluate the approach’s effectiveness for the treatment of advanced lung tumours resulting from either primary lung cancer or metastatic tumours in the lung. Although the trials are complete, the results have not yet been disseminated.

The results for NANOM FIM, a completed phase I/II clinical trial (NCT01270139) using silica-AuNP, were recently revealed. Developed for the treatment of coronary atherosclerosis, two approaches were taken: core-shell silica-AuNP group and core-shell silica-AuNP iron bearing group. For the former, NPs were administered via surgical inclusion of a patch composed of a sliced porous bovine pericardium biological scaffold with inserted growing multi-layered purified allogeneic stem cells with the initial mesenchymal phenotype. NPs were activated with an NIR laser at seven days after the intervention using a plasmon photothermal strategy. For the latter, the iron bearing NPs were managed with intracoronary infusion of allogeneic stem cells and CD68 targeted micro-bubbles. CD68 targeted micro-bubbles were destroyed by ultrasounds and the nanoparticles were magnetically targeted to the vessel and lesion. NPs were also detonated with the NIR laser at the end of the procedure under the

protection of anti-platelet therapy. For therapeutic analysis, quantitative coronary angiography and intravascular ultrasound were performed pre-, post-procedure and at a 12 months follow-up. The results showed 12.6% reduction in the percentage atheroma volume post procedure, 44.8% in the 12 months follow up for the first group, and 13.1% atheroma volume reduction post procedure, and 44.8% in the 12 months follow up for the second group. The plasmonic resonance therapy using silica-gold NP proved efficient regression of coronary atherosclerosis in both approaches with acceptable levels of safety [309].

1.6.9 Commercial Impact

Nanotechnology R&D continues to grow in importance both in terms of public and private funding. Indeed, global demand for nanotechnology medical products grew by 17% from 2009 to 2014 [310]. The United States National Nanotechnology Initiative investment in nanotechnology Research & Development (R&D), policy and regulation since 2001 now totals a staggering \$22 billion, with the 2016 US federal budget providing more than \$1.5 billion for the National Nanotechnology Initiative [311]. The European Union and Japan are investing substantial resources in nanotechnology, with a comparable level to the United States [312]. The returns are expected to surpass the investment, and the medical field appears to be a front runner in nanotechnology innovations. Nanoparticle based drug delivery is one of the major areas, providing a wide range of formulations that are now beginning pre-clinical or clinical trials. Besides the traditional hurdles conventional therapeutics face to enter the clinics, nanomedicines also face a lack (or the deficiency) of protocols for the characterization of these products in terms of absorption, distribution, metabolism, excretion, and toxicity [313, 314]. However, the FDA, in collaboration with the Nanotechnology Characterization Laboratory, has released guidelines describing how it defines a nanoscale product – specifically, as having at least one dimension between 1 and 100 nm, or as being less than a micron in size, and demonstrating size-dependent behaviour. These agencies are now drafting protocols to address nanomedicines' regulatory and safety gap. The European Commission has also established several goals in terms of nanotechnology regulation, patenting and business creation, with international cooperation being a key asset to improving R&D. Bringing the EU together with countries who are active in nanotechnology research (USA, Japan, Switzerland and Russia) could pave the way for standardized protocols and further initiatives [312]. The fact that nanotechnology is one of the sections included in the Horizon 2020, the biggest EU R&D Innovation Programme, shows the commitment to this subject and its importance in increasing Europe's competitiveness. Its main objectives include scaling up laboratory experience to industrial settings; ensuring the safe development and application of nanotechnologies in health and the environment; and proving the significant long-term benefits provided by nanotechnology-based systems, in terms of health care and quality of life [315].

Nanomedicines are still at an early development stage and, thus, their impact on health spending and cost effectiveness is still difficult to predict. Can these formulations compete with conventional products in the medical sector? For example, examining the cost-effectiveness of chemotherapy (gemcitabine)

vs. nanotherapy (PEGylated liposomal DOX) for ovarian cancer showed that the chemotherapy pre-treatment costs were cheaper by €1285. Nonetheless, these costs were more than offset by administration and hospitalization costs, which were €2670 in favour of nanotherapy. The clinical benefit associated with nanotherapy was proven, yielding not only positive cost-effectiveness results, but also significant financial savings [316].

Nanotheragnostics innovations, in particular, can have a significant impact on health costs by reducing the number of diagnostic tests and increasing therapy efficacy. Additional savings are expected due to the overall reduction of the number of days in hospital for each patient. Hence, the global market for nanomaterials used in theragnostic is anticipated to be more than \$187 billion in 2017 [317]. Despite these figures and expectations, for an overview of these accounts for all the nanoformulations reaching the (pre-) clinical stage, where those relating to AuNP alone are just the tip of the iceberg. Another good indicator of AuNP' increasing impact on the medical sector is the number of companies that are devoted to R&D in this area alone. Due to high competition among the market players and low yield coupled with high expenditures in R&D, most companies choose to invest in specific end-use applications: diagnostic tests for the point-of-care market, biomedical imaging or photothermal therapy. Successful examples include Nanospectra (Aurolase[®]) and Cytimmune (Aurimune[®]) whose flagship products are now facing clinical trials. Although the market for gold nanomaterials is still developing, their clinical and financial benefits are undeniable. In the future, efforts should be made to improve the bridge between academia, R&D companies, regulatory agencies and the pharmaceutical industry. In Table 1.3, we compiled a brief list of the theragnostic strategies using AuNP currently in pre-clinical and clinical studies.

Table 1.3 Compilation of gold strategies. Brief overview of current efforts in AuNP for theragnostic – pre-clinical and clinical studies.

Particle	Targeting	Therapeutic	Phototherapy	Imaging	Refs
PRE-CLINICAL STUDIES					
Silica-Gold Shells (150 nm)	-	-	Photothermal	MR	[318]
Gold Hollow Spheres (40 nm)	Melanocortin Type-1 Receptor	-	Photothermal	PET	[319]
Gold Spheres (60 nm)	EGFR	-	PNB	Scattering	[229]
Gold Hollow Spheres (40-50 nm)	Folate Receptor	Irinotecan + siRNA NF- κ B p65 subunit	-	PET	[237]
Gold Cages (48 nm)	-	-	Photothermal	PET	[241]
Gold Clusters (1 nm)	Folate Receptor	Doxorubicin	-	Fluorescence	[245]
Gold Hollow Spheres (37 nm)	Ephrin Type-B Receptor 4	Doxorubicin	Photothermal	SPECT	[247]
Gold Stars (25 nm)	RGD	Doxorubicin	Photothermal	Fluorescence	[244]
Iron Oxide-Gold Spheres (6-18 nm)	A33 Antigen	-	Photothermal	MR	[320]
Gold Spheres (33 nm)	-	Tumour Necrosis Factor α	Photothermal	Photoacoustic	[284]
Gold Spheres (90 nm)	EGFR	Cetuximab	-	Raman Scattering	[321]
Gold Spheres (60 nm)	EGFR	Doxorubicin	PNB	Photoacoustic	[230]
Gold Spheres (5 nm)	EGFR	PC 4	Photodynamic	Fluorescence	[228]
Gold-Cage (40-50 nm) + Silica Sphere Shell (50 nm)	-	Camptothecin	Photothermal	Fluorescence	[250]
PLGA-Gold Shell	Folate Receptor	Doxorubicin	Photodynamic;	Fluorescence	[251]
Gold Spheres (14 nm)	-	-	Photothermal	X-ray CT	[322]
PLGA-Iron Oxide-Gold Shells (374 nm)	-	-	Photothermal	US; MR	[291]
Gold Spheres (3.3 nm)	Folate Receptor	α -Tocopheryl Succinate	-	X-ray CT	[323]
Iron Oxide + Gold Clusters (150 nm)	Magnetic	Doxorubicin	Photothermal	MR	[324]
PLGA-Gold Shell (115 nm)	-	Doxorubicin	Photothermal	MR	[246]

Gold Rods + Liposome Hybrid	-	siRNA PLK1	-	Multispectral Optoacoustic Tomography	[325]
Gold Bellflowers (180 nm)	-	-	Photothermal	Photoacoustic; US	[326]
Gold-Silica Rattles (150 nm)	-	Doxorubicin	Photothermal	Fluorescence; MR; Photoacoustic	[327]
Gold (20 nm) Gelatin shell (150 nm)	RGD	Doxorubicin	-	Fluorescence	[328]
Gold Stars (70 nm)	-	-	Photothermal	Thermal	[329]
Gold Spheres (12 nm); Gold Stars (30 nm; 60 nm)	-	-	Photothermal	SERS; X-ray CT; Two Photon Luminescence	[290]
Gold Rods (10:37 nm)	Folate Receptor	-	Photoacoustic	Photoacoustic	[236]
Gold Spheres (15 nm)	Scavenger Receptor	siRNA VEGF	-	Fluorescence	[330]
Gold Rods (22:47 nm)	-	Doxorubicin + siRNA K-Ras	Photothermal	Fluorescence	[261]
Gold Spheres (15 nm)	-	Antisense K-Ras	-	Fluorescence	[253]
Gold Spheres (14 nm)	-	U5'-fluorouracile + siRNA MRP1	-	Fluorescence	[249]
PLGA-Gold-Iron-Gold	RGD; Magnetic	Methotrexate	Photothermal	NIR; MR	[300]
Gold Spheres (30 nm)	Sonoporation	Levosimendan	-	US	[221]
Gold Rods	protein A lipoprotein	-	Photothermal	Photoacoustic	[331]
Gold-Silver Core Shell (20 nm)	Anti-MRSA antibody	-	-	X-ray CT	[332]
Gold Rods (10:33 nm)	Folate Receptor	-	Photothermal	SPECT; X-ray CT	[286]
Gadolinium-Gold (2-2.5 nm)	-	Healthy Pancreatic Islet Cells	-	MR; US; CT	[333]

CLINICAL STUDIES

Gold Spheres (20 nm)	-	-	-	-	[307]
Gold Spheres (27 nm)	-	Tumour Necrosis Factor α	-	-	[308]
Silica-Gold Shell (60-15 nm; 70-40 nm)	-	-	Photothermal	US	[309]

Note: MR – Magnetic Resonance; PET – Positron Emission Tomography; SPECT – Single-Photon Emission Computed Tomography; US – Ultra Sound; NIR – Near Infrared; EGFR – Epidermal Growth Factor Receptor; PNB – Plasmonic Nanobubble.

1.7 Scope of Thesis

In chemotherapy, the major obstacles are the low specificity of drugs for cancer cells, triggering healthy tissue side effects such as: neutropenia, alopecia, myalgia, nausea, vomiting, diarrhoea and the development of acquired resistance that can lead to therapeutic failure. There is a constant need for the development of novel chemotherapeutic strategies, with focus on combined therapies that mitigate the mentioned obstacles. Nanomedicine has opened the possibility for innovative therapeutic approaches that enhance selectivity and efficacy of cancer therapy. AuNP are amongst the most versatile and explored metallic nanoparticles for medical purpose, mainly due to their reduced toxicity.

In this thesis we hope to extend the knowledge of cancer treatment, by studying the mechanism of action of chemical and physical agents and active targeting of moieties to the tumour site. The main objective of this thesis was to develop new targeted strategies to tackle tumour (acquired) resistance that may be effective with reduced toxic side effects. The work has been broadly divided into five stages, each one addressing a crucial aspect of developing nanomedicines capable to tackle tumour growth and drug resistance.

1. Characterization of novel chemical agents in biological context, with interest towards metal complexes that due to their versatile moieties allow improvement in drug design and whose mechanism may override existing drug resistance/adaptation mechanism from tumour cells;
2. Targeted vectorization of compounds using AuNP towards active targeting to tumour cells and loading of effector cargos and assessment of therapeutic effect *in vitro* and *in vivo*;
3. Use of AuNP for photothermal conversion towards directed hyperthermia capable of effectively killing cancer cells, and tackle survival/evasion mechanism (e.g. arrest neo-angiogenesis);
4. Specific and selective gene silencing to switch off critical genes responsible for drug resistance, thus increasing the efficacy of the compounds and decrease resistance; and
5. Combining these approaches around the crucial role of AuNP and provide cues to optimize a single platform to enhance the killing potential against cancer cells, circumventing drug resistance and decrease toxic side effect.

CHAPTER 2 – MATERIALS AND METHODS

All the materials and methods common to more than one chapter will be presented in this section to avoid repetition, and to ease the reading.

2.1 Materials

2.1.1 Reagents

All chemicals used are presented in Table 2.1 and all equipment in Table 2.2. All chemicals were of molecular biology grade. Ultrapure water used in these processes came from a Millipore water purification system (Merck Millipore, USA). Oligonucleotides were provided by STABVIDA (Portugal).

Table 2.1 List of reagents

Name	Company	Country
0.45- μ m Nitrocellulose Membrane	GE Healthcare	USA
0.5 % DeStreak	GE Healthcare	USA
24-Well Flate Cell Culture Plate	SPL Life Sciences	South Korea
2D Clean-Up Kit	GE Healthcare	USA
2-Morpholinoethanesulfonic acid monohydrate, MES	Sigma-Aldrich	USA
5-(and-6)-Carboxytetramethylrhodamine, TAMRA	Invitrogen	USA
96-Well Flate Cell Culture Plate	SPL Life Sciences	South Korea
Aberchrome 540	Extrasynthese	France
Acetic Acid	Sigma-Aldrich	USA
Acrylamide-Bisacrylamide Gel	Merck Millipore	Germany
Annexin V-FITC Apoptosis Detection Kit	Invitrogen	USA
Anti-Mouse IgG –TRITC	Sigma-Aldrich	USA
Anti-mouse IgG, HRP-linked Antibody	Cell Signaling	Netherlands
Anti- β -Actin antibody, Mouse monoclonal	Sigma-Aldrich	USA
Antibiotic-Antimycotic 100X	Invitrogen	USA
Apo-ONE® Homogeneous Caspase-3/7 Assay	Promega	USA
Blue Line NEXT individually ventilated cages	Tecniplast	Italy
Bovine Serum Albumine, BSA	Sigma-Aldrich	USA
Bradford Assay	ThermoFisher	USA
Bromophenol Blue	Merck	Germany
Calcium Chloride	Sigma-Aldrich	USA
Cell Culture Dish 35mm	SPL Life Sciences	South Korea
CellTiter 96® AQueous One Solution Cell Proliferation Assay	Promega	USA
Cetuximab, Erbitux	Merck	Germany
CHAPS	GE Healthcare	USA
Corning® opaque 96 well plates	Sigma-Aldrich	USA
Culture flask 75 cm ²	VWR	USA

DAPI-containing Fluoroshield Mounting Medium	Abcam	USA
Dimethyl sulfoxide, DMSO	Sigma-Aldrich	USA
Dithiothreitol, DTT	Promega	USA
Dulbecco's Modified Eagle Medium, DMEM	Invitrogen	USA
Doxorubicin	Sigma-Aldrich	USA
DPX Mountant	Sigma-Aldrich	USA
EGFR (D-8)	Santa Cruz	USA
Eosin	Sigma-Aldrich	USA
Ethanol	Sigma-Aldrich	USA
Ethylenediaminetetraacetic Acid, EDTA	Sigma-Aldrich	USA
Fetal Bovine Serum, FBS	Invitrogen	USA
Formalin solution, neutral buffered, 10%	Sigma-Aldrich	USA
Giemsa Stain	Sigma-Aldrich	USA
Glycerol	Panreact	USA
Gold(III) chloride trihydrate	Sigma-Aldrich	USA
Guanidinium thiocyanate, Trisure	Bioline	UK
Hematoxylin	Sigma-Aldrich	USA
Hydrogen Peroxide	Sigma-Aldrich	USA
HS-PEG(8)-COOH	Iris Biotech GMBH	Germany
Hoechst 33258 solution	Sigma-Aldrich	USA
Hydrochloric acid	Sigma-Aldrich	USA
Immobiline Drystrip, IPG strips	GE Healthcare	USA
Iodoacetamine	Sigma-Aldrich	USA
IPG buffer pH 3-10	GE Healthcare	USA
Isoflurane	Esteve Farma	Spain
JC-1	Abnova Corporation	USA
KAPA SYBR® FAST Kit	KAPABiosystems	South Africa
Low Melting Agarose	Sigma-Aldrich	USA
Mdr-1 Antibody (D-11), ABCB1	Santa Cruz	USA
Methanol	Sigma-Aldrich	USA
Milk Powder, Molico	Nestle	Swissland
N-(3-Dimethylaminopropyl)-N'-ethylcarbodiimide hydrochloride, EDC	Sigma-Aldrich	USA
Illustra™ NAP™ Columns, NAP-5	GE Healthcare	USA
MEM nonessential amino acid	Invitrogen	USA
Neutral Red for microscopy	Sigma-Aldrich	USA

N-Hydroxysuccinimide, NHS	Sigma-Aldrich	USA
NZY M-MuLV First-Strand cDNA Synthesis Kit	Nzytech	Portugal
O-(2-Mercaptoethyl)-O'-methyl-hexa(ethylene glycol), PEG	Sigma-Aldrich	USA
Paraffin – polyisobutylene mixture, Paraplast	Sigma-Aldrich	USA
Paraformaldehyde	Sigma-Aldrich	USA
Phenylmethylsulfonyl Fluoride, PMSF	Sigma-Aldrich	USA
Phosphatase Inhibitor, PhosStop	Roche	Switzerland
Pierce 660nm Protein Assay Reagent	ThermoFisher	USA
Potassium Chloride	Sigma-Aldrich	USA
ProLong [®] Gold Antifade Reagent with DAPI	Invitrogen	USA
Protease Inhibitor, cOmplete Mini	Roche	Switzerland
Quartz Spectrophotometer Cuvettes	Hellma-Analytcs	Germany
RnaseA	Sigma-Aldrich	USA
Roswell Park Memorial Institute 1640 medium, RPMI	Invitrogen	USA
SH-EG(8)-(CH ₂) ₂ -COOH, Carboxylated PEG	Iris Biotech	Germany
Sodium Alginate	Sigma-Aldrich	USA
Sodium Chloride	Sigma-Aldrich	USA
Sodium Dodecyl Sulfate, SDS	Sigma-Aldrich	USA
Sodium Hydroxid	Sigma-Aldrich	USA
Sodium phosphate dibasic	Sigma-Aldrich	USA
Sodium phosphate monobasic monohydrate	Sigma-Aldrich	USA
Tariquidar	Selleckchem	USA
Tergitol, NP-40	Sigma-Aldrich	USA
Thiourea	Merck	Germany
Thymidine	Sigma-Aldrich	USA
Triton X100	Sigma-Aldrich	USA
Trizma base	Sigma-Aldrich	USA
Trypan Blue Solution, 0.4%	Invitrogen	USA
TrypLE™ Express Enzyme (1×), Trypsin	Invitrogen	USA
Tween 20	Sigma-Aldrich	USA
Urea	BDH Prolabo	USA
WesternBright ECL Kit	Advansta	USA
Xylene	Sigma-Aldrich	USA

2.1.2 Equipment

Table 2.2 List of equipment

Name	Company	Country
Anthos Zenyth 3100	Anthos Labtec Instruments	Germany
Attune® Acoustic Focusing Flow Cytometer	Life Technologies	USA
Axioplan 2 Imaging Microscope with Nikon DXM1200F digital camera.	Zeiss	Germany
CO ² Incubator	Leec Changchun New Industries	UK China
CW32nm DPSS coupled to optical fiber	Optoelectronics Tech	
Digital Multimeter, MY-64	MASTECH	Hong Kong
Ettan IPGphor 3 IEF System	GE Healthcare	USA
Gel Doc imager	Bio-Rad	USA
Image Scanner II	GE Healthcare	USA
Infinite M200 Microplate reader	Tecan	Swissland
Jung RM2035 model rotary microtome	Leica Microsystems	Germany
Leica DFC 480	Leica Microsystems	UK
LSM 510 META confocal point-scanning microscope	Zeiss	Germany
Nanodrop ND-1000 Spectrophotometer	ThermoScientific	USA
Nanoparticle Analyzer SZ-100 ()	Horiba Scientific	Japan
SDS-PAGE Mini-PROTEAN®3 System	Bio-Rad	USA
Sigma 3-16K, Centrifuge	Sigma-Aldrich	USA
Ultrasonic Cleaner S30H	Elma	Germany
Sub-Cell model 96 apparatus	Bio-Rad	USA
Ti-U Eclipse model inverted microscope equipped with DS-Qi1Mc digital camera	Nikon	Japan
UVmini 1240 spectrophotometer	Shimadzu	Germany

2.2 Methods

2.2.1 Cell culture

HCT116 colorectal carcinoma (ATCC® CCL-247™), A549 lung adenocarcinoma (ATCC® CCL-185™), breast adenocarcinoma MCF-7 (ATCC® HTB-22™), V79-4 hamster lung fibroblasts (ATCC® CCL-93) and Primary Human Fibroblasts (ATCC® PCS-201-010™) obtained from ATCC (Chicago, IL) were grown in Dulbecco's Modified Eagle Medium (DMEM) and supplemented with 10 % (v/v) Foetal Bovine Serum (FBS) and 1 % (v/v) antibiotic/antimycotic. MCF-7 (ATCC® HTB-22™) were also supplemented with 1% of MEM nonessential amino acid. H1975 (ATCC® CRL-5908™) lung adenocarcinoma cells were grown in RPMI (Roswell Park Memorial Institute) 1640 medium supplemented with 10 % (v/v) FBS and 1 % (v/v) antibiotic/antimycotic solution. Cells were maintained in 75 cm² culture flasks at 37 °C in a 99 % humidified atmosphere of 5 % (v/v) CO₂. HCT116 DOX-Resistant (HCT116 DR) cells were derived from HCT116 (ATCC® CCL-247™) by successive culturing with increasing concentrations of DOX, over each passage, up to a final concentration of 3.6 μM of DOX. Analysis of mycoplasma was performed weekly, through PCR testing and/or Hoescht staining by a lab technician.

2.2.2 Cell viability

2.2.2.1 MTS assay

For cell viability studies of compounds and nanoformulations, we performed standard 3-(4,5-dimethylthiazol-2-yl)-5-(3-carboxymethoxyphenyl)-2-(4-sulfophenyl)-2H-tetrazolium (MTS) assay - CellTiter 96® AQueous One Solution Cell Proliferation Assay. This assay is a colorimetric method to estimate the number of viable cells. It is based on the dehydrogenation by metabolically active cells of MTS tetrazolium compound into formazan, a soluble coloured product. Briefly, a cell density of 7.5×10³ per well was seeded in a 96-well plate for 24 h, the medium was replaced with fresh medium containing the stimuli and incubated for an additional 24 h or 48 h. Then, the culture medium was removed from each well and replaced with fresh medium without phenol-red, supplemented with MTS solution. The 96 well plate was incubated for 45 min (or 1.5 h for irradiation experiments) at 37°C in a 99 % humidified atmosphere of 5 % (v/v) CO₂ and the absorbance was measured directly from plates in a microplate reader at 490 nm. Before cell viability experiments, MTS assay was performed in the absence of cells and using increasing concentrations of the tested compounds to confirm that they did not interact with MTS solution. No linear correlation between compound concentration and formazan formation was observed. During irradiation experiments, DMEM without phenol read was used and cells were grown for 24 h and exposed for 16 h to combined or individual therapies. The percentage of cell viability for each assay concentration was determined by subtracting a blank to all experiments and dividing its absorption by control (

Equation 2.1). At least three independent biological assays were performed.

$$\text{Cell Viability (\%)} = \frac{(\text{mean Abs.of treatment group})}{(\text{mean Abs.of control group})} \times 100 \quad (\text{Equation 2.1})$$

2.2.2.2 Trypan blue assay

Trypan blue is a dye impermeable to live cells. It can be used to access cell death since it can penetrate dead cells, or cells with permeability compromised membranes. To perform the assay cells were incubated in a well plate, with 100 μL of Trypan Blue 0.4 % (m/v) solution for 10 minutes, washed three times with phosphate buffer saline (PBS) 1 \times , imaged in bright field inverted microscope (Nikon TMS) and pictures were taken using a Digital Camera (Sony RX100 MK2).

2.2.3 3D cell culture

2.2.3.1 Cells imbedded alginate beads

HCT116 cells were immobilize in alginate beads. A final concentration of 4×10^4 cells per mL were mixed with sodium alginate to a final concentration of 1% w/v dissolved in water (3:1 – cells:alginate). Then, 20 μL were dropped using a micropipette, to a solution of 100 mM of CaCl_2 deposited in a 96-well plate. After 5 to 10 minutes, before the beads become totally transparent, the CaCl_2 solution was changed by fresh DMEM medium. After growing the cells inside de matrix for 24 h, beads were stained with trypan blue for 10 min.

2.2.3.2 Histological preparation

Alginate beads embedded with HCT116 for 72 h were fixed in 10% (v/v) neutral-buffered formalin solution for 24 h. After fixation, the samples were then washed in water, dehydrated in a progressive series of ethanol (30–100% v/v), intermediately infiltrated with xylene and embedded in paraffin. Paraffin-embedded samples were sectioned (5 μm thickness) with a rotary microtome. Beads were stained with Gill's Alum Hematoxylin and counterstained with alcoholic Eosin Y (H&E). After finishing the staining, all sections were dehydrated in ethanol, cleared in xylene and mounted with DPX Mountant. Histological analyses were made with Ti-U Eclipse model inverted microscope equipped with a DS-Qi1Mc digital camera.

2.2.4 RNA expression analysis

Total RNA was extracted from samples using TRIsure™ Reagent method according to the manufacturer's instructions. The quality of RNA was assessed using the Nanodrop ND-1000 Spectrophotometer. Total RNA extracted from samples was reverse transcribed using the NZY M-MuLV First-Strand cDNA Synthesis kit followed by quantitative polymerase chain reaction (qPCR) amplification using KAPA SYBR® FAST kit. The following conditions were used: initial denaturation at 95 °C for 5 min; 40 cycles of 95 °C for 30 s, annealing temperature (T_a) °C for 30 s, 72 °C for 1 min; and a final extension step at 72 °C for 10 min. The T_a for each set of primers is described in Table 2.3.

Table 2.3 List of primers, size of amplicon and melting temperature used for qPCR

Primers	Sequence 5'-3'	Size (bp)	Ta (°C)
GAPDH FW	GAGGAAAGGTCGCCTGGTGGATCG	290	55
GAPDH RV	GTGAGGACAAGCAGTGAGGAACG		
IL-8 FW	TCACAGCTCCACAAAACCTCA	120	60
IL-8 RV	CGTCCTACCTTGCGACAGA		
VEGFR-A2 FW	AGAAAATCACTGTGAGCCTTGCT	101	60
VEGFR-A2 RV	TGCAACGTGAGTCTGTGAATTTG		
FLT-1 FW	TCGACACTATCTTCACAGCGG	95	60
FLT-1 RV	GCTTCTGCAGTTTGGGCT		
MMP-9 FW	GGGTTTCCTCACCTTCGAG	349	55
MMP-9 RV	CGGGTCTTCACCTCTAAGCC		
18s FW	GTAACCCGTTGAACCCCAT	151	55
18s RV	CCATCCAATCGGTAGTAGCG		
ABC1 RV	TTGAAATGAAAATGTTGTCTGG	110	55
ABC1 FW	CAAAGAAACAACGGTTCGG		

2.2.5 Western Blot

Cells were washed twice with PBS 1×, centrifuged at 300×g for 5 min and resuspended in lysis buffer (150 mM NaCl, 50 mM Tris (pH 8.0), 1× phosphatase inhibitor, 5 mM EDTA, 2% (v/v) tergitol (NP-40), 1× protease inhibitor, 1 mM PMSF, and 0.1% (w/v) DTT). Cellular extracts were sonicated (10 times, 1 min each) and centrifuged at 8000×g for 10 min. The supernatant was recovered, and protein concentration was determined using the Pierce 660nm Protein Assay Reagent per manufacturer's specifications. Then, 25 µg total protein extracts were separated by SDS-PAGE in a 10% (37.5:1) acrylamide-bisacrylamide gel. Following overnight electrophoretic transfer onto a 0.45-µm nitrocellulose membrane and blocking with 5% (w/v) milk solution in Tris-buffered saline with 0.1% (v/v) Tween 20 (TBST) for 1 h, blots were incubated per manufacturer's instructions another hour at room temperature with primary antibodies and Anti-β-actin antibody. Membranes were further washed with 1× TBST and incubated with the appropriate secondary antibody conjugated with horseradish peroxidase. WesternBright ECL was applied to the membranes, and signal was acquired in a Gel Doc imager.

2.2.6 Synthesis and characterization of gold nanoparticles

2.2.6.1 Synthesis of gold nanoparticles

AuNP were synthesized by the citrate reduction method described by Lee and Meisel [334]. Briefly, to a boiling aqueous solution of tetrachloroauric acid (100 mL, 1 mM) was added a hot aqueous solution of trisodium citrate (5 mL, 2% w/v) under rapid stirring. Once a deep red colour, indicating the formation of nanoparticles, was observed, the solution was continuously stirred for 15 min and afterwards allowed to cool to room temperature. Citrate-capped AuNP (AuNP@citrate) were sterile-filtered using a 0.2 μm syringe filter and stored at 4 °C until further use.

2.2.6.2 AuNP characterization

AuNP were characterized by ultraviolet-visible (UV-Vis) absorption spectroscopy, dynamic light scattering (DLS), Zeta potential and transmission electron microscopy (TEM). UV-Visible absorption spectra were recorded at room temperature on a UV-Vis spectrophotometer in the range 400–800 nm with 1 cm path quartz Suprasil® cuvettes. Nanoparticles' hydrodynamic diameter and Z-potential was determined by DLS resorting to a Nanoparticle Analyzer SZ-100 at 25 °C, with a scattering angle of 90°. The AuNP formulations were diluted in milliQ water to a final concentration of 2 nM prior to analysis. A total of three measurements were performed for each sample.

For TEM analysis, AuNP were prepared by depositing 10 μL of the gold colloidal solution on carbon copper grids, washing twice with milli-Q water, and air dried. TEM service was provided by Instituto Superior Técnico (ICEMS/IST), Portugal.

2.2.6.3 Functionalization of AuNP with PEG (AuNP@PEG)

Polyethylene Glycol (PEG) is commonly conveyed in nanoparticles to enhance its stability, confer functional groups and increase its biocompatibility. In general PEG is attached to AuNP via a thiol group. Au has high affinity to thiol, forming a quasi-valent bond. Different types of PEG were functionalized on the surface of AuNP, with a similar functionalization method. An AuNP solution (10 nM) was incubated with 0.028 % (w/v) SDS, and PEG for a period of 16 h under agitation at room temperature. The excess of PEG chains was removed by centrifugation at 14 000 \times g for 30 min at 4 °C and the degree of PEG coverage on the AuNP' surface evaluated via Ellman's Assay. The last PEG concentration that had no detectable thiols in the supernatant was defined as 100% coverage. AuNP functionalized with PEG (AuNP@PEG) were characterized by UV-Vis and DLS as described in section 2.2.6.2.

2.2.7 Actinometry

Actinometrical measurements were performed with Aberchrome 540TM, E-form ((E)-a-(2,5-dimethyl-3-furylethylidene)(isopropylidene) succinic anhydride)) actinometer following literature recommendations [335]. A solution of 100 μM of Aberchrome 540TM was dissolved in absolute ethanol and irradiated at 342 nm during 1 h until a photo-stationary state corresponding to the maximum conversion into the C-form was obtained. The C-form solution was irradiated using a continuous wave 532 nm green diode-pumped solid-state laser coupled to an optical fibre. The solution was analysed by UV-Vis spectroscopy. For calculation of the photon flux, a photochemical quantum yield of $\phi=0.060$ was considered for the back reaction of C-form to E-form in ethanol.

2.2.8 Statistical analysis

In general, in all assays the mean of at least three independent experiments is represented and the corresponding standard deviation, except when stated otherwise. The appropriate statistical testing was used according to each case and is further stated.

CHAPTER 3 – NOVEL INORGANIC MOLECULES FOR CHEMOTHERAPY

The work presented in this chapter was possible due to the support of several colleagues. Their contribution will be further detailed. The ZnD compound was kindly provided by Luisa Martins (IST, Universidade Tecnica de Lisboa). The compound cytotoxic and cytostatic characterization was performed by Pedro Martins and Daniela Rosa (UCIBIO, Universidade Nova de Lisboa). The proteomic analysis was performed with the help of Margarida Ferreira-Silva (UCIBIO, Universidade Nova de Lisboa). The histological preparation and analysis were performed with the help of Pedro Costa (UCIBIO, Universidade NOVA de Lisboa). All the work was performed under the supervision and guidance of Pedro V. Baptista and Alexandra R. Fernandes (UCIBIO, Universidade NOVA de Lisboa). Data enclosed in this chapter were originally published in the following issues:

- **Pedrosa P**, Mendes R, Cabral R, Martins L, Baptista PV, Fernandes A. Combination of chemotherapy and Au-nanoparticle phototherapy in the visible light to tackle doxorubicin resistance in cancer cells. *Scientific Reports*. 2018, 8:11429 DOI: 10.1038/s41598-018-29870-0
- **Pedrosa P**, Corvo ML, Ferreira-Silva M, Martins P, Cola MC, Costa P, Martins C, Martins LMDR, Baptista PV, Fernandes AR. Targeting cancer resistance via multifunctional gold-nanoparticles: Cetuximab for improving delivery. *International Journal of Molecular Sciences*. 2019, 20(21): 5510 DOI: 10.3390/ijms20215510

3.1 Introduction

Apoptosis evasion is a milestone of cancer development and is nonspecific to the cause or type of cancer. Targeting apoptosis is an effective strategy for chemotherapy, since it is a general method for all types of cancer. Several anticancer drugs target various stages of apoptosis in both the intrinsic and extrinsic pathways [7–9]. Apoptosis can be triggered by severe damage to the DNA. Some chemotherapeutic agents cause cleavage of DNA strands, by direct interaction, or via the induction of ROS. In response to a DNA injury, cells induce a cell cycle arrest or delay it to repair the damage before arrival of the replication fork. In case of extensive damage, if repair systems fail, apoptosis is triggered [17]. Cancer cells often have an impaired DNA repair system as well. For this reason, damaged DNA will not be repaired as efficiently as in normal cells, causing more severe DNA damage in cancer than in normal cells. The concept of aiming at DNA as a target for anticancer drugs has inspired the development of numerous anticancer compounds: cisplatin, DOX, 5-fluorouracil, etoposide, and gemcitabine.

Chemotherapy agents, such as DOX, are frequently used in first-line therapy against colorectal and lung cancer, but the efficacy of these agents is limited by the development of drug resistance and severe side-effects in normal cells. These are major problems to improve treatment outcomes and extending the overall survival of patients. One way to overturn this drawback has been via the synthesis of novel compounds and their incorporation in innovative formulations suitable for the selective delivery to cancer cells, thus optimizing the therapeutic window and circumventing drug resistance to conventional chemotherapeutics. Among these novel compounds, our group has been devoted to the study of the antiproliferative potential and mechanisms of action of several metal coordination compounds [336–339]. One of such compound is ZnD ($[\text{Zn}(1,10\text{-phenanthroline-5,6-dione})_2]\text{Cl}_2$) (Fig. 3.1), which is composed of a zinc coordinated with two 1,10-phenanthroline-5,6-dione (PhenDION) groups. PhenDION group has been described to cleave DNA [340], interact with proteins and oxidize NADH [341]. ZnD has showed a high cytotoxic potential towards cancer cell lines particularly colorectal carcinoma cell line in comparison to human normal fibroblasts [336] and in canine mammary tumour cell lines (FR37-CMT) [141]. In fact, its IC_{50} at 48 h in HCT116 cells and FR37-CMT was lower than that of DOX and cisplatin – common chemotherapeutic agents [141]. However, these two molecules tend to have undesirable side effects, and in some cases acquired resistance by the tumour, makes them unsuitable for cancer therapy. It is therefore, essential to discover their mechanism of action, to use as primary or alternative line of treatment, and ultimately achieve clinical success [342]. In what concerns DOX therapy, besides its toxic side effects, the development of resistance is a key obstacle to the effective treatment [186]. The high cytotoxicity of ZnD towards HCT116 carcinoma cells [336] prompt us to further investigate the mechanism underlying cancer cells death and to test its effectiveness against DOX-resistant colorectal carcinoma cells (HCT116 DR).

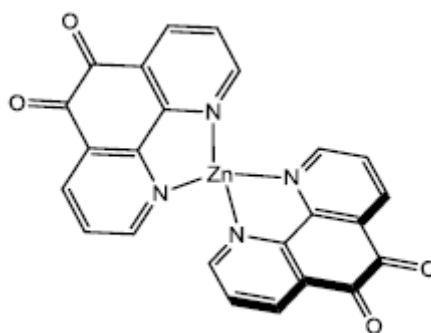


Fig. 3.1 Molecular formula of ZnD ($[\text{Zn}(1,10\text{-phenanthroline-5,6-dione})_2]\text{Cl}_2$).

3.2 Methods

3.2.1 Cell death mechanism

3.2.1.1 Hoechst 33258 labelling

Hoechst dye specifically marks nucleic acids and is permeable to cell membranes. Through fluorescence microscopy, it is possible to observe non-condensed chromatin uniformly distributed over the entire nucleus, in case of normal cells, and apoptotic bodies, condensate or fragmented chromatin, in case of apoptotic cells. This method constitutes a preliminary assay to evaluate viability loss due to compound's action.

HCT116 cells were plated in 35mm dishes at 1.5×10^5 cells per dish. Culture medium was removed 24 h after plating and replaced with 2 mL of fresh medium containing either free ZnD compound (IC_{50}) or sterile water (vehicle control). Afterwards, cells were readily fixed with 4% (v/v) paraformaldehyde, at room temperature in dark for 20 min, in microscope slides. For cell staining, paraformaldehyde was removed, and cells were washed three times with PBS 1 \times . Hoechst ($5 \mu\text{g}\cdot\text{mL}^{-1}$) in PBS 1 \times was added and incubated in the dark for 15 min, followed by three times washing with PBS 1 \times , and lamellae deposition with a droplet of glycerol. The samples were photographed in a fluorescent microscope.

3.2.1.2 Quantification of cell death by flow cytometry

When cells enter apoptosis, a family of calcium-dependent phospholipid-binding proteins are exposed in the outer leaflet of the plasma membrane. the extracellular distribution of this proteins marks them for phagocytosis. These proteins can be detected by fluorescently labelled Annexin V marking apoptotic cells. propidium iodide (PI) is an impermeable dye, only staining cells in necroes, with compromised cell membrane.

HCT116 cells were seeded into 35 mm dishes at 1.5×10^5 cells per dish. Culture medium was removed 24 h after plating and replaced with 2 mL of fresh medium containing ZnD compound (IC_{50}) or sterile water (vehicle control). Cells were incubated in the presence the compound for 48 h and then stained with PI and fluorescein isothiocyanate (FITC) labelled annexin V according to the manufacturer's instructions (Annexin V-FITC Apoptosis Detection Kit). Briefly, both floating and

adherent cells were collected, rinsed twice with cold PBS 1× and resuspended in 100 µL of 1× Annexin binding buffer. Annexin V-FITC and PI were added according to manufacturer's directions and samples were incubated in the dark for 15 minutes. 400 µL of 1× Annexin binding buffer was added to each sample. Data was analysed with *Attune® Cytometric software* (Life Technologies, USA).

3.2.1.3 Caspase-3/-7 Activity

During apoptosis, caspases (cysteine-aspartic proteases) such as caspase-3 and -7 participate in a cascade of cleavage events that disrupts key homeostatic and repair enzymes bringing the structural disassembly of dying cells. Caspase-3/7 enzymes cleave of the C-terminal side of the aspartate residue DEVD (Asp-Glu-Val-Asp) in the substrate (peptide) allowing the rhodamine 110 that is attached to the peptide to become fluorescent. The amount of fluorescent product generated is representative of the amount of active caspase-3/7 present in the sample.

HCT116 cells were plated at 7.5×10^3 cells per well in a black opaque 96-well microplate. Media was removed 24 h after plating and replaced with fresh media containing ZnD compound (IC_{50}) or sterile water (vehicle control). The blank control was made with culture medium without cells. Cells were incubated for 48 h at 37 °C and 5 % CO_2 . Caspase-3/-7 combined activity was quantified by using the Apo-ONE® Homogeneous Caspase-3/7 Assay according to manufacturer's instructions. Briefly, 100 µL of the mixture containing the profluorescent substrate was added to each well and after an incubation period of 2 h at 37 °C and 5% CO_2 , fluorescence was measured in an Anthos Zenyth 3100 plate reader with excitation and emission wavelengths of 485 and 535 nm, respectively.

3.2.1.4 Mitochondrial membrane potential

To evaluate the mitochondrial membrane potential, the fluorescent dye 5,5,6,6-tetrachloro-1,1,3,3-tetraethylbenzimidazolylcarbocyanine iodide (JC-1) was used. JC-1 is a cationic dye, widely used in apoptosis studies to monitor mitochondrial health. It exhibits potential-dependent accumulation in mitochondria, with a fluorescence emission shift from green to red due to the formation of red fluorescent J-aggregates. The mitochondrial depolarization is indicated by a decrease in the red/green fluorescence intensity ratio. HCT116 cells were seeded with a cell density of 7.5×10^4 cells/well in a 6-well plate for 24 h. After an exposure to the IC_{50} for DOX (0.42 µM) and ZnD for 48 h, JC-1 was added to the medium for 20 min. Fluorescence of the JC-1 monomer and dimer was analysed on an *Attune® Acoustic Focusing Flow Cytometer* and *Attune® Cytometric software* (Life Technologies, USA).

3.2.1.5 Cell cycle analysis

When cells undergo division, they double their amount of DNA. PI stoichiometrically binds to DNA allowing its quantification. Thus, it is possible to distinguish the stage of a specific cell in the cell cycle by quantifying PI fluoresce. Cells in G1 phase have exactly half the DNA of G2, and all the in-between are in S phase.

HCT116 cells were seeded in 25 cm² culture flasks with a density of 7.5×10³ cells per well and were synchronized in early S-phase by a double thymidine block. Cells were release from the second block by substituting the medium with 2 mM thymidine for fresh medium without thymidine and either with ZnD compound (IC₅₀) or sterile water (vehicle control). After incubation periods of 6 h and 12 h at 37 °C and 5 % CO₂ the media was removed, and cells were trypsinised, transferred to microtubes, harvested by centrifugation (1000×g for 5 minutes) and washed with PBS 1×. Cell pellet was resuspended in 1 mL of cold PBS 1× and 1 mL of cold 80 % ethanol was added drop by drop to each tube while gently vortexing. Cell suspension was kept on ice for 30 min and stored at 4 °C at least 14 h. Cells were pelleted, resuspended in 50 µg·mL⁻¹ RNase A in PBS 1× and incubated at 37 °C for 30 min. PI was added to a final concentration of 2.5 µg·mL⁻¹ and DNA content was analysed on an *Attune® Acoustic Focusing Flow Cytometer* and analysed with *Attune® Cytometric software*.

3.2.2 Chromosomal DNA alterations

3.2.2.1 Chromosomal Aberrations

1×10⁶ V79 cells were treated with 1.5 µM mitomycin C and ZnD compound (IC₅₀) for 16 h in 37 °C and 5 % CO₂. After 14 h incubation, 0.1 mL of a 4 mg·mL⁻¹ colchicine solution was added to each sample. Cell suspensions were then homogenized and incubated for another 2 h. Cells were harvested by centrifugation (1000×g for 5 min) and 8 mL of a pre-warmed (37 °C) KCl solution (75 µM) was added to each pellet. Samples were thawed in a water bath at 37 °C for 4 min, centrifuged (1000×g for 5 min) and incubated for 15 min at -20 °C with 5 mL of pre-chilled (-20 °C) solution of methanol:acetic acid 3:1 (v/v) (fixing solution). Cells were washed twice with fixing solution and resuspended in 3 mL of this same solution. Each cell suspension was mounted on to a glass slide and chromosomal aberrations were evaluated under a bright-field microscope by using Giemsa staining.

3.2.2.2 Genotoxicity assessment

Genotoxic effects were assessed by quantification of DNA strand breakage, through the alkaline version of comet-assay and frequency of nuclear abnormalities. In comet assay, cell's DNA undergoes electrophoresis, allowing the broken DNA fragments or damaged DNA to migrate away from the nucleus, resembling a comet. The amount of fluorescence in head and tail and length of tail indicate the extent of DNA damage.

HCT116 cells were plated at 1×10⁶ cells per dish in 35 mm dishes and allowed to attach for 24 h at 37 °C, 5% (v/v) CO₂. Culture medium was removed and replaced with 2 mL of fresh medium containing either ZnD (IC₅₀) or water (vehicle control) for 12 and 18 h, at 37 °C, 5% (v/v) CO₂. H₂O₂ was used as positive control at 0.05 % (v/v) for 30 min at room temperature. Glass microscope slides were initially prepared with a coating of 1% (w/v) agarose (normal melting point agarose) in Tris Acetate EDTA (TAE) 1× and left to solidify at 37 °C for at least 48 h. Cells were harvested by scrapping and cell density was determined by the trypan blue dye-exclusion assay. Solutions of 1×10⁵ cells·mL⁻¹ in PBS

1× were prepared and from this 10 µL were added to 90 µL 1 % (w/v) low melting point agarose in PBS 1× and dropped in the slides prepared previously, making a cell density of 1×10^3 cells per slide. A coverslip was used to spread the sample across the agarose layer and the slides were allowed to dry at 4 °C for 15 min. Upon agarose solidification, coverslips were removed and the slides dipped into lysis solution (450 mM NaCl; 3.72% EDTA; 5 mM TRIS; to which 10% (v/v) DMSO and 1% (v/v) Triton-X were added just before use) during 1 h at 4°C, followed by 40 min into cold electrophoresis solution (1 mM EDTA; 300 mM NaOH, pH 13) to ensure DNA unwinding and promote expression of alkali-labile sites. Electrophoresis was carried out at 4°C, for 30 min, at 25 V using a Sub-Cell model 96 apparatus. Afterwards, slides were placed into 0.1 M Tris-HCl buffer (pH 7.5) at 4 °C during 15 min for neutralisation, followed by 15 min in methanol at 4 °C and drying at 37 °C. For comets visualization, slides were hydrated with distilled water at 4 °C for 30 min and stained with 20 µL of an ethidium bromide work solution ($20 \mu\text{g}\cdot\text{mL}^{-1}$) and cover with new coverslips. The slides were observed under the fluorescence microscope Leica DFC 480 and analysed by the *CometScore software v.1.5* (TriTek Corp., USA). About 100 cells per sample are analysed. The percentage of DNA in the tail was used as measure of the total DNA strand-breakage.

3.2.3 Proteomics

3.2.3.1 Preparation of protein extracts and two-dimensional electrophoresis

HCT116 DR cells were seeded in 75 cm² flask at a density of 4×10^6 cells per flask. Culture medium was removed after 24 h and replaced with fresh medium containing either 0.108 µM of ZnD or MilliQ water. Cells were incubated for 48 h, washed with PBS 1×, collected in ice-cold lysis buffer (50 mM Tris-HCl, 150 mM NaCl, 5mM EDTA, pH 8) supplemented with 0.1 % DTT), 0.4 % Nonidet P-40, 1mM PMSF, 1× protease inhibitors and 1× phosphatase inhibitors and stored at -80 °C. To lyse cells, short ultrasound pulses were applied to each sample, protein extracts were centrifuged at 10 000×g, during 5 min and the supernatant were collected and maintained in ice. Protein concentrations were determined using the Pierce Protein Assay Kit and then, 200 µL of each extract were purified with 2D Clean-Up Kit according to the manufacturer's instructions. The pellets obtained were rehydrated in 120 µL of rehydration buffer solution containing 7 M urea, 2 M thiourea, 2 % (w/v) CHAPS, 0.1 % (w/v) DTT, 1 mM PMSF, 1 x phosphatase inhibitor, 1 x protease inhibitor and bromophenol blue. Samples were incubated at room temperature for 48 h and centrifuged at 12 000 g for 10 min. Supernatants were collected and proteins were quantified with the same procedure than before. Samples with 100 µg of protein in 125 µL of rehydration buffer solution supplemented with 0.5 % (v/v) IPG buffer and 0.5 % DeStreak were used in the rehydration of 7 cm Immobiline Drystrip with 3-10 non-linear pH that were placed in Ettan IPGphor 3 IEF instrument. Isoelectric focusing was performed with a maximum voltage of 5000 V and then, IPG strips were incubated for 15 min in equilibration buffer (50 mM Tris-HCl pH 8.8, 2 % (w/v) SDS, 6 M urea, 30 % (v/v) glycerol and traces of bromophenol blue) supplemented with

1 % (w/v) DTT, followed by another incubation for 15 min in equilibration. Finally, IPG strips were placed on top of a 10% polyacrylamide gel in SDS-PAGE Mini-PROTEAN®3 System. All 2-DE gel images were digitalized in an Image Scanner II.

3.2.3.2 Analysis of differentially expressed proteins

Gel images were analysed with *Melanie 7.0 Software* (GeneBio, Switzerland). Identification of protein spots was initially done by the software and afterwards there was a manual verification of each spot and the matching between spots in different gels. The ratio of the spot volume and the total volume of the spots with a match in all gels were used to calculate the protein expression and the concomitant fold variation between different conditions. It was considered that the protein expression level was different when the fold variation was lower than 0.7 (down-regulated) or higher than 1.5 (up-regulated).

3.2.3.3 Protein spot identification

For identification of proteins of interest, protein spots were manually excised from the gel and identified in the UniMS±Mass Spectrometry Unit, (ITQB/IBET, Portugal) using Peptide Mass fingerprint. The groups of altered proteins between conditions were analysed in STRING (Search tool for the retrieval of interacting genes/proteins) database [343] to infer possible protein-protein interactions, sub-cellular locations, and major altered pathways [344].

3.2.4 ABCB1 inhibition assays

ABCB1 efflux pump is specifically inhibited using the small molecule – Tariquidar. HCT116 DR were seeded at a density of 2×10^4 cells per well on a 96-well plate. Cell viability of HCT116 DR was assessed, after exposure to 3.6 μM of DOX mixed with varying concentrations of Tariquidar. MTS assay was performed 24 h after initial stimulus. In further assays 60 nM of Tariquidar was used.

3.3 Results and discussion

3.3.1 ZnD as a cytotoxic and cytostatic molecule

ZnD has shown a high cytotoxic potential towards HCT116 cell line in comparison to human normal fibroblasts [336]. We started by confirming these results in the same cell lines and two lung cancer cell lines A549 and H1975. A549 cells are human alveolar basal adenocarcinoma cells, and H1975 non-small cell lung adenocarcinoma cancer cells. MTS assay revealed a higher sensitivity of H1975 than A549 to ZnD. In fact, the IC_{50} of fibroblasts is the double of H1975, but similar to A549 (Table 3.1). These results show the potential of ZnD to be used as an anti-proliferative compound.

Table 3.1 Relative IC₅₀ (μM) of ZnD in HCT116, HCT116 DR, A549 and H1975 human cell lines at 48 h. Values shown are relative to mean of three independent assays and the error are correspondent to SEM.

Human cell line	Relative IC ₅₀ ± SEM
HCT116	0.215 ± 0.01
A549	0.714 ± 0.09
H1975	0.355 ± 0.04
Fibroblasts	0.600 ± 0.13

Understanding the mechanism of action of candidate compounds is of extreme relevance to ensure the selection of the pathways that can circumvent the known drug resistant mechanisms triggered by the conventional therapy. For that propose, cellular and molecular targets of ZnD were characterized. We exposed HCT116 cells to ZnD for 48 h at IC₅₀, and stained them with Hoechst, a dye that binds to DNA allowing the morphological observation of nucleus. Morphological alterations were observed after nuclei staining which indicate chromatin condensation and nuclear fragmentation (Fig. 3.2), common in genotoxic events, that lead to apoptosis. Double staining cells with PI and annexin V-FITC (Fig. 3.3), allows the determination of the apoptotic/necrotic stage of cells. In early-stage apoptosis, cells stain with Annexin V but not with PI. In late stage apoptosis, the cell membrane loses integrity double staining with Annexin V and PI. Cells stained only with PI are generally necrotic, not exposing apoptosis markers on their surface. We observed that after exposure to ZnD, the number of apoptotic cells, either in early (FITC+/PI-) or later stages (FITC+/PI+), increased 4-fold with only ~2% of cells in necrosis when compared to the control.

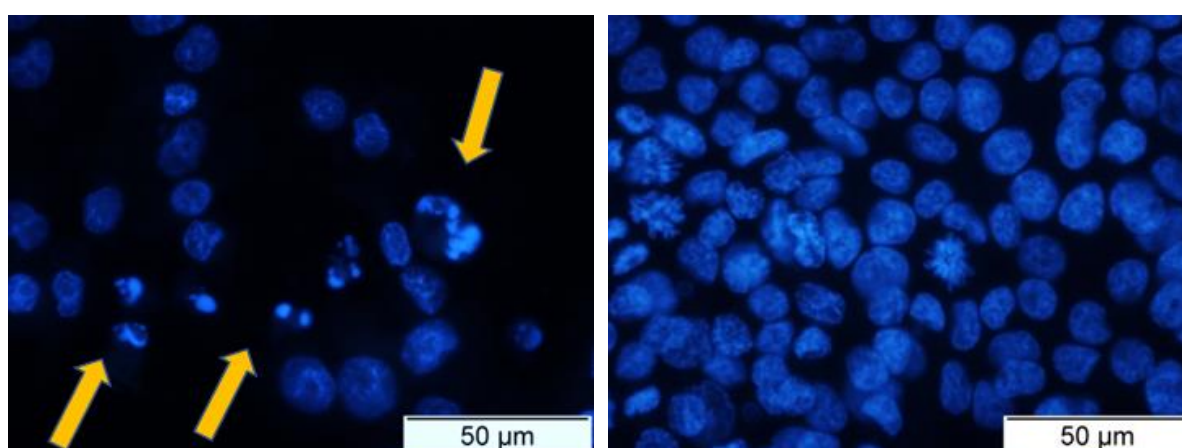


Fig. 3.2 Hoechst staining of HCT116 cells exposed to ZnD. Morphological alterations observed after nuclei staining with DNA-specific dye Hoechst 33258 in HCT116 cells exposed to ZnD (IC₅₀; 0.217 μM) (Fig. 3.2left) for 48 h compared to vehicle control (sterile water, right). Orange arrowheads indicate major alterations in nuclear morphology such as chromatin condensation and nuclear fragmentation.

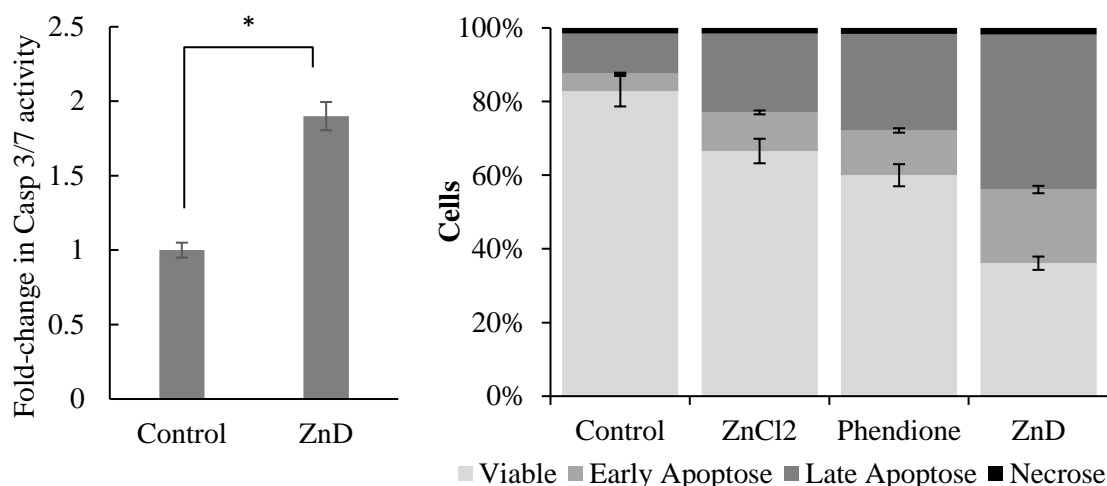


Fig. 3.3 Evaluation of apoptosis level (Left). Caspase 3/7 activity of HCT116 cell exposed to ZnD (IC₅₀) or water. (Right) Proportion of apoptotic and necrotic HCT116 cells after a period of incubation (48 h) in the presence of vehicle control (water), ZnCl₂ (0.22 μM), DION (0.44 μM) and ZnD (IC₅₀). Cell death was determined by flow cytometry after Annexin-V/FITC and PI double staining. Light Grey - Viable cells; grey - early apoptosis; dark grey - late apoptosis; black - necrosis. The results are expressed as the mean ± SEM percentage normalized to controls from three independent experiments.

This prompted us to evaluate the activation of the apoptotic pathway via caspase-3/7 activity since the activity of these enzymes is increased in apoptotic cells. Results showed a 2-fold increase of in caspase-3/7 activity in HCT116 exposed to ZnD (Fig. 3.3) compared to control. To understand if the apoptotic signalling was intrinsic or extrinsic, we evaluated the depolarization of the mitochondrial membrane potential, characteristic of intrinsic apoptosis. JC-1 is a cationic dye, widely used in apoptosis studies to monitor mitochondrial health. It exhibits potential-dependent accumulation in mitochondria, with a fluorescence emission shift from green to red due to the formation of red fluorescent J-aggregates. The mitochondrial depolarization is indicated by a decrease in the red/green fluorescence intensity ratio. The assessment of the mitochondrial membrane potential in these cells showed a depolarization of the membrane potential (in similar levels of those induced by DOX) that agrees with the induction of the intrinsic apoptotic pathway (Fig. 3.4). Together, these results confirm that ZnD induces HCT116 cell death via activation of the apoptotic pathway.

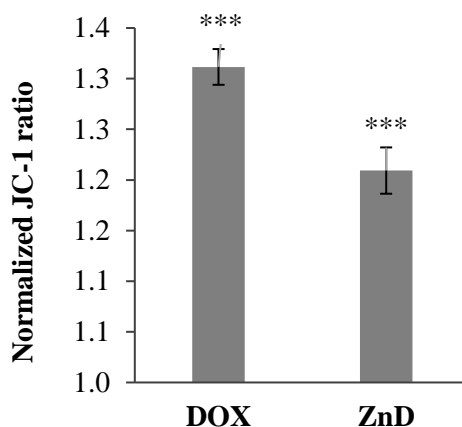


Fig. 3.4 Mitochondrial membrane potential of HCT116 cells challenged with ZnD. The fluorescence of JC-1 monomer, corresponding to green fluorescence, was acquired using filter BL1 (excitation and emission range wavelengths of 488 nm and 515-545 nm, respectively). The fluorescence of JC-1 aggregate, corresponding to red fluorescence, was acquired using filter BL2 (excitation and emission range wavelengths of 488 nm and 561-587 nm, respectively) JC-1 monomer/aggregate ratio obtained after 48 h incubation of HCT116 cells with DOX and ZnD. Values were normalized to the JC-1 ratio of control and are represented as the mean \pm SD of three independent experiments. *** p <0.0005 relative to control.

To understand if ZnD also had a cytostatic potential, cell cycle analysis of HCT116 cells exposed to the compound was assessed at 6 h and 12 h. Staining the cells with PI (a nucleic acid dye) it is possible to assess the cell cycle stage by flow cytometry, since cells double their genetic material when dividing. Cells were synchronized in the same stage of cell division cycle using thymidine double blockage. Challenging cells with ZnD induced a cell cycle arrest avoiding cells to enter in G2/mitosis (Fig. 3.5). Indeed, most of ZnD-treated HCT116 cells at 6 h and at 12 h are at S-phase while untreated cells have progressed to G2/Mitosis. These findings indicate that DNA synthesis method has been halted and prompted us to evaluate the capability of ZnD to induce chromosomal alterations. We treated Chinese hamster pulmonary fibroblasts (V79) with either IC₅₀ of ZnD for 24 h or mitomycin C (positive control) and stained the chromosomes with Giemsa. The results showed no alterations in chromosome number or structure in presence of ZnD (Fig. 3.6).

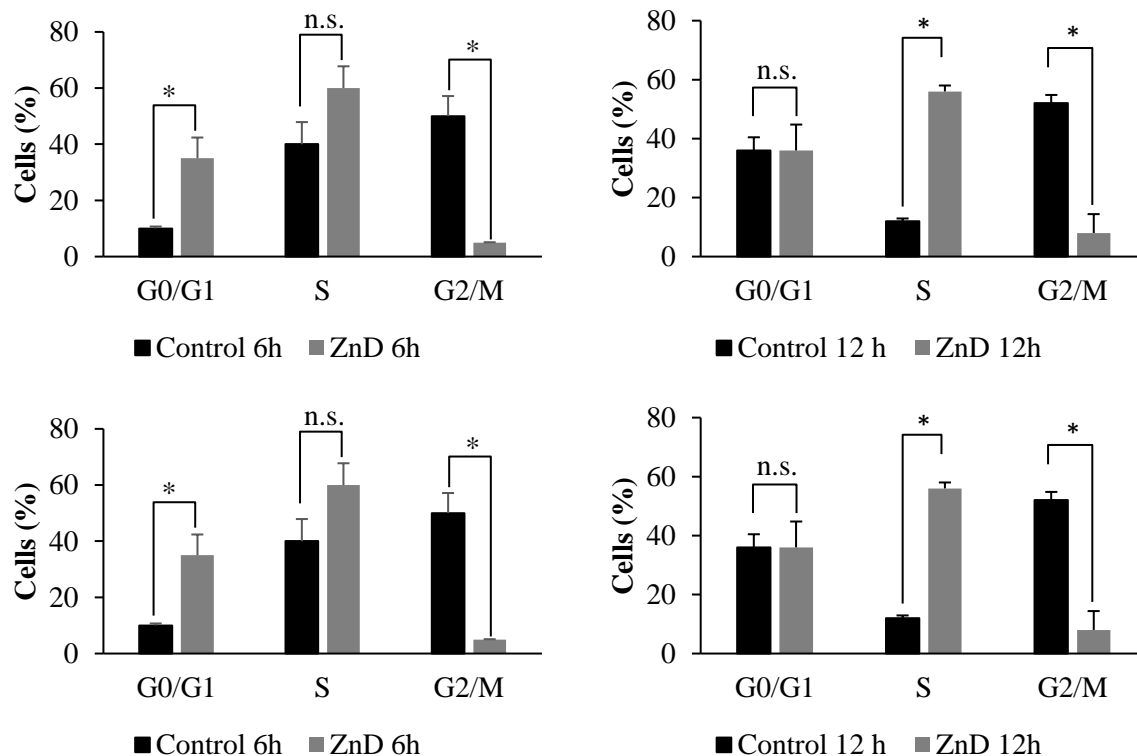


Fig. 3.5 Cell cycle evaluation. (Left) Percentage of HCT116 cells in the different phases of the cell cycle after incubation for 6 h (Left) and 12 h (Right) in the presence (0.217 μ M, IC_{50} at 48 h) or absence (water) of ZnD compound. PI fluorescent levels were determined by flow cytometry. The results are expressed as the mean \pm SEM percentage from three independent experiments.

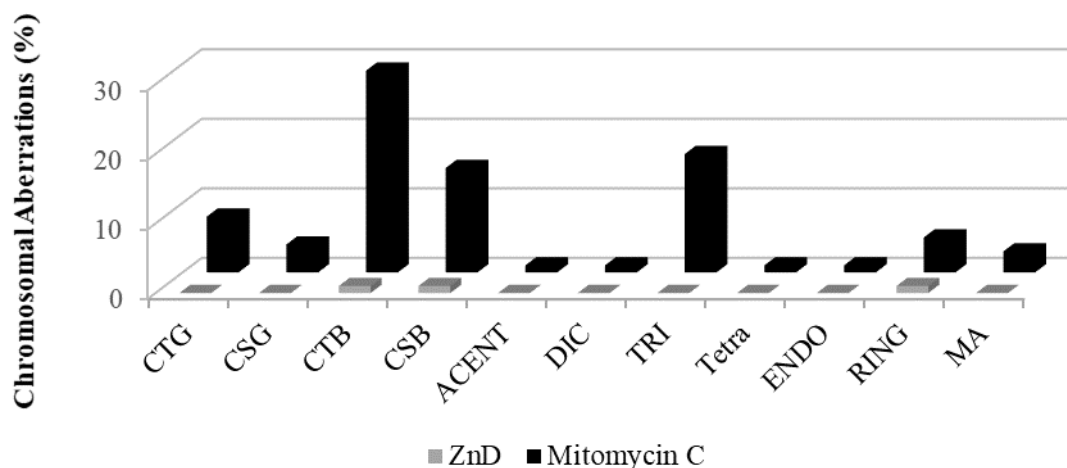


Fig. 3.6 Chromosomal Aberrations. Induction of chromosomal aberrations in V79 cells by 1.5 μ M mitomycin C (black) and 0.217 μ M of ZnD (light grey) exposure during 18 h. CTG, chromatid gap; CSG, chromosome gap; CTB, chromatid break; CSB, chromosome break; ACENT, acentric chromosome; DIC, dicentric chromosome; TRI, triradial chromosome; TETRA, tetradial chromosome; ENDO, endoreduplication; RING, ring chromosome; MA, cells with multiple chromosomal aberrations. B. DNA percentage in the tail (% DNA in tail) and C. the comet class distribution in HCT116 cells treated with 0.217 μ M ZnD for 9 and 18 h and H₂O (vehicle control) for 18 h.

To further analyse ZnD genotoxic potential, comet assays were performed in HCT116 cells exposed to its IC₅₀ at 48h for 9 h and 18 h (Fig. 3.7). Comet assays allows the determination of DNA fragmentation in the nucleus after electrophoretic analysis of the nuclear migration profile. Intact nuclear DNA tends to stay in place while fragmented DNA migrates, creating a tail (resembling a comet). The DNA percentage in the tail was used as a measure for total DNA strand-breakage. Cells treated with ZnD for 9 h and 18 h exhibited an average 11.0 ± 2.4 % and 11.5 ± 2.5 % DNA in tail which was not significantly different from the control (average 11 ± 2 % DNA in tail, $P < 0.05$) (Fig. 3.7). Furthermore, no major differences are observed in comet class distribution, where comets are normally distributed.

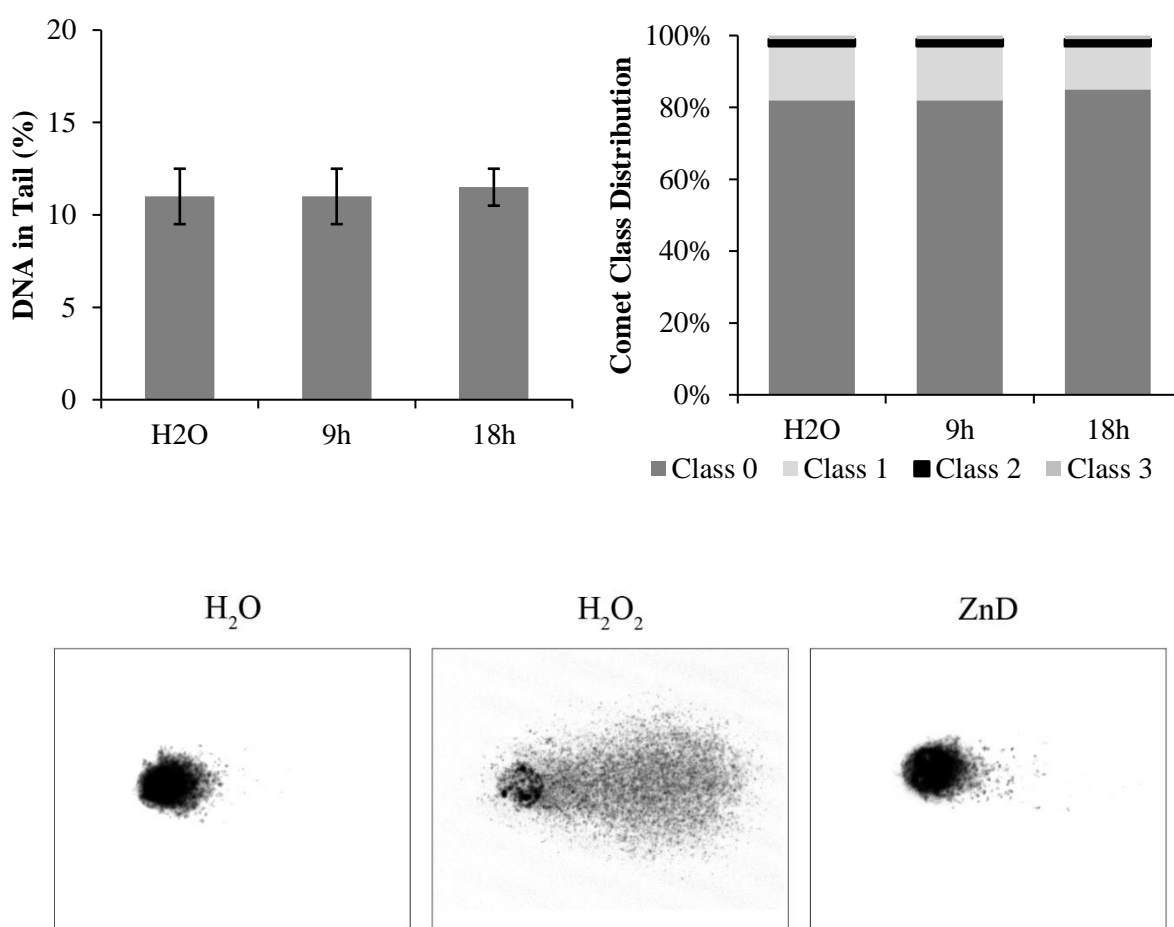


Fig. 3.7 Comet assay. (Top Left) DNA percentage in the tail, (Top Right) the comet class distribution in HCT116 cells treated with 0.217 μ M ZnD for 9 and 18 h and H₂O (vehicle control) for 18 h. (Down) Comets of cells exposed to H₂O, H₂O₂ and ZnD for 18h.

Considering these results and the cytotoxicity results we can conclude that ZnD is a cytostatic and cytotoxic compound that does not induce significant genotoxicity in HCT116 cells (at the IC₅₀ at 48 h). We then tried to track the internalization of ZnD in HCT116 cells. As the compound showed no fluorescence, we tested if it was possible to observe Zn by Inductively Coupled Plasma Mass Spectrometry (ICP-MS) analysis in different subcellular compartments and in the cytosol. To achieve

that we incubated the HCT116 with IC_{50} concentration for 6 h, 24 h and 48 h, and proceeded to the separation of cytosol, mitochondrial and nuclear fractions. After ICP-MS analysis all the samples but the supernatants revealed that Zn was under the limit of detection of the equipment. For that matter we tried to increase the amount of compound exposed to the cells by 10× and 20× the IC_{50} and decrease the exposure time to 6h to avoid killing all the cells. Again, the amount of Zn was only detectable in the supernatant. We also noted that after 6 h exposure, to such high concentration of ZnD cells started to detach from the flask, indicating cell death. It was therefore not possible to follow the intracellular localization of the compound.

3.3.2 ZnD and DOX-resistant cancer cells

We then tested the efficacy of ZnD to kill cancer cells with acquired resistance to DOX which is a commercial chemotherapeutic used for treatment of several cancer, and its capability to intercalate with DNA, RNA and proteins and to inhibit their synthesis, is well described. Interaction of DOX with the DNA molecule results in topoisomerase-II activity inhibition, the induction of single and double DNA strand breaks and chromosomal aberrations [190, 345]. Interestingly, the high cytotoxic and cytostatic potential of ZnD and the fact that it does not induce genotoxicity may indicate that its biological action is different from DOX, which might make ZnD suitable to inhibit the growth of DOX-resistant cancer cells.

We started by inducing resistance to DOX in colorectal carcinoma cell line, HCT116 (ATCC® CCL-247™) by passing the cells with increasing DOX concentrations up to 3.6 μM (Fig. 3.8).

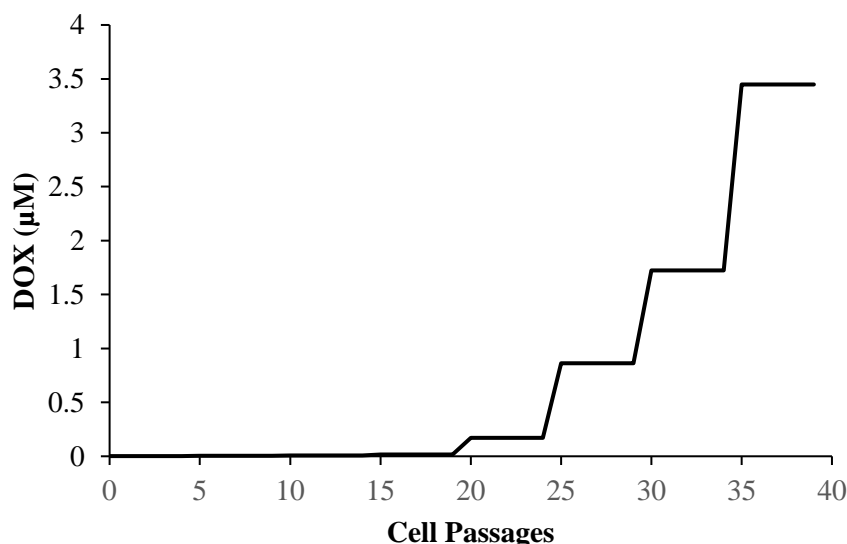


Fig. 3.8 Methodology for the growth of DOX resistant HCT116.

Cells were incubated in successive passages with increasing concentrations of DOX). These cells started to show small morphological alterations, with increased cytoplasm volume, higher number of vesicles, and tendency to grow in small aggregates (Fig. 3.9). These modified DOX Resistant (HCT116

DR) cells did not show any significant reduction in cell viability up to 6 μM of DOX by MTS assay (Fig. 3.10). This acquired resistance is generally the result of high expression of efflux pumps that remove xenobiotics from the intracellular space in a non-specific way, constituting a first line of cell defence against chemical insult. To confirm if ABCB1 expression was responsible for DOX resistance, we looked for a blocker of ABCB1 activity, hoping to overturn HCT116 DR cells to a DOX sensitive state. Tariquidar is a specific blocker of ABCB1 that failed clinical trials due to excessive toxicity [346]. We observed that in the presence of DOX, with increasing concentrations of tariquidar, cells reduced viability and recovered its sensitivity (Fig. 3.10). In contrast, cells exposed to tariquidar alone showed no reduction in cell viability. With this assay, it was confirmed that the up-regulation of the efflux pump in HCT116 DR was a major responsible for the acquired resistance.

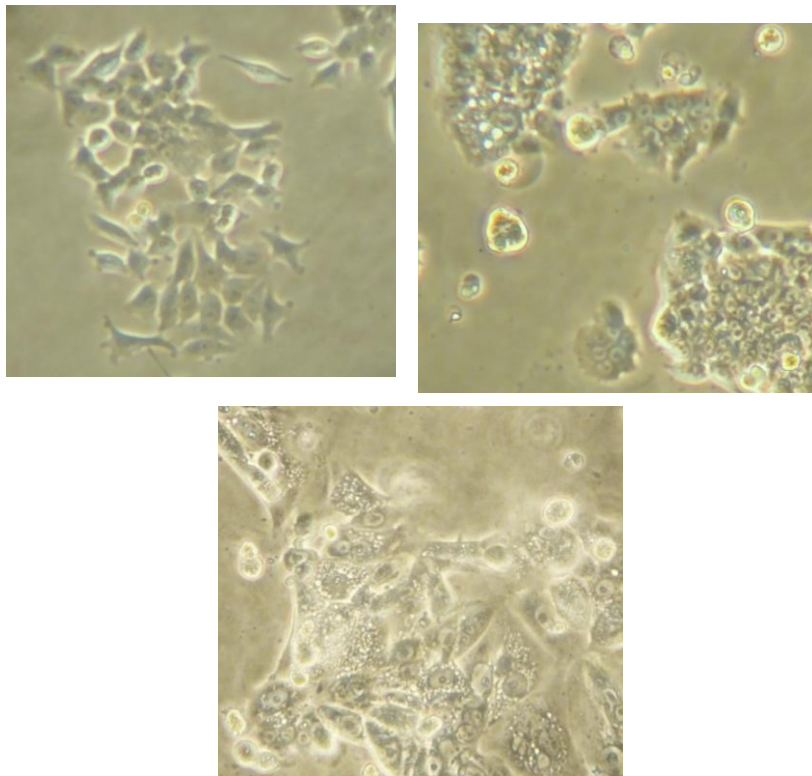


Fig. 3.9 Microscopy Images of HCT116 DR. Microscopy images (100 \times) of HCT116 (Left), with the characteristic star shape, and HCT116 DR (Middle and Right) highlighting the aggregates of cells (Middle) and vesicles (Right).

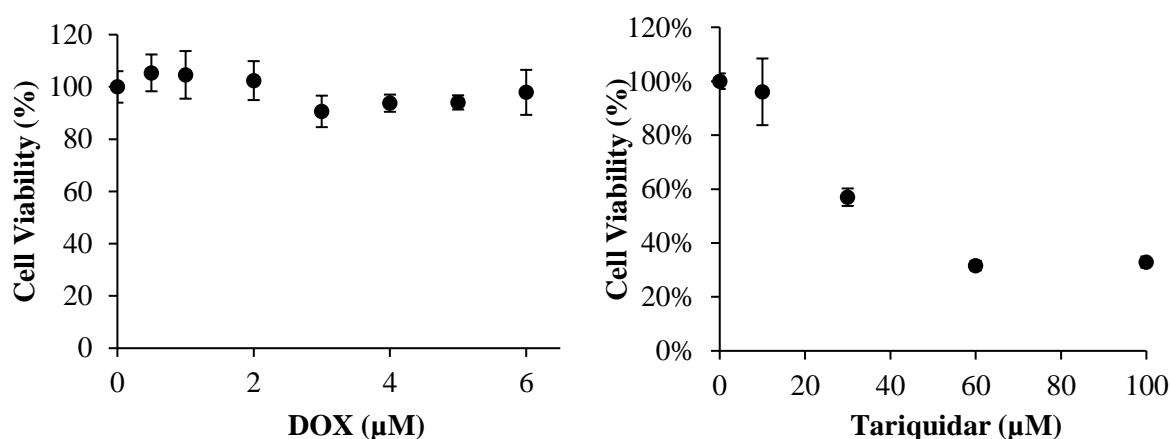


Fig. 3.10 MTS assay of HCT116 DR. (Left) Cells were exposed to several concentrations of DOX for 24h. (Right) Cells were exposed to 3.6 µM of DOX and varying concentrations of Tariquidar. MTS assay was performed 24 h after initial stimulus.

Cytotoxicity of ZnD in HCT116 DR cells was assessed by MTS assay. Interestingly, HCT116 DR which showed no decrease in cell viability up to 6 µM of DOX (Fig. 3.10) have increased sensitivity to ZnD compared with HCT116 parental cell line. The IC_{50} at 48 h, 0.108 µM for HCT116 DR, was half the corresponding values in HCT116 sensitive cells, 0.217 µM. These values are both below the IC_{50} for fibroblasts - 0.6 µM (Table 3.1). This indicates that ZnD mode of action is not affected by the overexpression of ABCB1 and its reduced effect on healthy fibroblasts, makes it a potential candidate for the treatment of DOX resistant colorectal cancers.

To investigate the main molecular players involved in the response to ZnD in HCT116 DR, protein extracts from HCT116 DR cells treated for 48 h with ZnD and untreated (control) were compared via a two-dimensional electrophoresis (2-DE) comparative analysis. For each condition, more than 500 protein spots were detected (Fig. 3.11 and Fig. 3.12) and to detect differences in protein expression, the fold variation between HCT116 DR cells treated with ZnD and the corresponding control was calculated (Table 3.2). Fold variations were considered significant compared to control cells if they were below 0.7 (down-regulated proteins) or above 1.5 (up-regulated proteins) with a p-value below 0.05. The 33 proteins that were most differentially expressed identified are described (Table 3.2, Fig. 3.11 and Fig. 3.12).

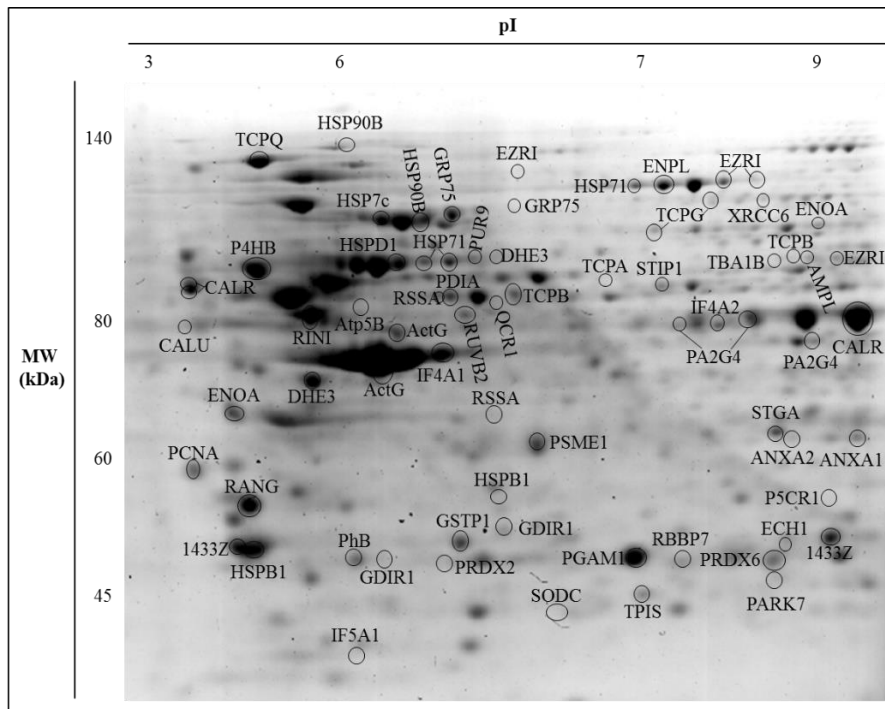


Fig. 3.11 2-DE proteome map of HCT116 DR untreated cells. Proteins were separated by isoelectric focusing (pI 3-10 non-linear) in the first dimension and SDS-PAGE in the second dimension. Visualization was done by staining with Coomassie brilliant blue R-350. Most relevant identified proteins are mentioned.

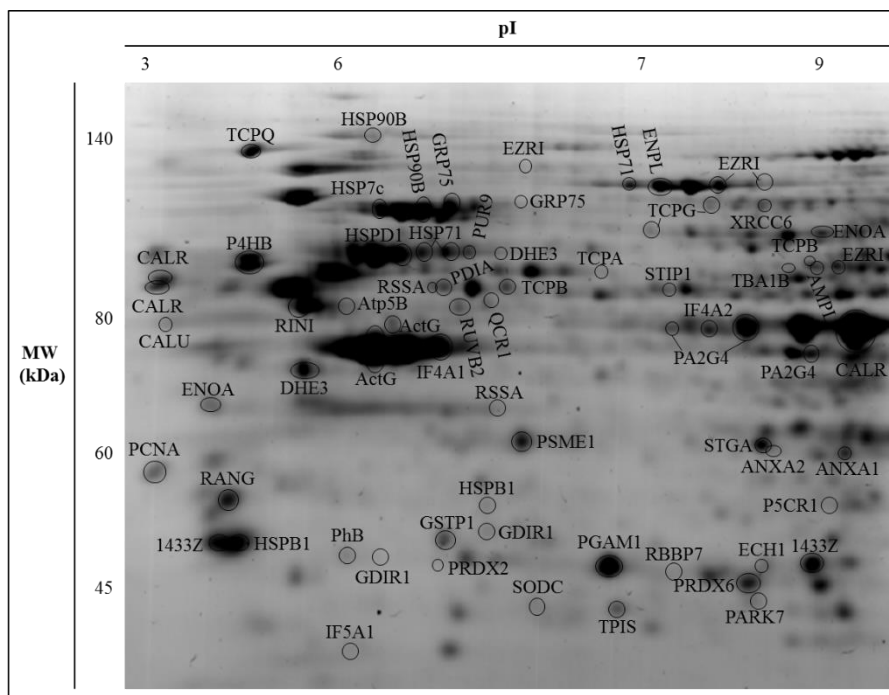


Fig. 3.12 2-DE proteome map of HCT116 DR treated with ZnD (IC₅₀) for 48 h. Proteins were separated by isoelectric focusing (pI 3-10 non-linear) in the first dimension and SDS-PAGE in the second dimension. Visualization was done by staining with Coomassie brilliant blue R-350. Most relevant identified proteins are mentioned.

Table 3.2 Fold variance of proteins between HCT116 DR cells treated for 48 h with ZnD compared with untreated controls.

Uniprot Kb identifier	Gene name	Protein name	HCT116 DR+ ZnD/HCT116 DR
P10809	HSPD1	60 kDa heat shock protein, mitochondrial	1.6
P38646	GRP75	Stress-70 protein, mitochondrial	1.5
P0DMV8	HSPA1A	Heat shock 70 kDa protein 1A	1.5
P08238	HSP90B	Heat shock protein HSP 90 – beta	1.7
P14625	GRP94	Endoplasmic	1.7
P30041	PRDX6	Peroxiredoxin-6	1.7
P00441	SOD1	Superoxide dismutase [Cu-Zn]	1.8
P12956	XRCC6	X-ray repair cross-complementing protein 6	2.2
P09211	GSTP1	Glutathione S-transferase P	0.7
P32119	PRDX2	Peroxiredoxin-2	0.2
P04792	HSPB1	Heat shock protein beta-1	0.50
P00367	GLUD1	Glutamate dehydrogenase 1, mitochondrial	0.6
P31939	ATIC	Bifunctional purine biosynthesis protein PURH	1.9
Q13011	ECH1	Delta(3,5)-Delta(2,4)-dienoyl-CoA isomerase, mitochondrial	0.6
P06733	ENO1	Alpha-enolase	1.5
P15311	EZR	Ezrin	4.4
P35232	PHB	Prohibitin	0.4
P63241	EIF5A	Eukaryotic translation initiation factor 5A-1	0.3
P63104	YWHAZ	14-3-3 protein zeta/delta	0.7
P12004	PCNA	Proliferating cell nuclear antigen	0.6
P78371	CCT2	T-complex protein 1 subunit beta	0.7
P49368	CCT3	T-complex protein 1 subunit gamma	0.6
P17987	TCP1	T-complex protein 1 subunit alpha	0.6
P43487	RANBP1	Ran-specific GTPase-activating protein	0.6
P31948	STIP1	Stress-induced-phosphoprotein 1	0.6
P52565	ARHGDI A	Rho GDP-dissociation inhibitor 1	0.5
P60174	TPI1	Triosephosphate isomerase	0.6
Q16576	RBBP7	Histone-binding protein RBBP7	0.3
P04083	ANXA1	Annexin A1	1.6
P27797	CALR	Calreticulin	1.8
O43852	CALU	Calumenin	1.8
P28838	LAP3	Cytosol aminopeptidase	2.2
P08865	RPSA	40S ribosomal protein SA	1.9

ZnD-treated cells exhibited overexpression of heat shock proteins (HSPs) namely HSPD1, GPR94, GRP75, HSPA1A, and HSP90B. The HSPs are a heterogeneous group of chaperones whose functions include the protection of cells from environmental stress damage through a protein quality control mechanism and the cooperation in newly synthesized polypeptides transport to target organelles [347, 348]. The high intracellular levels of these proteins could indicate a possible accumulation of radicals in the cells, culminating in cell death. These results agree with an increase in PRDX6 and SOD1 levels. These enzymes are involved in cellular protection against oxidative injury [348] suggesting that HCT116 DR cells tries to cope with the induction of ROS when exposed to ZnD. Interestingly, PRDX2 and GSTP1 that are usually overexpressed in colorectal carcinoma cells [349, 350] and important for tumourigenesis are reduced in the presence of ZnD. XRCC6 is involved in non-homologous end-joining and ATIC1 is involved in *de novo* purine biosynthesis and their up-regulation in the presence of ZnD might indicate that HCT116 DR cells are trying to counteract the damage induced by the compound [351, 352]. HSPB1 is a “survival protein” that interferes with several cell death pathways, specifically in upstream events (e.g., the release of cytochrome-c) of the apoptotic cascade and its levels are reduced in response to ZnD promoting its antiproliferative action [353]. GLUD1 has a pivotal role in nutritional stress and is associated with tumour aggressiveness and poor prognosis in colorectal cancer and is an important target in the treatment of refractory colorectal cancer [354]. Interestingly, GLUD1 level are reduced in HCT116 DR cells after exposure to ZnD compound indicating its capability to cope with tumour aggressiveness. Reduced EZR expression plays a critical role in the development, epithelial-mesenchymal transition induction and metastasis formation of colorectal carcinoma tumours [355]. ENO1 is a bifunctional protein which acts as a glycolytic enzyme and a transcription factor. In this last case, by repressing *c-MYC* gene which plays a critical role in cancer inhibition [356]. PHB overexpression has been also correlated with cancer. Considering this, exposure of HCT116 DR cells to ZnD allows to counteract these effects via EZR and ENO1 up-regulation and PHB down-regulation. EIF5A has been associated with cell proliferation and it can serve as a marker for malignant growth [357]. 1433Z is involved in the regulation of several signaling pathways including cell proliferation, cell apoptosis and angiogenesis. The overexpression of 1433Z can be positively correlated with cancer progression, metastasis and worse survival in patients [358]. PCNA is in the core of many essential cellular processes, such as DNA replication, repair of DNA damage, chromatin structure maintenance, chromosome segregation and cell-cycle progression [359]. All these proteins are repressed in the presence of ZnD which could be correlated with its antiproliferative/apoptotic effect. ANXA1 belongs to the family of phospholipid and calcium binding proteins, being involved in the anti-inflammatory process, regulation of differentiation, proliferation and apoptosis [360]. It has been described that increased expression of this protein promotes apoptosis with the activation of caspase-3 [361, 362]. CALU and CALR are a Ca²⁺ binding proteins that are normally found in the endoplasmic reticulum; however, CALU can be transported into the cytoplasm after cell cycle arrest or in late apoptosis and

CALR can be translated to cell surface and functioning as an “eat-me” signal during end stages of apoptosis [363–365] ANXA1, CALR and CALU are overexpressed in the presence of ZnD, which may indicate its ability to induce the apoptotic process as previously observed and that HCT116 DR cells are mostly found in late apoptosis [363, 364] (Fig. 3.3). CCT2, CCT3, TCP1 are cytoskeletal proteins, including tubulins, actin, and proteins involved in the control of cell cycle [366]. Thus, their down-regulation in the presence of ZnD might be correlated with a delay in the cell cycle progression and confirming the cytostatic potential of this compound (Fig. 3.5). This analysis confirmed that ZnD molecular targets are the induction of cell death, via ROS induction and apoptosis, and cell cycle arrest. Taken together these results reveal that, despite cancer cells - mostly the resistant to anticancer therapy - have an efficient mechanism of ROS detoxification that allows them to survival under pro-oxidizing conditions. The apoptotic and folding pathways that are activated upon ZnD treatment in HCT116 and HCT116 DR cells, lead to a concomitant high loss of cell viability.

3.3.3 Assessment of cell viability in 3D models

Cytotoxic efficacy of anticancer compounds has been extensively studied with monolayer-cultured cells. However, its efficacy under two-dimensional (2D) culture can differ from a three-dimensional (3D) arrangement. Growing cells in 3D culture, embedded on a matrix is physiologically more significant than would be possible in 2D, recapitulating tumour formation, cell adhesion, drug accessibility, etc [367, 368]. Alginate microbeads were reported for the first time in humans, in the 1980s, mimicking pancreatic islets. Since then, they have demonstrated high applicability as a scaffold for cell immobilization, at physiological conditions with preservation of cell viability and function. The hydrogel mesh allows diffusion of nutrients and waste materials [369, 370]. For these reasons, by using an alginate hydrogel, we tried to assess the cytotoxicity of ZnD in a 3D model.

Encapsulation of HCT116 cells in alginate beads were produced according to section 2.2.3.1. Bead diameter was measured by analysing Fig. 3.13, resulting in an average diameter of 2.5 ± 0.5 mm. Microscopic observation revealed individuals or pairs of cells immobilized in the matrix (Fig. 3.13). Trypan blue staining showed few cells were stained indicating that they remain viable in the beads for up to 72 h. Histological analysis of the alginate beads showed encapsulated cells, with uncondensed nuclei, typical of fast dividing tumour cells (Fig. 3.14). Cells seem to divide in small clusters, homogeneously distributed inside the bead, probably formed during bead gelation.

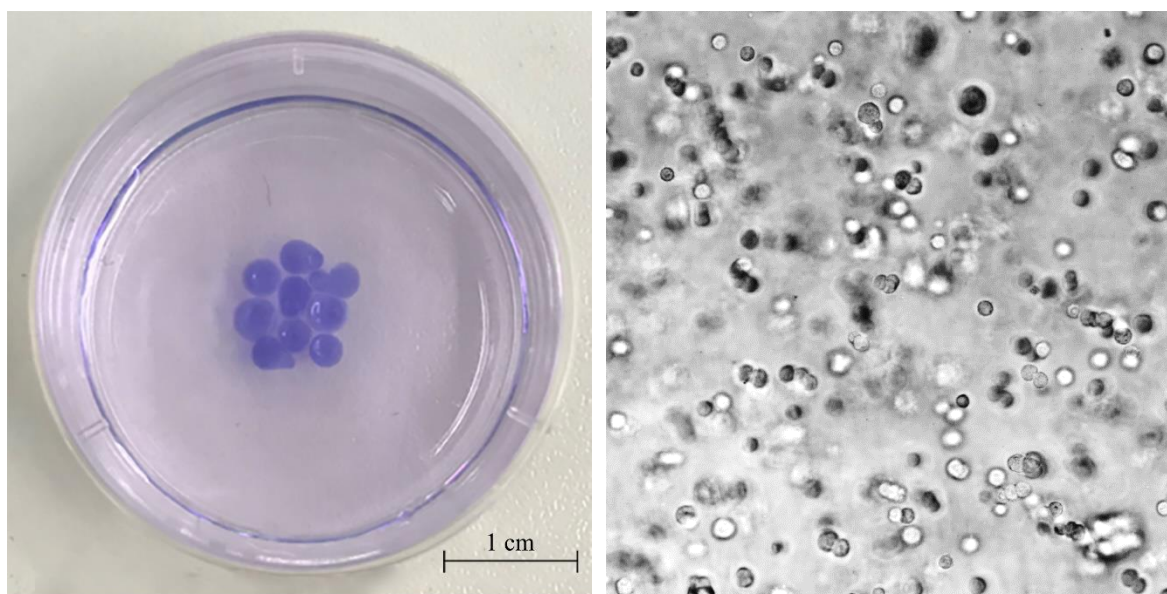


Fig. 3.13 Alginate beads stained with trypan blue to ease its visualization (Left). An average diameter of 2.5 ± 0.5 was calculated. (Right) Optical microscopy images of HCT116 cells grown for 24h in an alginate hydrogel (200× magnification)

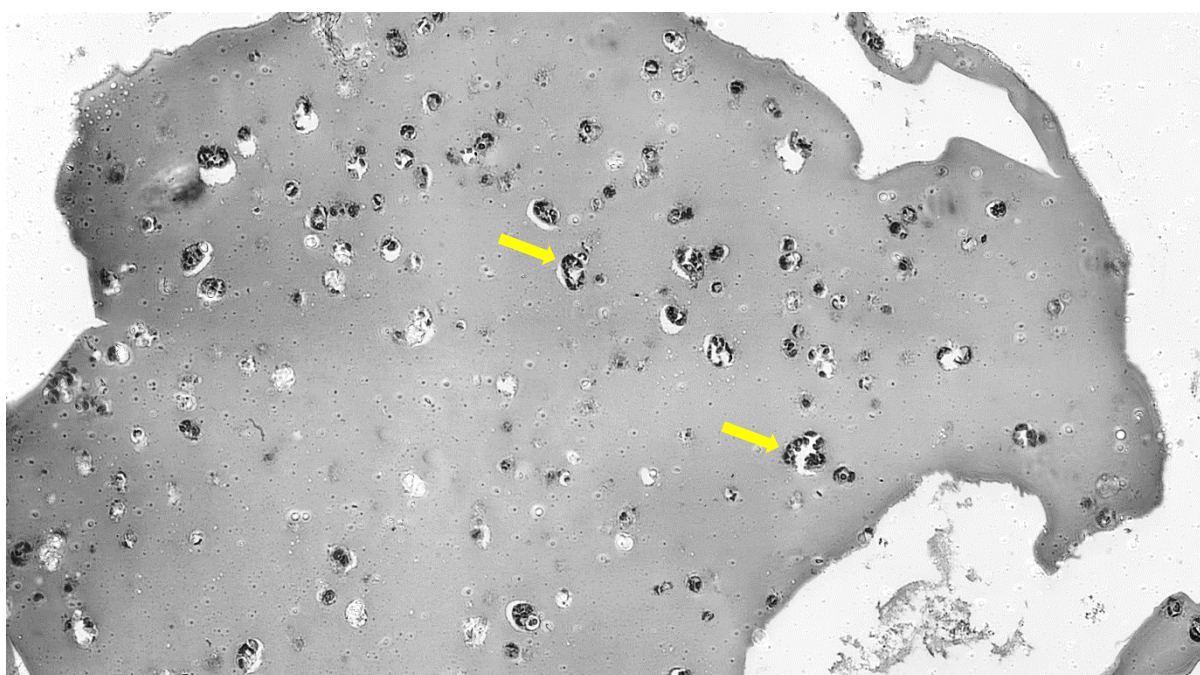


Fig. 3.14 Optical microscopy images of histological cut of HCT116 cells grown for 24h in an alginate hydrogel, stained with eosin and haematoxylin (40× magnification). In is observable in grey the alginate matrix and in black, cell aggregates, inside cavities (yellow arrows).

To access the toxicity of ZnD in 3D culture, we started by confirming the linear correlation between number of cells in the beads and MTS assay colour change (Fig. 3.15). We then exposed HCT116, HCT116 DR and Fibroblasts to ZnD and DOX and compared the results versus a 2D culture (Table 3.3). All 3D model conditions showed higher IC_{50} concentrations than 2D. Decrease in drug

efficacy in 3D cultures is reported in the literature by several groups. Ponce de León et al. described that lung cancer cells grown in 3D using agarose, had an increase in resistance to DOX, etoposide and methotrexate, compared with 2D cells. Our results show that, HCT116 DR for example, has an IC₅₀ for ZnD, 30× higher in 3D culture compared with 2D monolayer. We have seen before that HCT116 DR are more sensitive to ZnD than HCT116, however that effect is not recapitulated in the 3D model. In fact, although the IC₅₀ of ZnD in 3D cultured fibroblasts is still 85% higher than HCT116, it is lower than HCT116 DR. Meaning that ZnD could effectively kill HCT116 cells with a very low IC₅₀ (1.01 μM) with less effects on healthy fibroblasts (IC₅₀ 1.87 μM) but not HCT116 resistant cells (IC₅₀ 3 μM)

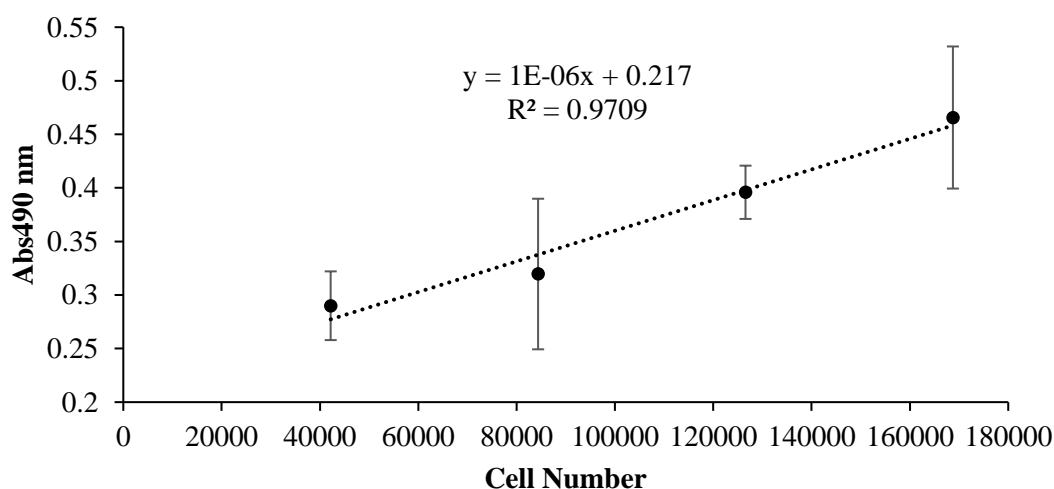


Fig. 3.15 MTS assay of HCT116 cells inside alginate beads. Different cell densities were seeded inside alginate matrix and MTS assay was performed to assess the performance of the assay in a 3D model.

Table 3.3 IC₅₀ (μM) at 48 h of Dox and ZnD in monolayer and alginate hydrogel beads for HCT116, HCT116 DR and Fibroblasts.

	HCT 116		HCT 116 DR		Fibroblasts	
	Monolayer	Alginate Beads	Monolayer	Alginate Beads	Monolayer	Alginate Beads
DOX	0.45 ± 0.3	3.51 ± 0.7	> 6	> 6	2.2 [140]	> 6
ZnD	0.22 ± 0.2	1.01 ± 0.4	0.1 ± 0.05	3 ± 0.4	0.6 ± 0.1	1.87 ± 0.8

3.4 Conclusions

Despite the effort put into the synthesis of novel compounds for cancer chemotherapy, they are often challenged by stability and solubility issues and, more importantly, lack of selectivity to cancer cells, thus inducing undesirable deleterious effects to healthy cells and tissues. In this chapter, we demonstrated that the high cytotoxic activity of the water-soluble Zn(II) coordination compound towards colorectal carcinoma cells. ZnD mode of action was associated with an increase of cell death

by intrinsic apoptosis and the induction of cell cycle arrest in S phase without observable genotoxicity. We developed a cell line derived from HCT116, resistant to DOX, and showed that ABCB1 efflux pump is the main responsible for the acquired resistance. We also show that ZnD is a promising chemotherapeutic agent against cancer cells refractory to DOX therapy, capable of bypassing the efflux pump overexpression. Cell cytotoxicity of ZnD in alginate hydrogels revealed that the IC_{50} of HCT116 is higher in a 3D model than in monolayer, possibly resembling more its efficacy in a tumour. Although in this model the IC_{50} values of HCT116 were lower than fibroblasts, they were higher for HCT116 DR, raising the question if this could be an effective compound to circumvent DOX acquired resistance in a 3D microenvironment.

CHAPTER 4 – NANOVECTORIZING MOLECULES FOR CHEMOTHERAPY

The work presented in this chapter was possible due to the support of several colleagues. Their contribution will be further detailed. The EGFR expression analysis was performed with the help of Rita Mendes. Internalization studies were performed by Pedro Martins and Rita Cabral (UCIBIO, Universidade Nova de Lisboa). Cytotoxicity studies of nanoconjugates were performed with the help of Pedro Martins. *In vivo* assays were performed with the help of Margarida Ferreira-Silva, Rita Mendes and Manuela Colla, under the supervision of Luisa Corvo (iMed, Universidade de Lisboa). The histological analysis was performed by Pedro Costa (UCIBIO, Universidade Nova de Lisboa). All the work was performed under the supervision and guidance of P.V. Baptista and A.R. Fernandes (UCIBIO, Universidade Nova de Lisboa). Data enclosed in this chapter were originally published in the following issues:

- **Pedrosa P**, Mendes R, Cabral R, Martins L, Baptista PV, Fernandes A. Combination of chemotherapy and Au-nanoparticle phototherapy in the visible light to tackle doxorubicin resistance in cancer cells. *Scientific Reports*. 2018, 8:11429 DOI: 10.1038/s41598-018-29870-0
- **Pedrosa P**, Corvo ML, Ferreira-Silva M, Martins P, Cola MC, Costa P, Martins C, Martins LMDR, Baptista PV, Fernandes AR. Targeting cancer resistance via multifunctional gold-nanoparticles: Cetuximab for improving delivery. *International Journal of Molecular Sciences*. 2019, 20(21): 5510 DOI: 10.3390/ijms20215510

4.1 Introduction

Nanomedicine has provided a wide range of tools suitable for directed and selective delivery of drugs to cancer cells. Recent advances have been focused towards designed multifunctional nanoparticles able to integrate diagnosis, drug monitoring, targeted delivery, and controlled drug release functions into a single particle [206, 243, 263, 371–373]. The ability to specifically deliver synergistic combinations of targeting moieties and therapeutic agents on a single nanoparticle has prompted an array of solutions aimed at selective combinatory delivery of drugs directed at cancer cells, lowering the toxic impact upon healthy tissues increasing therapy efficacy [217, 243, 372, 373]. AuNP, due to their ease of functionalization with functional biomolecules and low toxicity, are amongst the most promising solutions [216, 243, 373, 374]. Nanovectorization of chemotherapeutics to enhance therapeutic efficacy while circumventing drug resistance have provided for improved cancer management [375–377]. Selective delivery of these agents directly to the tumour site may be achieved by means of nanoparticle based vectorization, either via passive targeting associated to the EPR effect derived from the modified vasculature at the tumour site, or by using selective active targeting moieties, such as antibodies [378, 379]. The EGFR is often found overexpressed in cancer cells resistant to apoptosis, and may be specifically targeted via the therapeutic monoclonal antibody Cetuximab – FDA approved for clinical use in the treatment of colorectal cancer and lung cancer [129, 155, 156, 380–390]. Cetuximab blocks the receptor-dependent-signal transduction of EGFR leading to cell-cycle arrest, induction of apoptosis, inhibition of angiogenesis, inhibition of metastasis, internalization and down-regulation of EGFR itself [391]. EGFR-binding antibodies have been used for decorating nanovehicles for active targeting of tumour cells, specifically delivering their cargo, reducing it and increasing its therapeutic index [392]. In this chapter, we present a nanovectorization system (NanoZnD) harbouring ZnD compound and Cetuximab for active targeting. Its efficacy was tested in DOX-resistance colorectal carcinoma and lung adenocarcinoma cells *in vitro* and DOX-resistant xenografts *in vivo* (Fig. 4.1).

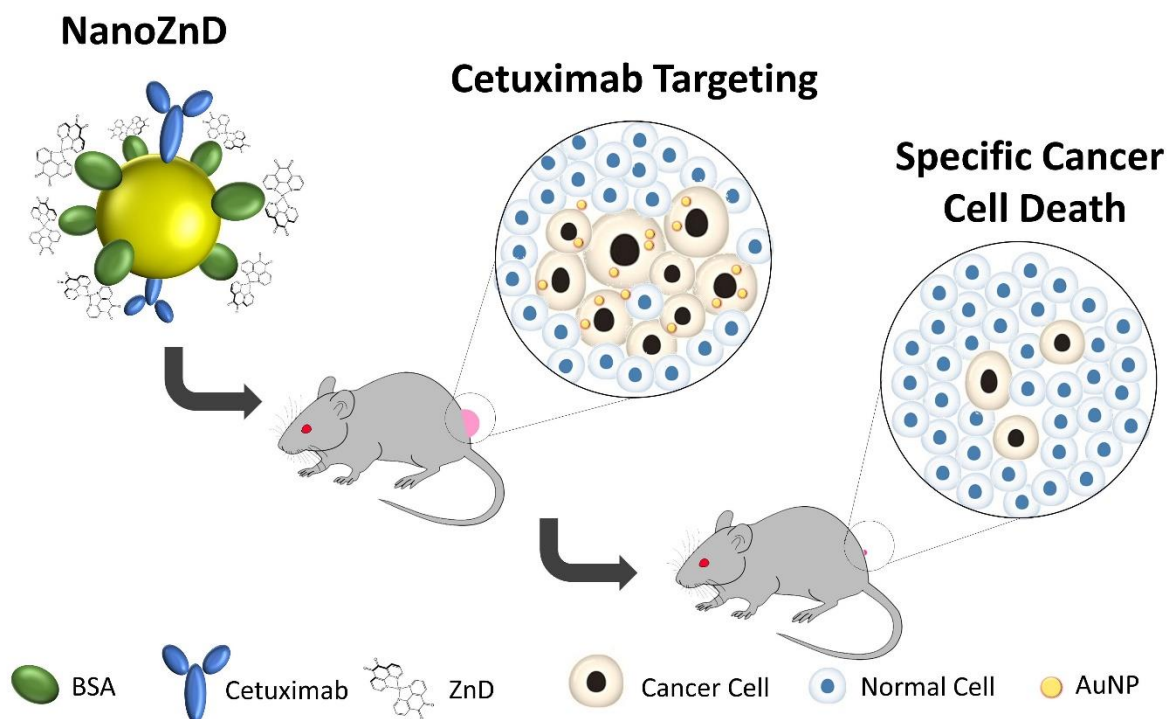


Fig. 4.1 Schematic representation of the NanoZnD strategy. AuNP core is covered by PEG for improved biocompatibility and stability in complex media; the antiproliferative compound - ZnD - is embedded within BSA; and the targeting moiety Cetuximab.

4.2 Methods

4.2.1 Interaction studies of ZnD with albumin

BSA stock solution was prepared by gently dissolving the protein in phosphate buffer pH 7.0 with 0.15M NaCl, gently swirled for 45 min to allow the protein to hydrate and fully dissolve. The concentration of BSA stock solution was determined by UV spectrophotometry using the molar extinction coefficient at 280 nm ($43824 \text{ M}^{-1} \cdot \text{cm}^{-1}$). Spectroscopic measurements were carried out on individually prepared samples to ensure the same pre-incubation time at $37.0 \pm 0.5 \text{ }^\circ\text{C}$ in each assay. BSA concentration was kept constant at $0.13 \text{ } \mu\text{M}$, while the concentration of the complex ranged from 0 to $375 \text{ } \mu\text{M}$. Samples were incubated at 37°C for 1 h.

4.2.2 Western blot

Western blot was performed according with section 2.2.5. The used primary antibody was against EGFR (EGFR (D-8), sc-365829, Santa Cruz, USA) and β -actin (reference no. A5441, Sigma, USA). The secondary antibody conjugated with horseradish peroxidase (reference no. 7074 or 7076, Cell Signaling Technology, USA) was used.

4.2.3 Assembly of Au-nanoconjugates and characterization

AuNP and AuNP@PEG were synthesized with HS-PEG(8)-COOH and characterized as described in section 2.2.6. For the preparation of AuNP@PEG@TAMRA and AuNP@PEG@BSA, TAMRA and BSA were respectively conjugated to AuNP via an EDC/NHS coupling reaction. Briefly, 20nM of AuNP@PEG, 1.25 mg·mL⁻¹ of sulfo-NHS and 312 µg·mL⁻¹ of EDC were incubated in 10mM MES, pH 6.1, and allowed to react for 30 min to activate the carboxylic group, to which 10⁻⁷ M TAMRA or 10 µg/mL of BSA were added. After an overnight period, the excess was washed twice by centrifuging at 14000×g for 30 min at 4 °C and removing the supernatant. For AuNP@PEG@BSA supernatants were recovered and tested for protein concentration using Bradford Assay.

AuNP@PEG were also functionalized with Cetuximab (Erbix®) (AuNP@PEG@CETUX) and with the same BSA concentration 1 h prior to antibody addition (AuNP@PEG@CETUX@BSA) under the previously described conditions. Cetuximab antibody was added to reaction mix at a final concentration of 3 mg·mL⁻¹. Following 1 h incubation with Cetuximab, BSA was added to the reaction mix at a final concentration of 10 µg·mL⁻¹ and the total volume allowed to react for 16 h at room temperature. Afterwards AuNP were centrifuged at 14 000×g for 30 min at 4 °C to remove the excess of proteins and the supernatants were recovered and tested for protein concentration using Bradford Assay to determine AuNP coverage. The total amount of conjugated BSA and/or Cetuximab was estimated by subtracting the amount of removed protein (during the centrifugation steps) to the total protein amount added in the first place for functionalization purposes. Resorting to a polynomial regression of Bradford's calibration curve it was possible to estimate the number of protein moles adsorbed at the surface of each AuNP hence allowing for the determination of the total number of protein molecules per nanoparticle.

For ZnD functionalization, solutions of 6 nM AuNP@PEG@BSA and 6 nM AuNP@PEG@CETUX@BSA were mixed separately with 50 µM of ZnD (dissolved in water) and incubated for 1 h at 4 °C to allow for compound adsorption to the nanoparticle systems to obtain AuNP@PEG@BSA@ZnD, and AuNP@PEG@CETUX@BSA@ZnD (NanoZnD), respectively. After this period, solutions were centrifuged at 14 000×g for 30 min at 4 °C, to remove excess of ZnD. The supernatants were recovered and analysed by UV/VIS spectrophotometer and ICP-MS to assess ZnD functionalization and the number of compound molecules per nanoparticle.

4.2.4 AuNP Internalization Studies

4.2.4.1 Confocal Fluorescence microscopy

Cells were seeded on coverslips in 24-well plates at a density of 1×10⁵ cells per well and grown for 24 h prior to incubation with 2.5 nM AuNP@PEG@TAMRA. Following 30 min or 4 h of incubation with AuNP, cells were fixed in 4% paraformaldehyde for 15 min, permeabilized with 0.1% (v/v) Triton X-100 (in PBS 1×) for 5 min and blocked with 3% (w/v) BSA (in PBS 1×) for 30 min. Cells were

incubated with Alexa Fluor 488-Phalloidin for 1 h and mounted with DAPI-containing Fluoroshield Mounting Medium. Confocal immunofluorescence microscopy Z-stack images were taken on a Zeiss LSM 510 META confocal point-scanning microscope. Images were processed using LSM image browser.

4.2.4.2 Flow cytometry

Cell uptake was also assessed by flow cytometry analysis. HCT116 cells and fibroblasts primary culture were seeded separately on 35 mm plates at a concentration of 1×10^4 cells per well in 2000 μ L of DMEM with 10 % (v/v) FBS and maintained at 37 °C, 5 % (v/v) CO₂. Nanoformulation exposure (AuNP@PEG and AuNP@PEG@CETUX) was allowed to react for a total period of 6 h in the conditions mentioned above to ensure AuNP uptake. Upon DMEM growth medium removal, cells were extracted by trypsinisation and stored in 2 ml microfuge tubes. Cell samples were duly analysed by flow cytometry on an Attune® Acoustic Focusing Flow Cytometer, through acquisition of at least 10000 events for each experimental condition.

4.2.5 Co-cultures – Selectivity Assay

HCT116 human colorectal carcinoma cell line and human primary fibroblasts were seeded at a cell density of 1×10^4 cell per well (1:1 ratio) over a cover slip within a 24-well plate well for 24 h, and then incubated with nanoconjugates for a further 6 h. Cells were fixed with 4 % (v/v) paraformaldehyde for 10 min at room temperature and permeabilized with 0.1 % (v/v) Triton X-100 for 5 min. Cells were double stained with anti-Vimentin 1:200 (fibroblasts staining that does not stain epithelial cells - HCT116) for 1 h, anti-mouse TRITC 1:64 for 30 min, and with Phalloidin 488 Alexa Fluor 3:200 for 20 min. Glass slides were mounted in ProLong® Gold Antifade Reagent with DAPI to allow for nuclear staining. Co-culture immunofluorescent images of HCT116 cell line and fibroblasts primary cell culture were acquired with a Zeiss Axioplan 2 Imaging Microscope and a Nikon DXM1200F digital camera. Cell number count and fluorescence quantification of co-culture's immunofluorescent images were performed for exposition to: i) fresh growth medium (control), ii) ZnD at its respective IC₅₀, iii) AuNP@ZnD and NanoZnD for 6 h using at least three different images. Cell number count and corrected total cell fluorescence (CTCF) ratio, of vimentin/phalloidin, was calculated through ImageJ software.

4.2.6 Animal model assays

All animal experiments were carried with the permission of the Portuguese Authority (Direcção Geral de Alimentação e Veterinária) and the study was approved by the Local Ethical Committee (Comissão de Ética Experimentação Animal da Faculdade de Farmácia, Universidade de Lisboa), and in accordance with the Declaration of Helsinki, the EEC Directive (2010/63/UE) and Portuguese law (DL 113/2013, Despacho no 2880/2015), and all following legislations for the humane care of animals

in research. Animals were kept under sterilized conditions using an Air Handling Easy Flow Ventilation Unit with single-sided racks and Blue Line NEXT individually ventilated cages. Animals were fed with sterilized commercial chow and given sterilized water ad libitum. Adequate measures were taken in order to minimize stress, pain or discomfort of the animals. A group of 30 (5 for each experimental condition) right hind leg of male BALB/c Nude Mouse (Charles River, France), 5 weeks old has been used. HCT116 DR-derived xenografts were induced by s.c. administration of 1×10^6 cells at the back hip of mice. Tumours were allowed to grow until an approximate size of 10 mm^3 and treatments were performed with two i.v. injection in the tail vein separated by 4 days. The administrations were performed according with the following groups: PBS 1 \times , free ZnD, AuNP@PEG, AuNP@PEG@CETUX, AuNP@ZnD and NanoZnD) $5.6 \text{ ng} \cdot \text{kg}^{-1}$ of ZnD per mice per injection (free or in the AuNP conjugates). Tumour volume was determined three times a week by measuring with callipers in two dimensions and by image analysis. Tumour volume (V) was estimated assuming an ellipsoid conformation were the height was estimated according to the tumour proportions at the day of sacrifice. Mice were monitored routinely for physical status. Mice were sacrificed 5 days after the last treatment. At the end of the experience mice were anesthetized with Isoflurane and animals were sacrificed by neck hyperextension and organs of interest (spleen and livers) and tumour were extracted weighted, washed with cold 0.154 M KCl to remove the excess blood and divided in two pieces: one for ICP-MS quantification of gold and the other for histological studies.

4.2.7 Histological analysis

Samples of liver, spleen and tumour were carefully excised fresh and immediately fixed in 10 % (v/v) neutral-buffered Formalin solution (Sigma-Aldrich, USA) for 24 h. After fixation, the samples were processed as described in [393]. Liver and spleen sections were stained with Gill's Alum Hematoxylin and counterstained with alcoholic Eosin Y (H&E). Tumours were stained with a tetrachrome stain for fibres and nuclei that include Alcian Blue, Weigert's Iron Hematoxylin and van Gieson's dye [394], similarly to our previous work [393]. Sections of all samples were stained with Neutral Red to enhance contrast and so detect metallic gold deposits with purplish colour. Finishing the staining, all sections were dehydrated in ethanol, cleared in xylene and mounted with DPX Mountant (Sigma-Aldrich, Portugal). Histological analyses were made with DM 2500 LED model microscope equipped with a MC 190 HD camera (both from Leica).

4.3 Results and discussion

4.3.1 Expression of EGFR in tumour and normal cells lines

The altered vascular and lymph uptake functions induced by growing tumours may lead to the observed differential accumulation of nanoscale materials at the cancer site, in what is called the EPR effect. As such, nanoscale vectors may passively make use of this EPR effect for the targeted delivery of chemotherapeutics [219, 395, 396]. This may be associated to active targeting via target selective

moieties coupled to the nanoparticles, making these nanoconjugates valuable tools to direct chemotherapeutics selectively to the cells/tissue of interest. In the case of solid tumours, this active targeting potentiates selective uptake by cancer cells, thus avoiding that drugs exert their deleterious effect on healthy tissues. Active targeting of nanomedicines is usually achieved by formulations that incorporate moieties to selectively discern the molecular biomarkers of interest, such as the EGFR [124]. Together, EPR and active targeting synergistically improve efficacy against tumour cells by improving the therapeutic effective doses.

Resistance of cancer cells to apoptosis has been linked to the overexpression of EGFR or EGFR mutations, observed in colorectal carcinoma and in 43-89% of NSCLC cases [186, 397–400]. As such, EGFR would be the obvious choice as a target for the selective delivery of a nanoformulation and it can be achieved via an anti-EGFR antibody, such as Cetuximab. Considering this, we confirmed the up-regulation of EGFR expression in HCT116, HCT116 DR, H1975 and A549 compared to normal human primary fibroblasts by western blot. Indeed, all tested cell lines showed overexpression of EGFR, with HCT116 DR showing a 3.4-fold higher expression compared to fibroblasts (Fig. 4.2). This confirmed that EGFR would be the ideal choice for targeting DOX-resistant cancer cells.

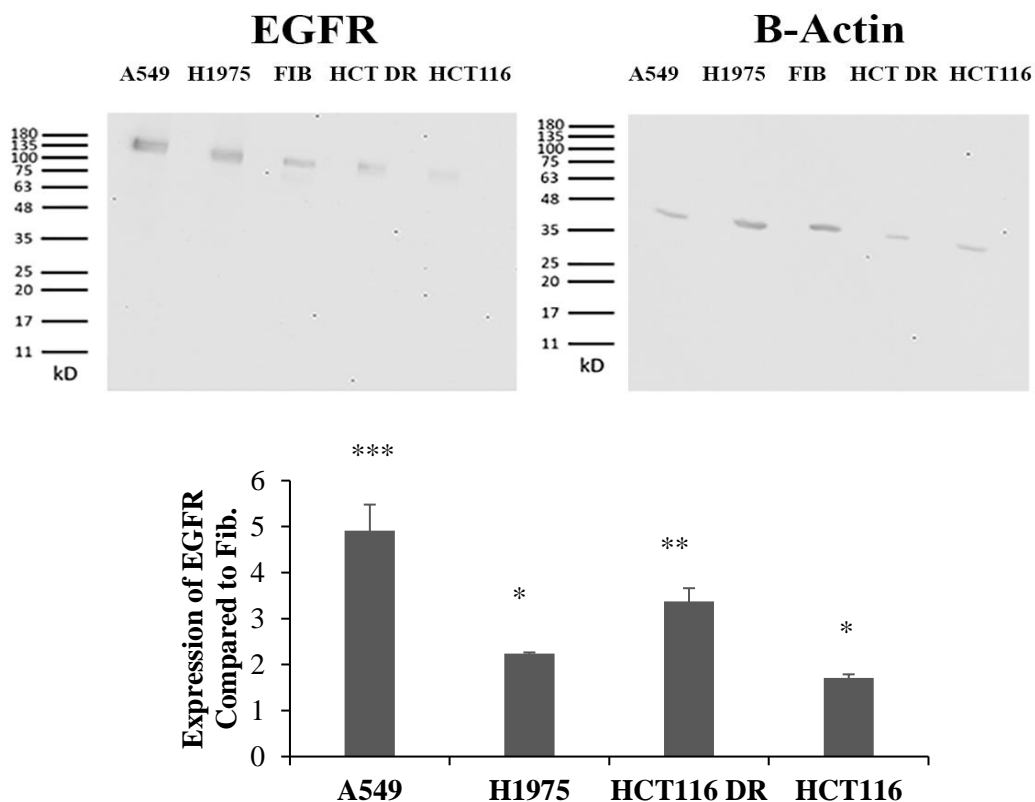


Fig. 4.2 Expression of EGFR in A549, H1975, HCT116 DR and HCT116 cells compared to Fibroblasts. (Top) EGFR (172 kDa) and ACTB (42 kDa) protein quantification was performed via western blotting on cell extracts. (Bottom) Fold expression of EGFR was compared with fibroblast expression for each cell line. Band quantification was normalized against ACTB. The results are expressed as the mean \pm SD percentage normalized to controls from two independent experiments (* $P < 0.05$; ** $P < 0.01$; *** $P < 0.001$).

Despite the higher cytotoxicity of ZnD in HCT116, HCT116 DR, and H1975 cells compared to human primary fibroblasts (Table 3.1) we attempted to enhance its cytotoxicity and at the same time its specificity by delivering ZnD to cancer cells using AuNP and an active targeting via Cetuximab [401, 402]. Due to the potential of AuNP as multifunctional delivery systems we looked forward to synthesizing and characterizing a nanoconstruct that harbours ZnD and Cetuximab (NanoZnD).

4.3.2 Nanformulation synthesis and characterization

It was previously described by our group that a Co(II) compound bearing the same ligand (PhenDION), could bind to serum albumin, and serve as “linker” to the AuNP. Serum albumin is the most abundant protein in blood plasma. This protein provides the intracellular binding, transportation and delivery of endogenous and exogenous compounds, such as fatty acids, steroids, metal compounds, metabolites and several pharmaceutical agents [403–405]. It is well known the ability of serum albumin to bind non-covalently to small molecules [403–405], resulting in an increased solubility of ligands in plasma and enhanced delivery to the target site [403–405]. Therefore, BSA has a great importance in nanomedicine due to its biocompatibility and water solubility. Its functionalisation with different functional groups on its surface makes it an interesting targeted based drug delivery system. Taking advantage of the intrinsic fluorescence of BSA due to its tryptophan residues, the fluorescence quenching of these tryptophan residues at various concentrations of ZnD was studied (Fig. 4.3).

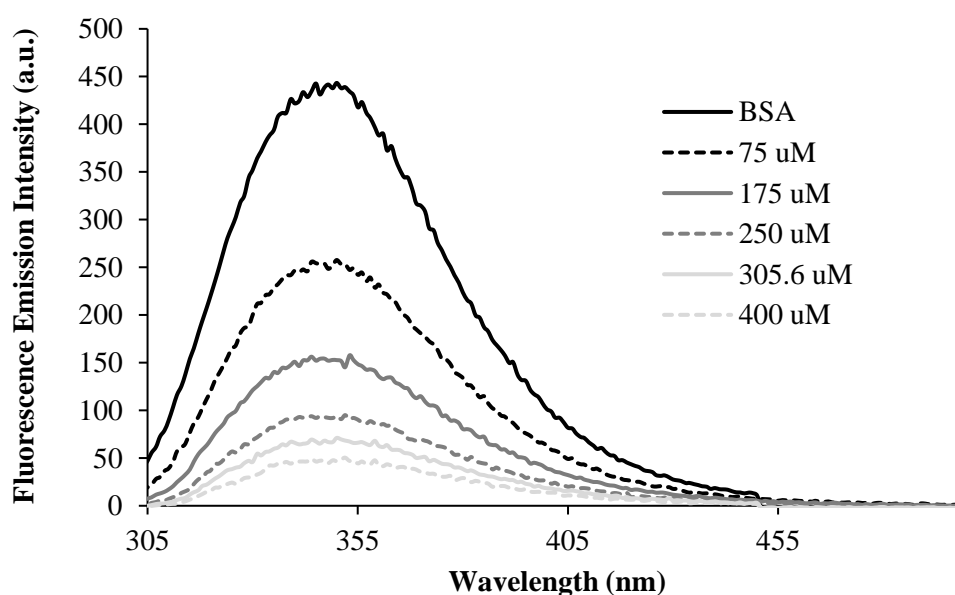


Fig. 4.3 Fluorescence spectra of BSA excited at 275 nm, with different concentrations of ZnD incubated for 1 hour at 37°C. Data is representative of at least three different assays.

In the absence of ZnD, the maximum emission wavelength was attributed only to the intrinsic fluorescence of BSA molecule and was observed at 350 nm (black line in Fig. 4.3). The effect of ZnD on BSA molecule was very pronounced, in which there was a remarkable decrease of BSA intrinsic fluorescence with the increase of compound concentration, reaching a decrease of about 89 % at the

highest ZnD concentration used (i.e. 400 μM) indicating the interaction between ZnD and BSA. Considering this interaction, we looked forward to developing a formulation harbouring AuNP, ZnD and Cetuximab.

AuNP were synthesized resorting to citrate reduction method. After characterization with methods described in 2.2.6.1 we observed a maximum absorption peak of 519 nm by UV-Vis Abs spectrum, an hydrodynamic diameter of 15 nm by DLS and a spherical shape of $14.2 (\pm 1.2)$ nm average diameter by TEM (Table 4.1 and Fig. 4.4). Solution concentration was estimated by Beer-Lambert law using the molar extinction coefficient predicted by Mie theory of $2.95 \text{ M}^{-1} \cdot \text{cm}^{-1}$ for 14 nm AuNP. AuNP were further functionalized with a coverage of PEG, harbouring a thiol group in one end and a carboxylic group in the other. The excess of PEG chains was removed by centrifugation and the degree of PEG coverage on the AuNP' surface evaluated via Ellman's Assay. The first PEG concentration that had detectable thiols in the supernatant was defined as 100% coverage ($0.01 \text{ mg} \cdot \text{mL}^{-1}$) (Fig. 4.5). AuNP@PEG were characterized by DLS and Zeta potential showing a slight increase in hydrodynamic radius and a decrease zeta potential indicating successful functionalization.

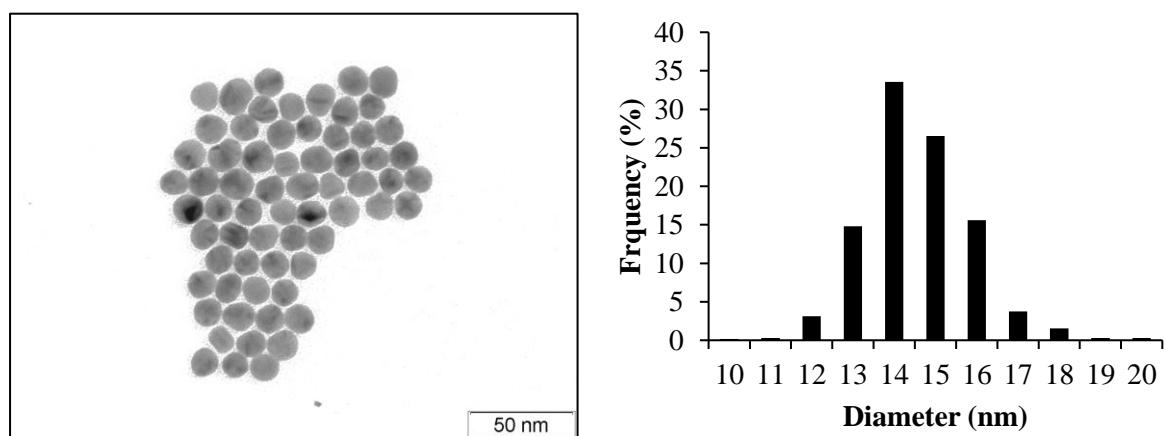


Fig. 4.4 TEM image of spherical citrate AuNP (Left). Histogram of diameter of AuNP with an average diameter of 14 ± 1 nm diameter (Right).

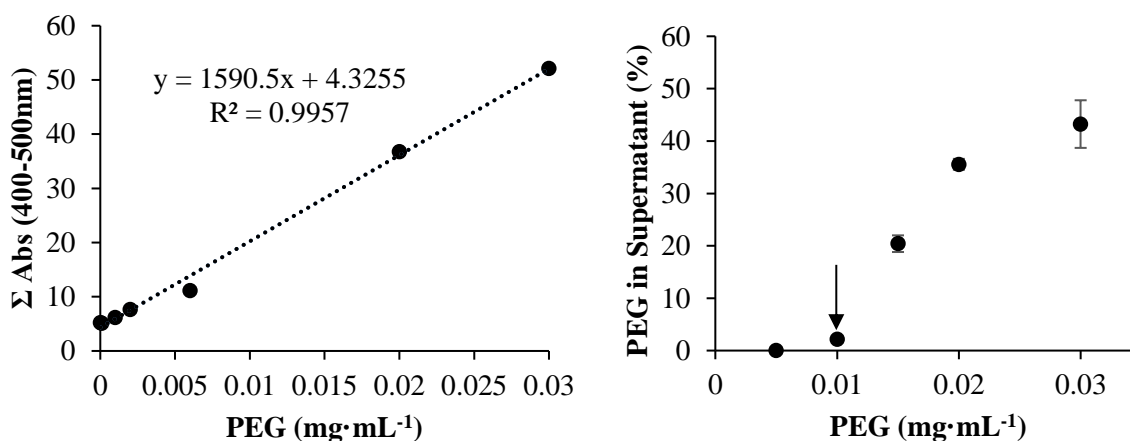


Fig. 4.5 Characterization of PEG functionalization at AuNP surface. (Left) Calibration curve of Elman's assay for amount of PEG and absorption at 400-500 nm. (Right) Percentage of PEG measured in the supernatant compared with PEG added to the AuNP.

AuNP@PEG were further functionalized with BSA (AuNP@PEG@BSA) and/or with Cetuximab (AuNP@PEG@CETUX; AuNP@PEG@CETUX@BSA) by EDC/Sulfo-NHS reaction. After successful functionalization, AuNP@PEG@BSA and AuNP@PEG@CETUX@BSA were subsequently functionalized with ZnD (AuNP@ZnD and NanoZnD respectively) and the amount of ZnD remaining in the supernatants quantified via UV-spectroscopy and ICP-MS. After each functionalization step, nanoconjugates were characterized by UV/Vis spectroscopy and DLS, consistent with increasing functionalization at the NPs' surface (Table 4.1 and Fig. 4.6). Bradford assay revealed a functionalization efficiency of approximately 7 BSAs (BSA:AuNP \approx 7) per gold nanoparticle. BSA is bound to the AuNP via covalent binding between amine groups present in both proteins and the PEG carboxyl group. AuNP@PEG@CETUX quantification of the supernatants using the Bradford assay revealed 2 Cetuximab per AuNP (Cetuximab: AuNP \approx 2).

Table 4.1 Nanoconjugates' functionalization moieties and hydrodynamic size determination by DLS. The different functional moieties and DLS size are discriminated (represented as means \pm SEM of at least three independent experiments).

AuNP Conjugate	Protein/AuNP	ZnD/AuNP	DLS (nm)
AuNP citrate	--	--	15.3 \pm 0.2
AuNP@PEG	--	--	18.6 \pm 0.3
AuNP@PEG@TAMRA	--	--	22.5 \pm 0.3
AuNP@PEG@BSA	7.0 \pm 0.5	--	27.4 \pm 0.4
AuNP@PEG@CETUX	1.6 \pm 0.2	--	78.3 \pm 0.7
AuNP@PEG@CETUX@BSA	6.9 \pm 0.5	--	110.4 \pm 0.8
AuNP@ZnD	7.0 \pm 0.5	402 \pm 32	118.7 \pm 0.9
NanoZnD	6.9 \pm 0.5	438 \pm 19	126.3 \pm 0.9

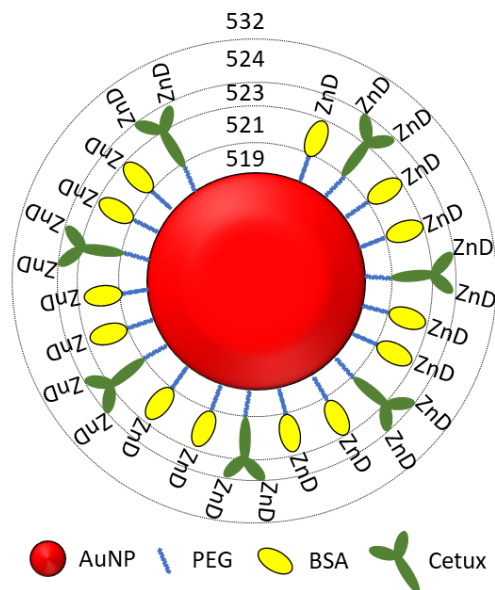


Fig. 4.6 AuNP construct with several functionalization layers: 1st PEG, 2nd BSA, 3rd Cetuximab, 4th ZnD compound. The numbers represent the maximum absorption peak after each functionalization step. A red shift is observed after each functionalization step.

4.3.3 AuNP internalization studies

There is plenty of literature on AuNP constructs that act inside animal cells. Despite some efforts to understand the mechanisms of internalization of AuNP they have not still been totally unravelled [406–408]. For that matter we wanted to confirm that our AuNP were accumulating inside cells, and that CETUX targeting could enhance internalization. We started by incubating HCT116 cells with AuNP functionalized with PEG and TAMRA for tracking internalization (at 30 min and 4 h) by confocal fluorescence microscopy. Cells were further stained with Alexa Fluor 488-Phalloidin (which labels F-actin) and Z-stacks were performed. Fig. 4.7 shows that after 30 min of incubation, the majority of nanoconjugates appear to be localized at the cell membrane. However, after 4 h of incubation, most nanoconjugates were localized closer to the nucleus (blue) and within the actin filaments (green), demonstrating internalization. This showed us that we needed at least 4 h of incubation with the nanoparticles to have internalization. To confirm that Cetuximab lead to an increase in internalization of AuNP, flow cytometry was used (Fig. 4.8). Observing the side scatter of HCT116, we can picture AuNP interaction with cells [409]. Cells challenged with AuNP@PEG, showed an increase in side scattering which we attribute to AuNP@PEG inside or at the membrane of cells (Fig. 4.8). The increase is even higher for AuNP@PEG@CETUX than AuNP@PEG. Although this technique cannot distinguish internalized from membrane bound AuNP, it indicates that AuNP@PEG@CETUX are interact more with HCT116 than AuNP@PEG.

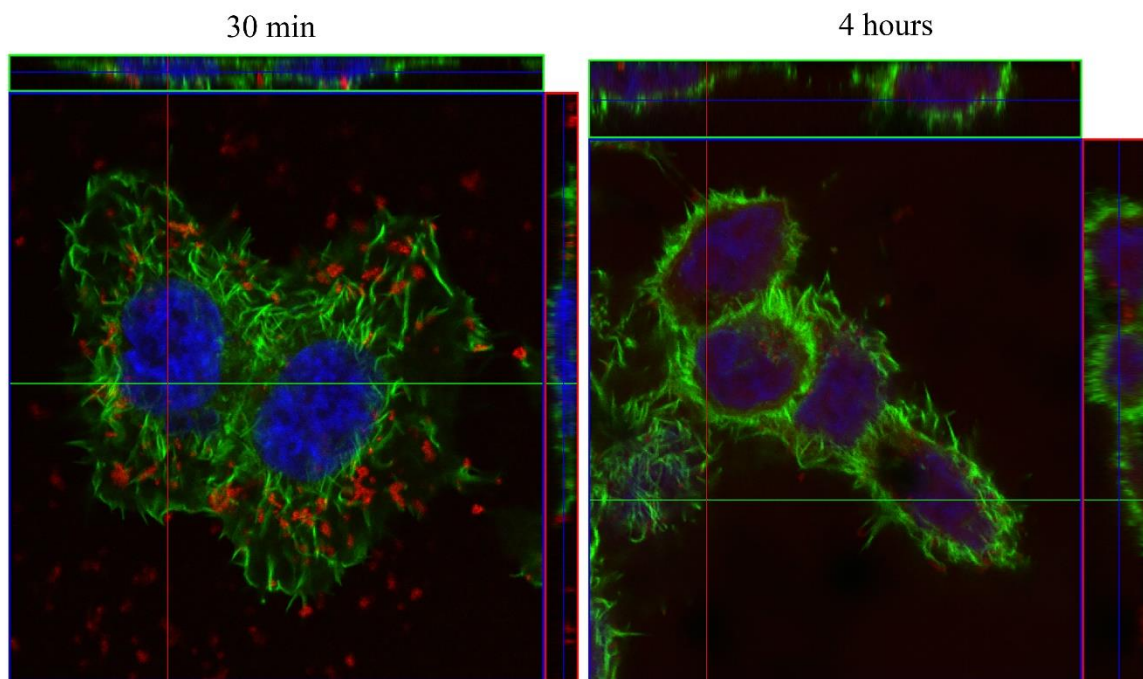


Fig. 4.7 Confocal fluorescence microscopy of HCT116 cells incubated with AuNP@PEG@TAMRA (red). Cells were stained with Alexa Fluor 488-Phalloidin (green) and the nuclear stain DAPI (blue). (Left) Cells exposed for 30min of AuNP where AuNP are mostly on cell surface and (Right) Cells exposed to 4H AuNP where AuNP are mostly inside cells.

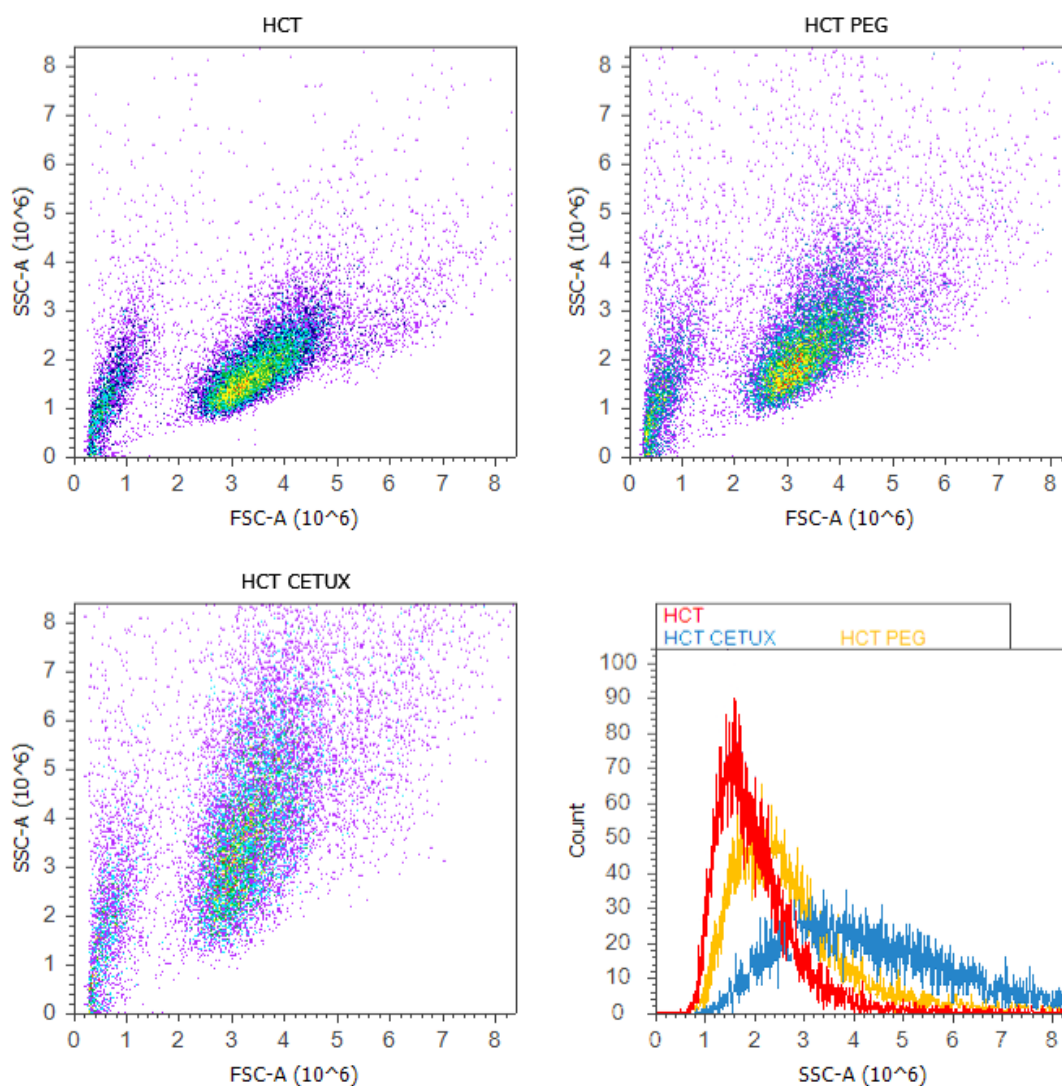


Fig. 4.8 Flow Cytometry of AuNP@PEG@CETUX. Forward and side scatter profiles at 488 nm of HCT116 cells after being exposed for 6 h to fresh growth medium (Top Left), and to the nanoparticle formulations, AuNP@PEG at 2nM (Top Right) and AuNP@PEG@CETUX (Down Left). Histogram plot evidencing the scattering profiles of HCT-116 cells when exposed to nanoparticle constructs (Down Right). FSC-A - Forward Scatter; SSC-A - Side Scatter.

4.3.4 Cytotoxicity of nanoconjugates in EGFR overexpressing cell lines

To test the efficacy of the NanoZnD compared with free ZnD we tested four cell lines (HCT116, HCT116 DR, A549 and H1975) expressing EGFR and incubated them for 24 h and 48 h in the presence of both formulations and respective controls (Fig. 4.10). The concentration of nanoconjugates used in all the assays were calibrated to deliver the same concentration of ZnD (IC_{50} at 48h for each cell line) and the control formulations without ZnD were used at the same AuNP concentration. Control AuNP without ZnD do not impair cell viability for all the cell lines tested (Fig. 4.9), which agrees with previous data that states that neither AuNP nor PEG nor BSA have cytotoxicity [206, 263, 393]. No cytotoxic effect was expected for AuNP@PEG@CETUX, since Cetuximab's concentration is at nanomolar

concentration in the formulation, which is largely below any reported cellular toxicity [410], acting only as targeting moiety.

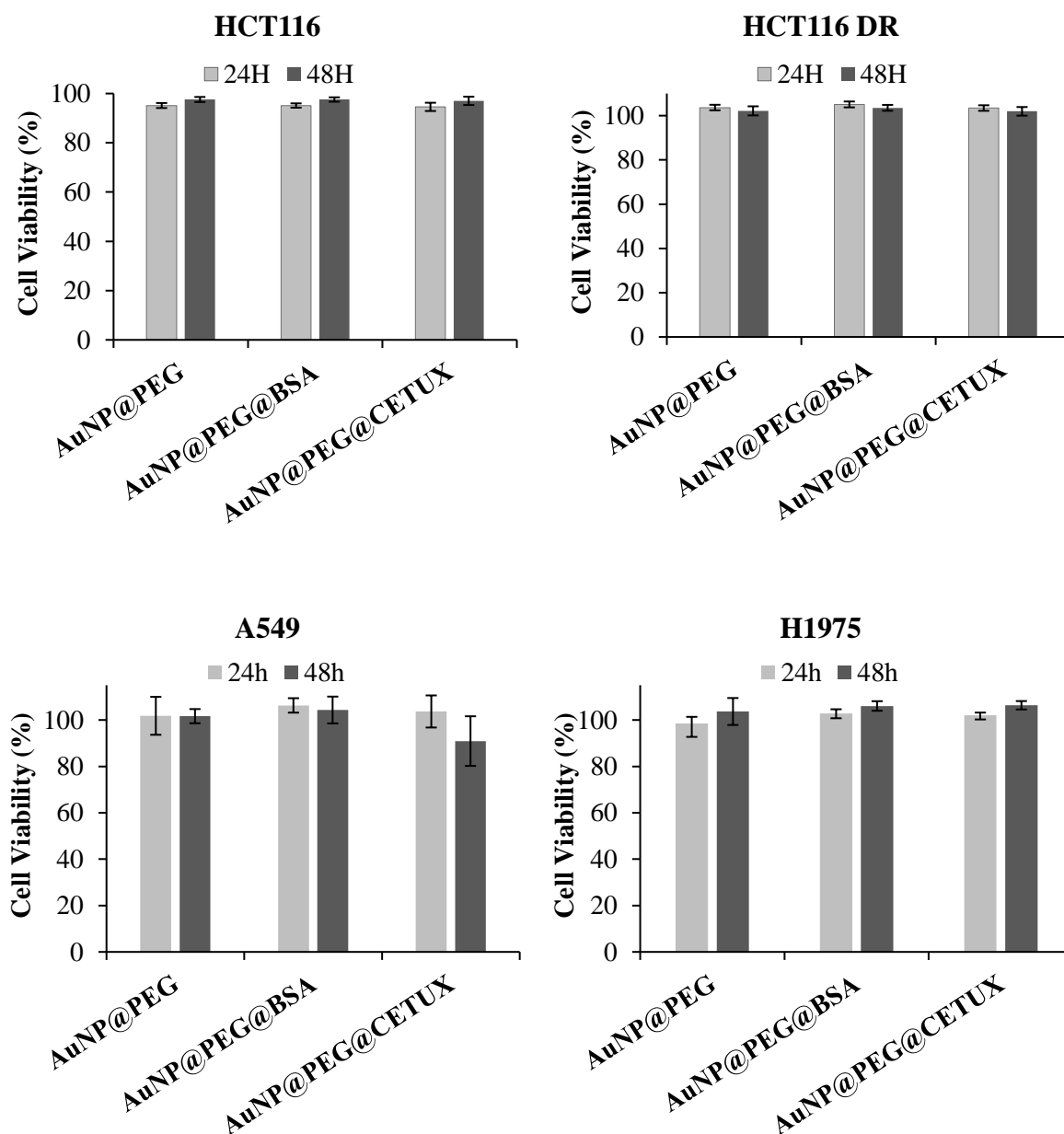


Fig. 4.9 Cell viability assessment of the control nanoconjugates in HCT116, HCT116 DR, A549, H1975 cell lines after 24 and 48 h incubation.

A strong reduction in cell viability for all four tumour cell lines (~20-50%) was observed when they were exposed to NanoZnD compared to free ZnD (Fig. 4.10) demonstrating the *in vitro* potential of ZnD nanoformulations particularly in DOX-resistant colorectal cancers and EGFR-overexpressing cell lines (mutated or not). Among the tested cell lines, the ZnD nanoconjugates seems to induce a higher cytotoxicity in lung adenocarcinoma cell lines (A549 and H1975) than colorectal cell lines (HCT116 and HCT116 DR) (Fig. 4.10 and Table 4.2). Also, lung adenocarcinoma cells with L858R/T790M-

EGFR mutations (H1975) are more susceptible to ZnD than Wild Type EGFR (A549) ($IC_{50}=0.355 \pm 0.04 \mu\text{M}$ compared to $0.714 \pm 0.09 \mu\text{M}$, respectively (Table 4.2).

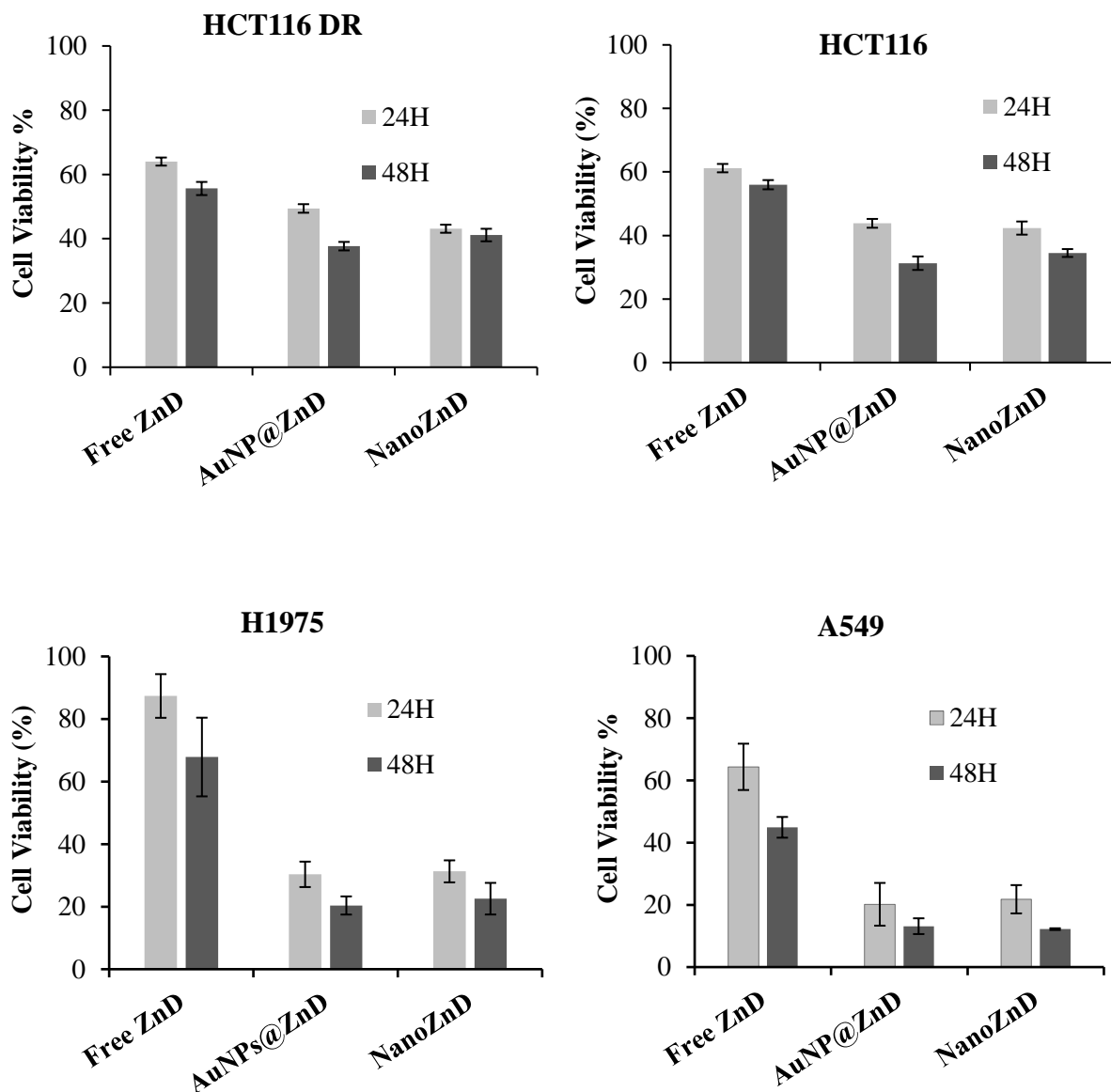


Fig. 4.10 Cell viability assessment of the nanoconjugates in various cell lines after 24 and 48 h incubation. Antiproliferative activities were assessed and compared to free ZnD at its IC_{50} at 48 h for each cell line. Cell viability was normalized to the control group without nanoparticle systems/compound. *p-value < 0.05 for AuNP@ZnD and NanoZnD compared to free ZnD.

Table 4.2 Cell viability obtained for HCT116, HCT11 DR, A549 and H1975 cell lines for the several nanoconjugates' formulations evaluated after 24 and 48 h after exposure. Data expressed as mean \pm SEM of at least three independent experiments.

Nanoparticle/drug formulation		Cell viability (%) (\pm SEM)	
		24 h	48 h
HCT116	AuNP@ZnD	43.8 (\pm 1.4)	31.3 (\pm 1.0)
	NanoZnD	42.3 (\pm 2.1)	34.5 (\pm 1.7)
	ZnD IC_{50}	61.2 (\pm 1.3)	56.0 (\pm 1.5)
HCT116 DR	AuNP@ZnD	49.4 (\pm 1.3)	37.7 (\pm 1.3)
	NanoZnD	43.1 (\pm 1.3)	41.1 (\pm 2.0)
	ZnD IC_{50}	64.0 (\pm 1.3)	55.6 (\pm 2.0)
A549	AuNP@ZnD	20.2 (\pm 6.9)	13.1 (\pm 2.5)
	NanoZnD	21.8 (\pm 4.5)	12.2 (\pm 0.3)
	ZnD IC_{50}	64.3 (\pm 7.4)	44.9 (\pm 3.3)
H1975	AuNP@ZnD	30.3 (\pm 4.1)	20.4 (\pm 2.9)
	NanoZnD	31.3 (\pm 3.5)	22.5 (\pm 5.1)
	ZnD IC_{50}	87.4 (\pm 7.0)	67.8 (\pm 12.6)

We also tested the same concentration of ZnD (IC_{50} of H1975) and nanoformulation for all cell lines (Fig. 4.11). The nanoconjugates showed a similar trend of relative cytotoxicity to that of the free ZnD with HCT116 DR > HCT116 > H1975 > Fibroblasts ~ A549 but with a higher cytotoxic effect compared with free ZnD. Despite the higher effect of the nanoformulation in A549 compared to ZnD free, the cytotoxicity of this compound is very similar to fibroblasts, hinders its use for this cell line.

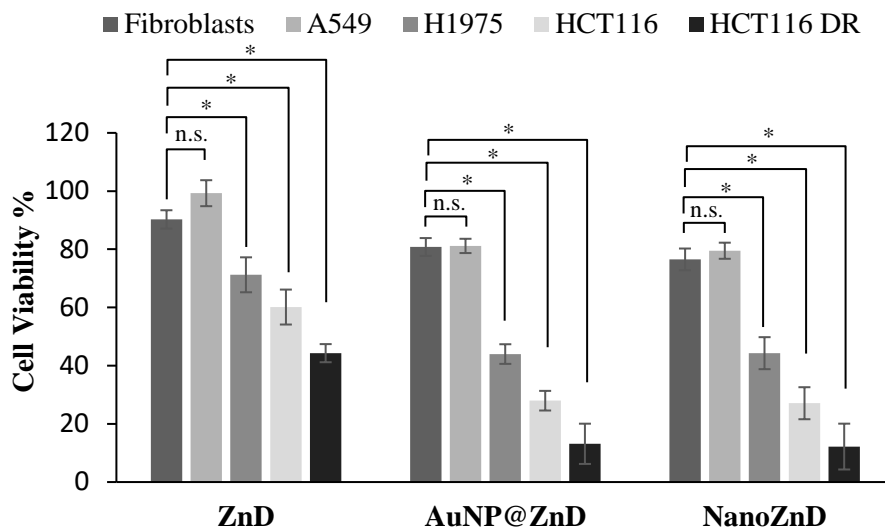


Fig. 4.11 Cell viability assessment of Free ZnD and nanoconjugates in fibroblasts, A549, H1975, HCT116 and HCT116 DR cell lines after 48 h incubation. Concentration of ZnD nanoconjugates correspond to same concentration of free ZnD (0.355 μ M). Data represented as mean \pm SEM of at least three independent experiments. Cell viability was normalized to the control cells without nanoparticles.

After examination of these results (Fig. 4.10 and Fig. 4.11) it seems that the active targeted nanoconjugate (NanoZnD) attained similar cell viability compared to the non-targeted counterpart (AuNP@ZnD) for all the tested cancer cell lines. To confirm if cetuximab was conferring selectivity to the formulation we co-cultured HCT116 cells and fibroblasts incubated with free ZnD and both nanoconjugates with and without Cetuximab for 6 h. Cell were stained with Vimentin that stains mesenchymal cells (fibroblasts), phalloidin that stains actin filaments (HCT116 and fibroblasts), and DAPI that stains nuclei (HCT116 and fibroblasts) – Fig. 4.12. Immunofluorescent images show that prior to incubation with the nanoconjugates both cell types are present at equivalent number in the co-culture. All formulations induced a decrease in the cellular density of each preparation, which is more evident in the NanoZnD nanoconjugates. What is more, the NanoZnD nanoformulation showed the highest degree of mortality to cancer cells, thus evidencing the effect of Cetuximab for selective targeting the cancer cells. The cell counts of co-cultures' immunofluorescent images evidences that NanoZnD nanoformulation targeting appears to elicit significant increase in the Fibro/HCT116 count ratio in an order of magnitude of 2- fold when compared with ZnD free compound and the control group (Fig. 4.13). This effect is more pronounced for the Cetuximab functionalized nanoconjugate than for its AuNP@ZnD counterpart. To corroborate these analyses, we quantified the corrected total cell fluorescence (CTCF) ratio vimentin/phalloidin of each sample. Co-culture preparations exposed to ZnD at its IC₅₀ and AuNP@ZnD does not exhibit significant changes to CTCF ratio. Conversely, NanoZnD induces a vimentin/phalloidin 5.6- fold increase. Although *in vitro* monoculture results indicate that Cetuximab targeting is no efficient, the higher fluorescence rate of vimentin/phalloidin provides a direct indication of the targeting success of NanoZnD (Fig. 4.13).

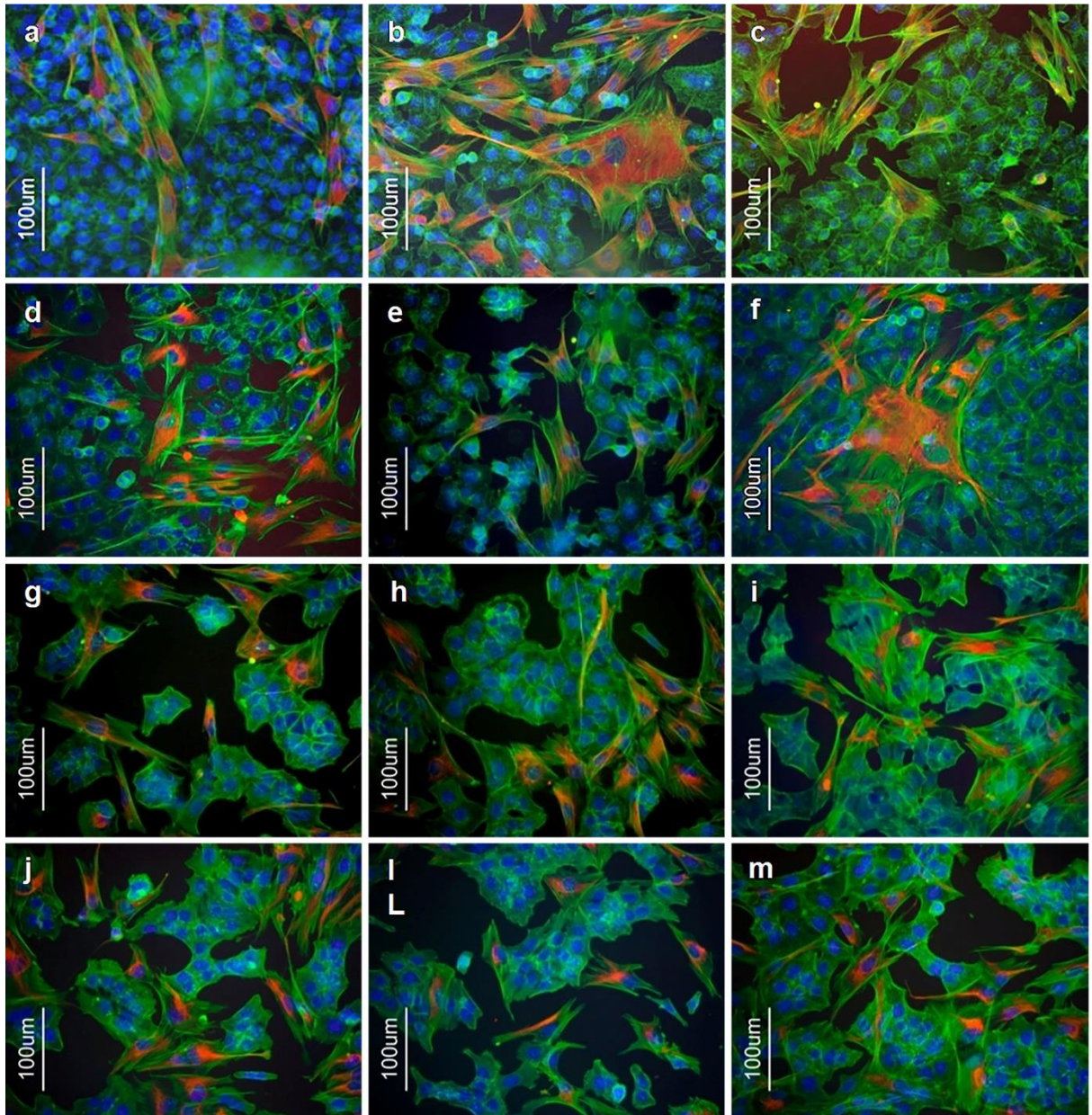


Fig. 4.12. Immunofluorescent images of HCT116 and Fibroblasts primary cell co-culture (Vimentin stained in orange). Co-cultures were incubated with fresh growth medium (a, b, c), ZnD at its respective IC_{50} at 48h (d, e, f), AuNP@ZnD nanoconjugate (g, h, i) and NanoZnD (j, l, m) for an incubation period of 6 h. Immunofluorescent images were acquired with a Zeiss Axioplan 2 Imaging Microscope and a Nikon DXM1200F digital camera.

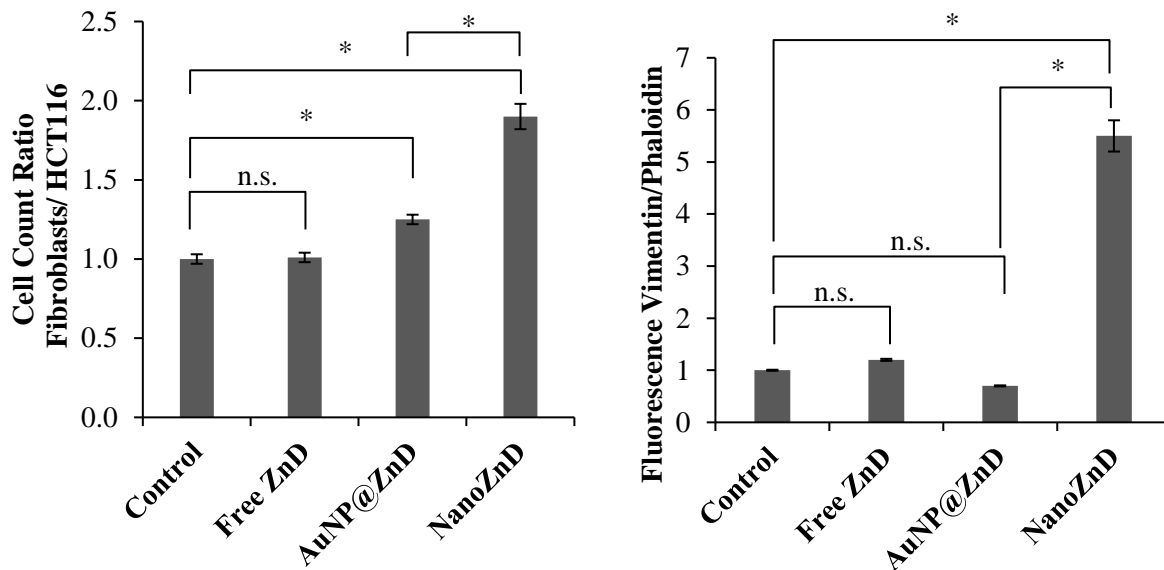


Fig. 4.13 Co-culture fluorescence analysis. (Left) Ratio of Fibroblasts/HCT116 cell count performed using ImageJ Software. (Right) Average corrected total cell fluorescence (CTCF) ratio, vimentin/phalloidin, of the co-cultures exposed to fresh growth medium, ZnD (IC₅₀) and with nanoparticle constructs functionalized with ZnD, AuNP@ZnD and NanoZnD. Data represents the mean of the fold variation compared to control sample without AuNP (fresh growth medium). Data represents the mean \pm SEM of at least three different images; *p < 0.05 compared to control.

4.3.5 *In Vivo* Assays

Proved the active targeting and cytotoxic potential of these gold nanoconjugates *in vitro*, we evaluated the *in vivo* efficacy on HCT116 DR-derived xenografts induced by sub-cutaneous administration of 1×10^6 cells at the right hind leg of male BALB/c Nude Mice (n=30). Tumours were allowed to grow until $\sim 10 \text{ mm}^3$ in size and treatments were performed with two intravenous tail injections separated by 4 days with the following formulations: PBS (n=5); free ZnD (n=4); AuNP@PEG (n=3), AuNP@PEG@CETUX (n=2); AuNP@ZnD (n=4); NanoZnD (n=5); and NanoZnD 2 \times (n=2). The tumour growth was followed every two days, by two calliper measurements per tumour and photographed. Five days after the second dose, mice were sacrificed, and tumour, spleen, and liver were extracted and divided for ICP-MS and histology. After sacrifice, one mouse from group NanoZnD revealed a tumour implant in the spleen and was not considerate for further analysis.

To analyse tumour growth data, it is generally assumed that tumours have an ellipsoid shape and two calliper measurements are taken corresponding to the shorter and larger diameters of the ellipse. Since not all tumour present a regular shape, to mitigate the errors of the latter assumption we tested if image analysis could better estimate tumour growth. Photographs can in theory estimate more accurately the tumour size than calliper because they take in consideration the tumour area instead of estimating it by longitudinal and transversal calliper measurements. It also reduces animal handling and operator error. To test the approach, we compared the real measurements of the tumour in the day of sacrifice, after tumour extraction, with the measurements estimated by the photographs and by the

calliper and observed that photographs have a better correlation at predicting tumour area than calliper (Fig. 4.14). For that reason, photography images were considerate for further analysis.

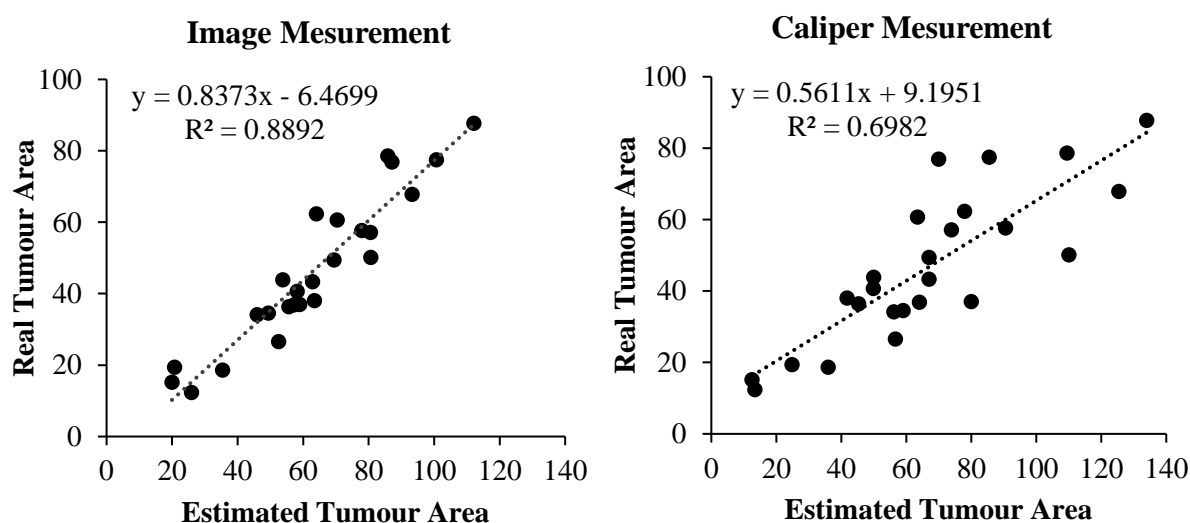


Fig. 4.14 Comparison of tumour area measured after excision (real area) with the area estimated by photograph and calliper prior to mice sacrifice.

To determine the tumour volume, it is necessary to know the tumour height. As the tumour height is difficult to measure, it is generally estimated as being equal to the smallest diameter of the ellipse. We observed that our tumour had irregular shapes and that the height was not correctly estimated by this method. So, to calculate tumour volume, we measured the real height of each tumour after the mice sacrifice and set a proportion of its area/height. We used that proportion to estimate the height and volume of the mouse during its growth. This method assumes that the shape of the tumour remained similar during its growth. For PBS, AuNP@PEG and AuNP@PEG@CETUX no reduction in the average tumour growth rate prior injection vs. after injection was observed. For ZnD free there was a reduction of tumour growth rate by 43%. For AuNP@ZnD we observed a reduction of 65% in tumour growth rate. For NanoZnD all the injected mice responded to treatment either in the first or the second injection, in such cases the average reduction in tumour growth rate was 84%. We also tested a single dosage of double concentration of NanoZnD, in this case the tumour growth rate reduced in average 152%. Both NanoZnD in single or split dosage revealed a significant decrease in tumour growth after injection compared to controls (PBS, AuNP@PEG) (Fig. 4.15 and Fig. 4.16E). These results show that NanoZnD efficiently reduced tumour growth with a reduction in tumour size. However, AuNP@ZnD and NanoZnD did not show a statistically significant difference, remaining the question of the impact of cetuximab active targeting in increasing the formulation efficacy. Although we cannot conclude it from our data, adding active targeting might reduce side effects with less accumulation in non-tumoural tissue.

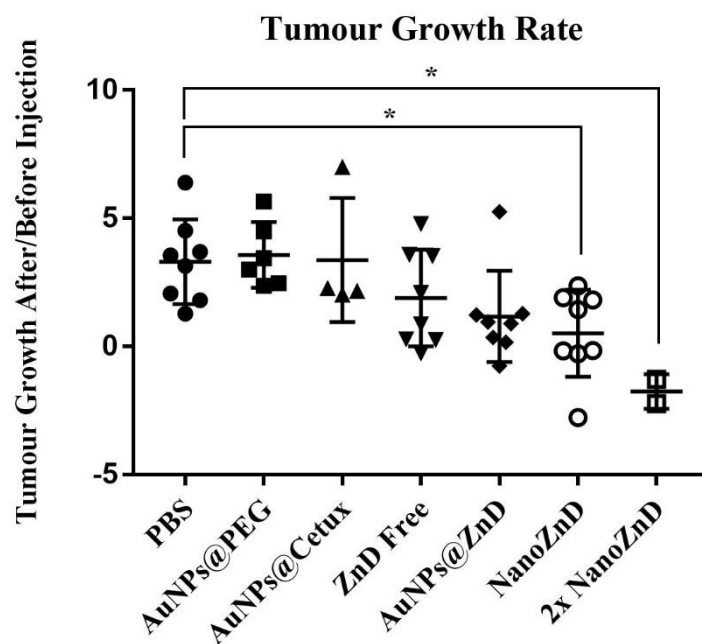


Fig. 4.15 Tumour growth rate in mice model. Ratio of tumour growth rate before (T0) and after injection of formulation (T1 or T2). Each point represents one injection. Values greater than one represent increase in tumour growth rate after injection. Values between one and zero represent decrease in tumour growth rate. Negative values indicate not only decrease in tumour growth rate but also tumour remission (Kruskal-Wallis test * $P < 0.05$).

The subcutaneous tumours presented a similar histological morphology between controls and treatments. Most tumours showed a mixed border configuration, which means that tumours had a fibrous encapsulation. However, in some cases, the mass was found to be aggressively intruding the surrounding mouse tissue (Fig. 4.16B). The neoplastic cells were actively proliferating, as indicated by a high frequency of cells in mitosis (Fig. 4.16B – Inset) independently of treatment. This is indicative of continuous development of the tumour mass. The central area of the tumour was invariably characterized by massive infiltration of inflammatory cells and lymphoid tissue (Fig. 4.16C). ICP-MS quantification showed the presence of gold only in the tumour samples with no detectable gold in spleen nor liver. Small metallic agglomerates were detected, in the histological preparations, inside a macrophage in tumours from mice injected with AuNP (Fig. 4.16C – Inset). No visible histopathological alterations were found in the liver (Fig. 4.16D) and spleen (Fig. 4.16E) of mice subjected to any of the experimental treatments, including controls. Oppositely to what was found in tumours, no metallic deposits consistent with AuNP agglomerates were detected in the liver and spleen of tested mice. These shows that the nanoformulations accumulate at the tumour by EPR and/or active targeting, confirming the delivery of ZnD.

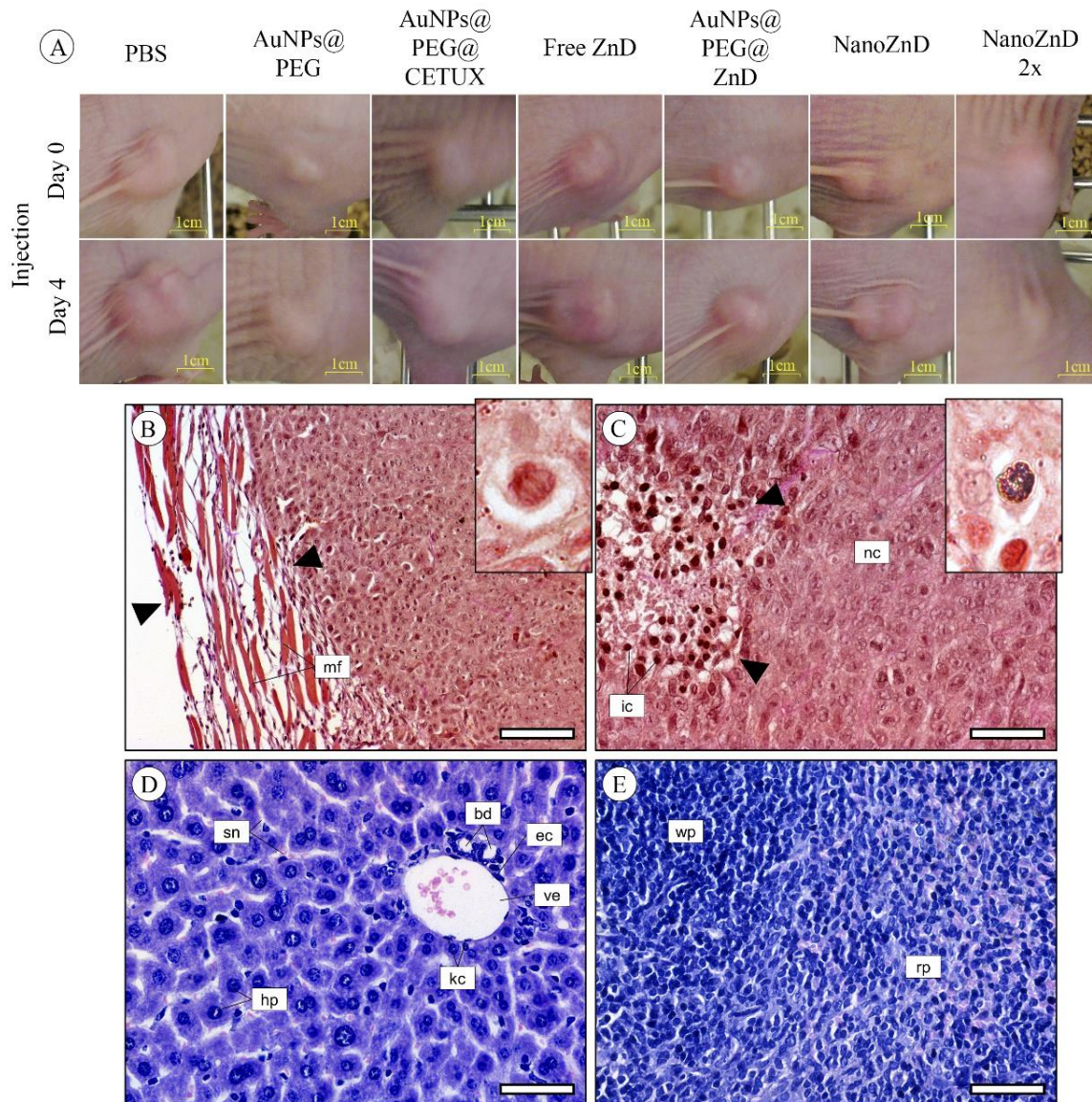


Fig. 4.16 A. Images of mice tumour xenografts on the day of injection of each formulation and four days later. B. Example of micrographs of representative histological sections of tumour, liver and spleen from tested mice. Mixed tumour border configuration, showing part of the fibrous encapsulation (between arrowheads), formed by connective tissue and muscle fibres (mf). Inset: Detail of a mitosis in tumour cells. C. Tumour presenting a compact mass of neoplastic cells (nc) and foci of infiltrating inflammatory cells (ic), within which are found debris of necrotic cells (arrowheads). Inset: Detail of a small metallic agglomerate inside a macrophage found in a tumour from a mouse injected with AuNP. D. Representative micrograph of the hepatic tissue of mice, showing the normal architecture of the organ, i.e. with regular-sized hepatocytes (hp) arranged in trabeculae. bd) Bile duct, ec) endothelial nucleus cell, kc) Kupffer cells, sn) sinusoids, ve) venule. E. Representative micrograph of the spleen of tested mice. Regardless of experimental treatment, no histopathological alterations were found in the organ. rp) red pulp, wp) white pulp. B and C, tetrachrome stain. D and E, H&E, Insets, Neutral Red. Scale bars: A: 100 μ m, B - D: 50 μ m.

In the batch of inoculated mice, 5 individuals did not grow a tumour after 50 days. In those cases, 5× (n=1), 10× (n=2), and 20× (n=2) the dosage of NanoZnD was tested to assess its toxicity levels. After 4 days all mice were sacrificed and spleen, and liver were weighted and cut in half for ICP-MS and histology. No visible alterations were detected in these mice, the ratio of organ to body weight of the tested organs was normal in all individuals (Fig. 4.17), and no visible histopathological alterations were found in the excised organs. No metallic deposits consistent with AuNP agglomerates were detected in the liver and spleen of this mice. These results indicate that 20× dosage of NanoZnD is safe to administer without acute reaction. These results, together with the increased effect of single dosage administration of NanoZnD show that there is chance for improving efficacy by escalating the dose without increasing toxicity, since neither accumulation of the vehicle for the remaining formulations nor toxicity effects were perceptible

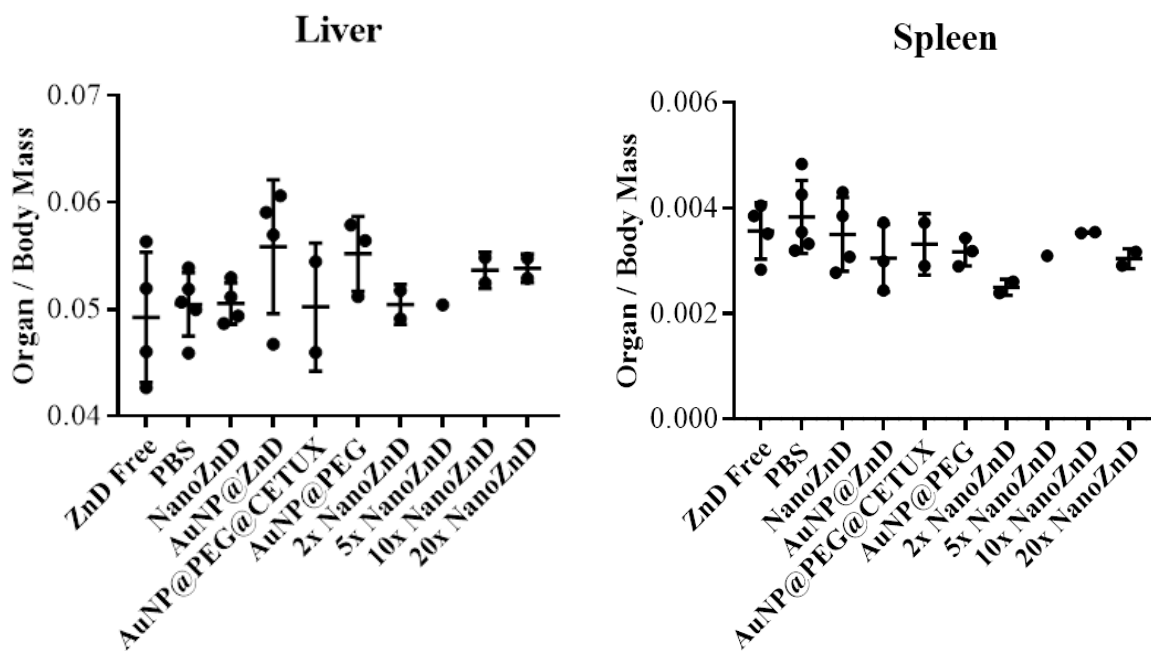


Fig. 4.17 Organ to body weight of liver and spleen of tested mice. Mice were weighted before sacrifice and liver and spleen were weighted after sacrifice. The organ to body weight was calculated for all tested formulations.

4.3.6 Conclusions

In this Chapter we successfully synthesized and functionalised AuNP with an anti-proliferative compound (ZnD) and an Anti-EGFR antibody (cetuximab). The gold nanoparticle-based formulation improved *in vitro* the potential of the compound against sensitive and DOX resistant colorectal carcinoma cell lines and two lung adenocarcinoma cancer cell lines (with and without EGFR mutation). Moreover, conjugation of Cetuximab provides for selective targeting capability *in vitro* and increased cell uptake of ZnD, resulting in enhanced selectivity towards cancer cells. The selective active targeting was clearly demonstrated through comparative experiments in non-tumourigenic cell line (fibroblasts primary cell culture), corroborated by fluorescence and flow cytometry data. The conceptual nanovectorization system here described may be used to target specifically DOX sensitive and resistant cancer cells and EGFR mutated lung adenocarcinoma cells with reduced cytotoxicity towards normal fibroblasts. The promising anti-cancer capability of this nanoformulation was further demonstrated *in vivo*, where it selectively hindered tumour growth without any deleterious effect to healthy tissues. The analysis of mouse xenografts revealed to be more accurate when analysed by photographs than calliper. What is more, the nanoformulation was capable to effectively reduce a xenograft of DOX-resistant colorectal cancer cells in a single dose without systemic toxicity. The advantage of active targeting with cetuximab, lacked more research, since it was not observed a statistical difference of adding cetuximab active targeting *in vivo*.

CHAPTER 5 – AUNP FOR COMBINED CHEMOTHERAPY AND PHOTOTHERAPY

The work presented in this chapter was possible due to the support of several colleagues. Their contribution will be further detailed. Laser characterization was performed under the guidance and supervision of João Lima (UCIBIO, Universidade Nova de Lisboa). All the work in this chapter was performed with the help of Rita Mendes, under the supervision and guidance of P.V. Baptista and A.R. Fernandes (UCIBIO, Universidade Nova de Lisboa). Data enclosed in this chapter were originally published in the following issues:

- Mendes R, **Pedrosa P**, Lima JC, Fernandes AR, Baptista PV. Photothermal enhancement of chemotherapy in breast cancer by visible irradiation of Gold Nanoparticles. *Scientific Reports*. 2017, 7(7):10872 DOI: 10.1038/s41598-017-11491-8
- **Pedrosa P**, Mendes R, Cabral R, Martins L, Baptista PV, Fernandes A. Combination of chemotherapy and Au-nanoparticle phototherapy in the visible light to tackle doxorubicin resistance in cancer cells. *Scientific Reports*. 2018, 8:11429 DOI: 10.1038/s41598-018-29870-0
- **Pedrosa P**, Lima JC, Fernandes A, Baptista PV. Temperature and salt mediated semi-reversible aggregation of PEG coated gold nanoparticles. (in preparation)

5.1 Introduction

PTT is a minimally-invasive therapeutic strategy, where light irradiation is converted by photothermal agents to heat, thus increasing the temperature of specific tissues [202]. Heating sources range from NIR and visible light to radiofrequency waves, microwaves, and ultrasound waves. PTT in cancer allows to selectively destroy cancer cells and spare healthy cells in the vicinity, since the former are more sensitive to an increase in temperature [202, 411]. Tissues and cells have got their natural photothermal agents, e.g. haemoglobin, cytochromes, but their absorption efficiency is very low, requiring high amounts of photon energy [202]. To enhance the photothermal effect, synthetic organic dyes are used, which may be selectively delivered to cancer cells, thus potentiating the destruction of malignant cells. Tumour environment is more hypoxic, acidic and nutrient-deficient than normal tissues, which are believed to increase the sensitivity of cancer cells to heat [412]. However, these dyes are prone to photobleaching that results in loss of anticancer activity [411]. Recently, the generation of nanoscale-based photothermal agents, such as AuNP, with higher absorption efficiency and without suffering from photobleaching, has relaunched PTT as an anti-cancer therapy [412]. AuNP exhibit unique physicochemical properties, including their surface plasmon resonance (SPR), which relies on the interaction between an electromagnetic wave and free conduction electrons at the AuNP' surface, causing them to oscillate coherently in resonance with the frequency of visible light, resulting in strong electromagnetic fields. This phenomenon greatly enhances both the scattering and the absorption of light by the AuNP suitable for different biomedical applications [295, 413]. AuNP are also recognised by their PTT capacities, converting electromagnetic radiation into heat due to electron excitation and relaxation [413], which has been used for thermal ablation of tumour cells. Indeed, AuNP of specific sizes and shapes, including gold nanorods, nanocages and nanoshells are capable to convert NIR radiation into heat [414–418]. NIR lasers are commonly used in AuNP induced PTT due to the optical window in the NIR, where haemoglobin, melanin and water absorption is reduced, allowing deeper light penetration into fluids and tissues [419]. Although visible light has been applied to superficial epithelial cells or in transparent organs (e.g. the eye), aiding in surgical ablation of cells or photo cauterisation of blood vessel, visible irradiation using AuNP has had less application to cancer therapy than the NIR. Visible light penetration into the tissue is reduced to less than a millimetre, which provides for higher precision in certain medical procedures [202]. Green lasers (495-570 nm) for instance have been used for decades in medical surgery for photocoagulation in several ocular disorders as a safe tool for tissue ablation without bleeding, such as in retinoblastoma [111, 420] focal therapy and vocal cords surgery [421, 422]. Spherical AuNP with diameters ranging from 10 to 30 nm are ideal photothermal agents for biomedical applications since they have been shown to be non-toxic [206, 265] and present a characteristic localized SPR band around 520 nm, i.e. in the visible region of the spectrum, with an efficient light-to-heat conversion because absorption corresponds almost totally to extinction [202, 299, 423, 424]. As such, AuNP as photothermal agents are an efficient way to induce precise heating, leading

to less damages to surrounding tissues, while destroying malignant, more thermosensitive cells [299, 413].

Thermal therapy is strongly dependent on cancer type, and tumour adaptation to temperature (i.e. thermos tolerance) may easily impact efficacy of PTT. The use of combined therapeutic approaches, relying on the synergistic interaction between heat and cytotoxic treatments has been proposed with clear advantages [175, 412]. For instance, preclinical studies showed a synergistic interaction between heat and cytostatic treatments [176, 425]. Several reports have demonstrated that DNA damaging agents, such as DOX, see an increase in efficacy by combination with hyperthermia, since DNA repair processes are temperature-dependent [175, 426]. As previously stated, DOX toxicity in healthy cells poses major concerns in effective treatment of patients, as well as increasing reports of therapy relapse, leading to increase in dosage with concomitant more severe adverse-effects [136, 187]. As demonstrated in section 3.3.2 the non-response in cancer cells can be associated to drug resistance over time namely by overexpressing of efflux pumps (Fig. 3.10) [187, 427].

Here, we show that PTT using visible light and AuNP as photothermal agents enhance the cytotoxic effect of DOX in cancer cells. By using a traditional drug as DOX, we illustrate the possibility to easily combine chemo- and PTT with improved efficacy and doing so by irradiation with existing lasers currently used in the clinics. We also show that the combination of an anti-tumour Co(II) metal compound (CoD), previously described and extensively studied by our group [393, 428, 429], and similar to ZnD (see section 3.3.1) has anti-tumour effect and can be coupled to photoinduced hyperthermia results in increased tumour cell death, and can circumvent DOX resistance (Fig. 5.1).

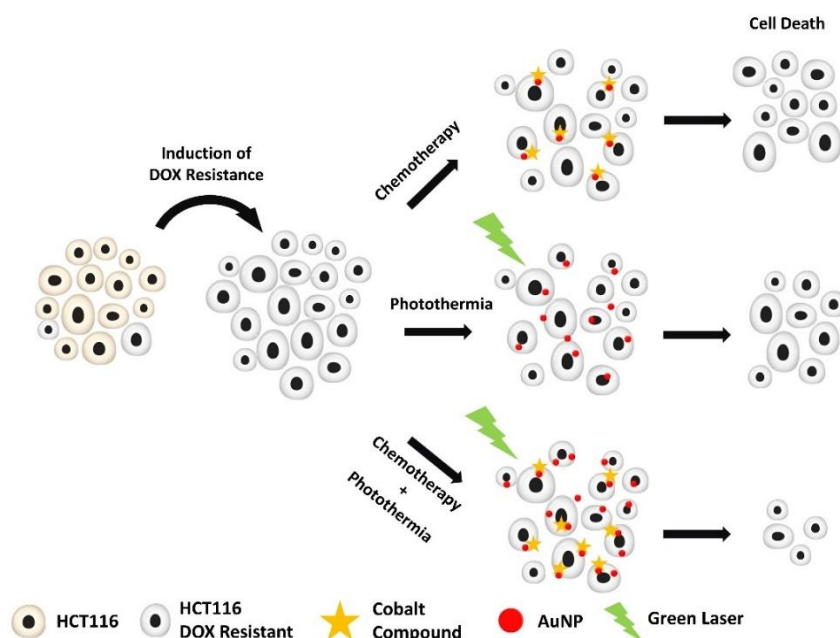


Fig. 5.1 Schematics of combined chemo-hyperthermia to tackle Resistant DOX HCT116. After induction of DOX resistance, cell death is assessed after chemotherapy, hyperthermia and combination of both therapies.

5.2 Materials and Methods

5.2.1 AuNP@PEG synthesis and characterization

AuNP@PEG were synthesized, functionalized and characterized as described in section 2.2.6.

5.2.2 Irradiation of cells

Prior to irradiation the laser source performance was characterized by actinometry as described in section 2.2.7. For HCT116 cell experiments, they were seeded with a density of 2×10^4 and then incubated with 8.2 nM AuNP@PEG ($\epsilon = 2.85 \times 10^{-8} \text{ M}^{-1} \cdot \text{cm}^{-1}$) for 4 h. For MCF-7 cells were seeded as described above and then challenged with 15 nM AuNP@PEG ($\epsilon = 2.85 \times 10^{-8} \text{ M}^{-1} \cdot \text{cm}^{-1}$) for 2 h. Subsequently, the culture medium was replaced by supplemented DMEM medium without phenol red pH indicator and irradiated with a continuous wave 532 nm green diode-pumped solid-state laser coupled to an optical fibre with a power set to $3.44 \text{ W} \cdot \text{cm}^{-2}$ for 60 s. Cell membrane integrity was immediately evaluated after irradiation by trypan blue assay and cellular viability by MTS assay 24 h after irradiation as described in section 2.2.2. For temperature measurements, a thermocouple was inserted in the wells (in contact with the cell culture medium) before and immediately after visible light irradiation. Cell viability was immediately evaluated by trypan blue assay.

For combined therapy, MCF-7 cells were seeded and incubated at 37°C in the absence or presence of DOX ($3 \mu\text{M}$) for 6 h, after which they were challenged with 15 nM AuNP@PEG ($\epsilon = 2.85 \times 10^{-8}$) for 2h. Medium as washed with phenol red free DMEM and irradiated ($3.44 \text{ W} \cdot \text{cm}^{-2}$ for 60 s as described above). As controls, cells without DOX, without AuNP@PEG and/or irradiation were assessed. Cell viability was evaluated by MTS and trypan blue assays (below) after 16 h. For HCT116, HCT116 DR and Fibroblasts the several formulations were incubated with a cell density of 2×10^4 for 4 h. The medium was replaced by phenol red free DMEM and irradiated ($3.44 \text{ W} \cdot \text{cm}^{-2}$ for 60 s as described above).

5.2.3 Statistics

Statistical significance of all data was verified by One-way ANOVA. The Tukey method allowed to determine statistically significant differences between mono and combined therapeutics. This analysis was performed with GraphPad Prism 6.0 (GraphPad Software, Inc) and results were considered statistically significant for $p < 0.05$. Data are the average of quadruplicated assays and the errors are calculated by the standard error mean.

5.3 Results and discussion

5.3.1 Laser Characterization

Laser irradiation was setup as shown in Fig. 5.2 and the photon flux characterised by actinometry to determine the exact amount of energy being irradiated in each experiment. Aberchrome 540TM is often

used for actinometry studies in the near-UV and visible regions due to its reversible photocyclisation to the deep red cyclised valence isomer 7,7a-dihydro-2,4,7,7,7a-pentamethylbenzo(b)furan-5,6-dicarboxylic anhydride (C-form). When irradiated with UV light E-form turns in C-form, which can in turn be reverted to E-form when irradiated with visible light. For these measurements, Aberchrome 540TM was dissolved in absolute ethanol and irradiated at 342 nm during 1 h until a photo-stationary state corresponding to the maximum conversion into the C-form was obtained. The C-form solution was irradiated using a continuous wave 532 nm green diode-pumped solid-state laser coupled to an optical fibre. The solution exposed to the green laser undergoes back conversion to the E-form and the number of converted molecules was quantified by UV-Vis spectroscopy ($\epsilon=8038 \text{ M}^{-1}\cdot\text{cm}^{-1}$). For the calculation of the photon flux, a photochemical quantum yield of $\phi=0.060$ was experimentally calculated (Fig. 5.3) for the back reaction of C-form to E-form in ethanol. We were able to establish a linear correlation between the laser input current and the amount of energy arriving to the microplate well (Fig. 5.3).

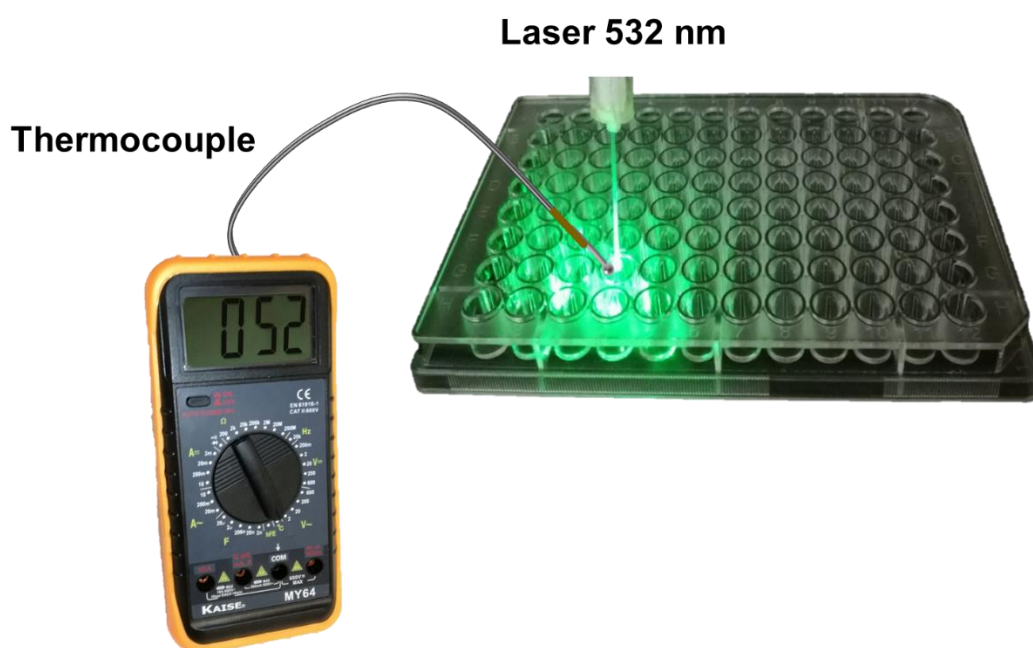


Fig. 5.2 Strategy for assessing efficacy of AuNP based PTT in the visible.

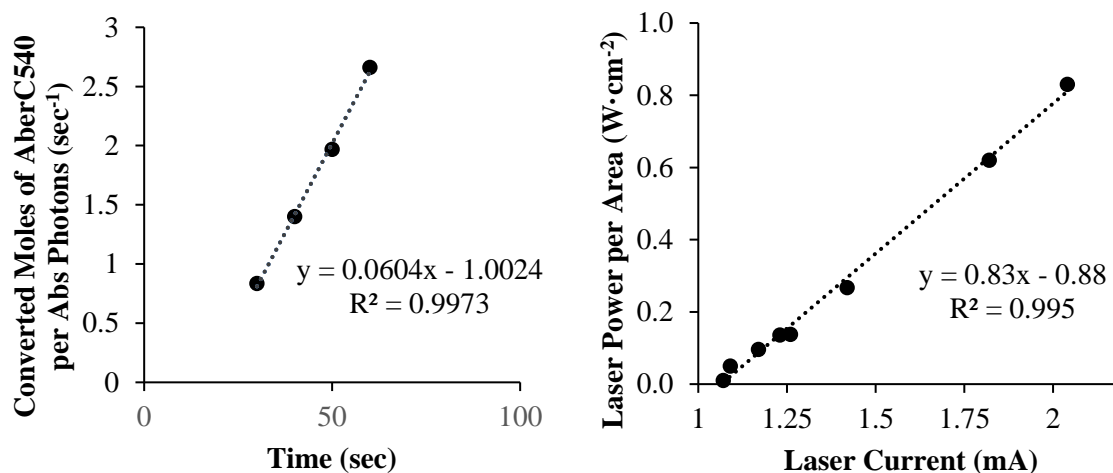


Fig. 5.3 Laser calibration measurements. (Left) AberChrome540 quantum yield of 0.06 defined by the slope of the curve of converted moles of actinometer per absorbed photon of light. (Right) Linear relation between input laser current and light power arriving to the sample.

5.3.2 AuNP@PEG irradiated by laser

AuNP were synthesized and characterized according to section 2.2.6. A maximum absorption peak of 520 nm was observed by UV-Vis, a hydrodynamic diameter of 19 nm by DLS and an average spherical shape of 14 nm diameter by TEM.

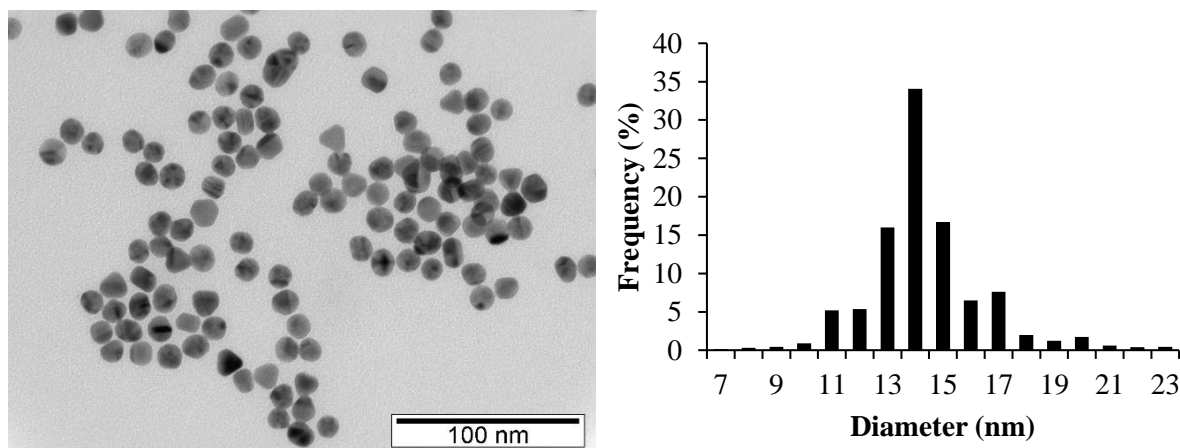


Fig. 5.4 TEM image of spherical citrate AuNP (Left). Histogram of diameter of AuNP centred at 14 ± 0.8 nm diameter (Right).

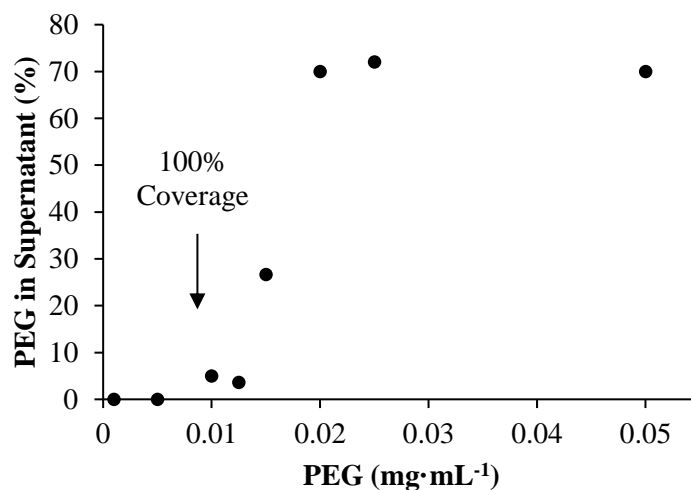


Fig. 5.5 Characterization of PEG functionalization at AuNP surface. Percentage of PEG measured in the supernatant compared with PEG added to the AuNP.

AuNP@PEG were further synthesized with increasing concentrations of PEG. The PEG coverage on the AuNP' surface was evaluated by Ellman's Assay. The concentration of 0.01 mg·mL⁻¹ of PEG was defined as 100% coverage, since it was the first concentration where PEG was detected in the supernatant (Fig. 5.5). It is noteworthy that the same concentration had been determined in section 4.2.3 in Fig. 4.5. To determine the capacity of AuNP@PEG to generate heat upon irradiation, we irradiated increasing concentrations of AuNP@PEG in water and measured the variation in temperature with a thermocouple. The observed increase in temperature, showed the photothermal capacity of 14nm diameter AuNP. We then determined the total heat (Q) generated per assay upon irradiation using

(

Equation 5.1. The variation in temperature (ΔT) was calculated by subtracting the final temperature to the initial temperature in each nanoparticle assay, minus the variation in temperature for irradiating only water. The thermal capacity of water 4.18 J·g⁻¹·K⁻¹ (q), and the irradiated mass (m) of 0.2 g were used. Thus, we have only the heat generated by the AuNP irradiation (Fig. 5.6). The number of nanoparticles was calculated by using beer lambert law with an $\epsilon = 2.85 \times 10^{-8} \text{ M}^{-1} \cdot \text{cm}^{-1}$ at 520 nm for 14 nm nanoparticles according to Navarro et. al [430] and Avogadro number. Then, by dividing the total heat generated per assay by the number of particles and by the irradiation time (60s) we obtained a photothermal power of $7.1 \times 10^{-13} \text{ W}$ per particle (Fig. 5.7 left).

$$Q = q \times \Delta T \times m \quad (\text{Equation 5.1})$$

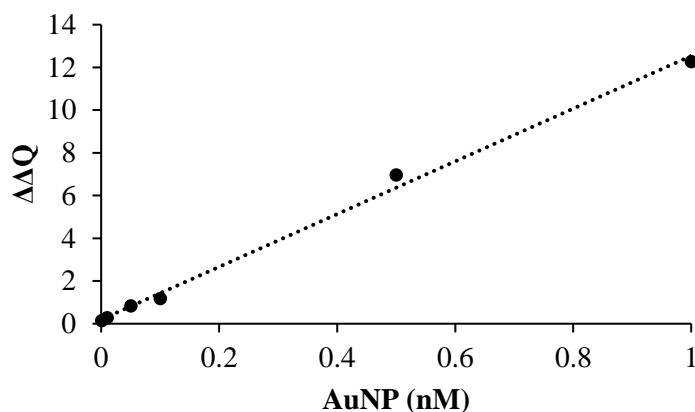


Fig. 5.6 Heat capacity of AuNP. The heat generated by the particles upon irradiation was calculated using the Equation 5.1.

However, this value is dependent on the irradiation power, therefore not comparable with other photothermal capacitors or laser intensities. We then calculated the photothermal efficiency of the nanoparticles by dividing the generated heat energy by the absorbed light energy. The generated heat was calculated using the (

Equation 5.1 as previously described. The light energy that gets to each sample solution is equal to the number of photons arriving during irradiation, multiplied by the energy of each photon. However not all the energy that arrives to the samples is absorbed. However, from the irradiated light, only a fraction is absorbed. To calculate amount of energy that was absorbed we first determined the absorbed intensity (I_A), using the equation (

Equation 5.2. The intensity absorbed fraction of laser (I_A) can be calculated, where I_0 is the irradiated intensity of the laser source and A is the absorption at irradiated wavelength.

$$I_A = I_0 \times (1 - 10^{-A}) \text{ (Equation 5.2)}$$

An efficiency of 77 % of photothermal conversion was determined (Fig. 5.7 right), which is in concordance with previous studies that projected an efficiency of 78 % for citrate capped 15.7 nm AuNP [431]. This shows that 14 nm AuNP are indeed strong visible light absorption agents capable to generate heat in a precise zone, and thus have a great potential to be applied in hyperthermia regimens [299, 413, 424, 432].

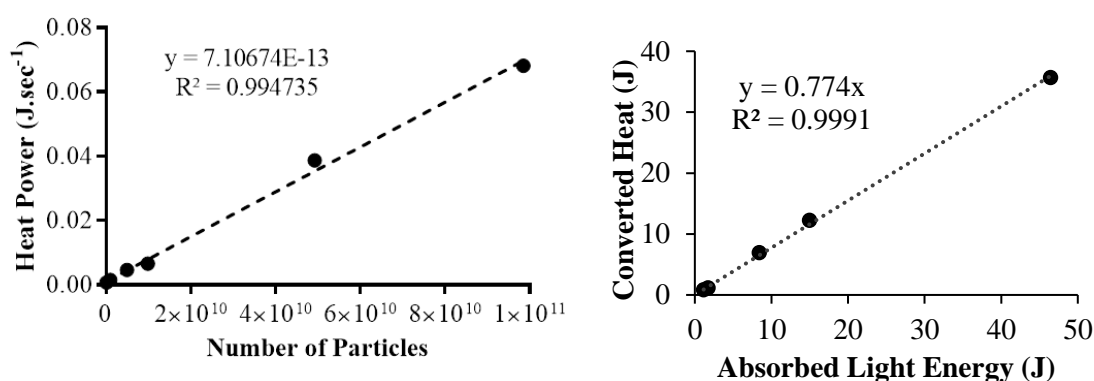


Fig. 5.7 Characterisation of Photothermal Effect of Gold Nanoparticles. (Left) Heat generated per second in function of number of particles irradiated. Several concentrations of AuNP were irradiated at $1.7 \text{ W}\cdot\text{cm}^{-2}$ for 60s and the temperature variation was measured. The slope of the curve gives the heat generated per nanoparticle per second. (Right) Photothermal efficiency of AuNP 14 nm.

To resemble more a biological environment, we also irradiated AuNP@PEG in PBS 1×, an isosmotic buffer that mimics the pH and ionic strength of biological fluids, instead of water. Surprisingly as temperature rose, AuNP spectrum red shifted, indicating aggregated nanoparticles. After a few minutes, the solution turned red again showing that this aggregation was reversible (Fig. 5.8 inset). To understand if this phenomenon was light dependent or temperature dependent, we exposed an AuNP solution with PBS to increasing temperature in a Peltier cell. We observed that specially around 80°C, the spectrum started to red shift, with a maximum absorption peak at 730nm, at 100°C (Fig. 5.8). After cooling down the solution, the same reversibility was observed. Meaning that the aggregation was temperature dependent, not light dependent.

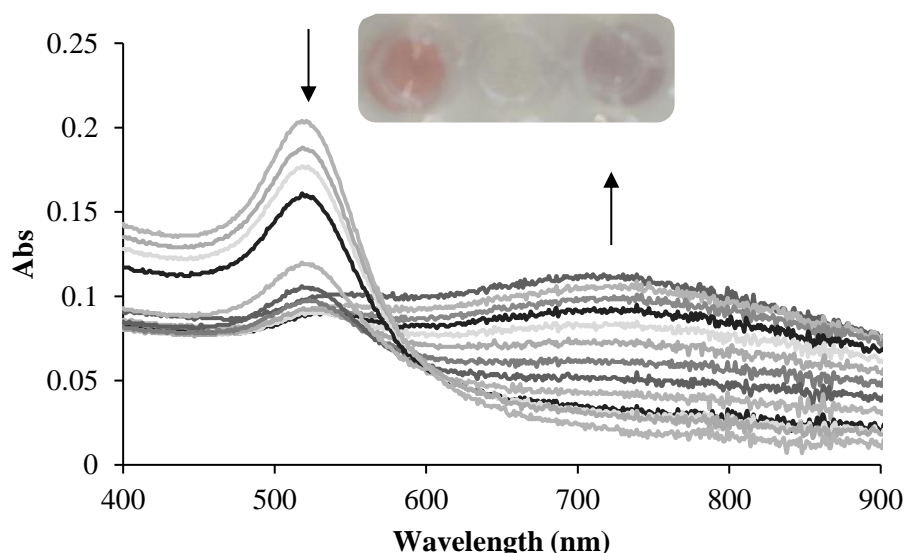


Fig. 5.8 AuNP@PEG UV-Vis variation with temperature increase. The red shift in nanoparticle absorption indicates nanoparticle aggregation. Inset it is a photo of irradiated particles for 1 min $3.44 \text{ W}\cdot\text{cm}^{-2}$ (right) (100°C) and particles irradiated at the same condition, after 10 min (left) (20 °C).

We also looked at the solution side scattering (90°) during temperature increase in PBS $1\times$. An increase in scattering is observed with the increase in temperature, reinforcing AuNP aggregation (Fig. 5.9 Left). With the system cooldown the side scattering decreases but not to the same values as before, indicating that some particles remain aggregated and the system is not totally reversible (Fig. 5.9 Right).

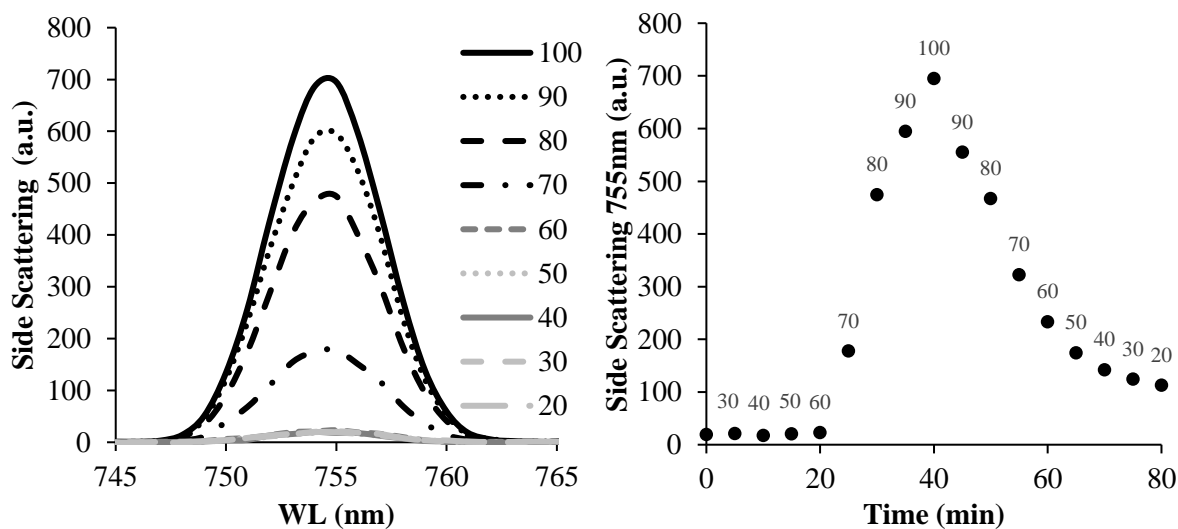


Fig. 5.9 AuNP side scattering in PBS $1\times$ and increased temperature. (Left) The side scattering at 90° was measured indicating AuNP aggregation with increase in temperature. (Right) After system cooldown the scattering decreased. The values on top represent the temperature of the system in $^\circ\text{C}$.

To investigate the effect of salt in solution, we added to the AuNP@PEG to PBS $2\times$ and $10\times$ and increased the temperature. We observed that the temperature needed to aggregate the particles decreased with the increase in ionic strength (Fig. 5.10).

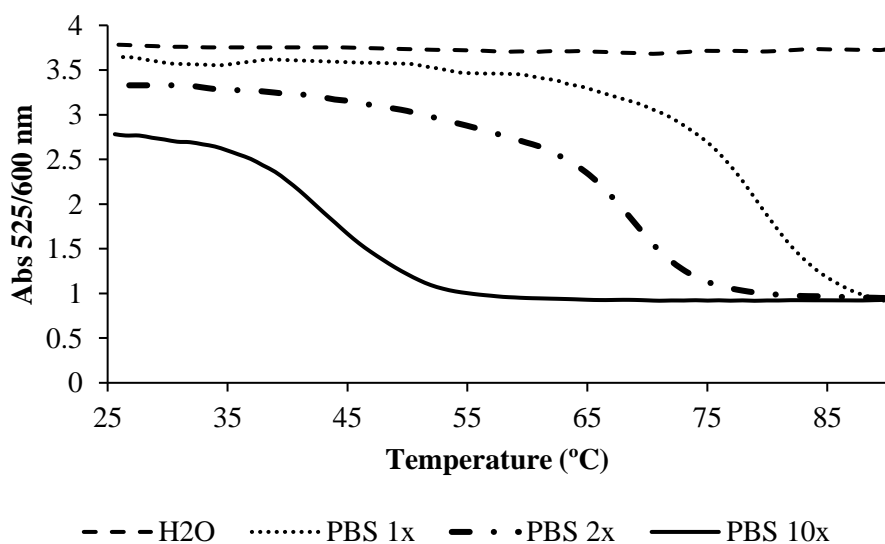


Fig. 5.10 AuNP@PEG aggregation profile at different temperatures and ionic strength. It is observed a decrease in the temperature needed to aggregate the particles with increasing ionic strength.

AuNP@citrate are known to aggregate with the addition of ions to solution due to creation of momentary dipoles at the surface of the particles [433]. PEG confers stability to the nanoparticles by creating steric hindrance with the increase in ionic strength, not allowing the AuNP to approximate. This aggregation phenomena suggest that the PEG structure collapses with the increase in temperature. This collapse is described for thermo responsive polymers [434, 435], but it was never described for this type of PEG. We believe that, PEG chains create Van-der-Wall bridges with the solvent keeping it in a strait conformation, when temperature increases these bonds are broken, leading to the collapse of PEG structure, and reduce its ability to create steric hindrance. When no salt is present in solution, the PEG ‘shrinks’ with the increase in temperature, and stretches again with the decrease in temperature but the particles remain disperse, as no force is promoting their aggregation. However, in the presence of salt, it generates particle dipoles strong enough to promote aggregation and the plasmon coupling. When PEG stretches the interparticle distance is higher, hindering the plasmon coupling. Interestingly we tested the aggregating conditions with nanoparticles functionalized with a similar PEG but this time with a carboxylic group in the end. In that case no aggregation was observed, not even at 100 °C at 10× PBS. When we reduced the pH to 3 at PBS 1×, 100 °C we observed nanoparticle aggregation. This can be explained since at pH 7 most carboxyl groups will be deprotonated conferring charge to the particles and promoting AuNP repulsion and dispersion. Only at pH 3 when the carboxyl groups are protonated, the particles can aggregate. These findings are relevant to understand the stability of these AuNP constructs when irradiated inside cells.

5.3.3 Photothermal Therapy induced by visible irradiation on AuNP in cells

To assure reproducibility in our experiments, to irradiate our samples in the same spot, with the same distance, we designed a manual plate mover that was further 3D printed in plastic PLA (Fig. 5.11D). It was placed inside a laminar flow chamber to avoid microbial contamination of animal cell cultures. An optic fibre was coupled to the laser source (Fig. 5.11A), a thermocouple was added to the system to measure temperature variations (Fig. 5.11B) and an infrared camera (Fig. 5.11C). Manual plate mover blueprints are represented in Fig. A.1 and Fig. A.2.

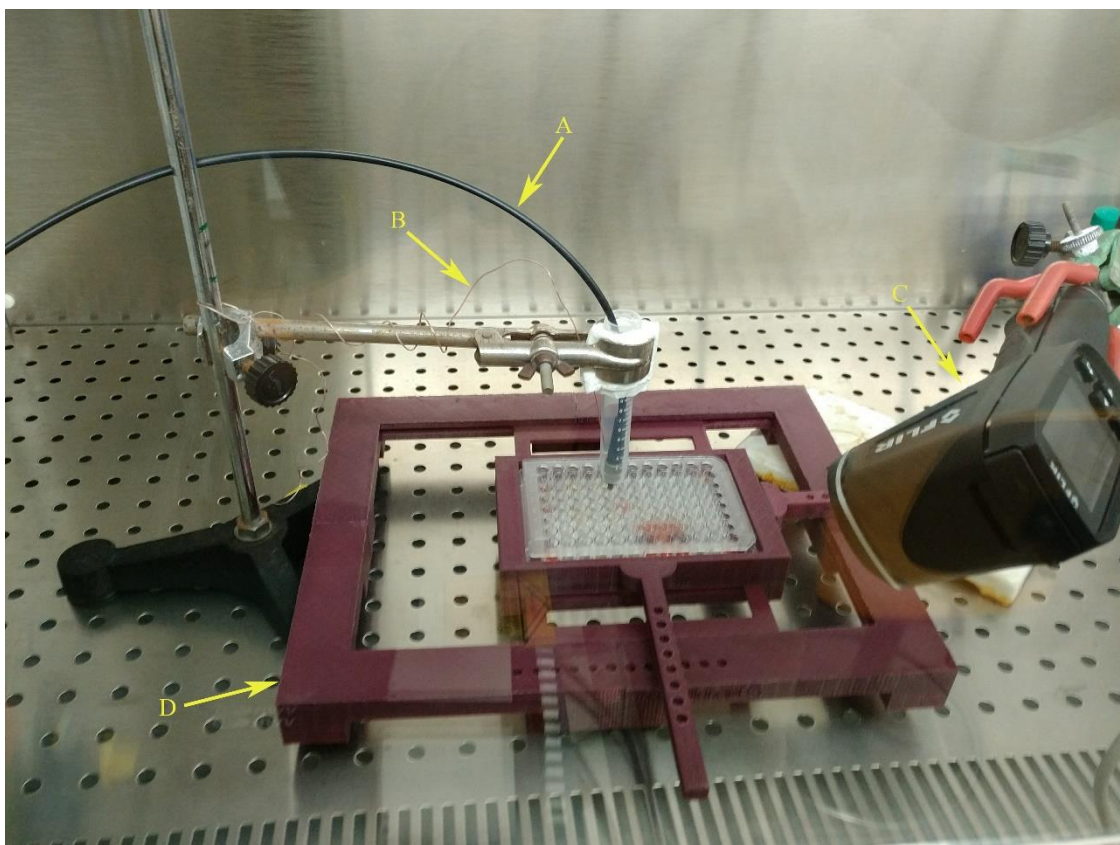





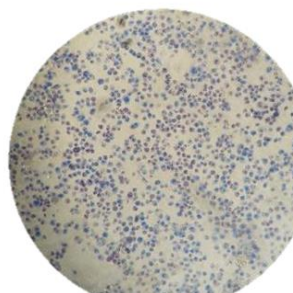

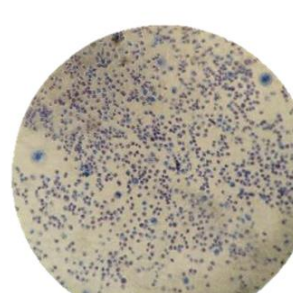
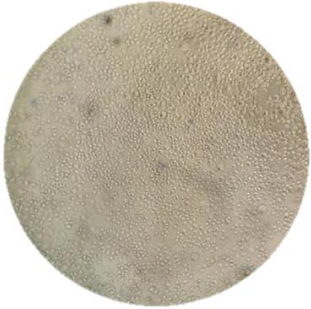
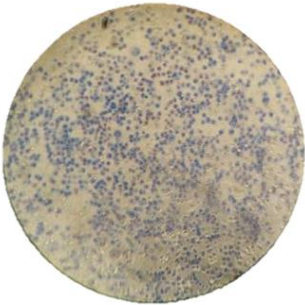

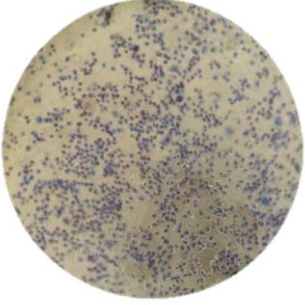

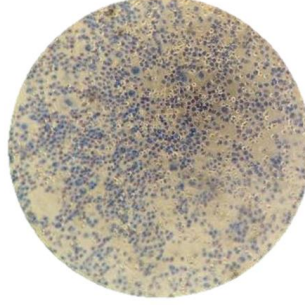

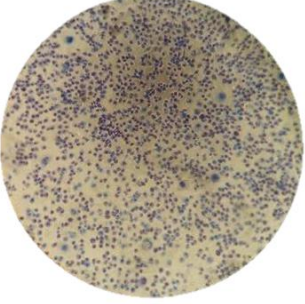


Fig. 5.11 Photograph of laser irradiation setup. (A) optic fibre (B) thermocouple (C) infrared camera (D) manual plate mover

To understand the effect of irradiation of AuNP within cells, MCF-7 breast adenocarcinoma cells were incubated with AuNP (15 nM) for 2 h and irradiated at different exposition times and intensities. The initial and final temperature was measured and trypan blue assay (section 2.2.2.2) was performed following irradiation. In the absence of AuNP and for all irradiation conditions, no trypan blue staining was observed despite an increase of the medium temperature, indicating that the membranes were intact and that cells were not affected by the laser. Some reports suggest that, at 40°C, cells are thermosensitive and their membranes ought to suffer permeability changes [175]. However, in our case, no damage of cell membranes was observed for all the exposure times and laser potencies, probably due to the transient nature of the temperature increase. Conversely, irradiation in presence of AuNP, cells showed a strong compromise to cell membranes (Table 5.1). Because the AuNP are inside, or at the membrane of cells when irradiation occurs, the intracellular surge in temperature strongly impacts cell membrane integrity. It seems that a minimum final temperature of 52°C is needed to damage the cellular membrane, since trypan blue only stained cells exposed to above temperatures. A laser potency of $3.44 \text{ W}\cdot\text{cm}^{-2}$ for 60 s was chosen for the subsequent cell assays relying on the highest temperature reached for cells irradiated with AuNP ($\Delta T 12 \text{ }^\circ\text{C}$) compared to cells irradiated without nanoparticles.

Table 5.1. Optimization of AuNP-induced PTT. MCF-7 Images of irradiated cells without AuNP and with AuNP under different laser intensities and exposure times. In all condition's cells were incubated with Trypan Blue dye for 10 min and pictures were taken right after in bright field (400× objective) using an inverted microscope. Final achieved temperatures are indicated at the bottom right in each picture.

Intensity - Time (total energy)	Cells	Cells + AuNP@PEG
3.99W·cm ⁻² 30s (33.7J)	 42°C	 50°C
2.37 W·cm ⁻² 60s (47J)	 38°C	 43°C
3.44W·cm ⁻² 60s (51.1J)	 40°C	 52°C
3.99W·cm ⁻² 60s (67.3J)	 48°C	 58°C

<p>2.9W·cm⁻² 90s (67.6J)</p>	 <p>43°C</p>	 <p>52°C</p>
<p>3.44W·cm⁻² 90s (67.6J)</p>	 <p>48°C</p>	 <p>56°C</p>
<p>2.37W·cm⁻² 120s (93.8J)</p>	 <p>43°C</p>	 <p>55°C</p>
<p>2.9W·cm⁻² 120s (114.8J)</p>	 <p>46°C</p>	 <p>58°C</p>

We tested similar conditions with HCT116 colorectal carcinoma cells. They were incubated with 8.2 nM of AuNP@PEG and irradiated for several exposure times after medium replacement ($3.44 \text{ W}\cdot\text{cm}^{-2}$) and the results were compared with irradiated HCT116 cells not exposed to the nanoparticles. Cells without AuNP@PEG were not affected by irradiation for all tested exposure times, whereas cells harbouring AuNP@PEG showed increased membrane permeability by trypan blue assay for exposure times of more than 60 s (Fig. 5.12).

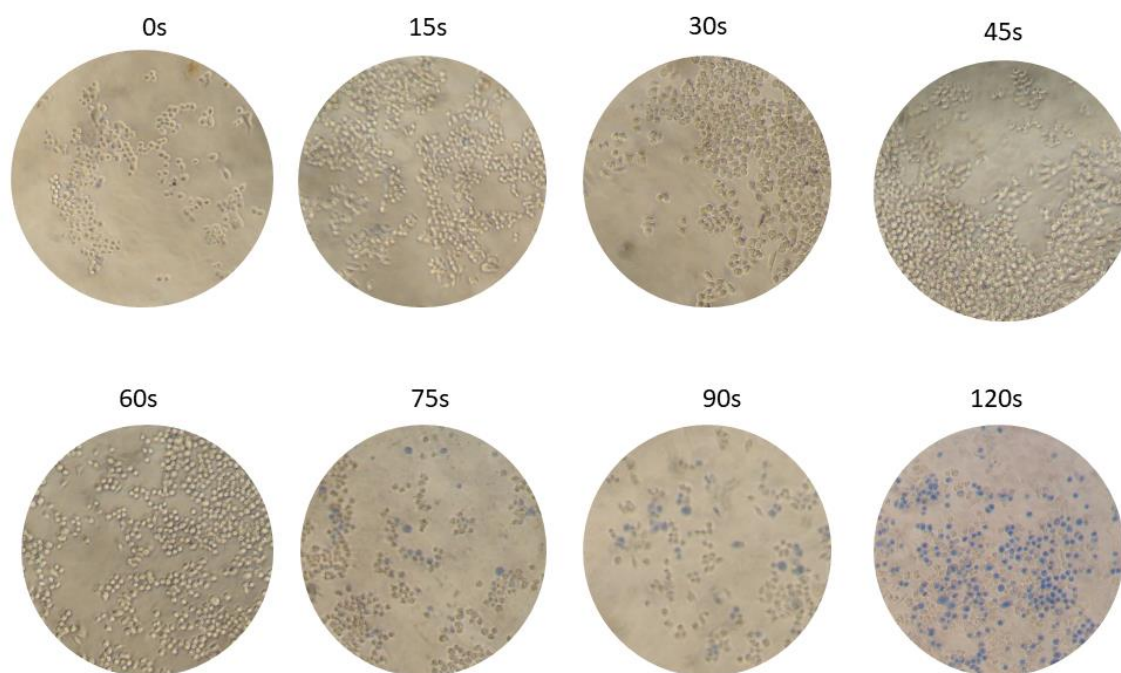


Fig. 5.12 Trypan blue assay of HCT116 cells irradiated with green laser. Cells were incubated with 8.2 nM AuNP@PEG for 4 h and medium was replaced. Later, they were irradiated with a power of $3.44 \text{ W}\cdot\text{cm}^{-2}$ for different exposure times and trypan blue assay was performed. Cells stain with trypan blue for exposure times greater than 60 s.

To assess how cell viability was affected by irradiation, we performed an MTS assay with and without AuNP at different exposure times, 24 h after irradiation. In contrast, with trypan blue results, for an irradiation time of 90 s, in the absence of AuNP, a decrease of viability was observed. For cells incubated with AuNP, the loss of cell viability starts much earlier, with only 45 s of exposure (Fig. 5.13). The reduction in viability of cells without AuNP might be explained due to the excitation at 532 nm of the cytochrome c [436–438], thus compromising mitochondrial activity and not affecting membrane integrity. In the case of cells with AuNP, loss of cell viability may be due to localized heat at the membrane, destabilizing the lipid bilayer, and permeabilizing it [439]. Also, endoskeleton damage is likely to happen, since it is where AuNP are mostly located at 4 h as seen in section 4.3.3. [440]. Interestingly, when this irradiation procedure was performed with HCT116 DR an increased sensitivity to AuNP' irradiation compared with HCT116 was observed. After 90 s of irradiation the percentage of

cell death was 91 % compared with 66 % for HCT116 (Fig. 5.14). However, HCT116 DR seem to be less sensitive to laser alone when compared with HCT116. These can be explained if by the Warburg effect which is associated with acquired drug resistance. With reduced mitochondrial activity, irradiation alone has less impact on these cells. Together these results demonstrate that irradiating ~14 nm AuNP@PEG with a green laser promotes a photothermal injury in different type of cancer cells, particularly improving cell injury in DOX resistant colorectal carcinoma cell line.

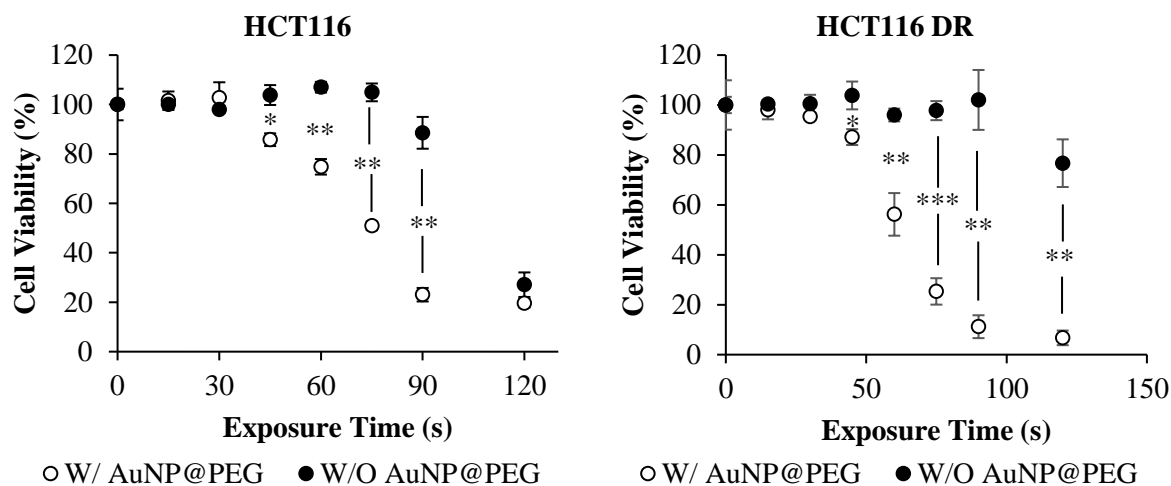


Fig. 5.13 Cell viability of HCT116 exposed to AuNP@PEG and Laser. (Left) HCT116 and (Right) HCT116 DR irradiated with a power of $3.44 \text{ W}\cdot\text{cm}^{-2}$ with (White) and without (Black) previous 4 h exposure to 8.2 nM of AuNP@PEG. MTS assay was performed 24 h after irradiation.

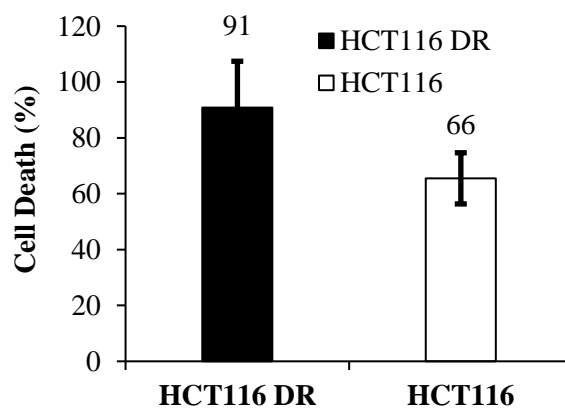


Fig. 5.14 Reduction in cell viability by MTS of HCT116 DR and HCT116 exposed to 8.2 nM of AuNP and irradiated with $3.44 \text{ W}\cdot\text{cm}^{-2}$ for 90 s normalized to the same irradiation without AuNP.

To further understand if this approach could be translated to a 3D model of cell culture, we tried to irradiate cells embedded in a calcium alginate matrix. HCT116 DR cells were grown in this hydrogel for 24 h and then incubated with AuNP@PEG for 4 h. After medium replacement the hydrogel was irradiated for different exposure times at $3.44 \text{ W}\cdot\text{cm}^{-2}$. We observed that the AuNP could internalize the alginate matrix and stayed inside for several minutes after washing (Fig. 5.15 Right). An increase in final temperature of the media was achieved, $67 \text{ }^\circ\text{C}$ in alginate beads compared with $53 \text{ }^\circ\text{C}$ in

monolayer. Cell viability assays with alginate beads revealed an increase standard error, this can be due to the increased complexity of a 3D model, which is more variable than monolayer, also because the alginate bead is not fixed in the middle of the well, partially missing the laser beam. Cells showed to be more sensitive to 60s irradiation in the 3D model (23% of cell viability) than in monolayer (56% of cell viability) (Fig. 5.13 Right and Fig. 5.15 Left). The confinement of the cells in a smaller area, compared with 2D model, also favours the concentration of heat. This result indicates that irradiating tumours with accumulation of nanoparticles is a promising strategy to destroy tumours.

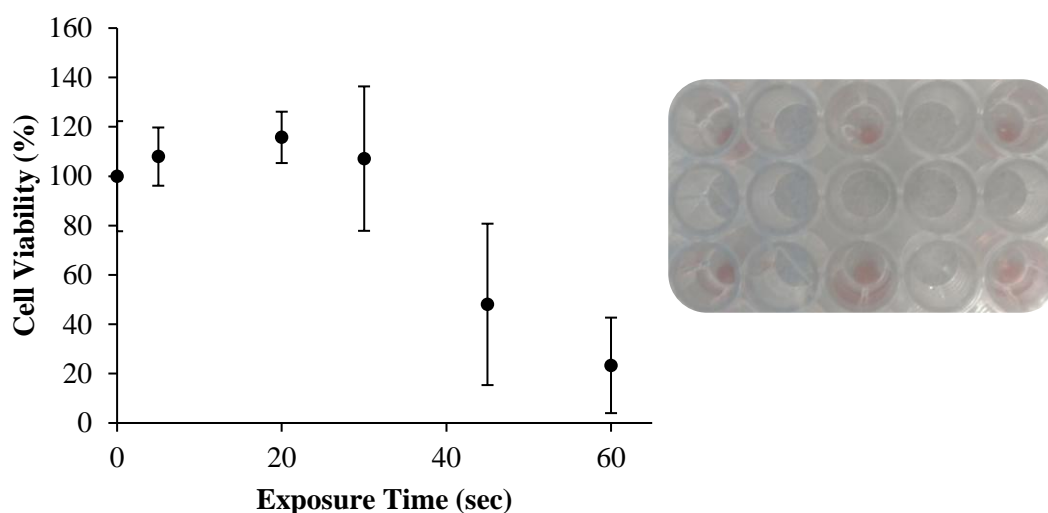


Fig. 5.15 Irradiation of HCT116 DR in a 3D model of alginate. (Left) Cell viability of HCT116 DR exposed to 8.2 nM AuNP@PEG for 4h and later laser irradiation with $3.44 \text{ W} \cdot \text{cm}^{-2}$. MTS assay was performed 24 h after irradiation. (Right) Alginate beads with HCT116 DR, after exposure with AuNP@PEG for 4 hours and medium replacement.

5.3.4 Combined photo-chemotherapy Therapy

DNA repair processes, which are crucial for the cell's response to aggression by cytotoxic drugs, are temperature dependent. As such, hyperthermia enhances the cell killing efficacy of antitumor drugs that rely on DNA damage [175, 426]. DOX is one of the most widely used anticancer drugs, particularly against breast cancer [441]. As such, with the aim of improving DOX efficiency against cancer cells, we combined DOX and hyperthermia with AuNP as heat-generator following irradiation with visible light. MCF-7 cells were exposed to $3 \mu\text{M}$ DOX for 6 h, and then incubated in presence or absence of AuNP and irradiated as depicted in Fig. 5.16. Cells challenged with DOX alone or DOX plus laser irradiation showed no staining with trypan blue (Fig. 5.16b and c), indicating that the membrane was still intact, since there was no heat shock. However, when cells are challenged with DOX plus AuNP, and laser irradiation is performed, almost all cells show clear signs of losing cell integrity (Fig. 5.16d). The combined effect of AuNP coupled to green laser irradiation and chemotherapeutic drug was further evaluated by the MTS assay. Cells exposed to laser only or AuNP only, show no decrease in cell viability. The combined therapy leads to loss of viability of 58% of cancer cells with an increase in

temperature of 22 °C. For DOX or photothermal alone, we observed a reduction of cell viability of 25% and 42%, respectively (Fig. 5.17). DOX irradiated with laser shows a synergistic reduction of 46% in cell viability with an increase of 11°C. These data are in accordance with previous reports that highlight DOX's increased toxicity at higher temperature in a trigger-dependent manner. This enhanced effect of DNA-damage has been attributed to a slowdown of the replication fork, leading to double strand breaks formation, which reduces cell survival [426]. Our combined strategy achieved the higher temperature and showed higher reduction in cell viability.

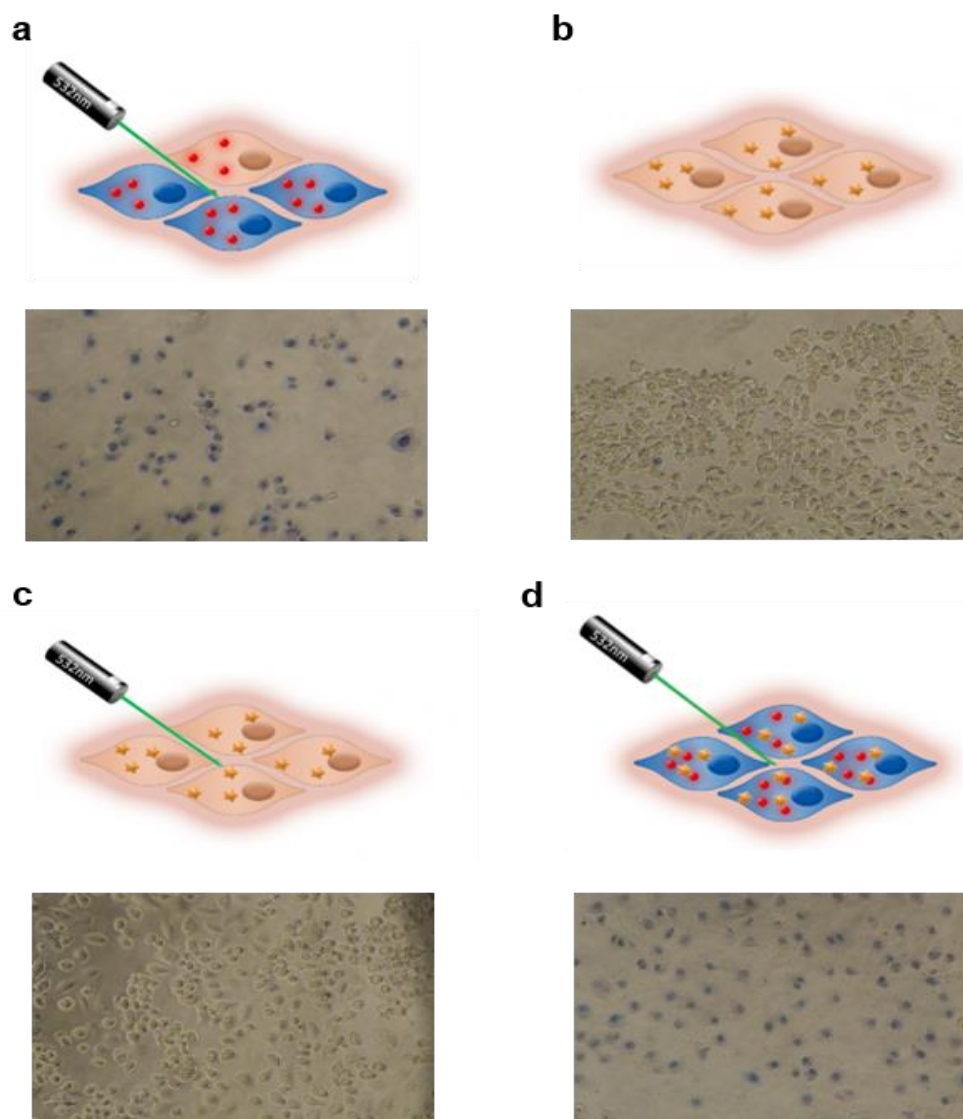


Fig. 5.16 Combined chemo and PTT induced by visible light and AuNP as photothermal agent. Schematic representation (above) and respective image after cell staining with trypan Blue (800×) (below). Cells were (a) exposed to AuNP (15 nM) and irradiated; challenged with DOX (3 μ M) for 6 h (b) without or (c) with laser irradiation; or (d) combined DOX with AuNP and irradiation. Cells were incubated with trypan Blue dye for 10 min, 16 h after laser irradiation. Images acquired in bright field using an inverted microscope.

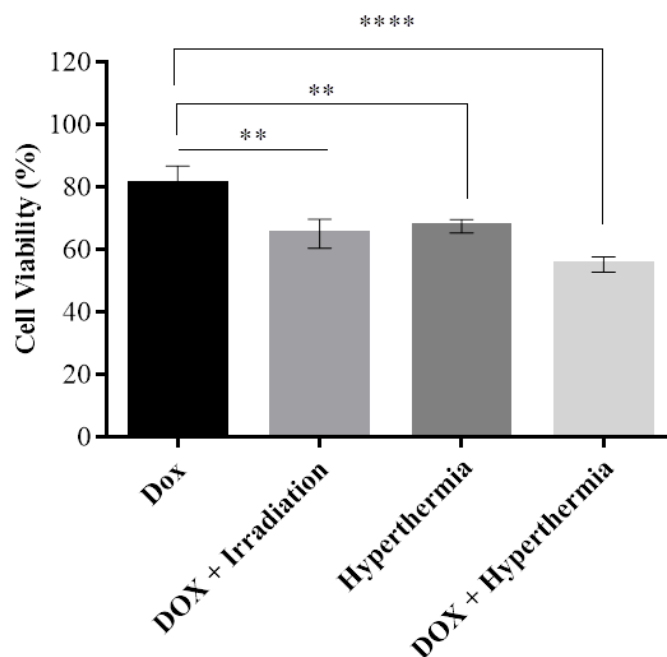


Fig. 5.17 Cell viability via the MTS assay in MCF-7 cells 16 h after combined therapy with DOX and AuNP induced PTT. Cells were incubated in DMEM supplemented with DOX (black bar); combination of DOX plus laser irradiation (light grey bar) ($p = 0.0016$); incubation with AuNP + Laser irradiation (dark grey bar) ($p = 0.0002$); or combined DOX + Laser irradiation with AuNP (white bar) ($p < 0.0001$). Cell viability of mono- and combined therapies normalised to the respective controls (not irradiated + 0.2 % DMSO), which were set to 100 %. Data are the average of quadruplicated assays and error bars correspondent to SEM (** $p \leq 0.01$, **** $p \leq 0.0001$).

Proven the efficacy of combining DOX with irradiation we wanted to evaluate the efficacy of our combined approach against cancer cells resistant to traditional chemotherapy. To achieve this we used CoD, a compound from the same family of the previously studied in chapters 3 and 4 but with a cobalt metal centre instead of zinc metal centre. This compound has been previously studied by our group with similar results to ZnD [393]. We assessed its cytotoxicity in HCT116 DR cells aiming to chemically circumvent DOX resistance in these cells. As such, we determined the relative IC_{50} of CoD in HCT116 DR and compared it to the normal HCT116 (DOX sensitive cells). After 24 h exposure, the relative IC_{50} of CoD in HCT116 DR and HCT116 was 0.14 and 0.13 μM , respectively. These data clearly show that as ZnD (Table 3.1), CoD is highly effective (within very low micromolar range IC_{50}) against a cancer cell line resistant to a first line chemotherapeutic – DOX. The effect of CoD in presence of tariquidar was also evaluated, which showed no difference in the IC_{50} , i.e. CoD effect is not affected by efflux pump activity (Table 5.2). Together, these data show that CoD might be used to tackle DOX resistance in colorectal carcinoma cells.

Table 5.2 Values for the relative IC₅₀ of HCT116 and HCT116 DR after 24 h exposure to DOX, CoD and their individual combination with tariquidar (inhibitor). Concentrations are expressed in μM.

Cell Culture	DOX	CoD	DOX + Inhibitor	CoD + Inhibitor
HCT116	0.38 ± 0.04	0.13 ± 0.01	0.38 ± 0.03	0.12 ± 0.01
HCT116 DR	> 6	0.14 ± 0.02	0.81 ± 0.06	0.15 ± 0.04

We then combined CoD and irradiation using AuNP to increase killing of drug resistant cancer cells without affecting normal cells. For that, we coupled CoD with AuNP in a similar process that ZnD (see methods section 4.2.1 and 4.2.3 and [393]) naming the formulation NanoCoD. The nanoformulation was characterized by UV-Vis absorption spectrum, with the maximum peak shifting to the red, indicating functionalization (Fig. 5.18). Nanoformulations were also characterized by DLS, showing increased hydrodynamic diameter with consecutive functionalization layers. That the hydrodynamic diameter of AuNP@PEG@BSA and NanoCoD seems to decrease upon functionalization but we believe that the diameter is actually very similar, and the standard error gives the false impression of decrease (Table 5.3). To determine proportion of each component in the nanoformulation, supernatants were measured. For PEG Ellman's assay was performed, for BSA Pierce method was used, and for CoD we did ICP-MS. By subtracting the amount detected on the supernatant to the added amount, we obtained the results summarized in Table 5.4.

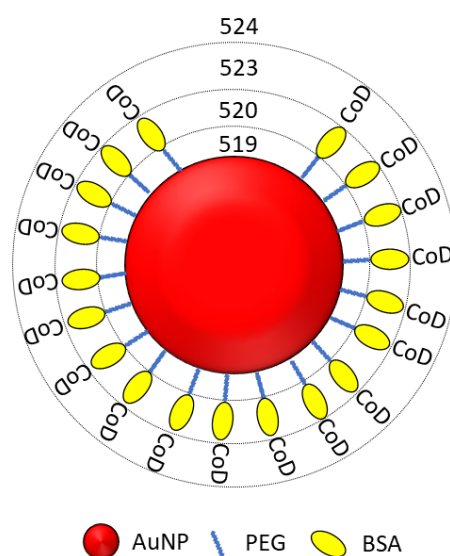


Fig. 5.18 AuNP construct with several functionalization layers: 1st PEG, 2nd BSA, 3rd CoD compound. The numbers represent the maximum absorption peak after each functionalization step. A red shift is observed after each functionalization step.

Table 5.3 Characterization of AuNP by Dynamic Light Scattering and Zeta Potential

	DLS		Zeta	
	Average (nm)	St Dev	Average (mV)	St Dev
AuNP	19.2	0.7	-60.1	2.1
AuNP@PEG	18.6	2.8	-74.9	2.9
AuNP@PEG@BSA	82.4	28.7	-14.8	3.9
NanoCoD	72.0	12.7	-21.1	2.2

Table 5.4 Characterization of NanoCoD.PEG was calculated using Ellman's assay to measure thiols in the supernatant. BSA was calculated using Pierce assay to measure protein in the supernatant. CoD was calculated by ICP-MS of Co in the supernatant.

Conjugate per AuNP	Average	St Dev
PEG	2320	280
BSA	6	2
CoD	186	23

We then incubated HCT116, HCT116 DR and fibroblasts (normal cell line) with NanoCoD (0.7 nM AuNP) corresponding to the IC_{50} of free CoD. Data show a 20 % reduction in cell viability for colorectal carcinoma cell lines – DOX sensitive and resistant (Fig. 5.19), and no significant reduction in fibroblasts (Fig. 5.20). This illustrates the higher cytotoxicity of this nanoformulation to cancer cells with limited toxicity to normal cells. Cells were then exposed to NanoCoD for 4 h with subsequent irradiation for 60 s at $3.44 \text{ W} \cdot \text{cm}^{-2}$ with the green laser. Despite that, a temperature increase of $\sim 5 \text{ }^\circ\text{C}$ was observed for all culture media, but only HCT116 DR suffered a significant decrease in cell viability (61 % reduction), corroborating that his cell line is more sensitive to a raise in temperature.

To escalate the photothermal effect, we increased the concentration of AuNP in the media. To warrant that, the concentration of CoD remains constant, a mix of NanoCoD and AuNP@PEG was prepared at a final concentration of 8.9 nM AuNP and added to the cell culture. Following irradiation, we attained a raise of $\sim 12 \text{ }^\circ\text{C}$ for all cell lines, resulting in a reduction of cell viability of $\sim 63 \text{ } \%$ for HCT116/HCT116 DR and 31 % for fibroblasts. This increase in temperature largely increased cell death of HCT116, without significative increment to HCT116 DR, where irradiated NanoCoD alone represented 61% of cell death (Fig. 5.19).

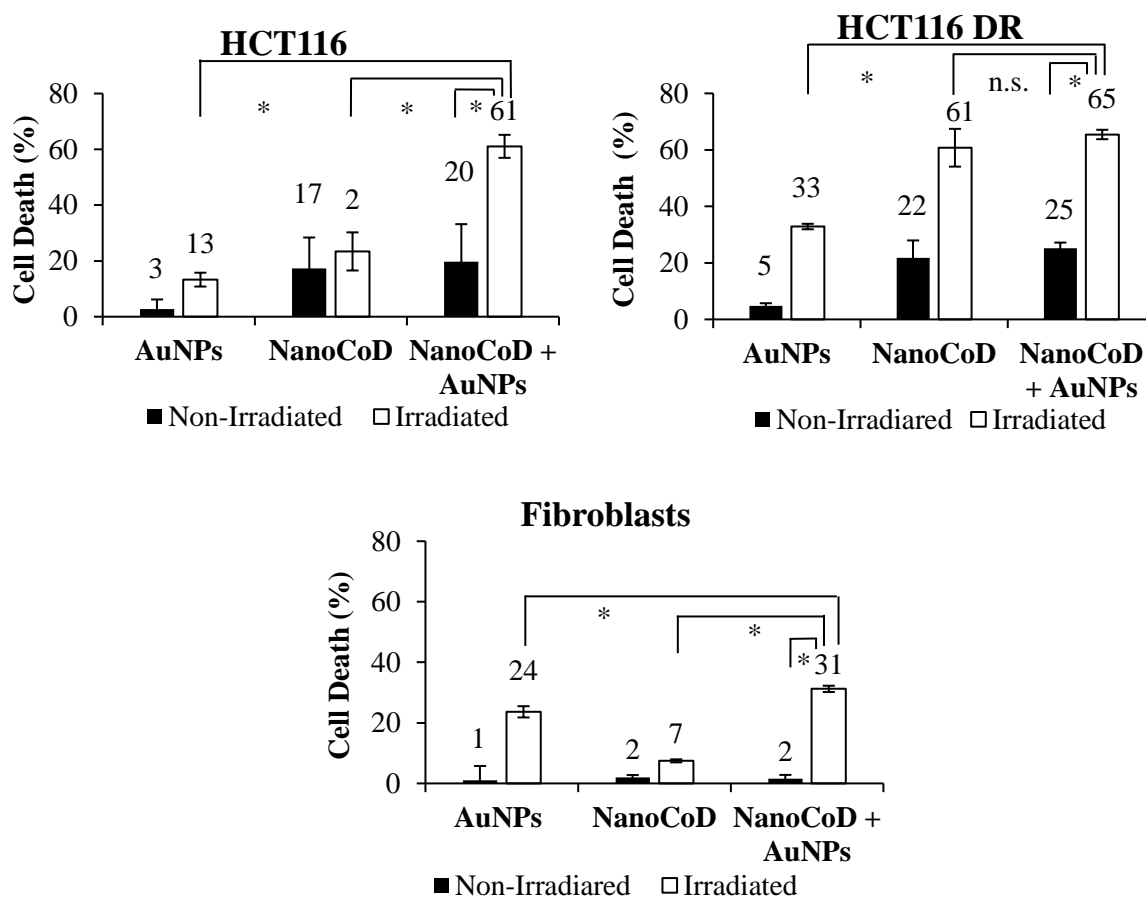


Fig. 5.19 Cell death induced by the combined AuNP@PEG based phototherapy and CoD.Reduction in cell viability of HCT116 (Top Left) HCT116 DR (Top Right) and Fibroblasts (Down) exposed to different formulations for 4 h. The concentration of AuNP is 8.2 nM. The concentration of NanoCoD is 0.7 nM of nanoparticles equivalent to the IC₅₀ of CoD free at 24 h. Irradiated cells were exposed to 3.44 W·cm⁻² for 60 s. MTS assay was performed 24 h after irradiation. Data are the average of at least three independent assays and error bars correspondent to standard deviation.

When we look at HCT116 DR irradiated with CoD Free it is interesting to note that it has a decrease in cell viability of 54% (Fig. 5.20). This result might be explained by the higher sensitivity of these cells to temperature. Possibly, even the increase of temperature of ~3°C of laser alone, has a synergic effect with CoD, that is not observed with hyperthermia or chemotherapy alone. It is important to note that chemotherapy has a systemic administration, and fibroblasts did not show toxicity with NanoCoD without irradiation. Although cell death is observed in fibroblasts when irradiating AuNP and NanoCoD + AuNP we should not forget that irradiation can be very precise, irradiating only desired tissues, thus fibroblasts should not be irradiated in the combined therapy. Together these results demonstrate the additive effect of CoD and phototherapy that allows to kill HCT116 cells and HCT116 DR with the same efficacy. Since fibroblasts are less sensitive to temperature variation, this approach is highly selective towards cancer cells.

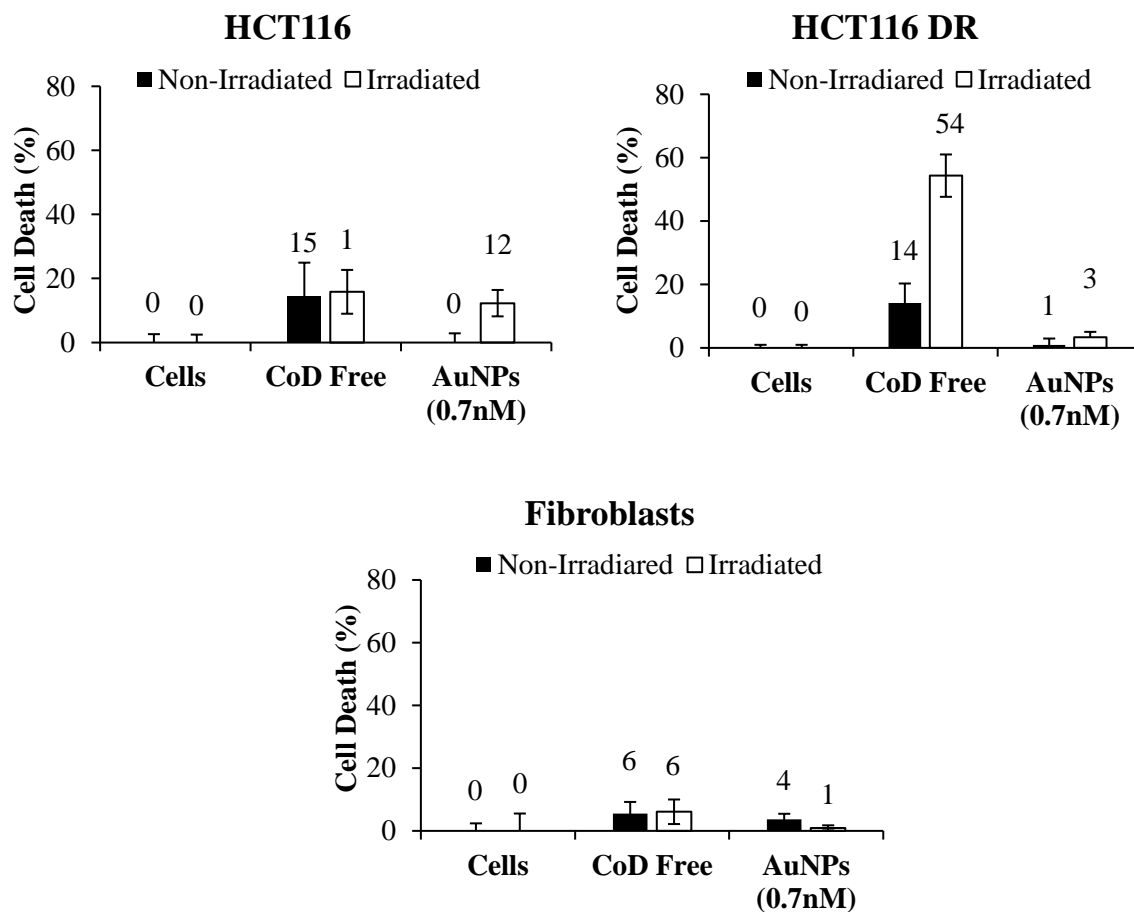


Fig. 5.20 Cell death induced by AuNP@PEG and CoD. Reduction in cell viability of HCT116, HCT116 DR and Fibroblasts exposed to different formulations for 4 h. The concentration of AuNP is 0.7 nM, which is the equivalent to the AuNP concentration of NanoCoD. The concentration of CoD Free is the IC₅₀ at 24 h. Irradiated cells were exposed to 3.44 W·cm⁻² for 60 s. MTS assay was performed 24 h after irradiation. Data are the average of at least three independent assays and error bars correspondent to standard deviation.

5.4 Conclusions

Several studies have highlighted the potential use of nanomaterials for hyperthermia approach against cancer cells. Most of these reports have focused on the use of NIR to raise the temperature locally and, thus, induce cell death in a controlled way. However, despite the higher light to heat conversion of visible light upon irradiation of spherical 14-20 nm AuNP, visible light irradiation for PTT has been neglected. In fact, only but a few reports describe the use of visible region lasers for cancer treatment, despite its extensive medical applicability [442–444]. In this chapter, we showed that spherical AuNP of 14 nm are perfect photothermal agents when irradiated with a green laser. In fact, a photoconversion efficiency of 77% was attained, which is much higher than conventional NIR. We showed that AuNP@PEG reversibly aggregates at high temperatures with high ionic strength medium, such as PBS. This phenomenon might be due to the collapse of the PEG structure at high temperatures, and consequent particle approximation due to increased ionic strengths. Regarding, PTT in the visible,

we reduced breast cancer cell viability by 60%, which was potentiated when used in combination with DOX. What is more, because green lasers have already been in use for surgical purposes, their combination with standard chemotherapy, allows for targeted and selective killing of cancer cells and/or the possibility of reducing the dosage of chemotherapeutic agents, without compromising efficacy but reducing side effects. We showed that CoD is a promising chemotherapeutic agent against cancer cells refractory to DOX therapy. DOX resistant cancer cells are more sensitive to hyperthermia than fibroblasts. However, since we are using visible radiation, it is possible to easily target and direct irradiation to the tumour with superior precision, minimizing its effect in healthy cells, which is not possible to achieve in chemotherapy, since its effect is systemic. Combination of selective anti-cancer compound (CoD) with AuNP enhanced phototherapy selectively kills resistant cancer cells while sparing healthy tissues. What is more, the additive affect allows to use smaller dose of chemotherapeutic agent, which further reduces adverse side effects associated to systemic delivery of chemotherapy. The described approach has great potential to be translate to clinical settings, since green lasers are commonly used for skin and retinal treatment with great promise to treat drug resistant tumours. This study paves the way for the use of green laser irradiation combined with AuNP in PTT regimens with impact in epithelial cancers.

CHAPTER 6 – AUNP PHOTOTHERAPY TO PREVENT NEO-ANGIOGENESIS

The work presented in this chapter was possible due to the support of several colleagues. Their contribution will be further detailed. The synthesis and characterization of the nanoparticle formulations was performed by Amelie Heuer-Jungemann and Antonios Kanaras (ILS, University of Southampton). The *in vivo* assays were performed with the help of Pedro Baptista. All the work in this chapter was performed under the supervision and guidance of P.V. Baptista and A.R. Fernandes (UCIBIO, Universidade Nova de Lisboa). Data enclosed in this chapter were originally published in the following issues:

- **Pedrosa P**, Heuer-Jungemann A, Kanaras AG, Fernandes, AR, Baptista PV. Potentiating angiogenesis arrest *in vivo* via laser irradiation of peptide functionalised gold nanoparticles. *Journal of Nanobiotechnology*. 2017, 15:85 DOI: 10.1186/s12951-017-0321-2

6.1 Introduction

In cancer development, tumour growth is associated with increasing need for oxygen and nutrients to supply the uncontrolled multiplication of malignant cells. As such, tumours release a series of growth factors to stimulate the formation of new blood vessels – neo-angiogenesis, which in turn provide for the very needed nutrients [42, 445]. Among these, the VEGF is responsible for the angiogenic trigger, leading to the foundation of new blood vessels surrounding the tumour tissue, thus allowing for its exponential growth [163, 446]. Upregulation of VEGF is a critical step in endothelial cell growth, survival and proliferation. The rapid growth of endothelial around tumours, results in an unorganised and leaky vasculature that potentiate further tumour growth and metastasis [446, 447]. Several FDA approved anti-angiogenic agents have already shown the potential to decrease tumour-induced neo-angiogenesis, but the considerable side effects towards the normal vascular architecture in other organs, and the development of resistance to these drugs decreases their effect [166, 445, 448, 449].

Nanoparticles hold great promise to deliver therapeutic agents selectively to tumours by increasing the local concentration of active molecules via the EPR effect at the tumour site [219, 396, 450]. EPR allows for the passive accumulation of the nanoparticles within the tumour site, where the confinement in a reduced volume permits lower dosages, improving the therapeutic effect while decreasing side effects [396, 448]. Our group have previously shown that AuNP functionalised with an anti-angiogenic peptide targeting the neuropilin-1 receptor (NRP-1), promote receptor internalisation and efficiently arrest angiogenesis *in vivo* [275, 451]. NRP-1 is a transmembrane glycoprotein and a co-receptor for VEGF [163, 452]. Although the precise mechanism for VEGF binding to NRP-1 in angiogenesis and in endothelial function remains to be unveiled, pre-clinical studies have linked NRP-1 blockade to suppression of tumour growth by blocking angiogenesis [453, 454]. The effect of our peptide-functionalised nanoparticles on human umbilical vein endothelial cells was potentiated by the simultaneous combination of laser irradiation in the NIR [276, 455]. However, precise irradiation on the target site is possible by using a laser of visible light (green). Indeed, green lasers have been used in medical surgery as a safe tool for tissue ablation without bleeding, inducing photocoagulation of capillaries and minimal destruction of surrounding tissue [421, 456, 457]. Initially used in retinoblastoma focal therapy, their applications were broadened to hyperthermia directed at epithelial cancers or photodynamic therapy, for accurate tumour removal or photo activation of chemotherapeutic agents [421, 456–459]. AuNP with a diameter <20 nm show a very intense LSPR band centred at 520 nm (close to the standard wavelength of surgical green lasers) that can be used for localised plasmon photothermal therapy. Spherical AuNP coupled to visible lasers have been reported as an efficient tool for hyperthermia, with increased photothermal efficiency [431] and are less influenced by particle polydispersity compared to gold nanorods [424]. In addition, green lasers have an increased effect on blood vessels, being an active tool against angiogenic conglomerates around tumours.

Here, we propose the combination of green laser irradiation with administration of a nanoformulation of 13 nm spherical AuNP functionalised with an anti-angiogenic peptide for the focalised phototherapy towards blockade of neovascularisation *in vivo*. For this, we used the chicken CAM model of angiogenesis to evaluate the anti-angiogenic effect of gold nanoconjugate formulations. CAM is a simple, highly vascularized extraembryonic membrane that is used as model of angiogenesis, tumour growth and metastasis [460], biocompatibility of engineered materials, drug distribution and toxicology, etc. It has been used as an *in vivo* platform for experimentation for the last 50 years. The main advantages of this model are its easy access, visibility, and capacity to form a small vascular network in a short period of time. This process occurs over a period of about 7 days starting of embryonic development day 3 to day 10.

6.2 Materials and Methods

6.2.1 Synthesis and functionalization of AuNP

The synthesis of AuNP was performed as described in 2.2.6.1. For functionalization, a freshly prepared aqueous solution of monocarboxy(1-mercaptoundec-11-yl) hexaethylene glycol (PEG, MW = 526.7 g·mol⁻¹, 200 µL) was added to a moderately stirring gold nanoparticle solution (10 mL, 5 nM). The mixture was continuously stirred for 2 h followed by an overnight incubation at 4°C. AuNP@PEG were then purified from excess PEG by three rounds of centrifugation (16 400 rpm, 15 min) and re-dispersion in borate buffer (10 mL, 0.01 M, pH 9). AuNP@PEG were stored at 4°C until further use.

Scramble and antiP peptides were then conjugated to AuNP@PEG. The peptide solution (100 µL, 1 mg·mL⁻¹, MW scramble = 922.1 g·mol⁻¹, MW antiP = 968.2 g·mol⁻¹, in 0.01 M sodium borate buffer, pH 9) was added to AuNP@PEG (5 mL, 1.5 nM in 0.01 M sodium borate buffer, pH 9) followed by aqueous solutions of EDC, 50 µL, 0.2 M and sulfo-NHS, 100 µL, 0.2 M. After shaking at room temperature for 24 h, the reaction mixture was purified by three rounds of centrifugation (16 400 rpm, 15 min) and re-dispersion in water followed by lyophilization.

6.2.2 RNA expression analysis

The description of the procedures followed in this chapter are described in section 2.2.4.

6.2.3 *Ex ovo* CAM assay

All the *in vivo* CAM experiments were performed according to the Directive 2010/63/EU of the European Parliament and of the council of 22 September 2010 on the protection of animals used for scientific purposes, which does not contain any kind of restriction to the use of non-mammal embryos. The use of this alternative animal model fits in the “3Rs policy” that was strictly followed during experiments.

Fertilised eggs were incubated at 37°C, 99% (v/v) relative humidity, until 72 h and gently opened into a petri dish, with the chicken CAM facing upwards. Afterwards four transparent plastic, O-rings (6

mm inside and 9 mm outside diameter) were placed on the CAM. Inside each O-ring, 40 μL of free peptides or peptide-conjugated AuNP were pipetted ($0.01 \text{ pmol} \cdot \mu\text{L}^{-1}$ for peptide concentration) [277]. For blood vessel modulation experiments each O-Ring per CAM contained PBS, scramble and antiP in the free form or in formulation with AuNP (AuNP@scramble and AuNP@antiP) and were further irradiated or kept in dark. Thus, each CAM is exposed to four different stimuli, one in each O-ring. After stimuli, the embryos were then incubated at 37°C , 99% (v/v) relative humidity for 24 h. Images were acquired at 0 and 24 h of incubation using a Digital USB Microscope Camera (Opti-Tekscope OT-V1). For mRNA expression analysis, all the O-rings in each CAM were pipetted with the same solution of PBS, scramble and antiP, in free form or in formulation with AuNP, and were after irradiated or kept in dark. Thus, each CAM was exposed to only one stimulus, the same in all O-rings. After stimuli, the embryos were then incubated at 37°C , 99% (v/v) relative humidity for 24 h and total mRNA was extracted.

6.2.4 Blood vessel modulation experiments

After image acquisition, the internal area of each O-ring was extracted from all images, then the green channel of the images was extracted using ImageJ 1.49k (Wayne Rasband, National Institutes of Health, USA). For image analysis, a noise tolerance of eight was considered for segmentation, excluding the edge maxima and binary performed. Using the skeleton plugin of ImageJ the number of branches was counted within the region treated with the sample formulations. The blood vessels in the image obtained after channel split were also counted manually for comparison. The formed blood vessels were calculated for 0 and 24 h. The percentage of newly formed vessels is given by dividing the values at 24 h by the values at 0 h.

6.2.5 Statistical analysis

Results are presented as average \pm standard deviation of triplicate experiments. An unpaired, parametric, T-student test was performed between each group and the respective scramble. Differences between groups were considered significant at $P < 0.05$ using GraphPad Prism 7.00.

6.3 Results and Discussion

6.3.1 Nanoconjugate characterisation

Spherical AuNP were synthesised as previously described in section 2.2.6.1. TEM imaging revealed an average size of $13 \pm 2 \text{ nm}$ which agrees with the previous synthesis (Fig. 6.1). AuNP@PEG were synthesised and showed an average hydrodynamic diameter of $21.0 \pm 0.2 \text{ nm}$ by Dynamic Light Scattering. Zeta potential measurements of AuNP@PEG and showed a negative charge ($-27.53 \pm 1.5 \text{ mV}$) possible derived from the presence of carboxylic groups. AuNP@PEG were subsequently conjugated with an anti-angiogenic peptide – KATWLPPR, (AuNP@antiP), capable to interact with NRP-1 receptor and inhibit the VEGF pathway. As a control, a scramble peptide (KPRQPSLP)

(AuNP@scramble) was used (Table 6.1). AuNP@scramble had a hydrodynamic diameter of 22.7 ± 3.3 while zeta changed by 4 mV (-23.40 ± 2.3 mV) due to the formation of amide bonds between carboxylic groups from the outer shell of PEG and N-terminus lysins form positively charged peptides; AuNP@antiP had a similar net charge with an average size of 22.2 ± 2.2 nm. All measurements were obtained in PBS 1 \times .

Table 6.1 Peptide Amino Acid Sequences

Name	Function	Sequence
Scramble	Scramble control	KPRQPSLP
AntiP	Anti-angiogenic	KATWLPPR

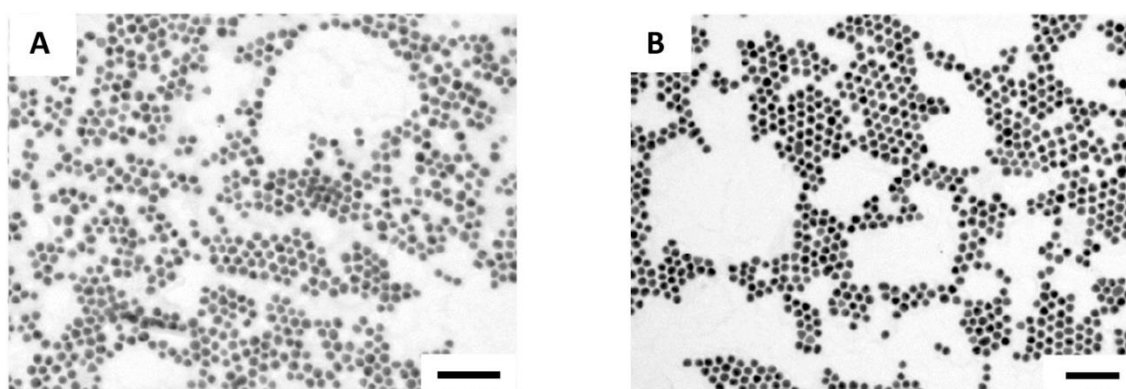


Fig. 6.1 TEM images of AuNP@antiP (A) and AuNP@scramble (B). Scale bars are 100nm.

6.3.2 Laser effect on albumen and blood

To understand the impact of irradiating AuNP on the biological matrix (chicken egg), we irradiated the egg white. It proved to be a good model matrix since it is transparent to visible light and mostly composed of water and albumin, where the effect of irradiation combined with AuNP@PEG could be easily perceived via the protein denaturation at high temperatures. We irradiated a solution of albumen with 0.3 nM of AuNP@PEG with different intensities and time exposures. Without AuNP@PEG the temperature only increased by 4.5 °C (ΔT) while in its presence the temperature increased up to 22 °C (ΔT) which led, in some conditions, to coagulation of the albumen (“boiled egg”) (Fig. 6.2). We chose two conditions ($3.83 \text{ W}\cdot\text{cm}^{-2}$ 300s and $5.1 \text{ W}\cdot\text{cm}^{-2}$ 180s) and irradiated the albumen containing increasing concentrations of AuNP@PEG (Fig. 6.3). Both irradiation settings showed similar increments in temperature (Fig. 6.4).

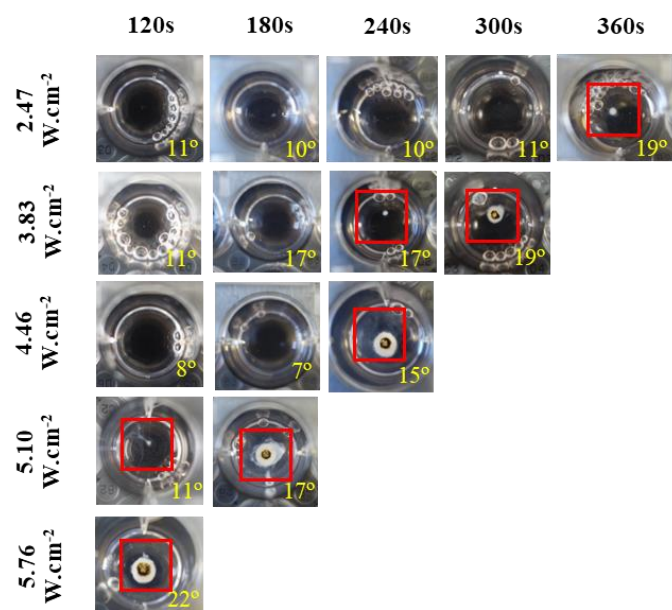


Fig. 6.2 Green laser irradiation of albumen (500uL) mixed with AuNP@PEG (Vf- 700uL) at varying potencies and time periods, with 0.43 nM AuNP@PEG. The ΔT ($^{\circ}\text{C}$) after irradiation is represented at the bottom left of each assay. The initial temperature was $29^{\circ}\text{C} \pm 1^{\circ}\text{C}$ for all assays.

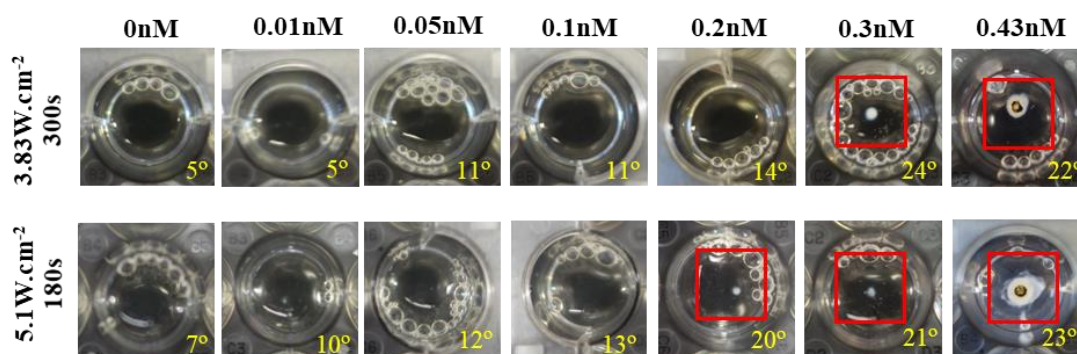


Fig. 6.3 Green laser irradiation of albumen (500uL) mixed with AuNP@PEG (Vf- 700uL) at fixed potencies and time periods, varying gold nanoparticle final concentration. The ΔT ($^{\circ}\text{C}$) after irradiation is represented at the bottom left of each assay. The initial temperature was $29^{\circ}\text{C} \pm 1^{\circ}\text{C}$ for all assays.

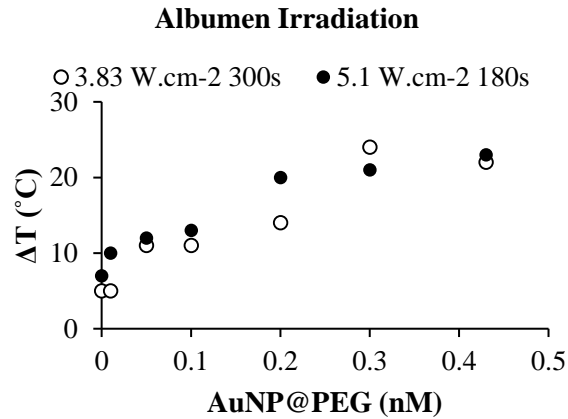


Fig. 6.4 Temperature variation of albumen after green laser irradiation. Albumen was mixed with AuNP@PEG at fixed potencies and time periods varying gold nanoparticle concentration. The initial temperature was $29\text{ }^{\circ}\text{C} \pm 1\text{ }^{\circ}\text{C}$ for all assays

We then assessed the effect of irradiating a blood sample with and without AuNP@PEG, at previously determined concentration that inhibits angiogenesis (16.4 nM), to mimic blood capillary cauterisation [275]. One minute of irradiation at $0.61\text{ W}\cdot\text{cm}^{-2}$ without AuNP@PEG caused blood to coagulate, thus setting the upper threshold for irradiation. Between 0.49 and $0.61\text{ W}\cdot\text{cm}^{-2}$, blood only cauterises in the presence of AuNP@PEG, determining the effective window for the CAM assay (Fig. 6.5). This clearly demonstrates the heating efficacy of AuNP@PEG when irradiated at their LSPR peak, where relatively low concentrations can induce high temperature variations in biological matrices.

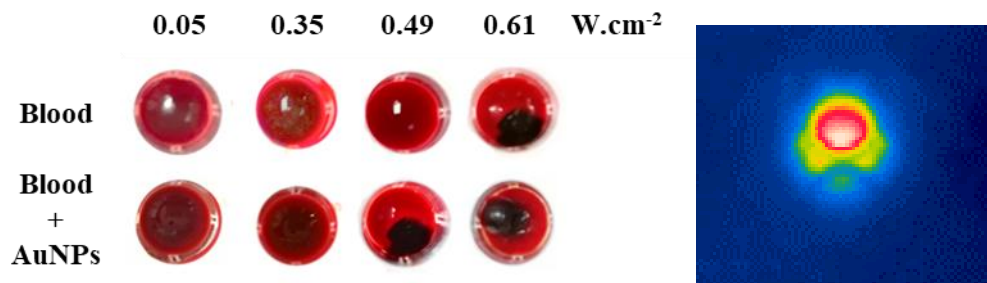


Fig. 6.5 Green Laser Irradiation of blood ($87\text{ }\mu\text{L}$) mixed with AuNP@PEG (16.4 nM) or water ($V_f=100\text{ }\mu\text{L}$) at varying potencies for 1 min at of AuNP@PEG. (Left) Cauterization of the blood samples can be seen as black spots. (Right) Infrared image of the blood well with nanoparticles irradiated with $0.61\text{ W}\cdot\text{cm}^{-2}$. The sample achieved a final temperature of $92\text{ }^{\circ}\text{C}$.

6.3.3 Irradiating CAM with AuNP@antiP

To perform angiogenesis analysis in CAM we cracked the eggs at the third day of embryogenic development and placed them in a petri plate, inside an incubator. Transparent plastic O-Ring were placed on top of the CAM to restrict nanoparticle administration place (Fig. 6.6).

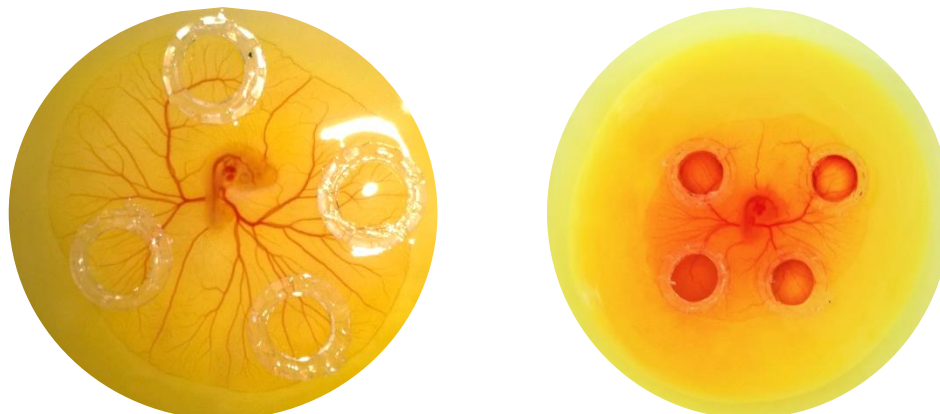


Fig. 6.6 Photographs of CAM (Left) after placing the O-Rings (Right) after application of AuNP@antiP at 16.4 nM.

We divided the *ex-ovo* CAMs into two groups: one exposed to AuNP@scramble and AuNP@antiP and not irradiated; and the test group, where embryos were exposed to each nanoformulation and irradiated with a potency of $0.49 \text{ W}\cdot\text{cm}^{-2}$ for 1 min with the green laser. An additional control ring with PBS $1\times$ was also used. To calculate the percentage of formed blood vessels we took photographs of the O-Rings at 0 h and 24h after administration of the nanoformulations. The images were processed by ImageJ, with the following steps: the image was circular cut to contain only the vasculature inside the O-ring; the blue and green channels were removed from the photos to have a black and white image of the vasculature only; skeleton tool was used to draw the vasculature network; the number of branches was used as an indication of vascularization degree. The percentage of the newly formed arterioles was compared from the images taken at 0 h and 24 h. By looking at Fig. 6.7 we can observe a cauterisation spot, ranging from 0.8 to 2.6 mm in diameter, solely for the CAMs challenged with AuNP and irradiated with the green laser (Fig. 6.7). Coagulation occurs due to photothermal conversion by AuNP, and not by the laser alone. This shows that irradiation of AuNP can be used for safe localised photothermal cauterisation without affecting the surrounding vessels. One can also observe that, nor the AuNP@scramble alone nor irradiated affect the formation of new blood vessels when compared with PBS (Fig. 6.8). The anti-angiogenic nanoformulation (AuNP@antiP) in the group kept in dark, induced a 73% reduction in the formation of new arterioles when compared to the scramble nanoconjugate, in accordance to previously reported results [277]. What is more, irradiation of the nanoconjugates potentiates this effect, mounting on its anti-angiogenic effect and leading to a 91% reduction of newly formed arterioles.

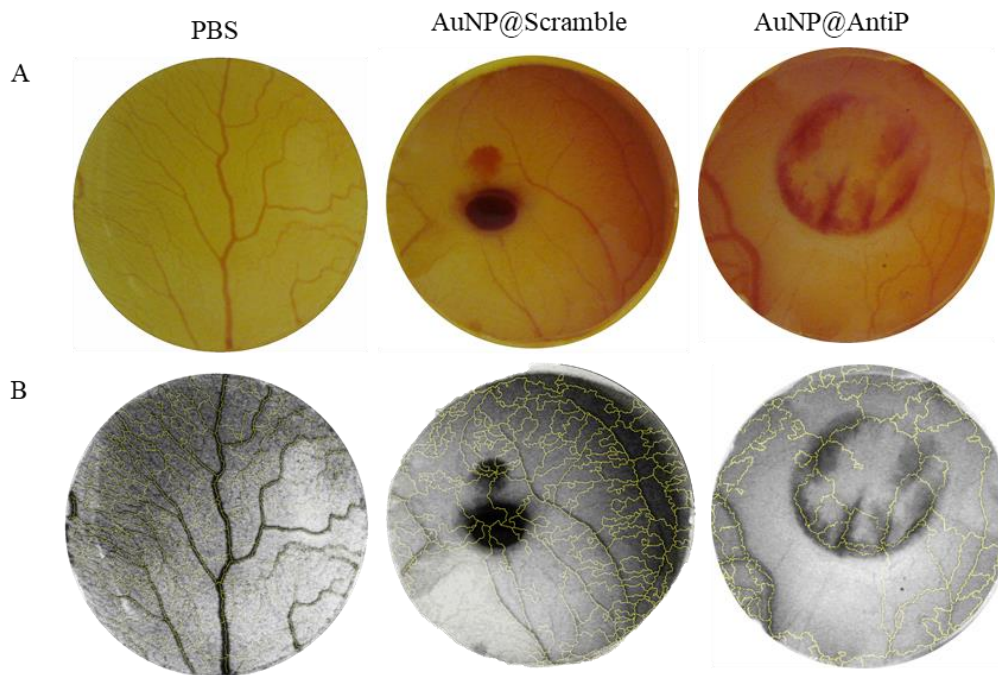


Fig. 6.7 CAM images 24 h after application of the nanoformulation and irradiation. (A) images before software analysis. (B) images after software analysis. The nanoparticle formulations were at 16.4 nM concentration and the irradiated conditions were exposed to $0.49 \text{ W}\cdot\text{cm}^{-2}$ for 60 sec.

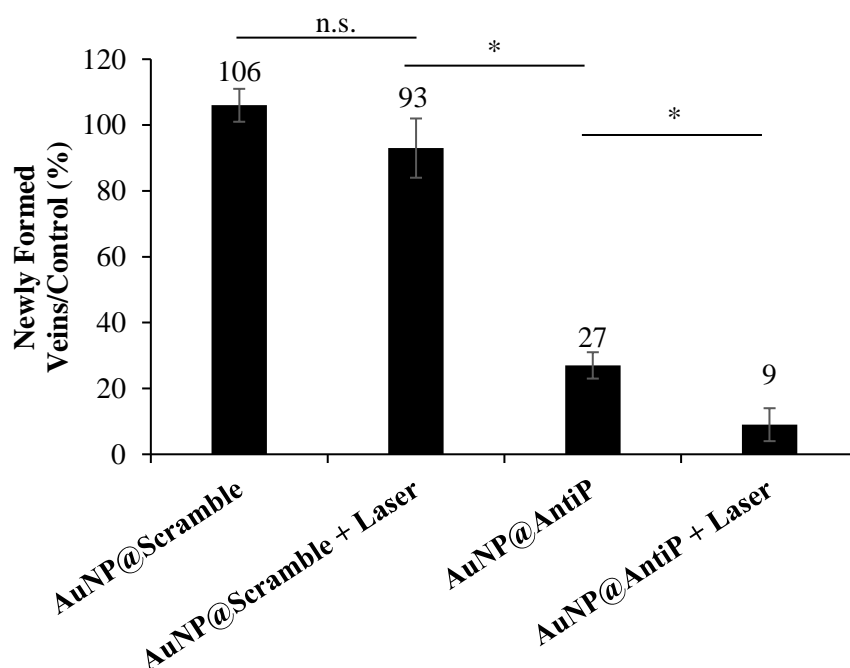


Fig. 6.8 Percentage of newly formed vessels over 24 h in CAM model compared with respective control. AuNP@scramble (16.4 nM) were compared with PBS and AuNP@antiP (16.4 nM) were compared with AuNP@scramble. Irradiated formulations (Laser) were exposed to $0.49 \text{ W}\cdot\text{cm}^{-2}$ for 60 sec. Differences between groups were considered significant at $P < 0.05$ (*).

6.3.4 Gene Expression Analysis

Neuropilin-1 is a protein encoded by the NRP-1 gene in humans and has been shown to interact with VEGF-A forming a co-receptor complex with VEGFR-2 and mediating VEGF signalling [452, 453]. VEGFA encodes for the most common growth factor of VEGF pathway. Fms Related Tyrosine Kinase 1 (FLT-1) encodes for the human VEGFR-1. It is a transmembrane protein with tyrosine kinase activity, important for the signalling of cell proliferation and differentiation, where the main function of VEGFR-1 is to regulate blood vessel morphogenesis. NRP-1 expression is upregulated in several human tumours, e.g. brain, prostate, breast, colon, and lung cancers, promoting the vascularisation and progression of cancer, as well as contributing to invasiveness and metastasis [163, 446]. To further understand the molecular mechanisms of angiogenesis modulation by the AuNP@antiP, we used qPCR to look for variations in mRNA expression of genes involved in VEGF pathway, IL-8, VEGF-A and MMP-9, when compared to the scramble peptide alone or conjugated to AuNP. MMP-9 is involved in the breakdown of extracellular matrix, and facilitates the vascularisation network growth [448, 461, 462]. Evidence shows that MMP-9 is up-regulated in some tumours and plays an important role in cancer angiogenesis, possibly by facilitating the access of VEGF to its receptors [448, 461, 462]. Concordantly, down-regulation of MMP-9 was shown to repress metastasis [448, 461, 462]. IL-8 is a chemokine that enhances endothelial permeability during early stages of angiogenesis, which requires activation of VEGFR-2 [463–466]. No alterations to gene expression were observed with the scramble peptide, neither free nor in nanoconjugate, when irradiated (Fig. 6.9 and Fig. 6.10). This indicates that laser irradiation per se does not affect VEGF pathway, despite vascular cauterisation. Irradiation of AuNP@antiP promotes a clear downregulation of FLT-1 and VEGF-A, 4- and 3.5-fold, respectively. Together, these data indicate that NRP-1 regulation over FLT-1 and VEGF-A expression is clearly enhanced upon laser irradiation. Our results show that MMP-9 is down-regulated in embryos exposed to AuNP@antiP by 1.9-fold and further repressed when irradiated (down 3.5-fold). IL-8 expression was not altered by the peptides or irradiation, indicating that the NRP-1 pathway does not influence IL-8 expression in our CAM angiogenesis model (Fig. 6.9 and Fig. 6.10). Together, these results show that green laser irradiation of AuNP@antiP modulates neovascularisation via VEGF pathway, regulating FLT-1, MMP-9, VEGF-A expression but not IL-8. *In vivo* cauterisation of vessels coupled to blockade of angiogenesis clearly shows the potential to be used in cancer therapy, hindering vascular supply required for tumour progression.

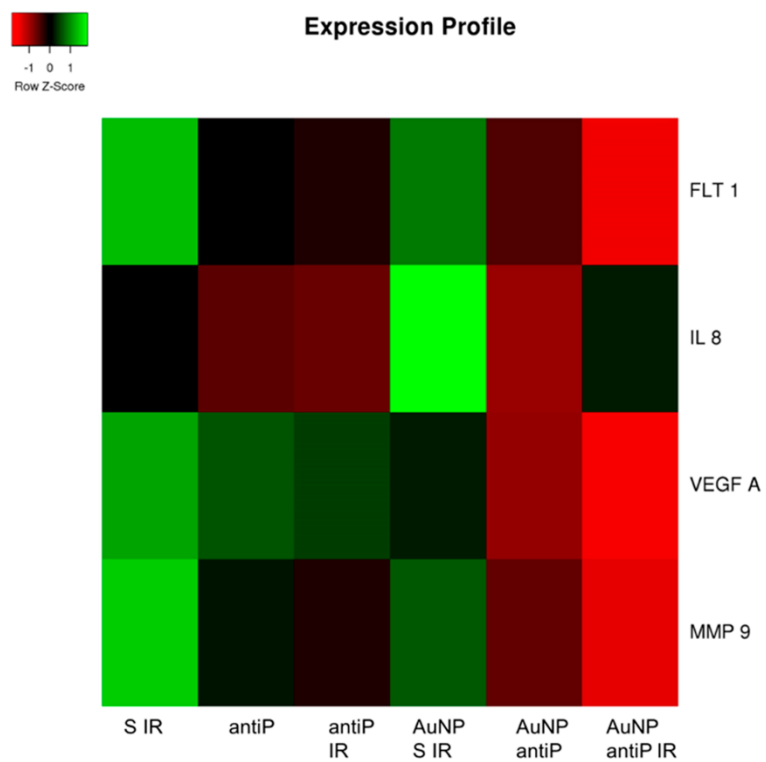


Fig. 6.9 Gene expression heatmap for data retrieved from qPCR. Gene expression measured for scramble peptide irradiated (S IR); antiP and antiP irradiated (antiP and antiP IR, respectively); and the respective nanoconjugates. The nanoparticle formulations were at 16.4 nM concentration and the irradiated conditions were exposed to $0.49 \text{ W}\cdot\text{cm}^{-2}$ for 60 sec.

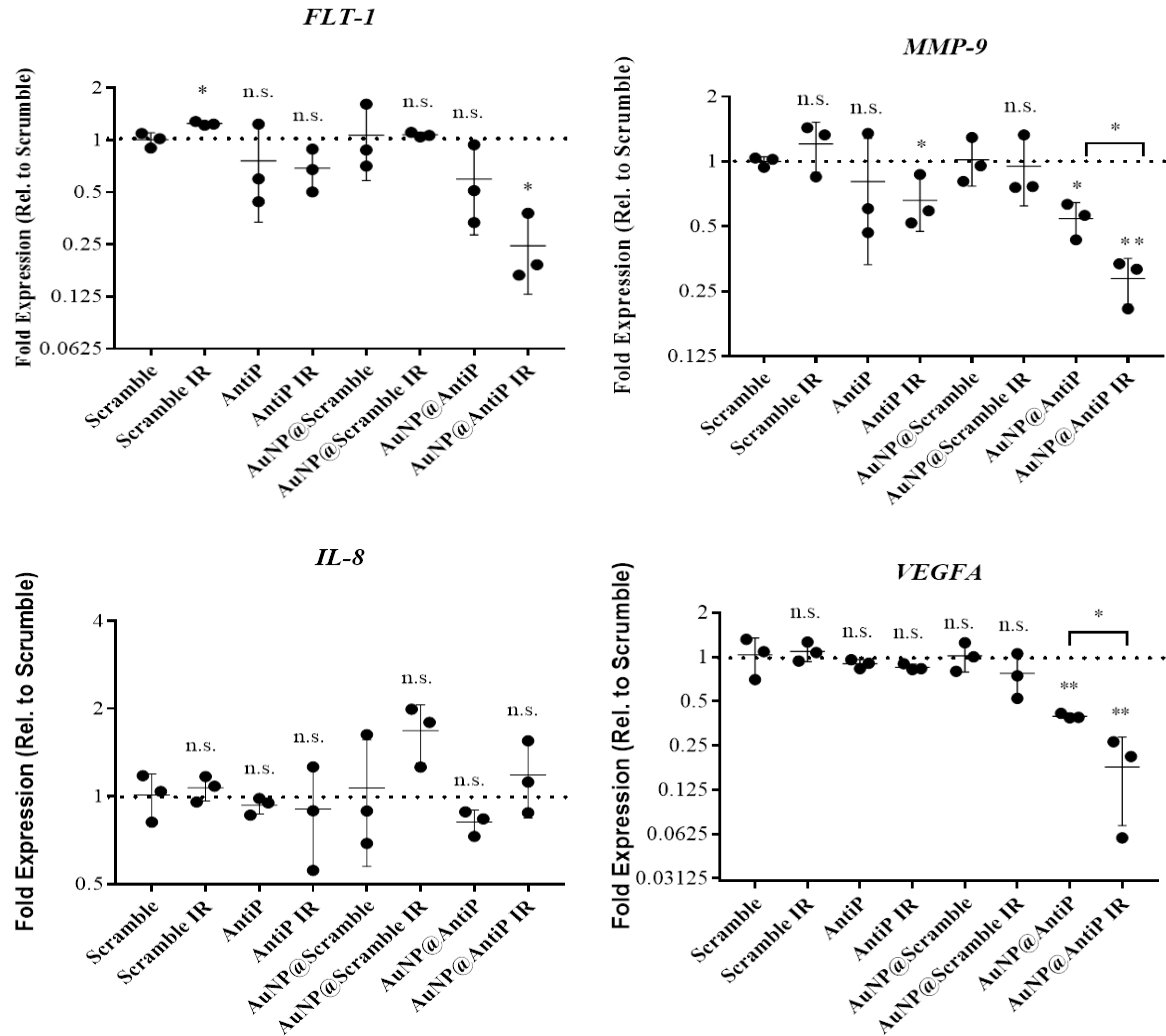


Fig. 6.10 Gene expression analysis of CAM for *FLT-1*, *MMP-9*, *IL-8*, *VEGFA* genes. Normalisation was performed with housekeeping *GAPDH*. The nanoparticle formulations were at 16.4 nM concentration and the irradiated conditions were exposed to 0.49 W·cm⁻² for 60 sec.

6.4 Conclusions

In this chapter, we showed that spherical AuNP conjugated to anti-angiogenic peptides may be used as efficacious photothermal agents in the visible region of the spectrum. These conjugates can denature albumin and haemoglobin via an extremely focalised irradiation that does not require guide light, since it is itself visible. This way, existing surgical green laser may be used directly to cauterise tissues harbouring these nanoconjugates. Furthermore, green laser irradiation of the gold nanoconjugates potentiates the anti-angiogenic effect *in vivo* via down regulation of the VEGF pathway. With this approach, we can specifically destroy vessels surrounding the tumour by laser ablation and inhibit neovascularisation through NPR-1 blockage. The proposed combination of chemo- and phototherapy allows for a reduction of dose of anti-angiogenic peptide, thus reducing possible side effect to the neighbouring tissues, while arresting blood vessel supply critical for tumour progression, which might become a valuable strategy for cancer treatment.

CHAPTER 7 – AUNP GENE SILENCING TO OVERCOME DRUG RESISTANCE

All the work in this chapter was performed under the supervision and guidance of P.V. Baptista and A.R. Fernandes (UCIBIO, Universidade Nova de Lisboa). Data enclosed in this chapter were originally published in the following issues:

Pedrosa P, Mendes R, Cabral R, Martins L, Baptista PV, Fernandes A. Combination of chemotherapy and Au-nanoparticle phototherapy in the visible light to tackle doxorubicin resistance in cancer cells. *Scientific Reports*. 2018, 8:11429 DOI: 10.1038/s41598-018-29870-0

7.1 Introduction

The impact of ABCB1 in cellular acquisition of resistance prompted us to investigate alternative ways to prevent tumour cells to become resistant. The main mechanisms involved in drug resistance is pump cellular resistance which involves the up regulation of membrane ATP-dependent efflux pumps which excrete the drug to the extracellular medium, decreasing the intracellular concentration of the drug below effective levels. These pumps are characterized by transmembrane domains and nucleotide-binding domains with the Walker A, Walker B, and Signature C motifs [192]. The human ABC transporters consist of a protein family of 49 members where, P-glycoprotein (ABCB1), breast cancer resistance protein (BCRP/MXR/ABC-P/ABCG2), and MDR-associated proteins (MRP1/ABCC1 and MRP2/ABCC2) are the most studied. ABCB1, encoded in humans by the *ABCB1* gene, confers cross-resistance to a variety of cytotoxic agents. The overexpression of ABCB1 is described as the main cause of pump cellular resistance. Downregulation of these mechanisms have indicated reversal of tumour cells to the sensitive state. Some studies have taken advantage of ASOs targeted against *ABCB1* mRNA to suppress MDR [193, 194]. However, vectoring nucleic acids into cells is a challenging task, their therapeutic efficacy is low, with low transfection efficiency and stability, being degraded by enzymes, and rapidly cleared from the systemic circulation. New vehicles of transfection have been tested to surpass this. Extensive investigation is being made in the design of AuNP formulations to improve siRNA [263, 467–469] delivery and efficiency, without undesirable immune response or off-target effects. AuNP-siRNA have been tested in cell cultures targeting reporter genes, such as luciferase or green fluorescence protein [263, 265]. AuNP can be optimal delivery vehicles for gene therapy because they protect the oligonucleotides against RNases and can easily be functionalized with targeting moieties. AuNP tend to be internalized by cells and showed to outperform traditional delivery systems with effective gene silencing [263, 467–470]. Previous studies show the capacity of ASO functionalized AuNP to knockdown gene expression at lower cell toxicity than lipofectamine antisense DNA [206, 263, 471]. In the following work we will try to silence *ABCB1* mRNA through AuNP ASO technology, to decrease the levels of *ABCB1* expression, and increase the effectiveness of DOX by avoiding its excretion (Fig. 7.1). For that purpose, a cell line described as expressing *ABCB1*, HCT116 was chosen for the experiments.

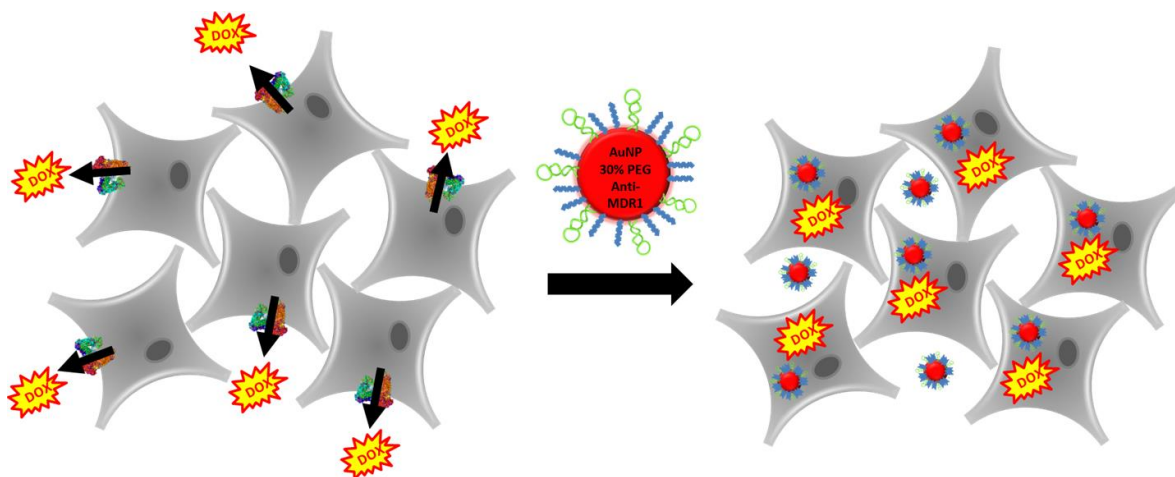


Fig. 7.1 Schematics of the hypothesis of *ABCB1* silencing. (Left) *ABCB1* pumps DOX outside the cells. (Right) AuNP@ASO enters the cell and silences the *ABCB1* mRNA, the protein is not translated and DOX concentration inside the cell, increases, reducing its viability.

7.2 Materials and Methods

The description of the procedures followed in this chapter are described in section: Cell culture 2.2.1; Cell Viability 2.2.2; Western Blot 2.2.5; RNA expression analysis (qPCR) 2.2.4.

7.2.1 Functionalization of AuNP with ASO

In this chapter we used AuNP previously characterized in section 5.3.2. AuNP@PEG with a coverage of 30% were synthesized and characterized as described in section 2.2.6.3. Thiol-modified oligonucleotide (STAB Vida, Portugal) was dissolved in 0.1M DTT for 4h to reduce the sulphide bonds. DTT was extracted through ethyl acetate by washing three times. The aqueous phase was filtered in a NAP-5 and further incubated with AuNP@PEG in a ratio of 1:200 (AuNP:ASO) and 0.01% (w/v) of SDS. Increasing concentrations of sodium chloride were added for every 20 min to the mixture up to a final concentration of 0.3M to promote AuNP@PEG and ASO interaction. The mixture was let stand in agitation for 16h. The solution was washed 4× with Mili-Q water by centrifugation 14 000×g for 45min. The resulting oily pellet stored in the dark at 4 °C till further use.

7.3 Results and discussion

7.3.1 AuNP@ASO synthesis and characterization

We choose an ASO sequence previously described in the literature as bearing the highest silencing activity of *ABCB1* gene, of the tested sequences [194]. To increase the specificity of this sequence, a hairpin structure was designed to open, only in the presence of a full complementary target. The capacity of the hairpin to open in the presence of the target was tested *in silico* confirming its function (Fig. 7.2).

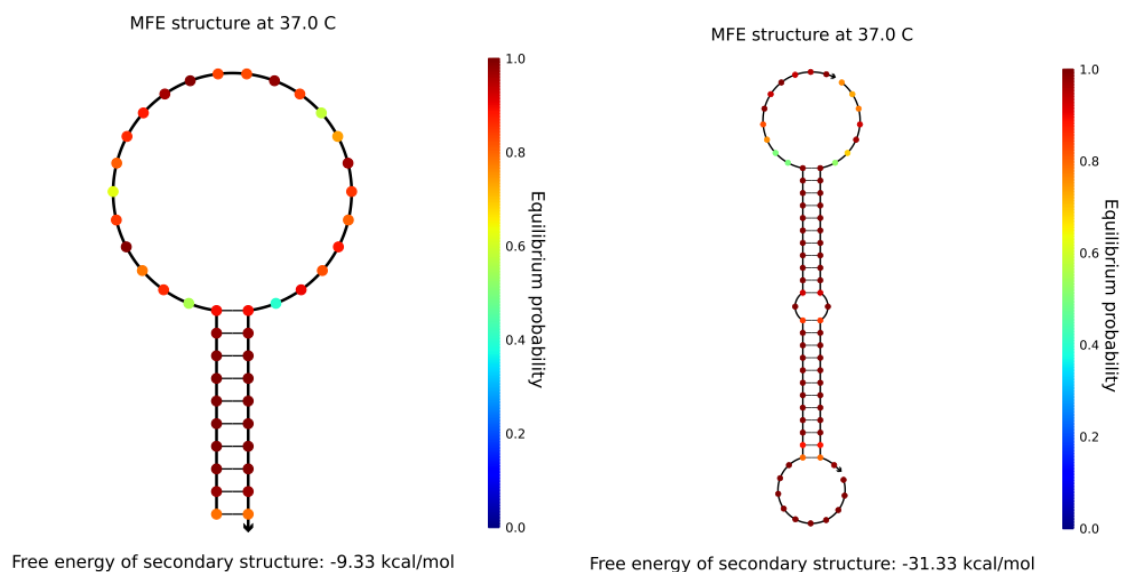


Fig. 7.2 In silico hybridization analysis. The probe and the complementary portion of mRNA was analysed at 37°C using standard Nupack settings[472].

The thiol modified ASO was functionalized by salt aging method into the spare spaces of AuNP@PEG surface. Functionalization was confirmed by a red shift in the UV-Vis absorption peak of 5 nm and an increase in the hydrodynamic diameter of 8 nm by DLS (Fig. 7.3).

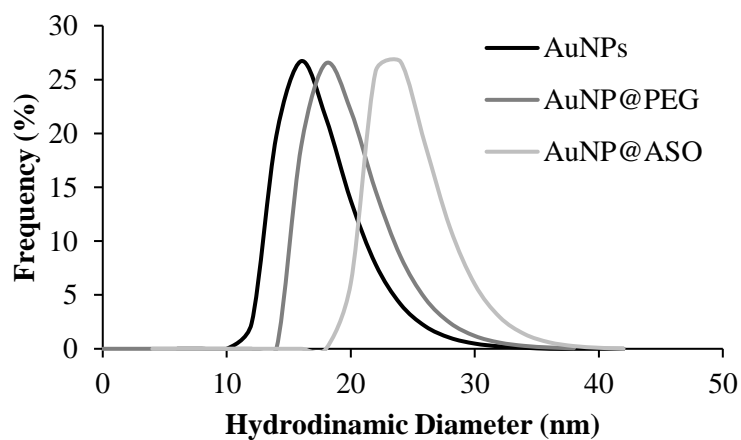


Fig. 7.3 DLS AuNP characterization of AuNP@ASO.

The amount of functionalized ASO was defined by measuring the supernatant optical absorption of DNA at 260 nm. By subtracting the amount of added DNA, we were able to establish the number of oligonucleotides attached to the AuNP, resulting in 1:30 AuNP:ASO proportion.

7.3.2 Gene Silencing

To assess the capacity of AuNP@ASO to silence *ABCB1* *in vitro*, we performed an RNA expression analysis by qPCR for HCT116 cells exposed to increasing concentrations of particles for 24 h, 48 h and 72 h. Ribosomal *18s* gene was taken as reference and AuNP@PEG were used as control. We could observe a decrease in gene silencing with increasing concentrations of silencer, being the most effective the 48 h exposure with 50 nM of ASO, reducing almost 3-fold the expression of the gene compared with control (Fig. 7.4). We observe that in general concentrations over 50 nM of ASO do not increase silencing. Also, incubation times longer than 48h seem to be less effective at silencing than 48h. This might be due to a cellular response to the silencing.

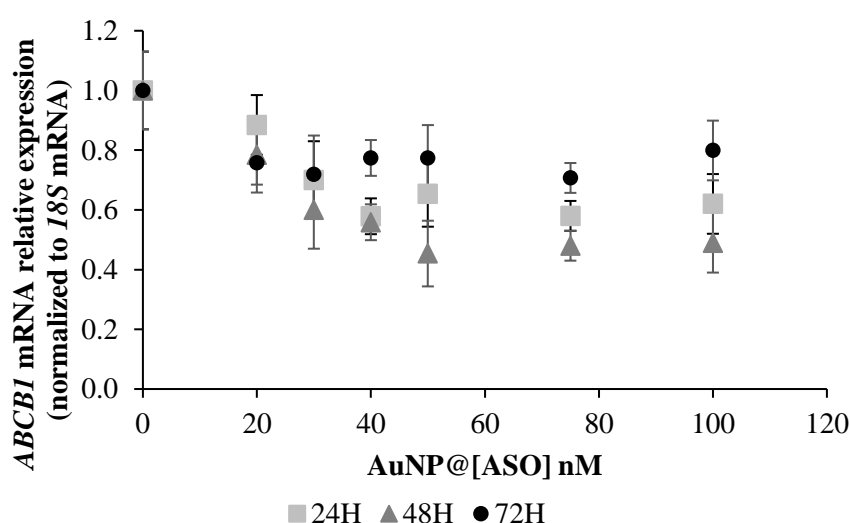


Fig. 7.4 Expression analysis of *ABCB1* mRNA, normalized to 18s, and AuNP@PEG. Different concentrations of AuNP@ASO were tested, for incubation times of 24h, 48h and 72h. The values in x axis represent the concentration of ASO added in each assay.

We then tested our hypothesis, if by silencing *ABCB1* we could increase the effect of DOX. We tested if by exposing cells at the optimal silencing conditions we could reduce HCT116 viability in combination with DOX. We could not observe a significant decrease in cell viability, for AuNP@ASO formulation, showing that it is not toxic. Also, the combined therapy compared with DOX alone showed no significant difference, against what was expected (Fig. 7.5). This could be explained by the low turnover of ABCB1 protein, of up to 72h in some cell lines [473], meaning that even if we were silencing the gene, the protein would still be active and pumping the DOX out of the cell. To confirm this, we added, as in Fig. 3.10, the specific blocker of ABCB1 protein, tariquidar. It is a molecule that showed remarkable inhibition of ABCB1 with K_d of 5.1 nM, although it failed clinical trials for excessive toxicity. Tariquidar showed no toxicity at tested conditions, and again no significant change in cell

viability was observed when cells were exposed to DOX, and the inhibitor compared with DOX alone (Fig. 7.5).

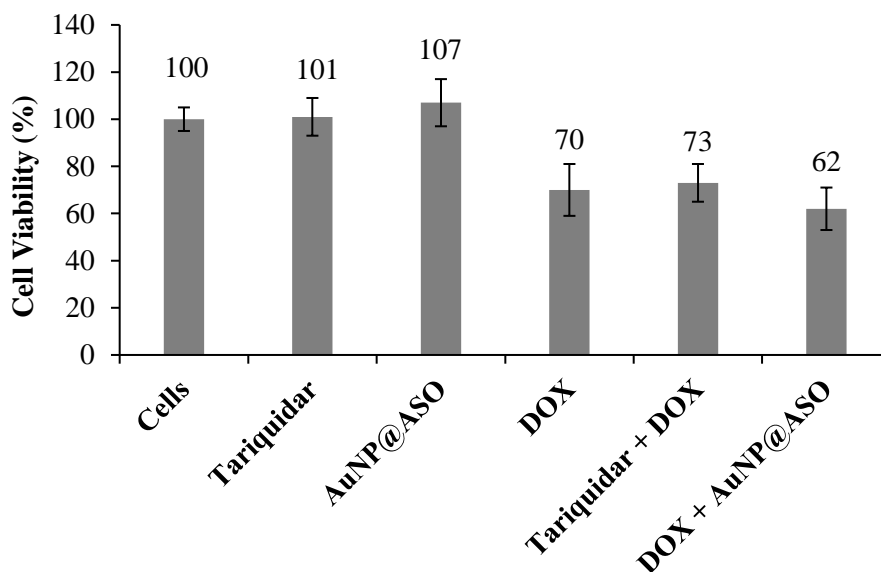


Fig. 7.5 Cell Viability of AuNP@ASO, DOX and Tariquidar. Cell viability was measured by MTS assay after an incubation period of 48h. Cell viability was calculated using cells as reference.

This means that blocking ABCB1 has no effect on HCT116 viability, which lead us to check the protein expression levels of ABCB1 in this cell line. Despite expressing *ABCB1* gene, we could not detect ABCB1 protein in HCT116 by western blot (Fig. 7.6).

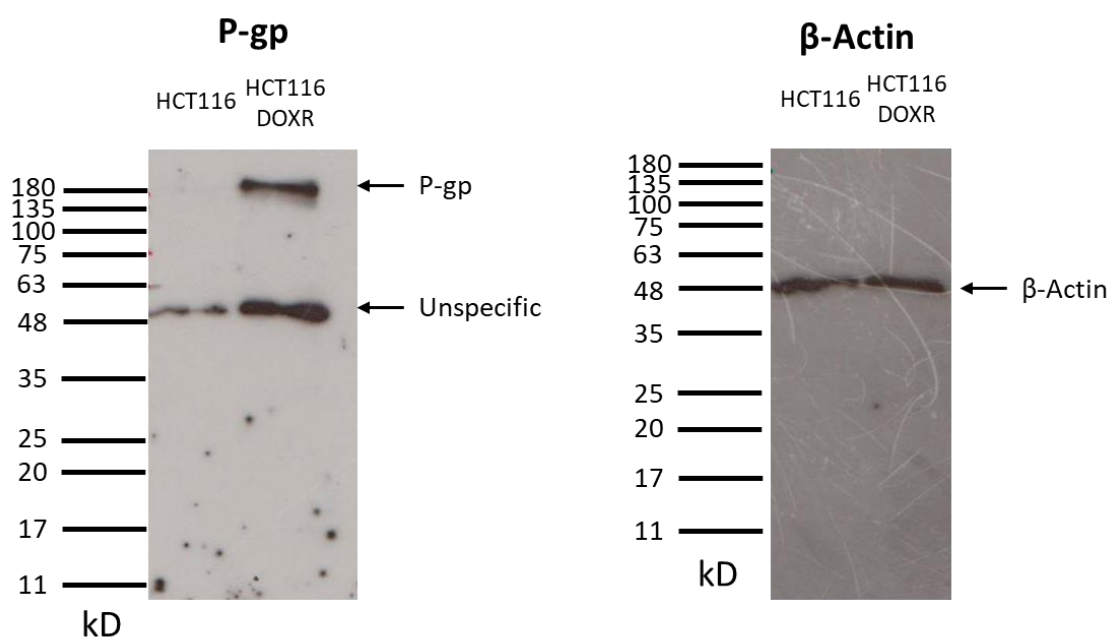


Fig. 7.6 Western blot of ABCB1 and β -Actin (control) in HCT116 and HCT116 DR.

We decided to repeat our silencing experiments in HCT116 DR to see if we could revert the resistance. After incubating HCT116 DR with DOX and AuNP@ASO at optimal conditions we could not observe significant alterations in cell viability. Again, this raised the question if the existing protein was still active, despite inhibition of synthesis. To confirm that we tried to add Tariquidar to block the active protein and at the same time silence *ABCB1* mRNA. This way we wanted to see if we could increase the effect Tariquidar by adding AuNP@ASO. We tested 10, 30, and 60 nM of tariquidar with AuNP@ASO and in all cases AuNP@ASO plus tariquidar and tariquidar alone, showed the same effect, at 24 h or 48 h exposure. This means that despite blocking the active protein the silencing is not being efficient at reverting the resistant phenotype (Fig. 7.7).

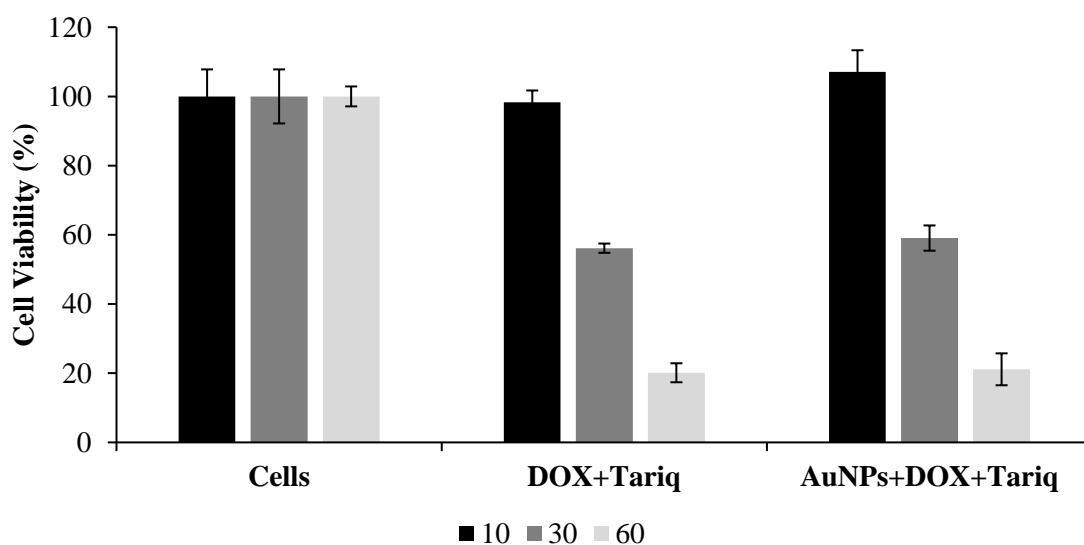


Fig. 7.7 Cell viability of HCT116 DR exposed to different concentrations of Tariquidar (10, 30, 60 nM) and DOX (3.6 μ M) with and without AuNP@ASO

Although not conclusive we can propose a hypothesis to these results. AuNP@ASO can silence *ABCB1* in HCT116 but it has no effect, since basal protein levels could not be detected. In HCT116 DR, a cell line that expresses *ABCB1* in higher levels, we assumed that AuNP@ASO had a similar silencing effect, however it was not confirmed. This inefficient silencing effect of AuNP@ASO might be due to accumulation of mutations after several passages in *ABCB1*. Genetic instability has been described in long term passage in cell culture [474–479]. Another possibility is that HCT116 DR might have different optimal conditions for effective silencing compared to HCT116. To confirm this last hypothesis, we should perform a mRNA expression analysis for HCT116 DR upon incubation with AuNP@ASO and optimize the silencing conditions for this cell line.

7.4 Conclusions

In this chapter we synthesized a nanoformulation of AuNP and an ASO to silence *ABCB1* gene. We showed that it is possible to downregulate the expression of *ABCB1* by using AuNP@ASO, with optimal conditions at 50 nM of antisense oligo and 48 h exposure in HCT116 cells. Although we

observed an expression of the *ABCB1* gene, we did not observe the expression of ABCB1 by western blot nor any evidence of its activity was observed since there was no effect in the presence of tariquidar. Despite the efficacy in *ABCB1* silencing in HCT116, we did not observe any additive effect of DOX in the presence of AuNP@ASO in HCT116 DR. Even when blocking ABCB1 protein, AuNP@ASO did not show an increasing effect to the blocker. We propose that the silencing conditions of HCT116 could be different from HCT116 DR, leading to an inefficient silencing. Optimization of silencing conditions for the resistant cell line ought to be performed to conclude the viability of this approach for acquired resistance cancer.

CHAPTER 8 – CONCLUSIONS AND FUTURE PERSPECTIVES

8.1 Conclusions

Acquired drug resistance by cancer cells is one of the main reasons for therapeutic failure. Therefore, the development of new therapeutic compounds that can overcome this resistance are widely needed. In this thesis we demonstrated that the novel water-soluble molecule, Zn(II) coordination compound (ZnD) exhibits a with high cytotoxic activity towards colorectal carcinoma (HCT116) and one lung cancer cell line (H1975) without impacting healthy cells (fibroblasts), either in monolayer or in a 3D culture. We showed that ZnD induces cell death by intrinsic apoptosis following cell cycle arrest in S phase but without noticeable genotoxicity.

To further our knowledge on cancer cell resistance to chemotherapy and on how to circumvent it, we developed a cell line resistant to DOX derived from HCT116 (HCT116 DR). We then showed that the ABCB1 efflux pump is the main mechanism responsible for the acquired resistance, since it is markedly upregulated in these resistant cells. Still, ZnD was able to kill HCT116 DR, bypassing the efflux pump. This way, ZnD can be taken as a good example to tackle this type of resistance, since cells do not seem to be able to remove the compound via efflux pumps.

Nanomedicine, in special AuNP, are attractive due to their low toxicity and capacity to interact with small molecules in a plethora of medical applications, namely on smart vectorization of compounds and treatments. So, we decided to vectorize ZnD on a gold nanoparticle to increase efficacy in tackling cell growth of both normal and resistant cells. Our nanoconjugate showed increased toxicity against the studied cell lines, decreasing the respective IC₅₀. Active targeting is settled to direct therapeutics selectively to the target cells and tissues, thus sparing healthy tissues from the deleterious effect of chemotherapy. Cetuximab is a monoclonal antibody that may be used as an effective targeting molecule. As such, we grafted Cetuximab to our nanoconjugates, providing for selective targeting capability and, consequently, increased cell uptake of ZnD. This targeting resulted in enhanced selectivity towards cancer cells *in vitro*. Also, *in vivo* studies proved the potential of the new nanoformulation, reducing tumour size in mice xenografts. Still, additional studies are required to confirm the full potential of the targeting strategy.

It is in general believed that combination therapy can be a more efficient therapeutic strategy than monotherapy. For that reason, we tried to take advantage of the photo-hyperthermia of AuNP and tested a combined photo-chemotherapy. We proved that spherical 14nm AuNP have a photoconversion efficiency of 77% when irradiated with a green laser, which is much higher than conventional NIR. We showed that cancer cells are more sensitive to hyperthermia than fibroblasts, and that photothermal therapy alone could reduce a breast cancer cell line viability by 60%, which was potentiated when used in combination with DOX. CoD, which is a promising chemotherapeutic agent against cancer cells, from the same family of ZnD, was able to kill HCT116 cell line, refractory to DOX therapy and in combination with AuNP enhanced phototherapy, selectively killing resistant cancer cells while sparing healthy tissues. This combined therapy has great potential to be translated to clinical settings, since

green lasers are commonly used for skin and retinal treatment because they can cauterize blood vessels precisely.

For that reason, we tested the viability of using AuNP coupled to green laser irradiation to arrest angiogenesis. It is one of the major milestones of the development of solid tumours, either sensitive or resistant to chemotherapy. We showed that AuNP conjugated to anti-angiogenic peptide may be used as efficacious photothermal agents, desaturating haemoglobin via an extremely focalized irradiation and at the same time inhibiting neovascularisation through NPR-1 blockage. We proved that the anti-angiogenic effect *in vivo* acts via down regulation of the VEGF pathway. The proposed combination of chemo- and phototherapy selectively destroys blood vessels critical for tumour supply and progression, which might become a valuable strategy for cancer treatment.

In the end of our work we synthesized a nanoformulation of AuNP and an ASO to silence ABCB1 gene. We showed that it is possible to downregulate the expression of ABCB1 by using AuNP ASO, however we did not observe any additive effect of DOX in the presence of AuNP@ASO in HCT116 DR. Even when blocking ABCB1 protein AuNP@ASO did not show an increasing effect to the blocker. As the regulation of efflux pumps in cells are complex, further studies needed to be performed to develop a gene therapy strategy to circumvent drug resistance.

8.2 Final considerations and future perspectives

In the beginning of this project we defined five topics we wanted to explore to expand the knowledge in the fight against resistant cancer. Throughout the chapters we addressed these topics, answering some questions, and leaving some for further work. In the first topic, i) Characterization of novel chemical agents in biological context, whose mechanism may override existing drug resistance/adaptation mechanism from tumour cells, we were pioneers with the characterization of the ZnD compound that might be a future second line of treatment for colorectal, or lung cancer. To get there, it would be important to know more about the cellular interaction mechanisms of this compound, i.e. to understand its mechanism of internalization by cancer and healthy cells. It would be interesting to block some active/passive transporters and check if we could see a reduction in ZnD cytotoxicity. Following its intracellular path could also give us some answers on its molecular targets. One approach could be to tag the molecule with a fluorophore and try to follow it by microscopy. The problem is that by modifying the molecule we could also be modifying its internalization pathway and mechanism of action. We also described for the first time the development of a new cell line resistant to DOX (HCT116 DR), whose resistance mechanism is due to ABCB1 overexpression, and the ability of ZnD to circumvent its resistance. Is this effect only for this type of resistance mechanism? Testing for a similar efficacy of ZnD in other resistant cell lines (due to different resistance mechanisms) could be extremely important to prove its value. Also, a better knowledge of the genomic alterations resulting from the continuous exposure of cancer cells to DOX such as changes in cell metabolism, are of utmost importance for finding personalized medicines. Whole genome sequencing, RNAseq, and mass

spectrometry to compare with the parental cell line would allow a better understanding of the constitutive genomic expression and metabolic alterations.

The next topic we proposed to address was ii) Targeted vectorization of compounds using AuNP towards active targeting to tumour cells and loading of effector cargos and assessment of therapeutic effect *in vitro* and *in vivo*. Our results clearly show *in vitro* and *in vivo* the advantage of vectorizing ZnD in a nanoparticle formulation. The vectorization revealed to be an effective strategy *in vivo*, especially when the total dosage was given in a single administration. Since 20× the dosage revealed no acute toxicity it would be important to test the effect of increasing concentrations of the nanoformulation. It would be interesting to proceed with studies of toxicity *in vivo*, of other organs, calculate the circulation time, half-life, excretion mechanism of the nanoformulation and perform long term survival studies. It is also important to test the formulation against other cell lines. Due to the promising results against DOX resistant cell line and depending on the results of the proposed pre-clinical trials, clinical trials could give us a definite answer on the feasibility of bringing this product to the clinic. The advantage of Cetux targeting was not conclusive. Raising the question of the advantage of active targeting over nanoparticle passive targeting. What is more, for each layer of complexity we add to a formulation we must always weight its cost/benefit to the final product. Antibodies such as Cetux are expensive and can increase the cost of the formulation. Unless further results reveal a drastic increase in the formulation efficacy and/or reduction of side effects, cetuximab targeting should not be used. The third proposed topic of this thesis was iii) the use of AuNP for photothermal conversion towards directed hyperthermia capable of effectively killing cancer cells, and tackle survival/evasion mechanism (e.g. arrest neo-angiogenesis). Only a few papers describe the use of hyperthermia using AuNP and visible irradiation. There is a general preference to explore NIR irradiation, due to the advantage in tissue penetration. In my opinion, visible irradiation has several advantages over NIR, especially in superficial or accessible tumours, that make it more suitable for tumour/tissue ablation. As it is visible you can precisely see the irradiation site without need of a guide light; only the irradiation focus is affected, not affecting other tissues, and it has an increased effect in blood vessels, destroying tissue blood supply. In this thesis, we showed the efficacy of this strategy *in vitro*, killing sensitive and resistant cancer cells to chemotherapy. Testing the performance of visible irradiation *in vivo* would elucidate the feasibility of this approach in clinical settings. It would be interesting to test this approach in mice or CAM xenografts, by administering AuNP, which would be irradiated after accumulation in the tumour. By combining *in vivo* chemotherapy, with hyperthermia and blood vessel ablation, we would be attacking a tumour in different fronts, reducing the probability of acquiring resistances.

Another topic we proposed to explore was iv) Specific and selective gene silencing to switch off critical genes responsible for drug resistance, thus increasing the efficacy of the compounds and decrease resistance. It was the least explored topic in this thesis. We showed that AuNP can be used as gene silencing moieties, downregulating *ABCB1*. However, the regulation mechanism of efflux pumps is not linear, therefore were not able to observe significant reduction in cell viability derived from gene

silencing. Further testing would be needed to better understand the effect of silencing *ABCBI* mRNA, in the overall protein expression levels.

The last topic proposed was v) combining the approaches in a single AuNP formulation, providing cues to optimize cancer cell killing, circumventing drug resistance and decreasing toxic side effect. We showed the advantages of combining therapy strategies. We combined novel ZnD chemotherapy compounds with AuNP. We further combined AuNP with hyperthermia and chemotherapy. The next step would be to combine all these strategies in a single platform, ZnD and AntiP peptide functionalized in AuNP irradiated with visible laser for hyperthermia and test it *in vivo*. The combination of these strategies that have different mechanisms of action in tumour cells, not only reduces the possibility of resistances, but was also proven to be effective in resistant tumours.

One of the biggest revolutions enabled by nanotechnology is the possibility of theragnostic, which was not explored in this thesis. Regarding that matter, imaging tools, such as x-ray fluorescence, or photoacoustic, could be used to visualize the accumulation of AuNP in tumour. This enables the specific irradiation of marked tissue, localizing metastasis.

In a distant future we can envision the use of a similar approach as the ones developed in this thesis in the clinics, where patients are injected with a nanoformulation that not only points the tumour location but can be directly irradiated, specifically killing cancer cells and surrounding blood vessels with precision, performing real time theragnostic. Coupling all the concepts of this thesis with robotic surgery used nowadays, it would be possible to have a fully autonomous surgeon robot that 3D scans patients, looking for tumour targeted AuNP and applies a laser mediated hyperthermia treatment. I hope for a time when cancer treatment side effects shall be a thing of the past, and cancer will be as harmless as the common flu.

REFERENCES

1. Bray F, Ferlay J, Soerjomataram I, Siegel RL, Torre LA, Jemal A. Global cancer statistics 2018: GLOBOCAN estimates of incidence and mortality worldwide for 36 cancers in 185 countries. *CA Cancer J Clin*. 2018;68:394–424. doi:10.3322/caac.21492.
2. Jönsson B, Hofmarcher T, Lindgren P, Wilking N. The cost and burden of cancer in the European Union 1995–2014. *Eur J Cancer*. 2016;66:162–70. doi:10.1016/j.ejca.2016.06.022.
3. Ferlay J, Colombet M, Soerjomataram I, Dyba T, Randi G, Bettio M, et al. Cancer incidence and mortality patterns in Europe: Estimates for 40 countries and 25 major cancers in 2018. *Eur J Cancer*. 2018;103:356–87. doi:10.1016/j.ejca.2018.07.005.
4. Cooper G. The Development and Causes of Cancer. In: *The Cell: A Molecular Approach*. 2nd edition. Sunderland, MA: Sinauer Associates; 2000.
5. Loud JT, Murphy J. Cancer Screening and Early Detection in the 21(st) Century. *Semin Oncol Nurs*. 2017;33:121–8. doi:10.1016/j.soncn.2017.02.002.
6. Anand P, Kunnumakkara AB, Sundaram C, Harikumar KB, Tharakan ST, Lai OS, et al. Cancer is a preventable disease that requires major lifestyle changes. *Pharm Res*. 2008;25:2097–116. doi:10.1007/s11095-008-9661-9.
7. Weiderpass E. Lifestyle and cancer risk. *J Prev Med Public Health*. 2010;43:459–71.
8. Khan N, Afaq F, Mukhtar H. Lifestyle as risk factor for cancer: Evidence from human studies. *Cancer Lett*. 2010;293:133–43. doi:10.1016/j.canlet.2009.12.013.
9. Golemis EA, Scheet P, Beck TN, Scolnick EM, Hunter DJ, Hawk E, et al. Molecular mechanisms of the preventable causes of cancer in the United States. *Genes Dev*. 2018;32:868–902. doi:10.1101/gad.314849.118.
10. Koeffler HP, McCormick F, Denny C. Molecular mechanisms of cancer. *West J Med*. 1991;155:505–14.
11. Hanahan D, Weinberg RA. Hallmarks of Cancer: The Next Generation. *Cell*. 2011;144:646–74. doi:10.1016/j.cell.2011.02.013.
12. Lemmon MA, Schlessinger J, Ferguson KM. The EGFR family: not so prototypical receptor tyrosine kinases. *Cold Spring Harb Perspect Biol*. 6:a020768–a020768. doi:10.1101/cshperspect.a020768.
13. Lemmon MA, Schlessinger J. Cell signaling by receptor tyrosine kinases. *Cell*. 2010;141:1117–

34.

14. Jones RG, Thompson CB. Tumor suppressors and cell metabolism: a recipe for cancer growth. *Genes Dev.* 2009;23:537–48.

15. Engel BE, Cress WD, Santiago-Cardona PG. The retinoblastoma protein: a master tumor suppressor acts as a link between cell cycle and cell adhesion. *Cell Health Cytoskelet.* 2015;7:1–10. doi:10.2147/CHC.S28079.

16. Liu J, Zhang C, Hu W, Feng Z. Tumor suppressor p53 and its mutants in cancer metabolism. *Cancer Lett.* 2015;356 2 Pt A:197–203. doi:10.1016/j.canlet.2013.12.025.

17. Elmore S. Apoptosis: a review of programmed cell death. *Toxicol Pathol.* 2007;35:495–516. doi:10.1080/01926230701320337.

18. Nagata S. Apoptosis and Clearance of Apoptotic Cells. *Annu Rev Immunol.* 2018;36:489–517. doi:10.1146/annurev-immunol-042617-053010.

19. Letai A. Apoptosis and Cancer. *Annu Rev Cancer Biol.* 2017;1:275–94. doi:10.1146/annurev-cancerbio-050216-121933.

20. Soini Y, Pääkkö P, Lehto VP. Histopathological evaluation of apoptosis in cancer. *Am J Pathol.* 1998;153:1041–53. doi:10.1016/S0002-9440(10)65649-0.

21. Lopez J, Tait SWG. Mitochondrial apoptosis: killing cancer using the enemy within. *Br J Cancer.* 2015;112:957. <https://doi.org/10.1038/bjc.2015.85>.

22. Ren D, Tu H-C, Kim H, Wang GX, Bean GR, Takeuchi O, et al. BID, BIM, and PUMA are essential for activation of the BAX- and BAK-dependent cell death program. *Science.* 2010;330:1390–3.

23. Shay JW, Wright WE. Hayflick, his limit, and cellular ageing. *Nat Rev Mol Cell Biol.* 2000;1:72–6. doi:10.1038/35036093.

24. Blasco MA. Telomeres and human disease: ageing, cancer and beyond. *Nat Rev Genet.* 2005;6:611–22. doi:10.1038/nrg1656.

25. Correia AL, Bissell MJ. The tumor microenvironment is a dominant force in multidrug resistance. *Drug Resist Updat.* 2012;15:39–49. doi:<https://doi.org/10.1016/j.drug.2012.01.006>.

26. Abadjian M-CZ, Edwards WB, Anderson CJ. Imaging the Tumor Microenvironment BT - Tumor Immune Microenvironment in Cancer Progression and Cancer Therapy. In: Kalinski P, editor. Cham: Springer International Publishing; 2017. p. 229–57. doi:10.1007/978-3-319-67577-0_15.

27. Vaupel P, Multhoff G. Hypoxia-/HIF-1 α -Driven Factors of the Tumor Microenvironment Impeding Antitumor Immune Responses and Promoting Malignant Progression BT - Oxygen Transport to Tissue XL. In: Thews O, LaManna JC, Harrison DK, editors. Cham: Springer International Publishing; 2018. p. 171–5. doi:10.1007/978-3-319-91287-5_27.
28. Huang Y, Lin D, Taniguchi CM. Hypoxia inducible factor (HIF) in the tumor microenvironment: friend or foe? *Sci China Life Sci.* 2017;60:1114–24. doi:10.1007/s11427-017-9178-y.
29. Sormendi S, Wielockx B. Hypoxia Pathway Proteins As Central Mediators of Metabolism in the Tumor Cells and Their Microenvironment. *Front Immunol.* 2018;9:40.
30. Gwangwa MV, Joubert AM, Visagie MH. Crosstalk between the Warburg effect, redox regulation and autophagy induction in tumourigenesis. *Cell Mol Biol Lett.* 2018;23:20. doi:10.1186/s11658-018-0088-y.
31. DeBerardinis RJ, Lum JJ, Hatzivassiliou G, Thompson CB. The biology of cancer: metabolic reprogramming fuels cell growth and proliferation. *Cell Metab.* 2008;7:11–20.
32. Hsu PP, Sabatini DM. Cancer Cell Metabolism: Warburg and Beyond. *Cell.* 2008;134:703–7. doi:10.1016/j.cell.2008.08.021.
33. Tsai M-J, Chang W-A, Huang M-S, Kuo P-L. Tumor microenvironment: a new treatment target for cancer. *ISRN Biochem.* 2014;2014:351959. doi:10.1155/2014/351959.
34. Lu J. The Warburg metabolism fuels tumor metastasis. *Cancer Metastasis Rev.* 2019. doi:10.1007/s10555-019-09794-5.
35. Kennedy KM, Dewhirst MW. Tumor metabolism of lactate: the influence and therapeutic potential for MCT and CD147 regulation. *Future Oncol.* 2010;6:127–48. doi:10.2217/fon.09.145.
36. Feron O. Pyruvate into lactate and back: From the Warburg effect to symbiotic energy fuel exchange in cancer cells. *Radiother Oncol.* 2009;92:329–33. doi:10.1016/j.radonc.2009.06.025.
37. Semenza GL. Tumor metabolism: cancer cells give and take lactate. *J Clin Invest.* 2008;118:3835–7. doi:10.1172/JCI37373.
38. Folkman J, Mendelsohn J, Howley PM, Israel MA, Liotta LA. The molecular basis of cancer. *J Mendelson, PM Howley, MA Israele, LA Liotta.* 1995;:206–32.
39. Mazure NM, Chen EY, Laderoute KR, Giaccia AJ. Induction of Vascular Endothelial Growth Factor by Hypoxia Is Modulated by a Phosphatidylinositol 3-Kinase/Akt Signaling Pathway in Ha-ras-Transformed Cells Through a Hypoxia Inducible Factor-1 Transcriptional Element. *Blood.*

1997;90:3322 LP – 3331.

40. De Palma M, Biziato D, Petrova T V. Microenvironmental regulation of tumour angiogenesis. *Nat Rev Cancer*. 2017;17:457. <https://doi.org/10.1038/nrc.2017.51>.

41. Klein D. The Tumor Vascular Endothelium as Decision Maker in Cancer Therapy. *Front Oncol*. 2018;8:367. doi:10.3389/fonc.2018.00367.

42. Nishida N, Yano H, Nishida T, Kamura T, Kojiro M. Angiogenesis in cancer. *Vasc Health Risk Manag*. 2006;2:213–9. doi:10.2147/vhrm.2006.2.3.213.

43. Yadav L, Puri N, Rastogi V, Satpute P, Sharma V. Tumour Angiogenesis and Angiogenic Inhibitors: A Review. *J Clin Diagn Res*. 2015;9:XE01–5. doi:10.7860/JCDR/2015/12016.6135.

44. Claesson-Welsh L, Welsh M, Ito N, Anand-Apte B, Soker S, Zetter B, et al. Angiostatin induces endothelial cell apoptosis and activation of focal adhesion kinase independently of the integrin-binding motif RGD. *Proc Natl Acad Sci U S A*. 1998;95:5579–83. doi:10.1073/pnas.95.10.5579.

45. Lucas R, Holmgren L, Garcia I, Jimenez B, Mandriota SJ, Borlat F, et al. Multiple Forms of Angiostatin Induce Apoptosis in Endothelial Cells. *Blood*. 1998;92:4730 LP – 4741. <http://www.bloodjournal.org/content/92/12/4730.abstract>.

46. André T, Kotelevets L, Vaillant J-C, Coudray AM, Weber L, Prévot S, et al. Vegf, vegf-B, vegf-C and their receptors KDR, FLT-1 and FLT-4 during the neoplastic progression of human colonic mucosa. *Int J Cancer*. 2000;86:174–81. doi:10.1002/(SICI)1097-0215(20000415)86:2<174::AID-IJC5>3.0.CO;2-E.

47. George ML, Tutton MG, Janssen F, Arnaout A, Abulafi AM, Eccles SA, et al. VEGF-A, VEGF-C, and VEGF-D in colorectal cancer progression. *Neoplasia*. 2001;3:420–7.

48. Furudoi A, Tanaka S, Haruma K, Kitadai Y, Yoshihara M, Chayama K, et al. Clinical significance of vascular endothelial growth factor C expression and angiogenesis at the deepest invasive site of advanced colorectal carcinoma. *Oncology*. 2002;62:157–66.

49. Kurebayashi J, Otsuki T, Kunisue H, Mikami Y, Tanaka K, Yamamoto S, et al. Expression of vascular endothelial growth factor (VEGF) family members in breast cancer. *Jpn J Cancer Res*. 1999;90:977–81.

50. Gunningham SP, Currie MJ, Han C, Robinson BA, Scott PA, Harris AL, et al. The short form of the alternatively spliced flt-4 but not its ligand vascular endothelial growth factor C is related to lymph node metastasis in human breast cancers. *Clin Cancer Res*. 2000;6:4278–86.

51. Kinoshita J, Kitamura K, Kabashima A, Saeki H, Tanaka S, Sugimachi K. Clinical significance of vascular endothelial growth factor-C (VEGF-C) in breast cancer. *Breast Cancer Res Treat.* 2001;66:159–64.
52. Skobe M, Hawighorst T, Jackson DG, Prevo R, Janes L, Velasco P, et al. Induction of tumor lymphangiogenesis by VEGF-C promotes breast cancer metastasis. *Nat Med.* 2001;7:192–8.
53. Decaussin M, Sartelet H, Robert C, Moro D, Claraz C, Brambilla C, et al. Expression of vascular endothelial growth factor (VEGF) and its two receptors (VEGF-R1-Flt1 and VEGF-R2-Flk1/KDR) in non-small cell lung carcinomas (NSCLCs): correlation with angiogenesis and survival. *J Pathol.* 1999;188:369–77.
54. Niki T, Iba S, Tokunou M, Yamada T, Matsuno Y, Hirohashi S. Expression of vascular endothelial growth factors A, B, C, and D and their relationships to lymph node status in lung adenocarcinoma. *Clin Cancer Res.* 2000;6:2431–9.
55. Kajita T, Ohta Y, Kimura K, Tamura M, Tanaka Y, Tsunezuka Y, et al. The expression of vascular endothelial growth factor C and its receptors in non-small cell lung cancer. *Br J Cancer.* 2001;85:255–60.
56. O-charoenrat P, Rhys-Evans P, Eccles SA. Expression of vascular endothelial growth factor family members in head and neck squamous cell carcinoma correlates with lymph node metastasis. *Cancer.* 2001;92:556–68.
57. Jussila L, Valtola R, Partanen TA, Salven P, Heikkila P, Matikainen MT, et al. Lymphatic endothelium and Kaposi's sarcoma spindle cells detected by antibodies against the vascular endothelial growth factor receptor-3. *Cancer Res.* 1998;58:1599–604.
58. Ohta Y, Shridhar V, Bright RK, Kalemkerian GP, Du W, Carbone M, et al. VEGF and VEGF type C play an important role in angiogenesis and lymphangiogenesis in human malignant mesothelioma tumours. *Br J Cancer.* 1999;81:54–61.
59. Garnier L, Gkoutidi A-O, Hugues S. Tumor-Associated Lymphatic Vessel Features and Immunomodulatory Functions. *Front Immunol.* 2019;10:720. doi:10.3389/fimmu.2019.00720.
60. Farnsworth RH, Karnezis T, Maciburko SJ, Mueller SN, Stacker SA. The Interplay Between Lymphatic Vessels and Chemokines. *Front Immunol.* 2019;10:518. doi:10.3389/fimmu.2019.00518.
61. Vajdic CM, van Leeuwen MT. Cancer incidence and risk factors after solid organ transplantation. *Int J cancer.* 2009;125:1747–54.
62. Goedert JJ, Coté TR, Virgo P, Scoppa SM, Kingma DW, Gail MH, et al. Spectrum of AIDS-

associated malignant disorders. *Lancet*. 1998;351:1833–9. doi:10.1016/S0140-6736(97)09028-4.

63. Vinay DS, Ryan EP, Pawelec G, Talib WH, Stagg J, Elkord E, et al. Immune evasion in cancer: Mechanistic basis and therapeutic strategies. *Semin Cancer Biol*. 2015;35:S185–98. doi:https://doi.org/10.1016/j.semcancer.2015.03.004.

64. Steven A, Seliger B. The Role of Immune Escape and Immune Cell Infiltration in Breast Cancer. *Breast Care (Basel)*. 2018;13:16–21.

65. Muenst S, Läubli H, Soysal SD, Zippelius A, Tzankov A, Hoeller S. The immune system and cancer evasion strategies: therapeutic concepts. *J Intern Med*. 2016;279:541–62. doi:10.1111/joim.12470.

66. Swann JB, Smyth MJ. Immune surveillance of tumors. *J Clin Invest*. 2007;117:1137–46.

67. Fridman WH, Remark R, Goc J, Giraldo NA, Becht E, Hammond SA, et al. The immune microenvironment: a major player in human cancers. *Int Arch Allergy Immunol*. 2014;164:13–26.

68. Joyce JA, Fearon DT. T cell exclusion, immune privilege, and the tumor microenvironment. *Science*. 2015;348:74–80.

69. Galdiero MR, Bonavita E, Barajon I, Garlanda C, Mantovani A, Jaillon S. Tumor associated macrophages and neutrophils in cancer. *Immunobiology*. 2013;218:1402–10.

70. Netea MG, Joosten LAB. Trained Immunity and Local Innate Immune Memory in the Lung. *Cell*. 2018;175:1463–5.

71. Italiani P, Boraschi D. From Monocytes to M1/M2 Macrophages: Phenotypical vs. Functional Differentiation. *Front Immunol*. 2014;5:514.

72. Goswami KK, Ghosh T, Ghosh S, Sarkar M, Bose A, Baral R. Tumor promoting role of anti-tumor macrophages in tumor microenvironment. *Cell Immunol*. 2017;316:1–10.

73. Jeong H, Hwang I, Kang SH, Shin HC, Kwon SY. Tumor-Associated Macrophages as Potential Prognostic Biomarkers of Invasive Breast Cancer. *J Breast Cancer*. 2019;22:38–51. doi:10.4048/jbc.2019.22.e5.

74. Prenen H, Mazzone M. Tumor-associated macrophages: a short compendium. *Cell Mol Life Sci*. 2019;76:1447–58.

75. Mantovani A, Ponzetta A, Inforzato A, Jaillon S. Innate immunity, inflammation and tumour progression: double-edged swords. *J Intern Med*. 2019;285:524–32. doi:10.1111/joim.12886.

76. Mantovani A, Barajon I, Garlanda C. IL-1 and IL-1 regulatory pathways in cancer progression and therapy. *Immunol Rev.* 2018;281:57–61.
77. DeNardo DG, Andreu P, Coussens LM. Interactions between lymphocytes and myeloid cells regulate pro- versus anti-tumor immunity. *Cancer Metastasis Rev.* 2010;29:309–16. doi:10.1007/s10555-010-9223-6.
78. Hui L, Chen Y. Tumor microenvironment: Sanctuary of the devil. *Cancer Lett.* 2015;368:7–13.
79. Labiano S, Palazon A, Melero I. Immune response regulation in the tumor microenvironment by hypoxia. *Semin Oncol.* 2015;42:378–86.
80. Bruno A, Mortara L, Baci D, Noonan DM, Albini A. Myeloid Derived Suppressor Cells Interactions With Natural Killer Cells and Pro-angiogenic Activities: Roles in Tumor Progression. *Frontiers in Immunology.* 2019;10:771.
81. Schupp J, Krebs FK, Zimmer N, Trzeciak E, Schuppan D, Tuettgenberg A. Targeting myeloid cells in the tumor sustaining microenvironment. *Cell Immunol.* 2017.
82. Pickup MW, Mouw JK, Weaver VM. The extracellular matrix modulates the hallmarks of cancer. *EMBO Rep.* 2014;15:1243–53.
83. Kai F, Drain AP, Weaver VM. The Extracellular Matrix Modulates the Metastatic Journey. *Dev Cell.* 2019;49:332–46.
84. Trivanovic D, Krstic J, Djordjevic IO, Mojsilovic S, Santibanez JF, Bugarski D, et al. The Roles of Mesenchymal Stromal/Stem Cells in Tumor Microenvironment Associated with Inflammation. *Mediators Inflamm.* 2016;2016:7314016.
85. Rivera-Cruz Cosette M.;Shearer JJ;Figueired. NMML. The Immunomodulatory Effects of Mesenchymal Stem Cell Polarization within the Tumor Microenvironment Niche. *Stem Cells Int.* 2017;2017. doi:10.1155/2017/4015039.
86. Sanford-Crane H, Abrego J, Sherman HM. Fibroblasts as Modulators of Local and Systemic Cancer Metabolism. *Cancers .* 2019;11.
87. Yoshida H, Lareau CA, Ramirez RN, Rose SA, Maier B, Wroblewska A, et al. The cis-Regulatory Atlas of the Mouse Immune System. *Cell.* 2019;176:897-912.e20.
88. Liu T, Zhou L, Li D, Andl T, Zhang Y. Cancer-Associated Fibroblasts Build and Secure the Tumor Microenvironment. *Front cell Dev Biol.* 2019;7:60. doi:10.3389/fcell.2019.00060.
89. Vahidian F, Duijf PHG, Safarzadeh E, Derakhshani A, Baghbanzadeh A, Baradaran B.

Interactions between cancer stem cells, immune system and some environmental components: Friends or foes? *Immunol Lett.* 2019;208:19–29. doi:<https://doi.org/10.1016/j.imlet.2019.03.004>.

90. Pearson GW. Control of Invasion by Epithelial-to-Mesenchymal Transition Programs during Metastasis. *J Clin Med.* 2019;8:646. doi:[10.3390/jcm8050646](https://doi.org/10.3390/jcm8050646).

91. Yao Q, Kou L, Tu Y, Zhu L. MMP-Responsive ‘Smart’ Drug Delivery and Tumor Targeting. *Trends Pharmacol Sci.* 2018;39:766–81. doi:<https://doi.org/10.1016/j.tips.2018.06.003>.

92. Netea-Maier RT, Smit JWA, Netea MG. Metabolic changes in tumor cells and tumor-associated macrophages: A mutual relationship. *Cancer Lett.* 2018;413:102–9.

93. Roma-Rodrigues C, Fernandes AR, Baptista PV. Exosome in tumour microenvironment: overview of the crosstalk between normal and cancer cells. *Biomed Res Int.* 2014;2014:179486. doi:[10.1155/2014/179486](https://doi.org/10.1155/2014/179486).

94. Hannafon BN, Ding W-Q. Intercellular communication by exosome-derived microRNAs in cancer. *Int J Mol Sci.* 2013;14:14240–69.

95. Franzen Carrie A.;Simms PE ;Va. HAF ;Forema. KE ;Ku. PC ;Gupt. GN. Characterization of Uptake and Internalization of Exosomes by Bladder Cancer Cells. *Biomed Res Int.* 2014;2014. doi:[10.1155/2014/619829](https://doi.org/10.1155/2014/619829).

96. Roma-Rodrigues C, Pereira F, Alves de Matos AP, Fernandes M, Baptista P V, Fernandes AR. Smuggling gold nanoparticles across cell types - A new role for exosomes in gene silencing. *Nanomedicine.* 2017;13:1389–98.

97. Chen W, Jiang J, Xia W, Huang J. Tumor-Related Exosomes Contribute to Tumor-Promoting Microenvironment: An Immunological Perspective. *J Immunol Res.* 2017;2017:1073947.

98. Eddy DM. Screening for Colorectal Cancer. *Ann Intern Med.* 1990;113:373–84. doi:[10.7326/0003-4819-113-5-373](https://doi.org/10.7326/0003-4819-113-5-373).

99. Fleming M, Ravula S, Tatishchev SF, Wang HL. Colorectal carcinoma: Pathologic aspects. *J Gastrointest Oncol.* 2012;3:153–73. doi:[10.3978/j.issn.2078-6891.2012.030](https://doi.org/10.3978/j.issn.2078-6891.2012.030).

100. Tomlinson I, Ilyas M, Johnson V, Davies A, Clark G, Talbot I, et al. A comparison of the genetic pathways involved in the pathogenesis of three types of colorectal cancer. *J Pathol.* 1998;184:148–52. doi:[10.1002/\(SICI\)1096-9896\(199802\)184:2<148::AID-PATH986>3.0.CO;2-M](https://doi.org/10.1002/(SICI)1096-9896(199802)184:2<148::AID-PATH986>3.0.CO;2-M).

101. Travis WD, Brambilla E, Riely GJ. New Pathologic Classification of Lung Cancer: Relevance for Clinical Practice and Clinical Trials. *J Clin Oncol.* 2013;31:992–1001.

doi:10.1200/JCO.2012.46.9270.

102. Mountain CF. Revisions in the International System for Staging Lung Cancer. *Chest*. 1997;111:1710–7. doi:<https://doi.org/10.1378/chest.111.6.1710>.

103. Dent R, Trudeau M, Pritchard KI, Hanna WM, Kahn HK, Sawka CA, et al. Triple-Negative Breast Cancer: Clinical Features and Patterns of Recurrence. *Clin Cancer Res*. 2007;13:4429 LP – 4434. doi:10.1158/1078-0432.CCR-06-3045.

104. Li CI, Uribe DJ, Daling JR. Clinical characteristics of different histologic types of breast cancer. *Br J Cancer*. 2005;93:1046–52. doi:10.1038/sj.bjc.6602787.

105. Benjamin DJ. The efficacy of surgical treatment of cancer – 20years later. *Med Hypotheses*. 2014;82:412–20. doi:<https://doi.org/10.1016/j.mehy.2014.01.004>.

106. Wyld L, Audisio RA, Poston GJ. The evolution of cancer surgery and future perspectives. *Nat Rev Clin Oncol*. 2014;12:115. <https://doi.org/10.1038/nrclinonc.2014.191>.

107. Holder-Murray J, Dozois EJ. Minimally invasive surgery for colorectal cancer: past, present, and future. *Int J Surg Oncol*. 2011;2011:490917. doi:10.1155/2011/490917.

108. Pennathur A, Abbas G, Christie N, Landreneau R, Luketich JD. Video assisted thoracoscopic surgery and lobectomy, sublobar resection, radiofrequency ablation, and stereotactic radiosurgery: advances and controversies in the management of early stage non-small cell lung cancer. *Curr Opin Pulm Med*. 2007;13:267–70.

109. Friedman M, Mikityansky I, Kam A, Libutti SK, Walther MM, Neeman Z, et al. Radiofrequency ablation of cancer. *Cardiovasc Intervent Radiol*. 2004;27:427–34. doi:10.1007/s00270-004-0062-0.

110. Mascaro A, Farina M, Gigli R, Vitelli CE, Fortunato L. Recent advances in the surgical care of breast cancer patients. *World J Surg Oncol*. 2010;8:5. doi:10.1186/1477-7819-8-5.

111. Yan Y, Olszewski AE, Hoffman MR, Zhuang P, Ford CN, Dailey SH, et al. Use of Lasers in Laryngeal Surgery. *J Voice*. 2010;24:102–9. doi:10.1016/j.jvoice.2008.09.006.

112. Ontario HQ. Robotic Surgical System for Radical Prostatectomy: A Health Technology Assessment. *Ont Health Technol Assess Ser*. 2017;17:1–172. <https://www.ncbi.nlm.nih.gov/pubmed/28744334>.

113. Koh DH, Jang WS, Park JW, Ham WS, Han WK, Rha KH, et al. Efficacy and Safety of Robotic Procedures Performed Using the da Vinci Robotic Surgical System at a Single Institute in Korea:

Experience with 10000 Cases. *Yonsei Med J.* 2018;59:975–81. doi:10.3349/ymj.2018.59.8.975.

114. Chen HHW, Kuo MT. Improving radiotherapy in cancer treatment: Promises and challenges. *Oncotarget.* 2017;8:62742–58. doi:10.18632/oncotarget.18409.

115. Baskar R, Lee KA, Yeo R, Yeoh K-W. Cancer and radiation therapy: current advances and future directions. *Int J Med Sci.* 2012;9:193–9. doi:10.7150/ijms.3635.

116. Baker S, Dahele M, Lagerwaard FJ, Senan S. A critical review of recent developments in radiotherapy for non-small cell lung cancer. *Radiat Oncol.* 2016;11:115. doi:10.1186/s13014-016-0693-8.

117. Glatzer M, Schmid S, Radovic M, Früh M, Putora PM. The role of radiation therapy in the management of small cell lung cancer. *Breathe.* 2017;13:e87 LP-e94. doi:10.1183/20734735.009617.

118. Häfner MF, Debus J. Radiotherapy for Colorectal Cancer: Current Standards and Future Perspectives. *Visc Med.* 2016;32:172–7. doi:10.1159/000446486.

119. Balaji K, Subramanian B, Yadav P, Anu Radha C, Ramasubramanian V. Radiation therapy for breast cancer: Literature review. *Med Dosim.* 2016;41:253–7.

120. Morris DE, Emami B, Mauch PM, Konski AA, Tao ML, Ng AK, et al. Evidence-based review of three-dimensional conformal radiotherapy for localized prostate cancer: an ASTRO outcomes initiative. *Int J Radiat Oncol Biol Phys.* 2005;62:3–19.

121. Keall PJ, Nguyen DT, O'Brien R, Zhang P, Happersett L, Bertholet J, et al. Review of Real-Time 3-Dimensional Image Guided Radiation Therapy on Standard-Equipped Cancer Radiation Therapy Systems: Are We at the Tipping Point for the Era of Real-Time Radiation Therapy? *Int J Radiat Oncol Biol Phys.* 2018;102:922–31.

122. Chabner BA, Roberts TG. Chemotherapy and the war on cancer. *Nat Rev Cancer.* 2005;5:65–72. doi:10.1038/nrc1529.

123. Arruebo M, Vilaboa N, Sáez-Gutierrez B, Lambea J, Tres A, Valladares M, et al. Assessment of the evolution of cancer treatment therapies. *Cancers (Basel).* 2011;3:3279–330. doi:10.3390/cancers3033279.

124. Seshacharyulu P, Ponnusamy MP, Haridas D, Jain M, Ganti AK, Batra SK. Targeting the EGFR signaling pathway in cancer therapy. *Expert Opin Ther Targets.* 2012;16:15–31. doi:10.1517/14728222.2011.648617.

125. Arora A, Scholar EM. Role of Tyrosine Kinase Inhibitors in Cancer Therapy. *J Pharmacol Exp*

Ther. 2005;315:971 LP – 979. doi:10.1124/jpet.105.084145.

126. Abdulkareem IH, Zurmi IB. Review of hormonal treatment of breast cancer. *Niger J Clin Pract.* 2012;15:9–14.

127. Prat A, Baselga J. The role of hormonal therapy in the management of hormonal-receptor-positive breast cancer with co-expression of HER2. *Nat Clin Pract Oncol.* 2008;5:531. <https://doi.org/10.1038/ncponc1179>.

128. Thomas A, Rajan A, Giaccone G. Tyrosine kinase inhibitors in lung cancer. *Hematol Oncol Clin North Am.* 2012;26:589–viii. doi:10.1016/j.hoc.2012.02.001.

129. Pabla B. Colon cancer and the epidermal growth factor receptor: Current treatment paradigms, the importance of diet, and the role of chemoprevention. *World J Clin Oncol.* 2015;6:133.

130. van Hellemond IEG, Geurts SME, Tjan-Heijnen VCG. Current Status of Extended Adjuvant Endocrine Therapy in Early Stage Breast Cancer. *Curr Treat Options Oncol.* 2018;19:26. doi:10.1007/s11864-018-0541-1.

131. Fabian CJ. The what, why and how of aromatase inhibitors: hormonal agents for treatment and prevention of breast cancer. *Int J Clin Pract.* 2007;61:2051–63. doi:10.1111/j.1742-1241.2007.01587.x.

132. Jameera Begam A, Jubie S, Nanjan MJ. Estrogen receptor agonists/antagonists in breast cancer therapy: A critical review. *Bioorg Chem.* 2017;71:257–74.

133. Lobo RA. Hormone-replacement therapy: current thinking. *Nat Rev Endocrinol.* 2016;13:220. <https://doi.org/10.1038/nrendo.2016.164>.

134. Hortobagyi GN. Anthracyclines in the treatment of cancer. An overview. *Drugs.* 1997;54 Suppl 4:1–7.

135. McGowan J V, Chung R, Maulik A, Piotrowska I, Walker JM, Yellon DM. Anthracycline Chemotherapy and Cardiotoxicity. *Cardiovasc drugs Ther.* 2017;31:63–75. doi:10.1007/s10557-016-6711-0.

136. Thorn CF, Oshiro C, Marsh S, Hernandez-Boussard T, McLeod H, Klein TE, et al. Doxorubicin pathways: pharmacodynamics and adverse effects. *Pharmacogenet Genomics.* 2011;21:440–6. doi:10.1097/FPC.0b013e328333ffb56.

137. Tacar O, Sriamornsak P, Dass CR. Doxorubicin: An update on anticancer molecular action, toxicity and novel drug delivery systems. *J Pharm Pharmacol.* 2013;65:157–70.

138. Octavia Y, Tocchetti CG, Gabrielson KL, Janssens S, Crijns HJ, Moens AL. Doxorubicin-

induced cardiomyopathy: From molecular mechanisms to therapeutic strategies. *J Mol Cell Cardiol.* 2012;52:1213–25. doi:<https://doi.org/10.1016/j.yjmcc.2012.03.006>.

139. Cheng J, Gu Y-J, Cheng SH, Wong W-T. Surface Functionalized Gold Nanoparticles for Drug Delivery. *Journal of Biomedical Nanotechnology.* 9:1362–9. <https://doi.org/10.1166/jbn.2013.1536>.

140. Arif IS, Hooper CL, Greco F, Williams AC, Boateng SY. Increasing doxorubicin activity against breast cancer cells using PPAR γ -ligands and by exploiting circadian rhythms. *Br J Pharmacol.* 2013;169:1178–88. doi:10.1111/bph.12202.

141. Raposo LR, Roma-Rodrigues C, Jesus J, Martins LMDRS, Pombeiro AJ, Baptista P V, et al. Targeting canine mammary tumours via gold nanoparticles functionalized with promising Co(II) and Zn(II) compounds. *Vet Comp Oncol.* 2017;15:1537–42. doi:10.1111/vco.12298.

142. Zhang X, Teodoro JG, Nadeau JL. Intratumoral gold-doxorubicin is effective in treating melanoma in mice. *Nanomedicine Nanotechnology, Biol Med.* 2015;11:1365–75. doi:<https://doi.org/10.1016/j.nano.2015.04.001>.

143. Mohan P, Rapoport N. Doxorubicin as a Molecular Nanotheranostic Agent: Effect of Doxorubicin Encapsulation in Micelles or Nanoemulsions on the Ultrasound-Mediated Intracellular Delivery and Nuclear Trafficking. *Mol Pharm.* 2010;7:1959–73. doi:10.1021/mp100269f.

144. Zhao N, Woodle MC, Mixson AJ. Advances in delivery systems for doxorubicin. *J Nanomed Nanotechnol.* 2018;9:519. doi:10.4172/2157-7439.1000519.

145. Hossain MK, Cho H-Y, Kim K-J, Choi J-W. In situ monitoring of doxorubicin release from biohybrid nanoparticles modified with antibody and cell-penetrating peptides in breast cancer cells using surface-enhanced Raman spectroscopy. *Biosens Bioelectron.* 2015;71:300–5. doi:10.1016/j.bios.2015.04.053.

146. Gabizon A, Shmeeda H, Barenholz Y. Pharmacokinetics of Pegylated Liposomal Doxorubicin. *Clin Pharmacokinet.* 2003;42:419–36. doi:10.2165/00003088-200342050-00002.

147. Jungwirth U, Kowol CR, Keppler BK, Hartinger CG, Berger W, Heffeter P. Anticancer Activity of Metal Complexes: Involvement of Redox Processes. *Antioxid Redox Signal.* 2011;15:1085–127. doi:10.1089/ars.2010.3663.

148. Frezza M, Hindo S, Chen D, Davenport A, Schmitt S, Tomco D, et al. Novel metals and metal complexes as platforms for cancer therapy. *Curr Pharm Des.* 2010;16:1813–25.

149. Yang H, Villani RM, Wang H, Simpson MJ, Roberts MS, Tang M, et al. The role of cellular reactive oxygen species in cancer chemotherapy. *J Exp Clin Cancer Res.* 2018;37:266.

doi:10.1186/s13046-018-0909-x.

150. Ndagi U, Mhlongo N, Soliman ME. Metal complexes in cancer therapy – An update from drug design perspective. *Drug Des Devel Ther.* 2017;11:599–616.

151. Desoize B. Metals and metal compounds in cancer treatment. *Anticancer Res.* 2004;24:1529–44.

152. Miliotou AN, Papadopoulou LC. CAR T-cell Therapy: A New Era in Cancer Immunotherapy. *Curr Pharm Biotechnol.* 2018;19:5–18.

153. Coulson A, Levy A, Gossell-Williams M. Monoclonal Antibodies in Cancer Therapy: Mechanisms, Successes and Limitations. *West Indian Med J.* 2014;63:650–4. doi:10.7727/wimj.2013.241.

154. Peterson GM, Thomas J, Yee KC, Kosari S, Naunton M, Olesen IH. Monoclonal antibody therapy in cancer: When two is better (and considerably more expensive) than one. *J Clin Pharm Ther.* 2018;43:925–30.

155. Spano JP, Lagorce C, Atlan D, Milano G, Domont J, Benamouzig R, et al. Impact of EGFR expression on colorectal cancer patient prognosis and survival. *Ann Oncol.* 2005;16:102–8.

156. Khambata-Ford S, Harbison CT, Hart LL, Awad M, Xu LA, Horak CE, et al. Analysis of potential predictive markers of cetuximab benefit in BMS099, a phase III study of cetuximab and first-line taxane/carboplatin in advanced non-small-cell lung cancer. *J Clin Oncol.* 2010;28:918–27.

157. Haddad RI, Posner M, Hitt R, Cohen EEW, Schulten J, Lefebvre J-L, et al. Induction chemotherapy in locally advanced squamous cell carcinoma of the head and neck: role, controversy, and future directions. *Ann Oncol Off J Eur Soc Med Oncol.* 2018;29:1130–40. doi:10.1093/annonc/mdy102.

158. Mehanna H, Robinson M, Hartley A, Kong A, Foran B, Fulton-Lieuw T, et al. Radiotherapy plus cisplatin or cetuximab in low-risk human papillomavirus-positive oropharyngeal cancer (De-ESCALaTE HPV): an open-label randomised controlled phase 3 trial. *Lancet.* 2019;393:51–60. doi:10.1016/S0140-6736(18)32752-1.

159. Cohen MH, Chen H, Shord S, Fuchs C, He K, Zhao H, et al. Approval summary: Cetuximab in combination with cisplatin or carboplatin and 5-fluorouracil for the first-line treatment of patients with recurrent locoregional or metastatic squamous cell head and neck cancer. *Oncologist.* 2013;18:460–6.

160. Bonner JA, Harari PM, Giralt J, Azarnia N, Shin DM, Cohen RB, et al. Radiotherapy plus

Cetuximab for Squamous-Cell Carcinoma of the Head and Neck. *N Engl J Med.* 2006;354:567–78. doi:10.1056/NEJMoa053422.

161. Yamaoka T, Ohba M, Ohmori T. Molecular-Targeted Therapies for Epidermal Growth Factor Receptor and Its Resistance Mechanisms. *Int J Mol Sci.* 2017;18:2420. doi:10.3390/ijms18112420.

162. Keating GM. Bevacizumab: a review of its use in advanced cancer. *Drugs.* 2014;74:1891–925.

163. Goel HL, Mercurio AM. VEGF targets the tumour cell. *Nat Rev Cancer.* 2013;13:871–82. doi:10.1038/nrc3627.

164. Kubota Y. Tumor angiogenesis and anti-angiogenic therapy. *Keio J Med.* 2012;61:47–56. doi:10.2302/kjm.61.47.

165. Ferrara N, Kerbel RS. Angiogenesis as a therapeutic target. *Nature.* 2005;438:967–74. doi:10.1038/nature04483.

166. Zhao Y, Adjei AA. Targeting Angiogenesis in Cancer Therapy: Moving Beyond Vascular Endothelial Growth Factor. *Oncologist.* 2015;20:660–73. doi:10.1634/theoncologist.2014-0465.

167. Keeler AM, ElMallah MK, Flotte TR. Gene Therapy 2017: Progress and Future Directions. *Clin Transl Sci.* 2017;10:242–8. doi:10.1111/cts.12466.

168. Dunbar CE, High KA, Joung JK, Kohn DB, Ozawa K, Sadelain M. Gene therapy comes of age. *Science (80-).* 2018;359:eaan4672. doi:10.1126/science.aan4672.

169. Anguela XM, High KA. Entering the Modern Era of Gene Therapy. *Annu Rev Med.* 2019;70:273–88. doi:10.1146/annurev-med-012017-043332.

170. Lundstrom K. Viral Vectors in Gene Therapy. *Dis (Basel, Switzerland).* 2018;6:42. doi:10.3390/diseases6020042.

171. Martinovich KM, Shaw NC, Kicic A, Schultz A, Fletcher S, Wilton SD, et al. The potential of antisense oligonucleotide therapies for inherited childhood lung diseases. *Mol Cell Pediatr.* 2018;5:3. doi:10.1186/s40348-018-0081-6.

172. Rinaldi C, Wood MJA. Antisense oligonucleotides: the next frontier for treatment of neurological disorders. *Nat Rev Neurol.* 2017;14:9. <https://doi.org/10.1038/nrneurol.2017.148>.

173. Kumar SRP, Markusic DM, Biswas M, High KA, Herzog RW. Clinical development of gene therapy: results and lessons from recent successes. *Mol Ther - Methods Clin Dev.* 2016;3. doi:10.1038/mtm.2016.34.

174. Behrouzkhia Z, Joveini Z, Keshavarzi B, Eyvazzadeh N, Aghdam RZ. Hyperthermia: How Can It Be Used? *Oman Med J*. 2016;31:89–97. doi:10.5001/omj.2016.19.
175. Wust P, Hildebrandt B, Sreenivasa G, Rau B, Gellermann J, Riess H, et al. Hyperthermia in combined treatment of cancer. *The Lancet-Oncology*. 2002;3:487–97.
176. Issels RD. Hyperthermia adds to chemotherapy. *Eur J Cancer*. 2008;44:2546–54.
177. Christie C, Molina S, Gonzales J, Berg K, Nair RK, Huynh K, et al. Synergistic chemotherapy by combined moderate hyperthermia and photochemical internalization. *Biomed Opt Express*. 2016;7:1240. doi:10.1364/BOE.7.001240.
178. Stakhursky VL, Arabe O, Cheng K-S, Macfall J, Maccarini P, Craciunescu O, et al. Real-time MRI-guided hyperthermia treatment using a fast adaptive algorithm. *Phys Med Biol*. 2009;54:2131–45. doi:10.1088/0031-9155/54/7/019.
179. Zhou Y, Sun J, Yang X. Molecular Imaging-Guided Interventional Hyperthermia in Treatment of Breast Cancer. *Biomed Res Int*. 2015;2015:505269. doi:10.1155/2015/505269.
180. Peeken JC, Vaupel P, Combs SE. Integrating Hyperthermia into Modern Radiation Oncology: What Evidence Is Necessary? *Front Oncol*. 2017;7:132. doi:10.3389/fonc.2017.00132.
181. Mantso T, Vasileiadis S, Anastopoulos I, Voulgaridou GP, Lampri E, Botaitis S, et al. Hyperthermia induces therapeutic effectiveness and potentiates adjuvant therapy with non-targeted and targeted drugs in an in vitro model of human malignant melanoma. *Sci Rep*. 2018;8:10724. doi:10.1038/s41598-018-29018-0.
182. Datta NR, Ordóñez SG, Gaipl US, Paulides MM, Crezee H, Gellermann J, et al. Local hyperthermia combined with radiotherapy and/or chemotherapy: Recent advances and promises for the future. *Cancer Treat Rev*. 2015;41:742–53. doi:10.1016/j.ctrv.2015.05.009.
183. Valdagni R, Amichetti M. Report of long-term follow-up in a randomized trial comparing radiation therapy and radiation therapy plus hyperthermia to metastatic lymph nodes in stage IV head and neck patients. *Int J Radiat Oncol Biol Phys*. 1994;28:163–9.
184. Kouloulias VE, Dardoufas CE, Kouvaris JR, Gennatas CS, Polyzos AK, Gogas HJ, et al. Liposomal doxorubicin in conjunction with reirradiation and local hyperthermia treatment in recurrent breast cancer: a phase I/II trial. *Clin Cancer Res*. 2002;8:374–82.
185. Kouloulias VE, Koukourakis G V, Petridis AK, Gouliamos IK and AD. The Efficacy of Caelyx and Hyperthermia for Anticancer Treatment. *Recent Patents on Anti-Cancer Drug Discovery*. 2007;2:246–50. doi:http://dx.doi.org/10.2174/157489207782497208.

186. Hu T, Li Z, Gao C-Y, Cho CH. Mechanisms of drug resistance in colon cancer and its therapeutic strategies. *World J Gastroenterol*. 2016;22:6876.
187. Housman G, Byler S, Heerboth S, Lapinska K, Longacre M, Snyder N, et al. Drug resistance in cancer: An overview. *Cancers (Basel)*. 2014;6:1769–92.
188. Mansoori B, Mohammadi A, Davudian S, Shirjang S, Baradaran B. The Different Mechanisms of Cancer Drug Resistance: A Brief Review. *Adv Pharm Bull*. 2017;7:339–48. doi:10.15171/apb.2017.041.
189. Shaloam Dasari and Paul Bernard Tchounwou. Cisplatin in cancer therapy: molecular mechanisms of action. *Eur J Pharmacol*. 2015;5:364–78.
190. Singh B, Gupta RS. Mutagenic Responses of Thirteen Anticancer Drugs on Mutation Induction at Multiple Genetic Loci and on Sister Chromatid Exchanges in Chinese Hamster Ovary Cells. *Cancer Res*. 1983;43:577–84.
191. Spaans JN, Goss GD. Drug resistance to molecular targeted therapy and its consequences for treatment decisions in non-small-cell lung cancer. *Front Oncol*. 2014;4:190.
192. Hoffmann U, Kroemer HK. The ABC Transporters MDR1 and MRP2: Multiple Functions in Disposition of Xenobiotics and Drug Resistance. *Drug Metab Rev*. 2004;36:669–701. doi:10.1081/DMR-200033473.
193. Lo Y-L, Liu Y. Reversing Multidrug Resistance in Caco-2 by Silencing MDR1, MRP1, MRP2, and BCL-2/BCL-xL Using Liposomal Antisense Oligonucleotides. *PLoS One*. 2014;9:e90180. <https://doi.org/10.1371/journal.pone.0090180>.
194. Pakunlu RI, Cook TJ, Minko T. Simultaneous Modulation of Multidrug Resistance and Antiapoptotic Cellular Defense by MDR1 and BCL-2 Targeted Antisense Oligonucleotides Enhances the Anticancer Efficacy of Doxorubicin. *Pharm Res*. 2003;20:351–9. doi:10.1023/A:1022687617318.
195. Carper MB, Claudio PP. Clinical potential of gene mutations in lung cancer. *Clin Transl Med*. 2015;4:33. doi:10.1186/s40169-015-0074-1.
196. No Title. <https://www.nano.gov/you/nanotechnology-benefits>. Accessed 30 Jul 2017.
197. nan'otechnology n. *Nat Nanotechnol*. 2006;1:8–10. doi:10.1038/nano.2006.77.
198. Patil M, Mehta DS, Guvva S. Future impact of nanotechnology on medicine and dentistry. *J Indian Soc Periodontol*. 2008;12:34–40. doi:10.4103/0972-124X.44088.
199. Tran S, DeGiovanni P-J, Piel B, Rai P. Cancer nanomedicine: a review of recent success in

drug delivery. *Clin Transl Med.* 2017;6:44. doi:10.1186/s40169-017-0175-0.

200. Grzelczak M, Pérez-Juste J, Mulvaney P, Liz-Marzán LM. Shape control in gold nanoparticle synthesis. *Chem Soc Rev.* 2008;37:1783–91. doi:10.1039/B711490G.

201. Kawamura Go;Nogami MA. Shape-Controlled Metal Nanoparticles and Their Assemblies with Optical Functionalities. *J Nanomater.* 2013;2013. doi:10.1155/2013/631350.

202. Cabral RM, Baptista P V. The Chemistry and Biology of Gold Nanoparticle-Mediated Photothermal Therapy: Promises and Challenges. *Nano Life.* 2013;03:1–18.

203. Sajanalal PR, Sreeprasad TS, Samal AK, Pradeep T. Anisotropic nanomaterials: structure, growth, assembly, and functions. *Nano Rev.* 2011;2:10.3402/nano.v2i0.5883. doi:10.3402/nano.v2i0.5883.

204. Conde J, Ambrosone A, Hernandez Y, Tian F, McCully M, Berry CC, et al. 15 years on siRNA delivery: Beyond the State-of-the-Art on inorganic nanoparticles for RNAi therapeutics. *Nano Today.* 2015;10:421–50. doi:https://doi.org/10.1016/j.nantod.2015.06.008.

205. Gerber A, Bundschuh M, Klingelhofer D, Groneberg DA. Gold nanoparticles: recent aspects for human toxicology. *J Occup Med Toxicol.* 2013;8:32.

206. Conde J, Larginho M, Cordeiro A, Raposo LR, Costa PM, Santos S, et al. Gold-nanobeacons for gene therapy: evaluation of genotoxicity, cell toxicity and proteome profiling analysis. *Nanotoxicology.* 2014;8:521–32.

207. Soenen SJ, Parak WJ, Rejman J, Manshian B. (Intra)Cellular Stability of Inorganic Nanoparticles: Effects on Cytotoxicity, Particle Functionality, and Biomedical Applications. *Chem Rev.* 2015;115:2109–35. doi:10.1021/cr400714j.

208. Nazareus M, Zhang Q, Soliman MG, Del Pino P, Pelaz B, Carregal-Romero S, et al. In vitro interaction of colloidal nanoparticles with mammalian cells: What have we learned thus far? *Beilstein J Nanotechnol.* 2014;5:1477–90.

209. Mironava T, Hadjiargyrou M, Simon M, Jurukovski V, Rafailovich MH. Gold nanoparticles cellular toxicity and recovery: effect of size, concentration and exposure time. *Nanotoxicology.* 2010;4:120–37.

210. Zhang X-D, Wu H-Y, Wu D, Wang Y-Y, Chang J-H, Zhai Z-B, et al. Toxicologic effects of gold nanoparticles in vivo by different administration routes. *Int J Nanomedicine.* 2010;5:771–81.

211. Favi PM, Gao M, Johana Sepulveda Arango L, Ospina SP, Morales M, Pavon JJ, et al. Shape

and surface effects on the cytotoxicity of nanoparticles: Gold nanospheres versus gold nanostars. *J Biomed Mater Res A*. 2015;103:3449–62.

212. Sultana S, Djaker N, Boca-Farcau S, Salerno M, Charnaux N, Astilean S, et al. Comparative toxicity evaluation of flower-shaped and spherical gold nanoparticles on human endothelial cells. *Nanotechnology*. 2015;26:55101.

213. Chu Z, Zhang S, Zhang B, Zhang C, Fang C-Y, Rehor I, et al. Unambiguous observation of shape effects on cellular fate of nanoparticles. *Sci Rep*. 2014;4:4495.

214. Maldiney T, Richard C, Seguin J, Wattier N, Bessodes M, Scherman D. Effect of Core Diameter, Surface Coating, and PEG Chain Length on the Biodistribution of Persistent Luminescence Nanoparticles in Mice. *ACS Nano*. 2011;5:854–62. doi:10.1021/nn101937h.

215. Zhao J, Feng S-S. Effects of PEG tethering chain length of vitamin E TPGS with a Herceptin-functionalized nanoparticle formulation for targeted delivery of anticancer drugs. *Biomaterials*. 2014;35:3340–7. doi:https://doi.org/10.1016/j.biomaterials.2014.01.003.

216. Vinhas R, Cordeiro M, Carlos FF, Mendo S, Fernandes AR, Figueiredo S, et al. Gold nanoparticle-based theranostics: disease diagnostics and treatment using a single nanomaterial. *Nanobiosensors Dis Diagnosis*. 2015;Volume 4:11.

217. Yu MK, Park J, Jon S. Targeting strategies for multifunctional nanoparticles in cancer imaging and therapy. *Theranostics*. 2012;2:3–44.

218. Dreaden EC, Austin LA, Mackey MA, El-Sayed MA. Size matters: gold nanoparticles in targeted cancer drug delivery. *Ther Deliv*. 2012;3:457–78. doi:10.4155/tde.12.21.

219. Kobayashi H, Watanabe R, Choyke PL. Improving conventional enhanced permeability and retention (EPR) effects; What is the appropriate target? *Theranostics*. 2014;4:81–9. doi:10.7150/thno.7193.

220. Maeda H. Macromolecular therapeutics in cancer treatment: The EPR effect and beyond. *J Control Release*. 2012;164:138–44. doi:https://doi.org/10.1016/j.jconrel.2012.04.038.

221. Spivak MY, Bubnov R V, Yemets IM, Lazarenko LM, Tymoshok NO, Ulberg ZR. Development and testing of gold nanoparticles for drug delivery and treatment of heart failure: a theranostic potential for PPP cardiology. *EPMA J*. 2013;4:20. doi:10.1186/1878-5085-4-20.

222. Chanda N, Kattumuri V, Shukla R, Zambre A, Katti K, Upendran A, et al. Bombesin functionalized gold nanoparticles show in vitro and in vivo cancer receptor specificity. *Proc Natl Acad Sci*. 2010;107:8760 LP – 8765. doi:10.1073/pnas.1002143107.

223. Ahmed M, Pan DW, Davis ME. Lack of in vivo antibody dependent cellular cytotoxicity with antibody containing gold nanoparticles. *Bioconjug Chem.* 2015;26:812–6.
224. Qian Y, Qiu M, Wu Q, Tian Y, Zhang Y, Gu N, et al. Enhanced cytotoxic activity of cetuximab in EGFR-positive lung cancer by conjugating with gold nanoparticles. *Sci Rep.* 2014;4:7490.
225. Kuan CT, Wikstrand CJ, Bigner DD. EGF mutant receptor vIII as a molecular target in cancer therapy. *Endocrine-related cancer Endocr Relat Cancer Endocr Relat Cancer.* 2001;8:83–96. <https://erc.bioscientifica.com/view/journals/erc/8/2/11397666.xml>.
226. Karmani L, Labar D, Valembois V, Bouchat V, Nagaswaran PG, Bol A, et al. Antibody-functionalized nanoparticles for imaging cancer: influence of conjugation to gold nanoparticles on the biodistribution of ⁸⁹Zr-labeled cetuximab in mice. *Contrast Media Mol Imaging.* 2013;8:402–8. doi:10.1002/cmml.1539.
227. Kao H-W, Lin Y-Y, Chen C-C, Chi K-H, Tien D-C, Hsia C-C, et al. Biological characterization of cetuximab-conjugated gold nanoparticles in a tumor animal model. *Nanotechnology.* 2014;25:295102. doi:10.1088/0957-4484/25/29/295102.
228. Meyers JD, Cheng Y, Broome A-M, Agnes RS, Schluchter MD, Margevicius S, et al. Peptide-Targeted Gold Nanoparticles for Photodynamic Therapy of Brain Cancer. *Part Part Syst Charact.* 2015;32:448–57. doi:10.1002/ppsc.201400119.
229. Wagner DS, Delk NA, Lukianova-Hleb EY, Hafner JH, Farach-Carson MC, Lapotko DO. The in vivo performance of plasmonic nanobubbles as cell theranostic agents in zebrafish hosting prostate cancer xenografts. *Biomaterials.* 2010;31:7567–74. doi:<https://doi.org/10.1016/j.biomaterials.2010.06.031>.
230. Lukianova-Hleb EY, Ren X, Sawant RR, Wu X, Torchilin VP, Lapotko DO. On-demand intracellular amplification of chemoradiation with cancer-specific plasmonic nanobubbles. *Nat Med.* 2014;20:778. <https://doi.org/10.1038/nm.3484>.
231. Kalli KR, Oberg AL, Keeney GL, Christianson TJH, Low PS, Knutson KL, et al. Folate receptor alpha as a tumor target in epithelial ovarian cancer. *Gynecol Oncol.* 2008;108:619–26. doi:10.1016/j.ygyno.2007.11.020.
232. Bahrami B, Mohammadnia-Afrouzi M, Bakhshaei P, Yazdani Y, Ghalamfarsa G, Yousefi M, et al. Folate-conjugated nanoparticles as a potent therapeutic approach in targeted cancer therapy. *Tumor Biol.* 2015;36:5727–42. doi:10.1007/s13277-015-3706-6.
233. Zhu J, Fu F, Xiong Z, Shen M, Shi X. Dendrimer-entrapped gold nanoparticles modified with

RGD peptide and alpha-tocopheryl succinate enable targeted theranostics of cancer cells. *Colloids Surfaces B Biointerfaces*. 2015;133:36–42. doi:<https://doi.org/10.1016/j.colsurfb.2015.05.040>.

234. Topete A, Alatorre-Meda M, Iglesias P, Villar-Alvarez EM, Barbosa S, Costoya JA, et al. Fluorescent Drug-Loaded, Polymeric-Based, Branched Gold Nanoshells for Localized Multimodal Therapy and Imaging of Tumoral Cells. *ACS Nano*. 2014;8:2725–38. doi:10.1021/nn406425h.

235. Topete A, Alatorre-Meda M, Villar-Alvarez EM, Carregal-Romero S, Barbosa S, Parak WJ, et al. Polymeric-Gold Nanohybrids for Combined Imaging and Cancer Therapy. *Adv Healthc Mater*. 2014;3:1309–25. doi:10.1002/adhm.201400023.

236. Zhong J, Wen L, Yang S, Xiang L, Chen Q, Xing D. Imaging-guided high-efficient photoacoustic tumor therapy with targeting gold nanorods. *Nanomedicine Nanotechnology, Biol Med*. 2015;11:1499–509. doi:<https://doi.org/10.1016/j.nano.2015.04.002>.

237. Lu W, Zhang G, Zhang R, Flores LG, Huang Q, Gelovani JG, et al. Tumor Site-Specific Silencing of $\text{NF-}\kappa\text{B p65}$ by Targeted Hollow Gold Nanosphere-Mediated Photothermal Transfection. *Cancer Res*. 2010;70:3177 LP – 3188. doi:10.1158/0008-5472.CAN-09-3379.

238. Chiche J, Brahimi-Horn MC, Pouyssegur J. Tumour hypoxia induces a metabolic shift causing acidosis: a common feature in cancer. *J Cell Mol Med*. 2010;14:771–94. doi:10.1111/j.1582-4934.2009.00994.x.

239. Arachchige MCM, Reshetnyak YK, Andreev OA. Advanced targeted nanomedicine. *J Biotechnol*. 2015;202:88–97. doi:<https://doi.org/10.1016/j.jbiotec.2015.01.009>.

240. Chen J, Glaus C, Laforest R, Zhang Q, Yang M, Gidding M, et al. Gold Nanocages as Photothermal Transducers for Cancer Treatment. *Small*. 2010;6:811–7. doi:10.1002/sml.200902216.

241. Yavuz MS, Cheng Y, Chen J, Cobley CM, Zhang Q, Rycenga M, et al. Gold nanocages covered by smart polymers for controlled release with near-infrared light. *Nat Mater*. 2009;8:935. <https://doi.org/10.1038/nmat2564>.

242. Cobley CM, Au L, Chen J, Xia Y. Targeting gold nanocages to cancer cells for photothermal destruction and drug delivery. *Expert Opin Drug Deliv*. 2010;7:577–87. doi:10.1517/17425240903571614.

243. Conde J, Dias JT, Graça V, Moros M, Baptista P V., de la Fuente JM. Revisiting 30 years of biofunctionalization and surface chemistry of inorganic nanoparticles for nanomedicine. *Front Chem*. 2014;2 July:1–27.

244. Chen H, Zhang X, Dai S, Ma Y, Cui S, Achilefu S, et al. Multifunctional gold nanostar conjugates for tumor imaging and combined photothermal and chemo-therapy. *Theranostics*. 2013;3:633–49. doi:10.7150/thno.6630.
245. Chen H, Li S, Li B, Ren X, Li S, Mahounga DM, et al. Folate-modified gold nanoclusters as near-infrared fluorescent probes for tumor imaging and therapy. *Nanoscale*. 2012;4:6050–64. doi:10.1039/C2NR31616A.
246. Jing L, Liang X, Li X, Lin L, Yang Y, Yue X, et al. Mn-porphyrin conjugated Au nanoshells encapsulating doxorubicin for potential magnetic resonance imaging and light triggered synergistic therapy of cancer. *Theranostics*. 2014;4:858–71.
247. You J, Zhang R, Xiong C, Zhong M, Melancon M, Gupta S, et al. Effective Photothermal Chemotherapy Using Doxorubicin-Loaded Gold Nanospheres That Target EphB4 Receptors in Tumors. *Cancer Res*. 2012;72:4777 LP – 4786. doi:10.1158/0008-5472.CAN-12-1003.
248. Dhar S, Daniel WL, Giljohann DA, Mirkin CA, Lippard SJ. Polyvalent Oligonucleotide Gold Nanoparticle Conjugates as Delivery Vehicles for Platinum(IV) Warheads. *J Am Chem Soc*. 2009;131:14652–3. doi:10.1021/ja9071282.
249. Conde J, Oliva N, Artzi N. Implantable hydrogel embedded dark-gold nanoswitch as a theranostic probe to sense and overcome cancer multidrug resistance. *Proc Natl Acad Sci*. 2015;112:E1278 LP-E1287. doi:10.1073/pnas.1421229112.
250. Shi P, Liu Z, Dong K, Ju E, Ren J, Du Y, et al. A Smart “Sense-Act-Treat” System: Combining a Ratiometric pH Sensor with a Near Infrared Therapeutic Gold Nanocage. *Adv Mater*. 2014;26:6635–41. doi:10.1002/adma.201402522.
251. Svenson S, Wolfgang M, Hwang J, Ryan J, Eliasof S. Preclinical to clinical development of the novel camptothecin nanopharmaceutical CRLX101. *J Control Release*. 2011;153:49–55. doi:10.1016/j.jconrel.2011.03.007.
252. Blasiak B, van Veggel FCJM, Tomanek B. Applications of Nanoparticles for MRI Cancer Diagnosis and Therapy. *J Nanomater*. 2013;2013:1–12. doi:10.1155/2013/148578.
253. Bao C, Conde J, Curtin J, Artzi N, Tian F, Cui D. Bioresponsive antisense DNA gold nanobeacons as a hybrid in vivo theranostics platform for the inhibition of cancer cells and metastasis. *Sci Rep*. 2015;5. doi:10.1038/srep12297.
254. Huang X, Hu Q, Braun GB, Pallaoro A, Morales DP, Zasadzinski J, et al. Light-activated RNA interference in human embryonic stem cells. *Biomaterials*. 2015;63:70–9.

doi:10.1016/j.biomaterials.2015.06.006.

255. Chen Z, Zhang L, He Y, Shen Y, Li Y. Enhanced shRNA Delivery and ABCG2 Silencing by Charge-Reversible Layered Nanocarriers. *Small*. 2014;11:952–62. doi:10.1002/sml.201401397.

256. Bishop CJ, Tzeng SY, Green JJ. Degradable polymer-coated gold nanoparticles for co-delivery of DNA and siRNA. *Acta Biomater*. 2015;11:393–403. doi:10.1016/j.actbio.2014.09.020.

257. Kim HJ, Takemoto H, Yi Y, Zheng M, Maeda Y, Chaya H, et al. Precise Engineering of siRNA Delivery Vehicles to Tumors Using Polyion Complexes and Gold Nanoparticles. *ACS Nano*. 2014;8:8979–91. doi:10.1021/nn502125h.

258. Conde J, Rosa J, de la Fuente JM, Baptista P V. Gold-nanobeacons for simultaneous gene specific silencing and intracellular tracking of the silencing events. *Biomaterials*. 2013;34:2516–23.

259. Cao-Milán R, Liz-Marzán LM. Gold nanoparticle conjugates: recent advances toward clinical applications. *Expert Opin Drug Deliv*. 2014;11:741–52. doi:10.1517/17425247.2014.891582.

260. Webb JA, Bardhan R. Emerging advances in nanomedicine with engineered gold nanostructures. *Nanoscale*. 2014;6:2502. doi:10.1039/c3nr05112a.

261. Yin F, Yang C, Wang Q, Zeng S, Hu R, Lin G, et al. A Light-Driven Therapy of Pancreatic Adenocarcinoma Using Gold Nanorods-Based Nanocarriers for Co-Delivery of Doxorubicin and siRNA. *Theranostics*. 2015;5:818–33. doi:10.7150/thno.11335.

262. Randeria PS, Seeger MA, Wang X-Q, Wilson H, Shipp D, Mirkin CA, et al. siRNA-based spherical nucleic acids reverse impaired wound healing in diabetic mice by ganglioside GM3 synthase knockdown. *Proc Natl Acad Sci*. 2015;112:5573–8. doi:10.1073/pnas.1505951112.

263. Conde J, Ambrosone A, Sanz V, Hernandez Y, Marchesano V, Tian F, et al. Design of multifunctional gold nanoparticles for in vitro and in vivo gene silencing. *ACS Nano*. 2012;6:8316–24.

264. Rosa J, Conde J, de la Fuente JM, Lima JC, Baptista P V. Gold-nanobeacons for real-time monitoring of RNA synthesis. *Biosens Bioelectron*. 2012;36:161–7. doi:10.1016/j.bios.2012.04.006.

265. Conde J, Rosa J, Baptista P. Gold-Nanobeacons as a theranostic system for the detection and inhibition of specific genes. *Protoc Exch*. 2013;:1–35.

266. Conde J, de la Fuente JM, Baptista P V. In vitro transcription and translation inhibition via DNA functionalized gold nanoparticles. *Nanotechnology*. 2010;21:505101. doi:10.1088/0957-4484/21/50/505101.

267. Liu Y, Xu M, Chen Q, Guan G, Hu W, Zhao X, et al. Gold nanorods/mesoporous silica-based

nanocomposite as theranostic agents for targeting near-infrared imaging and photothermal therapy induced with laser. *Int J Nanomedicine*. 2015;:4747. doi:10.2147/ijn.s82940.

268. Lim C-K, Heo J, Shin S, Jeong K, Seo YH, Jang W-D, et al. Nanophotosensitizers toward advanced photodynamic therapy of Cancer. *Cancer Lett*. 2013;334:176–87. doi:10.1016/j.canlet.2012.09.012.

269. Yu J, Hsu C-H, Huang C-C, Chang P-Y. Development of Therapeutic Au–Methylene Blue Nanoparticles for Targeted Photodynamic Therapy of Cervical Cancer Cells. *ACS Appl Mater Interfaces*. 2014;7:432–41. doi:10.1021/am5064298.

270. Zhang Y, Xiong X, Huai Y, Dey A, Hossen MN, Roy RV, et al. Gold Nanoparticles Disrupt Tumor Microenvironment - Endothelial Cell Cross Talk To Inhibit Angiogenic Phenotypes in Vitro. *Bioconjug Chem*. 2019;30:1724–33.

271. Mukherjee P, Bhattacharya R, Wang P, Wang L, Basu S, Nagy JA, et al. Antiangiogenic properties of gold nanoparticles. *Clin Cancer Res*. 2005;11:3530–4.

272. Arvizo RR, Rana S, Miranda OR, Bhattacharya R, Rotello VM, Mukherjee P. Mechanism of anti-angiogenic property of gold nanoparticles: role of nanoparticle size and surface charge. *Nanomedicine*. 2011;7:580–7.

273. Li W, Li X, Liu S, Yang W, Pan F, Yang X-Y, et al. Gold nanoparticles attenuate metastasis by tumor vasculature normalization and epithelial-mesenchymal transition inhibition. *Int J Nanomedicine*. 2017;12:3509–20.

274. Pan F, Yang W, Li W, Yang X-Y, Liu S, Li X, et al. Conjugation of gold nanoparticles and recombinant human endostatin modulates vascular normalization via interruption of anterior gradient 2-mediated angiogenesis. *Tumour Biol*. 2017;39:1010428317708547.

275. Bartczak D, Muskens OL, Sanchez-Elsner T, Kanaras AG, Millar TM. Manipulation of in vitro angiogenesis using peptide-coated gold nanoparticles. *ACS Nano*. 2013;7:5628–36. doi:10.1021/nn402111z.

276. Bartczak D, Muskens OL, Nitti S, Millar TM, Kanaras AG. Nanoparticles for inhibition of in vitro tumour angiogenesis: synergistic actions of ligand function and laser irradiation. *Biomater Sci*. 2015;3:733–41. doi:10.1039/C5BM00053J.

277. Roma-Rodrigues C, Heuer-Jungemann A, Fernandes AR, Kanaras AG, Baptista P V. Peptide-coated gold nanoparticles for modulation of angiogenesis in vivo. *Int J Nanomedicine*. 2016;11:2633–9. doi:10.2147/IJN.S108661.

278. Willmann JK, van Bruggen N, Dinkelborg LM, Gambhir SS. Molecular imaging in drug development. *Nat Rev Drug Discov*. 2008;7:591–607. doi:10.1038/nrd2290.
279. Janib SM, Moses AS, MacKay JA. Imaging and drug delivery using theranostic nanoparticles. *Adv Drug Deliv Rev*. 2010;62:1052–63. doi:10.1016/j.addr.2010.08.004.
280. Hong H, Zhang Y, Sun J, Cai W. Molecular imaging and therapy of cancer with radiolabeled nanoparticles. *Nano Today*. 2009;4:399–413. doi:10.1016/j.nantod.2009.07.001.
281. Lusic H, Grinstaff MW. X-ray-Computed Tomography Contrast Agents. *Chem Rev*. 2012;113:1641–66. doi:10.1021/cr200358s.
282. Hasebroock KM, Serkova NJ. Toxicity of MRI and CT contrast agents. *Expert Opin Drug Metab Toxicol*. 2009;5:403–16. doi:10.1517/17425250902873796.
283. Wang L V, Hu S. Photoacoustic Tomography: In Vivo Imaging from Organelles to Organs. *Science (80-)*. 2012;335:1458–62. doi:10.1126/science.1216210.
284. Shao J, Griffin RJ, Galanzha EI, Kim J-W, Koonce N, Webber J, et al. Photothermal nanodrugs: potential of TNF-gold nanospheres for cancer theranostics. *Sci Rep*. 2013;3. doi:10.1038/srep01293.
285. Dreifuss T, Betzer O, Shilo M, Popovtzer A, Motiei M, Popovtzer R. A challenge for theranostics: is the optimal particle for therapy also optimal for diagnostics? *Nanoscale*. 2015;7:15175–84. doi:10.1039/c5nr03119b.
286. Jang B, Park S, Kang SH, Kim JK, Kim S-K, Kim I-H, et al. Gold nanorods for target selective SPECT/CT imaging and photothermal therapy in vivo. *Quant Imaging Med Surg*. 2012;2:1–11.
287. Kosaka N, Ogawa M, Choyke PL, Kobayashi H. Clinical implications of near-infrared fluorescence imaging in cancer. *Futur Oncol*. 2009;5:1501–11. doi:10.2217/fon.09.109.
288. Kievit FM, Zhang M. Cancer Nanotheranostics: Improving Imaging and Therapy by Targeted Delivery Across Biological Barriers. *Adv Mater*. 2011;23:H217–47. doi:10.1002/adma.201102313.
289. Louie A. Multimodality Imaging Probes: Design and Challenges. *Chem Rev*. 2010;110:3146–95. doi:10.1021/cr9003538.
290. Liu Y, Ashton JR, Moding EJ, Yuan H, Register JK, Fales AM, et al. A Plasmonic Gold Nanostar Theranostic Probe for In Vivo Tumor Imaging and Photothermal Therapy. *Theranostics*. 2015;5:946–60. doi:10.7150/thno.11974.
291. Ke H, Wang J, Tong S, Jin Y, Wang S, Qu E, et al. Gold Nanoshelled Liquid Perfluorocarbon Magnetic Nanocapsules: a Nanotheranostic Platform for Bimodal Ultrasound/Magnetic Resonance

Imaging Guided Photothermal Tumor Ablation. *Theranostics*. 2014;4:12–23. doi:10.7150/thno.7275.

292. Lammers T, Kiessling F, Hennink WE, Storm G. Drug targeting to tumors: Principles, pitfalls and (pre-) clinical progress. *J Control Release*. 2012;161:175–87. doi:10.1016/j.jconrel.2011.09.063.

293. Martins P, Marques M, Coito L, Pombeiro A, Baptista P, Fernandes A. Organometallic Compounds in Cancer Therapy: Past Lessons and Future Directions. *Anticancer Agents Med Chem*. 2014;14:1199–212. doi:10.2174/1871520614666140829124925.

294. Cole JT, Holland NB. Multifunctional nanoparticles for use in theranostic applications. *Drug Deliv Transl Res*. 2015;5:295–309. doi:10.1007/s13346-015-0218-2.

295. Sharma H, Mishra PK, Talegaonkar S, Vaidya B. Metal nanoparticles: a theranostic nanotool against cancer. *Drug Discov Today*. 2015;20:1143–51.

296. Kojima R, Aubel D, Fussenegger M. Novel theranostic agents for next-generation personalized medicine: small molecules, nanoparticles, and engineered mammalian cells. *Curr Opin Chem Biol*. 2015;28:29–38. doi:10.1016/j.cbpa.2015.05.021.

297. Ryu JH, Lee S, Son S, Kim SH, Leary JF, Choi K, et al. Theranostic nanoparticles for future personalized medicine. *J Control Release*. 2014;190:477–84. doi:10.1016/j.jconrel.2014.04.027.

298. Bellan LM, Wu D, Langer RS. Current trends in nanobiosensor technology. *Wiley Interdiscip Rev Nanomedicine Nanobiotechnology*. 2011;3:229–46. doi:10.1002/wnan.136.

299. Cabral RM, Baptista P V. Anti-cancer precision theranostics: a focus on multifunctional gold nanoparticles. *Expert Rev Mol Diagn*. 2014;14:1–12.

300. Kim HJ, Lee S-M, Park K-H, Mun CH, Park Y-B, Yoo K-H. Drug-loaded gold/iron/gold plasmonic nanoparticles for magnetic targeted chemo-photothermal treatment of rheumatoid arthritis. *Biomaterials*. 2015;61:95–102. doi:10.1016/j.biomaterials.2015.05.018.

301. Prabhu P, Patravale V. The Upcoming Field of Theranostic Nanomedicine: An Overview. *J Biomed Nanotechnol*. 2012;8:859–82. doi:10.1166/jbn.2012.1459.

302. Sharma P, Maheshwari R, Tekade M, Tekade R. Nanomaterial Based Approaches for the Diagnosis and Therapy of Cardiovascular Diseases. *Curr Pharm Des*. 2015;21:4465–78. doi:10.2174/1381612821666150910113031.

303. Lapotko D. Plasmonic Nanobubbles as Tunable Cellular Probes for Cancer Theranostics. *Cancers (Basel)*. 2011;3:802–40. doi:10.3390/cancers3010802.

304. Lukianova-Hleb EY, Ren X, Townley D, Wu X, Kupferman ME, Lapotko DO. Plasmonic

Nanobubbles Rapidly Detect and Destroy Drug-Resistant Tumors. *Theranostics*. 2012;2:976–87. doi:10.7150/thno.5116.

305. Muthu MS, Mei L, Feng S-S. Nanotheranostics: advanced nanomedicine for the integration of diagnosis and therapy. *Nanomedicine*. 2014;9:1277–80. doi:10.2217/nmm.14.83.

306. Pillay V, Frank D, Tyagi C, Tomar LK, Choonara YE, du Toit LC, et al. Overview of the role of nanotechnological innovations in the detection and treatment of solid tumors. *Int J Nanomedicine*. 2014;:589. doi:10.2147/ijn.s50941.

307. E. ABRAHAM PETER B. HIMMEL GUY. Management of Rheumatoid Arthritis: Rationale for the Use of Colloidal Metallic Gold. *J Nutr Environ Med*. 1997;7:295–305. doi:10.1080/13590849762411.

308. Libutti SK, Paciotti GF, Byrnes AA, Alexander HR, Gannon WE, Walker M, et al. Phase I and Pharmacokinetic Studies of CYT-6091, a Novel PEGylated Colloidal Gold-rhTNF Nanomedicine. *Clin Cancer Res*. 2010;16:6139–49. doi:10.1158/1078-0432.ccr-10-0978.

309. Kharlamov AN, Tyurnina AE, Veselova VS, Kovtun OP, Shur VY, Gabinsky JL. Silica–gold nanoparticles for atheroprotective management of plaques: results of the NANOM-FIM trial. *Nanoscale*. 2015;7:8003–15. doi:10.1039/c5nr01050k.

310. Grand View Research I. *Nanoparticles Market Analysis by End-Use (Medical & Dentistry, Electronics, Catalysis) and Segment Forecasts to 2020*. San Francisco, CA, USA; 2015.

311. National Nanotechnology Initiative, Federal Budget 2016. <http://www.nano.gov/about-nni/what/funding>. Accessed 29 Jul 2015.

312. Commission of the European Communities: Towards a European Strategy for Nanotechnology. http://ec.europa.eu/research/industrial_technologies/pdf/policy/nano_com_en.pdf. Accessed 29 Jul 2015.

313. Monteiro-Riviere NA, Tran CL, editors. *Nanotoxicology: Progress toward Nanomedicine*, Second Edition. 2nd edition. 2016.

314. Bawa R. FDA and Nanotech: Baby Steps Lead to Regulatory Uncertainty. *Bio-Nanotechnology*. 2013;:720–32. doi:10.1002/9781118451915.ch41.

315. Horizon 2020, Leadership in Enabling and Industrial Technologies: Nanotechnologies, Advanced Materials, Biotechnology and Advanced Manufacturing and Processing Revised. http://ec.europa.eu/research/participants/data/ref/h2020/wp/2014_2015/main/h2020-wp1415-leit-nmp_en.pdf. Accessed 29 Jul 2015.

316. Bosetti R, Ferrandina G, Marneffe W, Scambia G, Vereeck L. Cost-effectiveness of gemcitabine versus PEGylated liposomal doxorubicin for recurrent or progressive ovarian cancer: comparing chemotherapy with nanotherapy. *Nanomedicine*. 2014;9:2175–86. doi:10.2217/nnm.14.150.
317. Markets G. *Nanomaterials in Theranostics*. New York, NY, USA; 2013.
318. Diagaradjane P, Shetty A, Wang JC, Elliott AM, Schwartz J, Shentu S, et al. Modulation of in Vivo Tumor Radiation Response via Gold Nanoshell-Mediated Vascular-Focused Hyperthermia: Characterizing an Integrated Antihypoxic and Localized Vascular Disrupting Targeting Strategy. *Nano Lett*. 2008;8:1492–500. doi:10.1021/nl080496z.
319. Lu W, Xiong C, Zhang G, Huang Q, Zhang R, Zhang JZ, et al. Targeted photothermal ablation of murine melanomas with melanocyte-stimulating hormone analog-conjugated hollow gold nanospheres. *Clin Cancer Res*. 2009;15:876–86.
320. Kirui DK, Khalidov I, Wang Y, Batt CA. Targeted near-IR hybrid magnetic nanoparticles for in vivo cancer therapy and imaging. *Nanomedicine Nanotechnology, Biol Med*. 2013;9:702–11. doi:10.1016/j.nano.2012.11.009.
321. Conde J, Bao C, Cui D, Baptista P V, Tian F. Antibody–drug gold nanoantennas with Raman spectroscopic fingerprints for in vivo tumour theranostics. *J Control Release*. 2014;183:87–93. doi:10.1016/j.jconrel.2014.03.045.
322. Deng H, Zhong Y, Du M, Liu Q, Fan Z, Dai F, et al. Theranostic Self-Assembly Structure of Gold Nanoparticles for NIR Photothermal Therapy and X-Ray Computed Tomography Imaging. *Theranostics*. 2014;4:904–18. doi:10.7150/thno.9448.
323. Zhu J, Zheng L, Wen S, Tang Y, Shen M, Zhang G, et al. Targeted cancer theranostics using alpha-tocopheryl succinate-conjugated multifunctional dendrimer-entrapped gold nanoparticles. *Biomaterials*. 2014;35:7635–46. doi:10.1016/j.biomaterials.2014.05.046.
324. Peng J, Qi T, Liao J, Chu B, Yang Q, Qu Y, et al. Mesoporous Magnetic Gold “Nanoclusters” as Theranostic Carrier for Chemo-Photothermal Co-therapy of Breast Cancer. *Theranostics*. 2014;4:678–92. doi:10.7150/thno.7869.
325. Taruttis A, Lozano N, Nunes A, Jasim DA, Beziere N, Herzog E, et al. siRNA liposome-gold nanorod vectors for multispectral optoacoustic tomography theranostics. *Nanoscale*. 2014;6:13451–6. doi:10.1039/c4nr04164j.
326. Huang P, Rong P, Lin J, Li W, Yan X, Zhang MG, et al. Triphase Interface Synthesis of

Plasmonic Gold Bellflowers as Near-Infrared Light Mediated Acoustic and Thermal Theranostics. *J Am Chem Soc.* 2014;136:8307–13. doi:10.1021/ja503115n.

327. Hembury M, Chiappini C, Bertazzo S, Kalber TL, Drisko GL, Ogunlade O, et al. Gold–silica quantum rattles for multimodal imaging and therapy. *Proc Natl Acad Sci.* 2015;112:1959–64. doi:10.1073/pnas.1419622112.

328. Ruan S, He Q, Gao H. Matrix metalloproteinase triggered size-shrinkable gelatin-gold fabricated nanoparticles for tumor microenvironment sensitive penetration and diagnosis of glioma. *Nanoscale.* 2015;7:9487–96. doi:10.1039/c5nr01408e.

329. Wang S, Teng Z, Huang P, Liu D, Liu Y, Tian Y, et al. Reversibly Extracellular pH Controlled Cellular Uptake and Photothermal Therapy by PEGylated Mixed-Charge Gold Nanostars. *Small.* 2015;11:1801–10. doi:10.1002/sml.201403248.

330. Conde J, Bao C, Tan Y, Cui D, Edelman ER, Azevedo HS, et al. Dual Targeted Immunotherapy via In Vivo Delivery of Biohybrid RNAi-Peptide Nanoparticles to Tumor-Associated Macrophages and Cancer Cells. *Adv Funct Mater.* 2015;25:4183–94. doi:10.1002/adfm.201501283.

331. Galanzha EI, Shashkov E, Sarimollaoglu M, Beenken KE, Basnakian AG, Shirtliff ME, et al. In Vivo Magnetic Enrichment, Photoacoustic Diagnosis, and Photothermal Purging of Infected Blood Using Multifunctional Gold and Magnetic Nanoparticles. *PLoS One.* 2012;7:e45557. doi:10.1371/journal.pone.0045557.

332. Huo D, Ding J, Cui YX, Xia LY, Li H, He J, et al. X-ray CT and pneumonia inhibition properties of gold–silver nanoparticles for targeting MRSA induced pneumonia. *Biomaterials.* 2014;35:7032–41. doi:10.1016/j.biomaterials.2014.04.092.

333. Arifin DR, Long CM, Gilad AA, Alric C, Roux S, Tillement O, et al. Trimodal Gadolinium-Gold Microcapsules Containing Pancreatic Islet Cells Restore Normoglycemia in Diabetic Mice and Can Be Tracked by Using US, CT, and Positive-Contrast MR Imaging. *Radiology.* 2011;260:790–8. doi:10.1148/radiol.11101608.

334. Lee PC, Meisel D. Adsorption and surface-enhanced Raman of dyes on silver and gold sols. *J Phys Chem.* 1982;86:3391–5. doi:10.1021/j100214a025.

335. Rappon M, Syvitski RT. Kinetics of photobleaching of Aberchrome 540 in various solvents: solvent effects. *J Photochem Photobiol A Chem.* 1996;94:243–7. doi:10.1016/1010-6030(95)04216-4.

336. Silva TFS, Smoleński P, Martins LMDRS, Guedes da Silva MFC, Fernandes AR, Luis D, et al. Cobalt and Zinc Compounds Bearing 1,10-Phenanthroline-5,6-dione or 1,3,5-Triaza-7-

phosphaadamantane Derivatives - Synthesis, Characterization, Cytotoxicity, and Cell Selectivity Studies. *Eur J Inorg Chem.* 2013;2013:3651–8. doi:10.1002/ejic.201300197.

337. Martins M, Baptista P V., Mendo AS, Correia C, Videira P, Rodrigues AS, et al. In vitro and in vivo biological characterization of the anti-proliferative potential of a cyclic trinuclear organotin(IV) complex. *Mol BioSyst.* 2016;12:1015–23.

338. Ma Z, Zhang B, Guedes da Silva MFC, Silva J, Mendo AS, Baptista PV, et al. Synthesis, characterization, thermal properties and antiproliferative potential of copper(II) 4'-phenyl-terpyridine compounds. *Dalt Trans.* 2016;45:5339–55. doi:10.1039/C5DT02744F.

339. Lenis-Rojas OA, Roma-Rodrigues C, Fernandes AR, Marques F, Pérez-Fernández D, Guerra-Varela J, et al. Dinuclear Ru^{II} (bipy)₂ Derivatives: Structural, Biological, and in Vivo Zebrafish Toxicity Evaluation. *Inorg Chem.* 2017;56:7127–44.

340. Ghosh S, Barve AC, Kumbhar AA, Kumbhar AS, Puranik VG, Datar PA, et al. Synthesis, characterization, X-ray structure and DNA photocleavage by cis-dichloro bis(diimine) Co(III) complexes. *J Inorg Biochem.* 2006;100:331–343. doi:10.1016/j.jinorgbio.2005.11.022.

341. Yokoyama K, Asakura T, Nakamura N, Ohno H. Chemical modification of cytochrome c by a ruthenium complex containing phenanthroline quinone. *Inorg Chem Commun.* 2006;9:281–3. doi:10.1016/J.INOCHE.2005.11.019.

342. Ali I, A Wani W, Saleem K, Haque A. Platinum compounds: a hope for future cancer chemotherapy. *Anti-Cancer Agents Med Chem (Formerly Curr Med Chem Agents).* 2013;13:296–306.

343. CONSORTIUM S. STRING. 2019. <https://string-db.org/>.

344. Gomes SE, Pereira DM, Roma-Rodrigues C, Fernandes AR, Borralho PM, Rodrigues CMP. Convergence of miR-143 overexpression, oxidative stress and cell death in HCT116 human colon cancer cells. *PLoS One.* 2018;13:e0191607.

345. Yu Y, Xu Z, Hsie AW. Adriamycin induces large deletions as a major type of mutation in CHO cells. *Mutat Res Lett.* 1994;325:91–8.

346. Pusztai L, Wagner P, Ibrahim N, Rivera E, Theriault R, Booser D, et al. Phase II study of tariquidar, a selective P-glycoprotein inhibitor, in patients with chemotherapy-resistant, advanced breast carcinoma. *Cancer.* 2005;104:682–91. doi:10.1002/cncr.21227.

347. Sarto C, Binz PA, Mocarelli P. Heat shock proteins in human cancer. *Electrophoresis.* 2000;21:1218–26.

348. Karsani SA, Saihen NA, Zain RB, Cheong S-C, Abdul Rahman M. Comparative proteomics analysis of oral cancer cell lines: identification of cancer associated proteins. *Proteome Sci.* 2014;12:3. doi:10.1186/1477-5956-12-3.
349. Nicolussi A, D’Inzeo S, Capalbo C, Giannini G, Coppa A. The role of peroxiredoxins in cancer. *Mol Clin Oncol.* 2017;6:139–53. doi:10.3892/mco.2017.1129.
350. Dang DT, Chen F, Kohli M, Rago C, Cummins JM, Dang LH. Glutathione S-Transferase $\pi 1$ Promotes Tumorigenicity in HCT116 Human Colon Cancer Cells. *Cancer Res.* 2005;65:9485 LP – 9494. <http://cancerres.aacrjournals.org/content/65/20/9485.abstract>.
351. Fell VL, Schild-Poulter C. The Ku heterodimer: function in DNA repair and beyond. *Mutat Res Rev Mutat Res.* 2015;763:15–29.
352. Yin J, Ren W, Huang X, Deng J, Li T, Yin Y. Potential Mechanisms Connecting Purine Metabolism and Cancer Therapy. *Front Immunol.* 2018;9:1697. doi:10.3389/fimmu.2018.01697.
353. Gibert B, Hadchity E, Czekalla A, Aloy M-T, Colas P, Rodriguez-Lafrasse C, et al. Inhibition of heat shock protein 27 (HspB1) tumorigenic functions by peptide aptamers. *Oncogene.* 2011;30:3672–81.
354. Miyo M, Konno M, Nishida N, Sueda T, Noguchi K, Matsui H, et al. Metabolic Adaptation to Nutritional Stress in Human Colorectal Cancer. *Sci Rep.* 2016;6:38415.
355. Haynes J, Srivastava J, Madson N, Wittmann T, Barber DL, Nusrat A. Dynamic actin remodeling during epithelial–mesenchymal transition depends on increased moesin expression. *Mol Biol Cell.* 2011;22:4750–64. doi:10.1091/mbc.e11-02-0119.
356. Milone MR, Pucci B, Colangelo T, Lombardi R, Iannelli F, Colantuoni V, et al. Proteomic characterization of peroxisome proliferator-activated receptor-gamma (PPAR γ) overexpressing or silenced colorectal cancer cells unveils a novel protein network associated with an aggressive phenotype. *Mol Oncol.* 2016;10:1344–62.
357. Mathews MB, Hershey JWB. The translation factor eIF5A and human cancer. *Biochim Biophys Acta.* 2015;1849:836–44.
358. Hodgkinson VC, ELFadl D, Agarwal V, Garimella V, Russell C, Long ED, et al. Proteomic identification of predictive biomarkers of resistance to neoadjuvant chemotherapy in luminal breast cancer: A possible role for 14-3-3 theta/tau and tBID? *J Proteomics.* 2012;75:1276–83. doi:<https://doi.org/10.1016/j.jprot.2011.11.005>.
359. Stoimenov I, Helleday T. PCNA on the crossroad of cancer. *Biochem Soc Trans.* 2009;37 Pt

3:605–13.

360. Lecona E, Barrasa JI, Olmo N, Llorente B, Turnay J, Lizarbe MA. Upregulation of Annexin A1 Expression by Butyrate in Human Colon Adenocarcinoma Cells: Role of p53, NF- κ B, and p38 Mitogen-Activated Protein Kinase. *Mol Cell Biol.* 2008;28:4665 LP – 4674. <http://mcb.asm.org/content/28/15/4665.abstract>.

361. Parente L, Solito E. Annexin 1: more than an anti-phospholipase protein. *Inflamm Res.* 2004;53:125–32.

362. Beck HC, Petersen J, Nielsen SJ, Morsczeck C, Jensen PB, Sehested M, et al. Proteomic profiling of human colon cancer cells treated with the histone deacetylase inhibitor belinostat. *Electrophoresis.* 2010;31:2714–21.

363. Bull VH, Fargestad EM, Strozynski M, Thiede B. Temporal proteome profiling of taxol-induced mitotic arrest and apoptosis. *Electrophoresis.* 2010;31:1873–85.

364. Huang Y-H, Chang AYW, Huang C-M, Huang S-W, Chan SHH. Proteomic analysis of lipopolysaccharide-induced apoptosis in PC12 cells. *Proteomics.* 2002;2:1220–8.

365. Lu Y-C, Weng W-C, Lee H. Functional Roles of Calreticulin in Cancer Biology. *Biomed Res Int.* 2015;2015:1–9. doi:10.1155/2015/526524.

366. Coghlin C, Carpenter B, Dundas SR, Lawrie LC, Telfer C, Murray GI. Characterization and over-expression of chaperonin t-complex proteins in colorectal cancer. *J Pathol.* 2006;210:351–7.

367. Duval K, Grover H, Han L-H, Mou Y, Pegoraro AF, Fredberg J, et al. Modeling Physiological Events in 2D vs. 3D Cell Culture. *Physiology (Bethesda).* 2017;32:266–77. doi:10.1152/physiol.00036.2016.

368. Kapalczyńska M, Kolenda T, Przybyła W, Zajączkowska M, Teresiak A, Filas V, et al. 2D and 3D cell cultures - a comparison of different types of cancer cell cultures. *Arch Med Sci.* 2018;14:910–9. doi:10.5114/aoms.2016.63743.

369. Lim F, Sun AM. Microencapsulated islets as bioartificial endocrine pancreas. *Science (80-).* 1980;210:908 LP – 910. doi:10.1126/science.6776628.

370. Andersen T, Auk-Emblem P, Dornish M. 3D Cell Culture in Alginate Hydrogels. *Microarrays (Basel, Switzerland).* 2015;4:133–61. doi:10.3390/microarrays4020133.

371. Bao G, Mitragotri S, Tong S. Multifunctional Nanoparticles for Drug Delivery and Molecular Imaging. *Annu Rev Biomed Eng.* 2013;15:253–82.

372. Conde J, Doria G, Baptista P. Noble Metal Nanoparticles Applications in Cancer. *J Drug Deliv.* 2012;2012:1–12.
373. Bao C, Conde J, Polo E, Pino P, Moros M, Pedro V. A promising road with challenges : where are gold nanoparticles in translational research? *Nanomedicine.* 2014;9(15):2353–70.
374. Baptista P. Gold nanobeacons: a potential nanotheranostics platform. *Nanomedicine (Lond).* 2014;9:2247–50.
375. Martins P, Jesus J, Santos S, Raposo LR, Roma-Rodrigues C, Baptista PV, et al. Heterocyclic anticancer compounds: Recent advances and the paradigm shift towards the use of nanomedicine's tool Box. *Molecules.* 2015;20:16852–91.
376. Millard M, Yakavets I, Zorin V, Kulmukhamedova A, Marchal S, Bezdetnaya L. Drug delivery to solid tumors: The predictive value of the multicellular tumor spheroid model for nanomedicine screening. *Int J Nanomedicine.* 2017;12:7993–8007.
377. Panzarini E, Inguscio V, Anna Tenuzzo B, Carata E, Dini L. Nanomaterials and autophagy: New insights in cancer treatment. *Cancers (Basel).* 2013;5:296–319.
378. Sato Y, Sakurai Y, Kajimoto K, Nakamura T, Yamada Y, Akita H, et al. Innovative Technologies in Nanomedicines: From Passive Targeting to Active Targeting/From Controlled Pharmacokinetics to Controlled Intracellular Pharmacokinetics. *Macromol Biosci.* 2017;17:1–16.
379. Pedrosa P, Vinhas R, Fernandes A, Baptista VP. Gold Nanotheranostics: Proof-of-Concept or Clinical Tool? *Nanomaterials .* 2015;5.
380. Jonker DJ, O'Callaghan CJ, Karapetis CS, Zalcborg JR, Tu D, Au H-J, et al. Cetuximab for the treatment of colorectal cancer. *N Engl J Med.* 2007;357:2040–8.
381. Ohsaki Y, Tanno S, Fujita Y, Toyoshima E, Fujiuchi S, Nishigaki Y, et al. Epidermal growth factor receptor expression correlates with poor prognosis in non-small cell lung cancer patients with p53 overexpression. *Oncol Rep.* 2000;7:603–7.
382. Kim ES, Mauer AM, Jr WNW, Tran HT, Liu D, Lee JJ, et al. A Phase 2 Study of Cetuximab in Combination With Docetaxel in Chemotherapy-Refractory/Resistant Patients With Advanced Nonsmall Cell Lung Cancer. 2016;95:222–42.
383. Rosell R, Robinet G, Szczesna A, Ramlau R, Constenla M, Mennequier BC, et al. Randomized phase II study of cetuximab plus cisplatin/vinorelbine compared with cisplatin/vinorelbine alone as first-line therapy in EGFR-expressing advanced non-small-cell lung cancer. *Ann Oncol.* 2008;19:362–9.

384. Sgambato A, Casaluce F, Maione P, Rossi A, Ciardiello F, Gridelli C. Cetuximab in advanced non-small cell lung cancer (NSCLC): The showdown? *J Thorac Dis.* 2014;6:578–80.
385. Jalal S, Waterhouse D, Edelman MJ, Nattam S, Ansari R, Koneru K, et al. Pemetrexed plus cetuximab in patients with recurrent non-small cell lung cancer (NSCLC): a phase I/II study from the Hoosier Oncology Group. *J Thorac Oncol.* 2009;4:1420–4.
386. Devaiah A, Murchison C. Analysis of 473 US Head and Neck Cancer Trials (1996-2014): Trends, Gaps, and Opportunities. *Otolaryngol Head Neck Surg.* 2016;154:309–14.
387. Yazdi MH, Faramarzi MA, Nikfar S, Abdollahi M. A comprehensive review of clinical trials on EGFR inhibitors such as cetuximab and panitumumab as monotherapy and in combination for treatment of metastatic colorectal cancer. *Avicenna J Med Biotechnol.* 2015;7:134–44.
388. Deng Y, Kurland BF, Wang J, Bi J, Li W, Rao S, et al. High epidermal growth factor receptor expression in metastatic colorectal cancer lymph nodes may be more prognostic of poor survival than in primary tumor. *Am J Clin Oncol Cancer Clin Trials.* 2009;32:245–52.
389. Inamura K, Ninomiya H, Ishikawa Y, Matsubara O. Is the epidermal growth factor receptor status in lung cancers reflected in clinicopathologic features? *Arch Pathol Lab Med—Vol.* 2010;134 January:66–72.
390. Pirker R, Filipits M. Cetuximab in non-small-cell lung cancer. *Transl Lung Cancer Res.* 2012;1:54–60.
391. Bou-Assaly W, Mukherji S. Cetuximab (Erbix). *Am J Neuroradiol.* 2010;31:626–7.
392. Master AM, Sen Gupta A. EGF receptor-targeted nanocarriers for enhanced cancer treatment. *Nanomedicine.* 2012;7:1895–906.
393. Fernandes AR, Jesus J, Martins P, Figueiredo S, Rosa D, Martins LMRDRS, et al. Multifunctional gold-nanoparticles: A nanovectorization tool for the targeted delivery of novel chemotherapeutic agents. *J Control Release.* 2017;245:52–61. doi:10.1016/j.jconrel.2016.11.021.
394. Costa PM. Chapter 4 - Staining Protocols. In: Costa PMBT-TH of HP in AE, editor. Academic Press; 2018. p. 83–117. doi:<https://doi.org/10.1016/B978-0-12-812032-3.00004-6>.
395. Maeda H. Tumor-Selective Delivery of Macromolecular Drugs via the EPR Effect: Background and Future Prospects. *Bioconjug Chem.* 2010;21:797–802. doi:10.1021/bc100070g.
396. Nguone R, Peters A, von Elverfeldt D, Winkler K, Pütz G. Accumulating nanoparticles by EPR: A route of no return. *J Control Release.* 2016;238:58–70. doi:10.1016/j.jconrel.2016.07.028.

397. Bethune G, Bethune D, Ridgway N, Xu Z. Epidermal growth factor receptor (EGFR) in lung cancer: An overview and update. *J Thorac Dis.* 2010;2:48–51.
398. Masuda H, Zhang D. Role of epidermal growth factor receptor in breast cancer. *Breast cancer Res* 2012;136:1–21.
399. Miller DL, El-Ashry D, Cheville a L, Liu Y, McLeskey SW, Kern FG. Emergence of MCF-7 cells overexpressing a transfected epidermal growth factor receptor (EGFR) under estrogen-depleted conditions: evidence for a role of EGFR in breast cancer growth and progression. *Cell growth Differ.* 1994;5 December:1263–74.
400. Hsieh SY, He JR, Hsu CY, Chen WJ, Bera R, Lin KY, et al. Neuregulin/erythroblastic leukemia viral oncogene homolog 3 autocrine loop contributes to invasion and early recurrence of human hepatoma. *Hepatology.* 2011;53:504–16.
401. Colombo V, Lupi M, Falcetta F, Forestieri D, D’Incalci M, Ubezio P. Chemotherapeutic activity of silymarin combined with doxorubicin or paclitaxel in sensitive and multidrug-resistant colon cancer cells. *Cancer Chemother Pharmacol.* 2011;67:369–79.
402. Li J, Liu H, Yu J, Yu H. Chemoresistance to doxorubicin induces epithelial-mesenchymal transition via upregulation of transforming growth factor β signaling in HCT116 colon cancer cells. *Mol Med Rep.* 2015;12:192–8.
403. Larsen MT, Kuhlmann M, Hvam ML, Howard KA. Albumin-based drug delivery: harnessing nature to cure disease. *Mol Cell Ther.* 2016;4:3.
404. Trnkova L, Bousova I, Kubicek V, Drsata J. Binding of naturally occurring hydroxycinnamic acids to bovine serum albumin. *Nat Sci.* 2010;02:563–70. doi:10.4236/ns.2010.26071.
405. Gomathi Sankareswari V, Vinod D, Mahalakshmi A, Alamelu M, Kumaresan G, Ramaraj R, et al. Interaction of oxovanadium(IV)–salphen complexes with bovine serum albumin and their cytotoxicity against cancer. *Dalt Trans.* 2014;43:3260–72. doi:10.1039/C3DT52505H.
406. Bannunah AM, Vllasaliu D, Lord J, Stolnik S. Mechanisms of Nanoparticle Internalization and Transport Across an Intestinal Epithelial Cell Model: Effect of Size and Surface Charge. *Mol Pharm.* 2014;11:4363–73. doi:10.1021/mp500439c.
407. Wang S-H, Lee C-W, Chiou A, Wei P-K. Size-dependent endocytosis of gold nanoparticles studied by three-dimensional mapping of plasmonic scattering images. *J Nanobiotechnology.* 2010;8:33. doi:10.1186/1477-3155-8-33.
408. Xie X, Liao J, Shao X, Li Q, Lin Y. The Effect of shape on Cellular Uptake of Gold

Nanoparticles in the forms of Stars, Rods, and Triangles. *Sci Rep.* 2017;7:3827. doi:10.1038/s41598-017-04229-z.

409. Park J, Ha MK, Yang N, Yoon TH. Flow Cytometry-Based Quantification of Cellular Au Nanoparticles. *Anal Chem.* 2017;89:2449–56. doi:10.1021/acs.analchem.6b04418.

410. Sanger Institute, Center W, Cancer General Hospital M. Genomics of Drug Sensitivity in Cancer_Compound: BIRB 0796. 2016. <http://www.cancerrxgene.org/translation/Drug/1042>.

411. Huang X, El-Sayed MA. Plasmonic photo-thermal therapy (PPTT). *Alexandria J Med.* 2011;47:1–9.

412. Abadeer NS, Murphy CJ. Recent Progress in Cancer Thermal Therapy using Gold Nanoparticles. *J Phys Chem C.* 2016;120:4691–718.

413. Huang X, El-Sayed MA. Gold nanoparticles: Optical properties and implementations in cancer diagnosis and photothermal therapy. *J Adv Res.* 2010;1:13–28.

414. Hirsch LR, Stafford RJ, Bankson JA, Sershen SR, Rivera B, Price RE, et al. Nanoshell-mediated near-infrared thermal therapy of tumors under magnetic resonance guidance. *PNAS.* 2003;100:13549–13554.

415. Elbially N, Abdelhamid M, Youssef T. Low Power Argon Laser-Induced Thermal Therapy for Subcutaneous Ehrlich Carcinoma in Mice Using Spherical Gold Nanoparticles. *J Biomed Nanotechnol.* 2010;6:1–7.

416. El-Sayed IH, Huang X, El-Sayed M a. Selective laser photo-thermal therapy of epithelial carcinoma using anti-EGFR antibody conjugated gold nanoparticles. *Cancer Lett.* 2006;239:129–35.

417. Huang X, Jain PK, El-Sayed IH, El-Sayed M a. Determination of the Minimum Temperature Required for Selective Photothermal Destruction of Cancer Cells with the Use of Immunotargeted Gold Nanoparticles. *Photochem Photobiol.* 2006;82:412.

418. Huang X, Qian W, El-Sayed IH, El-Sayed M a. The potential use of the enhanced nonlinear properties of gold nanospheres in photothermal cancer therapy. *Lasers Surg Med.* 2007;39:747–53.

419. König K. Multiphoton microscopy in life sciences. *J Microsc.* 2000;200 Pt 2:83–104.

420. Zeitels SM, Barbu AM, Landau-zemer T, Lopez-guerra G, Burns JA, Friedman AD, et al. Local Injection of Bevacizumab (Avastin) and Angiolytic KTP Laser Treatment of Recurrent Respiratory Papillomatosis of the Vocal Folds : A Prospective Study. *Ann Otol Rhinol Laryngol.* 2011;120:627–34.

421. Kozak I, Luttrull JK. Modern retinal laser therapy. *Saudi J Ophthalmol.* 2015;29:137–46. doi:10.1016/j.sjopt.2014.09.001.
422. Cheng J, Buys YM. Lasers in Open Angle Glaucoma. 2014;:50–3.
423. Jain S, Hirst DG, O’Sullivan JM. Gold nanoparticles as novel agents for cancer therapy. *Br J Radiol.* 2012;85:101–13.
424. Qin Z, Wang Y, Randrianalisoa J, Raeesi V, Chan WCW, Lipiński W, et al. Quantitative Comparison of Photothermal Heat Generation between Gold Nanospheres and Nanorods. *Sci Rep.* 2016;6:29836. doi:10.1038/srep29836.
425. Mendes R, Pedrosa P, Lima JC, Fernandes AR, Baptista P V. Photothermal enhancement of chemotherapy in breast cancer by visible irradiation of Gold Nanoparticles. *Sci Rep.* 2017;7:10872.
426. Schaaf L, Schwab M, Ulmer C, Heine S, Murdter TE, Schmid JO, et al. Hyperthermia synergizes with chemotherapy by inhibiting PARP1-dependent DNA replication arrest. *Cancer Res.* 2016;76:2868–75.
427. Liang X, Chen C, Zhao Y, Wang PC. Circumventing Tumor Resistance to Chemotherapy by Nanotechnology. *Methods Mol Biol.* 2010;596:467–88.
428. Silva A, Luís D, Santos S, Silva J, Mendo AS, Coito L, et al. Biological characterization of the antiproliferative potential of Co(II) and Sn(IV) coordination compounds in human cancer cell lines: a comparative proteomic approach. *Drug Metabol Drug Interact.* 2013;28. doi:10.1515/dmdi-2013-0015.
429. Luís D V., Silva J, Tomaz AI, de Almeida RFM, Larginho M, Baptista P V., et al. Insights into the mechanisms underlying the antiproliferative potential of a Co(II) coordination compound bearing 1,10-phenanthroline-5,6-dione: DNA and protein interaction studies. *JBIC J Biol Inorg Chem.* 2014;19:787–803. doi:10.1007/s00775-014-1110-0.
430. Navarro JRG, Werts MH V. Resonant light scattering spectroscopy of gold, silver and gold–silver alloy nanoparticles and optical detection in microfluidic channels. *Analyst.* 2013;138:583–92.
431. Jiang K, Smith DA, Pinchuk A. Size-Dependent Photothermal Conversion Efficiencies of Plasmonically Heated Gold Nanoparticles. *J Phys Chem C.* 2013;117:27073–80. doi:10.1021/jp409067h.
432. Raji V, Kumar J, Rejiya CS, Vibin M, Shenoi VN, Abraham A. Selective photothermal efficiency of citrate capped gold nanoparticles for destruction of cancer cells. *Exp Cell Res.* 2011;317:2052–8.

433. Pamies R, Cifre JGH, Espín VF, Collado-González M, Baños FGD, de la Torre JG. Aggregation behaviour of gold nanoparticles in saline aqueous media. *J Nanoparticle Res.* 2014;16:2376. doi:10.1007/s11051-014-2376-4.
434. Yusa S, Fukuda K, Yamamoto T, Iwasaki Y, Watanabe A, Akiyoshi K, et al. Salt Effect on the Heat-Induced Association Behavior of Gold Nanoparticles Coated with Poly(N-isopropylacrylamide) Prepared via Reversible Addition–Fragmentation Chain Transfer (RAFT) Radical Polymerization. *Langmuir.* 2007;23:12842–8. doi:10.1021/la702741q.
435. Zhang Z, Maji S, Antunes AB da F, De Rycke R, Zhang Q, Hoogenboom R, et al. Salt Plays a Pivotal Role in the Temperature-Responsive Aggregation and Layer-by-Layer Assembly of Polymer-Decorated Gold Nanoparticles. *Chem Mater.* 2013;25:4297–303. doi:10.1021/cm402414u.
436. Boni L De, Corrêa DS, Mendonça CR. Nonlinear Optical Absorption of Organic Molecules for Applications in Optical Devices. In: Costa N, Cartaxo A, editors. *Advances in Lasers and Electro Optics.* InTech; 2010. p. 33–58.
437. Anwer AG, Gosnell ME, Perinchery SM, Inglis DW, Goldys EM. Visible 532 nm laser irradiation of human adipose tissue-derived stem cells: Effect on proliferation rates, mitochondria membrane potential and autofluorescence. *Lasers Surg Med.* 2012;44:769–78. doi:10.1002/lsm.22083.
438. Kassák P, Przygodzki T, Habodászová D, Bryszewska M, Sikurová L. Mitochondrial alterations induced by 532 nm laser irradiation. *Gen Physiol Biophys.* 2005;24:209–20. <http://www.ncbi.nlm.nih.gov/pubmed/16118473>.
439. Torchi A, Simonelli F, Ferrando R, Rossi G. Local Enhancement of Lipid Membrane Permeability Induced by Irradiated Gold Nanoparticles. *ACS Nano.* 2017;:acs.nano.7b06690. doi:10.1021/acs.nano.7b06690.
440. Tsai S-W, Huang W-Y, Liaw J-W, Rau L-R. Photothermal effects of laser-activated surface plasmonic gold nanoparticles on the apoptosis and osteogenesis of osteoblast-like cells. *Int J Nanomedicine.* 2016;Volume 11:3461–73. doi:10.2147/IJN.S108152.
441. American Cancer Society - Chemotherapy for Breast Cancer.
442. Dierickx CC, Anderson RR. Visible light treatment of photoaging. *Dermatol Ther.* 2005;18:191–208.
443. Azadgoli B, Baker RY. Laser applications in surgery. *Ann Transl Med.* 2016;4:452–452.
444. Schulze M. Medical Applications of Lasers : Diversity is Key to Success. *Laser iTechnik J.* 2010;7:32–5.

445. Weis SM, Cheresh DA. Tumor angiogenesis: molecular pathways and therapeutic targets. *Nat Med.* 2011;17:1359–70. doi:10.1038/nm.2537.
446. Verheul HM, Pinedo HM. The role of vascular endothelial growth factor (VEGF) in tumor angiogenesis and early clinical development of VEGF-receptor kinase inhibitors. *Clin Breast Cancer.* 2000;1:S80–4. doi:10.3816/CBC.2000.s.015.
447. Petreaca ML, Yao M, Liu Y, DeFea K, Martins-Green M. Transactivation of Vascular Endothelial Growth Factor Receptor-2 by Interleukin-8 (IL-8/CXCL8) Is Required for IL-8/CXCL8-induced Endothelial Permeability. *Mol Biol Cell.* 2007;18:5014–23. doi:10.1091/mbc.E07-01-0004.
448. Ziche M, Donnini S, Morbidelli L. Development of new drugs in angiogenesis. *Curr Drug Targets.* 2004;5:485–93. doi:10.2174/1389450043345371.
449. Vasudev NS, Reynolds AR. Anti-angiogenic therapy for cancer: Current progress, unresolved questions and future directions. *Angiogenesis.* 2014;17:471–94. doi:10.1007/s10456-014-9420-y.
450. Bazak R, Houry M, El Achy S, Hussein W, Refaat T. Passive targeting of nanoparticles to cancer: A comprehensive review of the literature. *Mol Clin Oncol.* 2014;2:904–8. doi:10.3892/mco.2014.356.
451. Bartczak D, Sanchez-Elsner T, Louafi F, Millar TM, Kanaras AG. Receptor-mediated interactions between colloidal gold nanoparticles and human umbilical vein endothelial cells. *Small.* 2011;7:388–94. doi:10.1002/sml.201001816.
452. Lampropoulou A, Ruhrberg C. Neuropilin regulation of angiogenesis: Figure 1. *Biochem Soc Trans.* 2014;42:1623–8. doi:10.1042/BST20140244.
453. Herzog B, Pellet-Many C, Britton G, Hartzoulakis B, Zachary IC. VEGF binding to NRP1 is essential for VEGF stimulation of endothelial cell migration, complex formation between NRP1 and VEGFR2, and signaling via FAK Tyr407 phosphorylation. *Mol Biol Cell.* 2011;22:2766–76. doi:10.1091/mbc.E09-12-1061.
454. Raimondi C, Brash JT, Fantin A, Ruhrberg C. NRP1 function and targeting in neurovascular development and eye disease. *Prog Retin Eye Res.* 2016;52:64–83. doi:10.1016/j.preteyeres.2016.02.003.
455. Bartczak D, Muskens OL, Millar TM, Sanchez-Elsner T, Kanaras AG. Laser-Induced damage and recovery of plasmonically targeted human endothelial cells. *Nano Lett.* 2011;11:1358–63. doi:10.1021/nl104528s.
456. Capon A, Mordon S. Can thermal lasers promote skin wound healing? *Am J Clin Dermatol.*

2003;4:1–12. doi:10.2165/00128071-200304010-00001.

457. Evans JR, Michelessi M, Virgili G. Laser photocoagulation for proliferative diabetic retinopathy. In: Evans JR, editor. *The Cochrane database of systematic reviews*. Chichester, UK: John Wiley & Sons, Ltd; 2014. p. CD011234. doi:10.1002/14651858.CD011234.pub2.

458. Niederer P, Fankhauser F. Theoretical and practical aspects relating to the photothermal therapy of tumors of the retina and choroid: A review. *Technol Heal Care*. 2016;24:607–26. doi:10.3233/THC-161163.

459. Capon A, Iarmarcovai G, Mordon S. Laser-assisted skin healing (LASH) in hypertrophic scar revision. *J Cosmet Laser Ther*. 2009;11:220–3. doi:10.3109/14764170903352878.

460. Nowak-Sliwinska P, Segura T, Iruela-Arispe ML. The chicken chorioallantoic membrane model in biology, medicine and bioengineering. *Angiogenesis*. 2014;17:779–804. doi:10.1007/s10456-014-9440-7.

461. Mira E, Lacalle RA, Buesa JM, de Buitrago GG, Jiménez-Baranda S, Gómez-Moutón C, et al. Secreted MMP9 promotes angiogenesis more efficiently than constitutive active MMP9 bound to the tumor cell surface. *J Cell Sci*. 2004;117:1847–57. doi:10.1242/jcs.01035.

462. Hanahan D, Bergers G, Brekken R, McMahon G, Vu TH, Itoh T, et al. Matrix metalloproteinase-9 triggers the angiogenic switch during carcinogenesis. *Nat Cell Biol*. 2000;2:737–44. doi:10.1038/35036374.

463. Ning Y, Manegold PC, Hong YK, Zhang W, Pohl A, Lurje G, et al. Interleukin-8 is associated with proliferation, migration, angiogenesis and chemosensitivity in vitro and in vivo in colon cancer cell line models. *Int J Cancer*. 2011;128:2038–49. doi:10.1002/ijc.25562.

464. Petzelbauer P, Watson CA, Pfau SE, Pober JS. IL-8 and angiogenesis: evidence that human endothelial cells lack receptors and do not respond to IL-8 in vitro. *Cytokine*. 1995;7:267–72. doi:10.1006/cyto.1995.0031.

465. Brat DJ, Bellail AC, Van Meir EG. The role of interleukin-8 and its receptors in gliomagenesis and tumoral angiogenesis. *Neuro Oncol*. 2005;7:122–33. doi:10.1215/S1152851704001061.

466. Li A, Dubey S, Varney ML, Dave BJ, Singh RK. IL-8 directly enhanced endothelial cell survival, proliferation, and matrix metalloproteinases production and regulated angiogenesis. *J Immunol*. 2003;170:3369–76. doi:10.4049/jimmunol.170.6.3369.

467. Guo S, Huang Y, Jiang Q, Sun Y, Deng L, Liang Z, et al. Enhanced Gene Delivery and siRNA Silencing by Gold Nanoparticles Coated with Charge-Reversal Polyelectrolyte. *ACS Nano*.

2010;4:5505–11. doi:10.1021/nn101638u.

468. Paul AM, Huang F, Bai F. Gold nanoparticle-mediated delivery of siRNA: a promising strategy in the treatment of mosquito-borne viral diseases? *Future Virol.* 2014;9:931–4. doi:10.2217/fvl.14.64.

469. Heinemann D, Schomaker M, Kalies S, Schieck M, Carlson R, Escobar HM, et al. Gold Nanoparticle Mediated Laser Transfection for Efficient siRNA Mediated Gene Knock Down. *PLoS One.* 2013;8:e58604. doi:10.1371/journal.pone.0058604.

470. Mendes R, Fernandes AR, Baptista P V. Gold Nanoparticle Approach to the Selective Delivery of Gene Silencing in Cancer-The Case for Combined Delivery? *Genes (Basel).* 2017;8:94. doi:10.3390/genes8030094.

471. Paul AM, Shi Y, Acharya D, Douglas JR, Cooley A, Anderson JF, et al. Delivery of antiviral small interfering RNA with gold nanoparticles inhibits dengue virus infection in vitro. *J Gen Virol.* 2014;95 Pt 8:1712–22. doi:10.1099/vir.0.066084-0.

472. Zadeh JN, Steenberg CD, Bois JS, Wolfe BR, Pierce MB, Khan AR, et al. NUPACK: Analysis and design of nucleic acid systems. *J Comput Chem.* 2011;32:170–3. doi:10.1002/jcc.21596.

473. Zhang W, Ling V. Cell-cycle-dependent turnover of P-glycoprotein in multidrug-resistant cells. *J Cell Physiol.* 2000;184:17–26. doi:10.1002/(SICI)1097-4652(200007)184:1<17::AID-JCP2>3.0.CO;2-U.

474. O'Driscoll L, Gammell P, McKiernan E, Ryan E, Jeppesen PB, Rani S, et al. Phenotypic and global gene expression profile changes between low passage and high passage MIN-6 cells. *J Endocrinol.* 191:665–76. doi:10.1677/joe.1.06894.

475. Wenger SL, Senft JR, Sargent LM, Bamezai R, Bairwa N, Grant SG. Comparison of Established Cell Lines at Different Passages by Karyotype and Comparative Genomic Hybridization. *Biosci Rep.* 2004;24:631 LP – 639. doi:10.1007/s10540-005-2797-5.

476. Mouriaux F, Zaniolo K, Bergeron M-A, Weidmann C, De La Fouchardière A, Fournier F, et al. Effects of Long-term Serial Passaging on the Characteristics and Properties of Cell Lines Derived From Uveal Melanoma Primary Tumors Characteristics of Passaged UM Cells. *Invest Ophthalmol Vis Sci.* 2016;57:5288–301. doi:10.1167/iovs.16-19317.

477. Tosca L, Feraud O, Magniez A, Bas C, Griscelli F, Bennaceur-Griscelli A, et al. Genomic instability of human embryonic stem cell lines using different passaging culture methods. *Mol Cytogenet.* 2015;8:30. doi:10.1186/s13039-015-0133-8.

478. Chang-Liu C-M, Woloschak GE. Effect of passage number on cellular response to DNA-

damaging agents: cell survival and gene expression. *Cancer Lett.* 1997;113:77–86. doi:[https://doi.org/10.1016/S0304-3835\(97\)04599-0](https://doi.org/10.1016/S0304-3835(97)04599-0).

479. Kim M, Rhee J-K, Choi H, Kwon A, Kim J, Lee GD, et al. Passage-dependent accumulation of somatic mutations in mesenchymal stromal cells during in vitro culture revealed by whole genome sequencing. *Sci Rep.* 2017;7:14508. doi:[10.1038/s41598-017-15155-5](https://doi.org/10.1038/s41598-017-15155-5).

APPENDICES

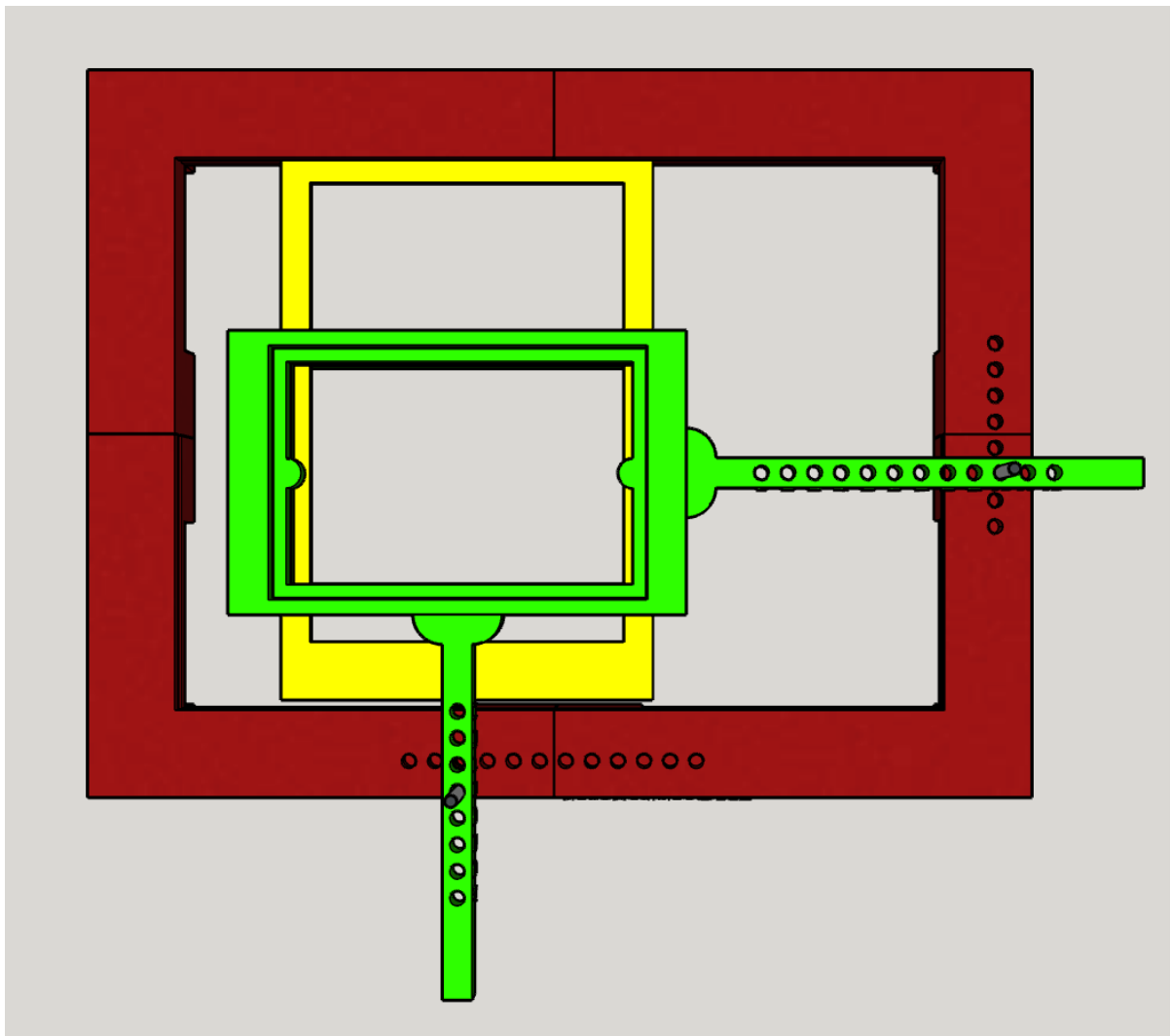


Fig. A.1 Top view of the blueprint of manual well plate mover.

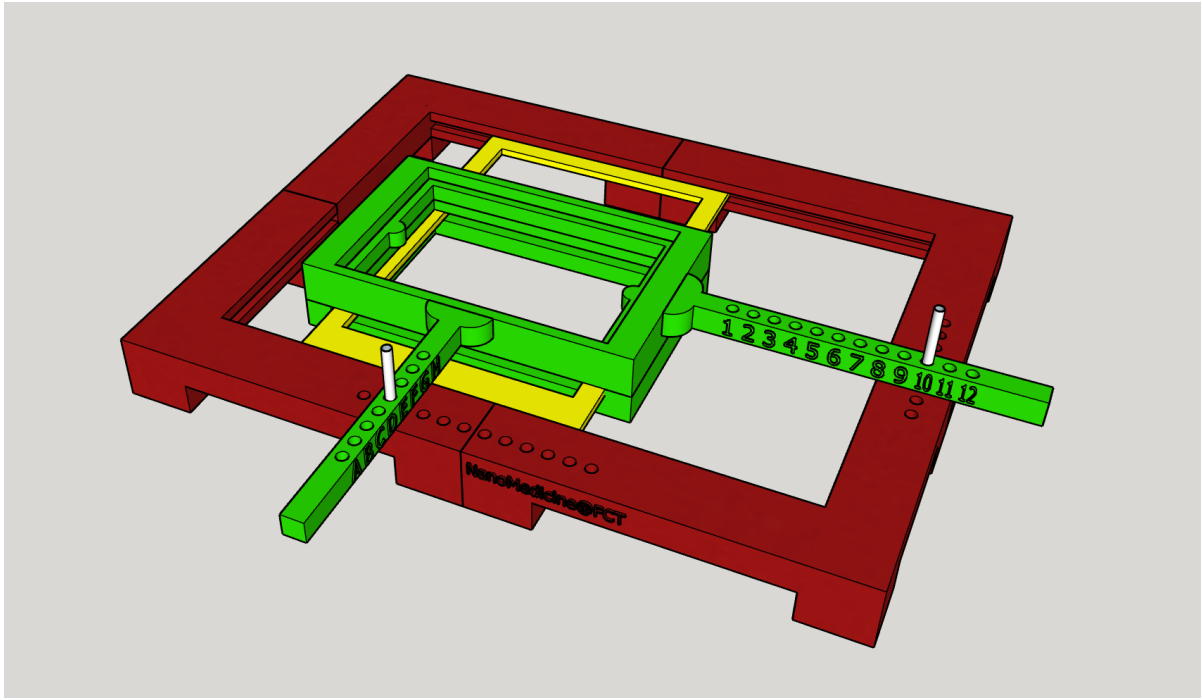


Fig. A.2 Perspective view of the blueprint of manual well plate mover.